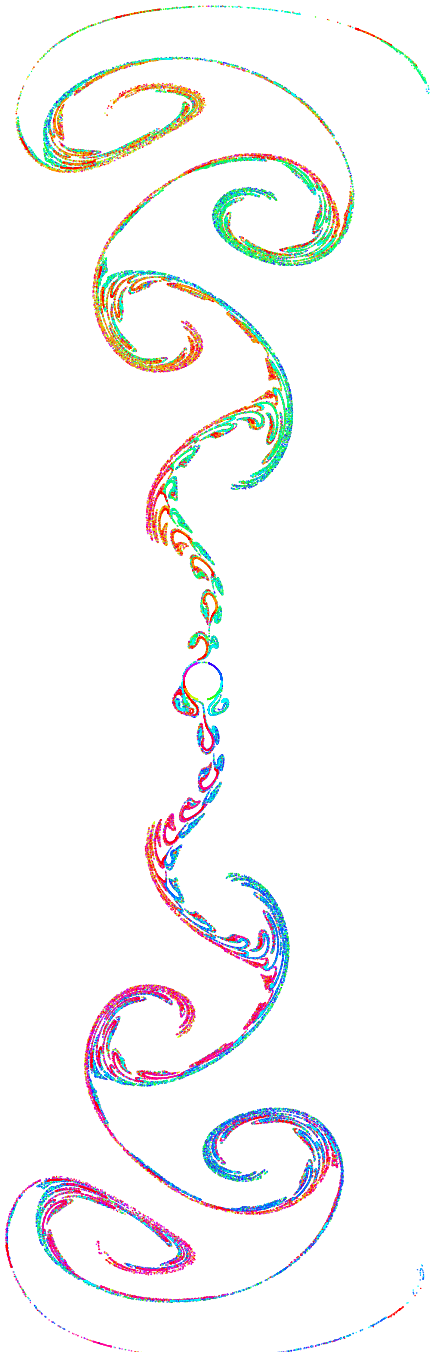

The Structures and Instabilities of Flow Generated by an Oscillating Circular Cylinder



A thesis submitted in accordance with the
regulations of Monash University, Australia
in partial fulfillment of the requirements
for the degree of Doctor of Philosophy.

By

John Robert Elston

BSc.(Appl. Maths, Phys) BE.(Mech, *Hons*)

Submitted

March 14, 2006

Department of Mechanical Engineering
Monash University, Victoria, 3800
Australia

Table of Contents

Abstract	iv
Statement of Originality	vi
Acknowledgements	vii
Publications Relating to Thesis	viii
Nomenclature	ix
1 Introduction	1
1.1 Research Problem Definition	3
1.2 Structure of the Thesis	7
2 Literature Review	8
2.1 Stationary Cylinder in a Free Stream	9
2.1.1 Laminar Steady Regime ($Re < 46$)	9
2.1.2 Primary Wake Instability ($Re \approx 46$)	11
2.1.3 Laminar Vortex Shedding Regime ($46 < Re < 188.5$)	11
2.1.4 Secondary Instability ($Re \approx 188.5$)	12
2.1.5 3-D Wake Transition Regime ($188.5 < Re < 259$)	14
2.1.6 Fine Scale 3-D Wake Regime ($259 < Re < 1000$)	17
2.2 Forced Cylinder Vibration in a Free Stream	17
2.2.1 Transverse Oscillations	18
2.2.1.1 Primary Lock-In Region	18
2.2.1.2 Vortex Shedding Structures	20
2.2.1.3 Vortex Shedding Timing in the Lock-In Regime	20
2.2.2 Inline and Oblique Oscillations	21
2.3 Rotational Oscillation in a Free Stream	23
2.4 Rectilinear Oscillation in Quiescent Fluid	25
2.5 Combined Rotational and Rectilinear Oscillation	37
2.5.1 Carangiform Motion	41

2.6	Summary	42
3	Numerical Method: Spectral Element Method	43
3.1	Governing Flow Equations	44
3.1.1	Moving Frame of Reference	44
3.2	Spectral Element Method	46
3.2.1	Temporal Discretisation	46
3.2.2	Spatial Discretisation	48
3.2.2.1	Two-Dimensional Spectral Element Discretisation . . .	48
3.2.2.2	Three-Dimensional Fourier Discretisation	51
3.3	Post Processing	52
3.3.1	Force Calculation	52
3.3.2	Vorticity Calculation	52
3.3.3	Energy Calculation	53
3.4	Validation	54
3.4.1	Mesh Selection	54
3.4.1.1	Temporal Resolution	54
3.4.1.2	Domain Size Resolution	55
3.4.1.3	Spatial Order Resolution	58
3.5	Chapter Summary	60
4	Numerical Methods: Floquet Stability Analysis	61
4.1	Linearised Navier–Stokes Formulation	62
4.2	Stability Analysis of Steady-State Flows	63
4.3	Floquet Analysis	65
4.4	Validation Tests	67
4.4.1	Poiseuille Flow - A Steady State Problem	68
4.4.2	Circular Cylinder Wake - A Floquet Problem	70
4.5	Chapter Summary	72
5	Rectilinear Oscillation: Symmetric Synchronised Flow	73
5.1	Introduction	73
5.2	Two-Dimensional Base States	75
5.2.1	Point I: $KC=2, \beta = 80.0$	77
5.2.2	Point II: $KC=4, \beta = 40.0$	82
5.2.3	Point III: $KC=7, \beta=10.0$	84
5.2.4	Point IV: $KC=3, \beta = 80.0$	87
5.3	Discussion	92
5.4	Symmetry Definitions	94

5.5	Summary	96
6	Rectilinear Oscillation: Symmetry Breaking in a Two–Dimensional Subspace	97
6.1	Curve of Marginal Stability	99
6.2	Synchronous Regime S	104
6.3	Quasi-Periodic Regime QP	111
6.4	Secondary Transitions beyond Criticality	124
6.5	Discussion	130
6.6	Summary	136
7	Rectilinear Oscillation: Symmetry Breaking in Three–Dimensional Space	137
7.1	Marginal Stability Curves	139
7.2	Regime A [*] – B	143
7.3	Regime A – D	151
7.4	Regime C	160
7.5	Discussion	166
7.6	Summary	169
8	The ‘Swimming’ Cylinder	170
8.1	Problem Definition & Numerical Validation	171
8.1.1	Mesh and Boundary Conditions	172
8.1.2	Convergence Studies	173
8.2	‘Fixed’ Cylinder at $V_r = 1.0$	175
8.3	‘Swimming’ Cylinder at $V_r = 1.0$	179
8.4	‘Swimming’ Cylinder Simulations with Varying V_r	181
8.5	Discussion	187
8.6	Summary	189
9	Conclusions	190
9.1	Rectilinear Oscillations of a Circular Cylinder	190
9.2	The ‘Swimming’ Cylinder	193
9.3	Directions for Future Work	195
A	Bibliography	196

Abstract

This computational study investigates the primary instabilities of the flow produced by a circular cylinder with simple harmonic motion in quiescent fluid and additionally examines the effect on the flow structures generated by combining this with a rotational oscillation. A circular cylinder performing simple harmonic rectilinear oscillations in a quiescent fluid, or, alternatively, oscillating flow past a stationary cylinder, at low Keulegan–Carpenter numbers, KC , and Stokes numbers, β , is known to produce a number of flow regimes within the control-parameter range ($KC \in [0, 10]$, $\beta \in [0, 100]$), each with distinctive spatial and temporal characteristics. The identification and location of these regimes in (KC, β) -space has in the past primarily been achieved through experimental visualisation of dye and particle shedding patterns. In this investigation the characteristics and locations of the two- and three-dimensional instabilities of the initially two-dimensional symmetric flow generated by a circular cylinder in rectilinear oscillation are determined via Floquet analysis and direct numerical simulation. Additionally, it has also been shown numerically that by combining a rotational oscillation with the rectilinear motion, a thrust can be generated in a direction perpendicular to the axis of rectilinear oscillation. This thrust is examined and the influence of the velocity ratio between the two oscillations is qualitatively studied.

At very low amplitudes and frequencies of rectilinear oscillation the flow produced by a circular cylinder is known to be symmetrical and two-dimensional. It is found that while the initial bifurcations produced by increasing the parameters can be to three-dimensional flows, much of the behaviour can be explained in terms of two-dimensional symmetry breaking instabilities. These have two primary manifestations: at low Stokes numbers, the instability is synchronous with the imposed oscillation, and gives rise to a boomerang-shaped mode, while at higher Stokes numbers, the instability is quasi-periodic, with a well-defined second period, which becomes infinite as Stokes numbers are reduced along the marginal stability boundary, ‘freezing’ the quasi-periodic mode into a synchronous one. The synchronous two-dimensional mode is, with further small increase in control parameter, unstable to three-dimensional secondary instabilities with the resultant flow resembling the flow observed by experimental visualisation. A three-dimensional instability mode occurs at approximately the same location as a portion of the two-dimensional quasi-periodic mode. It has the same signature temporal characteris-

tics of the two-dimensional quasi-periodic mode and resembles experimentally observed flows at the same location in (KC, β) -space. At low Keulegan–Carpenter numbers, and high Stokes numbers, below the onset in (KC, β) -space of a portion of the two-dimensional quasi-periodic mode, a primary three-dimensional instability occurs. This primary instability arises directly from the two-dimensional symmetrical state and gives rises to flows that were first reported by Honji (1981).

When rotational oscillation is added to the two-dimensional rectilinear oscillation of a circular cylinder in quiescent fluid it is possible to generate time-mean forces in a direction perpendicular to the axis of rectilinear oscillation. If the cylinder is permitted to move along the axis perpendicular to the rectilinear oscillation in response to the time-mean force it eventually reaches a terminal velocity, at which point the time-mean force propelling the cylinder is balanced by the force due to the incident flow. The force propelling the cylinder is due to both a viscous component and a pressure component that arise from the combination of oscillations employed. Particular ratios of the rectilinear to rotational velocity are found to be more effective at creating a time-mean force. The velocity ratio of the oscillations also produces significant changes in the wake of the ‘swimming’ cylinder with the narrowest wake structure corresponding with the highest terminal velocity.

Statement of Originality

This thesis contains no material which has been accepted for the award of any other degree or diploma in any university, and, to the best of my knowledge and belief, contains no material previously published or written by another person, except where due reference is made in the text.

John R. Elston
March 14, 2006

Acknowledgements

I would like to express my gratitude to my supervisors Professor John Sheridan and Dr Hugh Blackburn for all the assistance and guidance they have provided over the duration of my candidature. They have shown a remarkable amount of patience over that time, and in truth, it is probably more than I deserved. In particular I would like to extend my heartfelt thanks to Dr Hugh Blackburn who has both provided the numerical tools employed in this thesis and for all the countless hours of guidance and technical assistance.

This work was aided by the provision of experimental images and a template for the implementation of a Floquet solver. I would like to thank D. Barkley, whose implementation of a Floquet solver served as the backbone for much of the research conducted in this Thesis. I would also like to thank M. Tatsuno and P. W. Bearman for their assistance in supplying many of the experimental images used in this thesis.

To all my fellow postgraduate students, office-dwellers and cubicle inhabitants: thank you for the times we have shared, the technical assistance and, of course, the ample avenues of distraction and procrastination you have provided.

I wish to thank the Department of Mechanical Engineering for providing the resources necessary for the completion of this study and most importantly I extend my thanks to the staff who made things happen.

I have received financial assistance from a number of sources over the duration of my candidature and I would like to gratefully acknowledge the support provided through an Australian Postgraduate Award (APA) scholarship and a Departmental scholarship sponsored by CSIRO. This research also received support from both the Australian Partnership for Advanced Computing and the Victorian Partnership for Advanced Computing. I would also like to extend my thanks to my employer in recent times, Professor Rhys Jones, who has shown patience with me as I completed my studies.

Publications Relating to Thesis

Elston, J. R., Sheridan, J. and Blackburn H. M. (2001). The transition to three-dimensionality in the flow produced by an oscillating circular cylinder, *In proceedings of the 14th Australasian Fluid Mechanics Conference*. University of Adelaide, Adelaide, South Australia, Australia, December 2001. pp. 319–322.

Elston, J. R., Sheridan, J. and Blackburn H. M. (2002). Two-dimensional Floquet stability analysis of the flow produced by an oscillating circular cylinder in quiescent fluid, *In proceedings of the 3rd Conference on Bluff Body and Vortex Induced Vibrations*. Rydges Reef Resort, Port Douglas, Queensland, Australia. December 2002. pp. 179–182.

Elston, J. R., Sheridan, J. and Blackburn H. M. (2004). Two-dimensional Floquet stability analysis of the flow produced by an oscillating circular cylinder in quiescent fluid, *European Journal of Mechanics B/Fluids*. **23**: 99–106.

Elston, J. R., Sheridan, J. and Blackburn H. M. (2005). Three-dimensional Floquet stability analysis of the flow produced by an oscillating circular cylinder in quiescent fluid, *In proceedings of the 4th Conference on Bluff Body and Vortex Induced Vibrations*. Santorini, Greece, June 2005.

Elston, J. R., Blackburn, H. M. and Sheridan, J. (2005). The primary and secondary instabilities of flow generated by an oscillating circular cylinder, *Accepted for publication in J. Fluid Mech.* September 2005.

Nomenclature

Symbol	Description
β	Stokes number.
β_θ	Rotational Stokes number.
χ	Angle between rectilinear oscillation and free stream flow.
ϕ	Phase angle between rotational and rectilinear oscillations.
θ	Angular displacement.
ν	Kinematic viscosity.
μ	Floquet multiplier.
	Dynamic viscosity.
ρ	Density.
λ	Spanwise wavelength.
ξ	Vorticity vector.
σ	Floquet exponent = $\log(\mu/T)$.
$\omega_x, \omega_y, \omega_z$	Vorticity components along the x , y and z axis respectively.
Ω	Computational domain.
∇	Vector gradient operator (grad).
∇^2	Del squared (or div grad) operator.
\mathbf{a}	Acceleration vector of the reference frame.
A_θ	Amplitude of rotational oscillation in radians.
A_t	Amplitude of rectilinear oscillation.
b	Damping constant.
B	Operator evolving the perturbation to the base flow over one period, T .
c	Stiffness constant.
\hat{C}_{fy}	Peak coefficient of force per unit length along the y -axis.
C_{pb}	Base pressure coefficient.
C_{px}	Coefficient of force due to pressure in the x -direction.
C_{vx}	Coefficient of force due to viscosity in the x -direction.
\bar{C}_x	Mean force coefficient in the x -direction.
D	Cylinder Diameter.
E_k	Normalised amount of energy in each Fourier mode k .

Continued on next page...

Symbol	Description
f_θ	Frequency of rotational oscillation.
f_n	Natural frequency of vortex shedding.
f_t	Frequency of rectilinear oscillation.
f_v	Frequency of vortex shedding.
\mathbf{f}_p	Force vector due to pressure.
\mathbf{f}_v	Force vector due to viscosity.
\mathbf{f}_T	Total force vector.
F_x	Net force per unit length along the x -axis.
H_1	A spatio-temporal symmetry.
H_2	A spatio-temporal symmetry.
k	Spanwise wavenumber.
K	Order of Krylov matrix.
K_x	Reflection symmetry in $x = 0$.
K_z	Reflection symmetry in $z = 0$.
KC	Keulegan–Carpenter number.
L	Linear operator of the Navier–Stokes equations.
L_N	Legendre polynomial of degree N .
L_z	Spanwise length scale.
m	Mass per unit length.
\mathbf{n}	Vector normal.
N_{el}	Number of elements in a computational domain.
N_p	Order of the spectral element interpolants.
N_U	T -periodic linearised operator $\equiv (\mathbf{u}' \cdot \nabla) \mathbf{U} + (\mathbf{U} \cdot \nabla) \mathbf{u}'$.
$\mathbf{N}(\mathbf{u})$	Non-linear advection term in the Navier–Stokes equations.
p	Pressure field.
	Interpolant polynomial order.
p'	Pressure field of perturbation.
\tilde{p}	Field coupling the momentum and continuity equations.
P	Kinematic pressure $= p/\rho$.
R_α	Translation symmetry along the $z - axis$.
Re	Reynolds number based on free stream velocity and cylinder diameter.
Re_t	Reynolds number of an oscillating cylinder $= KC\beta$.
St	Strouhal Number.
St_f	Strouhal Number based on frequency of rotational oscillation.
t	Time.
T	Oscillation period.
T_s	Secondary oscillation period.

Continued on next page...

Symbol	Description
u, v, w	Velocity components in the x, y and z directions respectively.
$\tilde{u}(t)$	T -periodic Floquet eigenfunction.
\mathbf{u}	Velocity vector.
\mathbf{u}^n	Semi-discrete approximation (in time) to the velocity vector.
\mathbf{u}'	Perturbation velocity vector.
\mathbf{u}_θ	Rotational velocity vector of a point on the surface of the cylinder.
$\hat{\mathbf{u}}$	Fourier component of the velocity field.
\mathbf{U}	Two-dimensional ‘base’ flow.
U_p	Prescribed velocity on a boundary of the computational domain.
U_{rms}	Root Mean Square velocity.
U_∞	Free stream velocity.
v_t	Peak velocity of rectilinear oscillation.
v_θ	Peak velocity of rotational oscillation.
\mathbf{v}	Velocity vector of the reference frame.
V_r	Velocity ratio between translational and rotational oscillation = v_t/v_θ .

Chapter 1

Introduction

This thesis presents the results of a numerical investigation into the flows produced by a bluff body subjected to oscillatory motion in a Newtonian fluid. Oscillatory flow about bluff bodies is a situation that occurs in a multitude of cases involving man-made structures and throughout nature. In such cases the oscillatory flow relative to the bluff body can, dependent upon the amplitude and frequency of oscillation, produce flow structures that are either constant or varying along the cylinder span, which in turn, results in a variety of hydrodynamic forces acting upon the bluff body. Typical situations where this occurs with man-made structures are seen by analysing the action of waves against pier pylons and past the support structures of offshore oil platforms. In nature, a number of oceanic animals have evolved a highly efficient propulsive mechanism that is, in its simplest form, a body subjected to both a lateral and twisting oscillatory motion. This means of propulsion, known as Carangiform motion, involves the animals tail fin being subjected to a twisting motion at the extreme ends of the fins lateral oscillatory motion. It is a highly effective form of propulsion and is used by a number of the fastest swimming oceanic lifeforms such as dolphins, marlin and some families of sharks. The symmetrical winglike fins used in generating this thrust all have a large aspect ratio in common and are decidedly streamlined. However in this thesis, a circular cylinder is used as the bluff body due to its geometrical and mathematical simplicity, its applicability to man made structures and the abundance of literature and previous investigations regarding flow-cylinder interactions.

The structures formed by an oscillating cylinder are highly dependent upon the characteristics of the cylinder oscillation and are additionally influenced by the presence of an external flow. In a quiescent fluid, at very low amplitudes and frequencies of rectilinear oscillation, the flow about a circular cylinder is symmetric about its axis of oscillation and is two-dimensional (it has no variation along the span), attached and non-turbulent. However as either, or both, of these parameters increase, the flow structures produced by the cylinder change dramatically. The initial symmetry is lost and a number of two-

and three-dimensional structures are seen in the cylinder wake. An example of this is the ‘streaked flow’ observed by Honji (1981) wherein regularly spaced chains of dye were seen to form along the cylinder span for a particular envelope of amplitudes and frequencies of oscillation.

If, in addition to the translational oscillation of the cylinder relative to the surrounding flow, a rotational oscillation is imposed upon the cylinder, the structures formed and the forces produced on the cylinder alter substantially. There have been many studies of simple individual cases of cylinders performing a single oscillation type in either a quiescent or free stream flow. However, there is a notable absence of research into the effects of combining the rotational and rectilinear oscillation types. To date only a limited investigation by Elston (1997), Blackburn, Elston and Sheridan (1998) and Blackburn, Elston and Sheridan (1999) has been performed into this topic. A key finding of these investigations was that a time-averaged net thrust could be generated by the forced oscillation of a circular cylinder in a combination of rotational and translational motion.

The previous paragraphs outlined two aspects that were focused upon in this investigation: namely the onset of two- and three-dimensional flow structures for a cylinder in rectilinear motion and secondly the situation where an additional rotational oscillation was applied to the cylinder in rectilinear motion. This investigation was conducted using a spectral element method to directly model the fluid dynamics. As a component of the research involves determining stability boundaries and three-dimensional wavelengths, a technique known as Floquet analysis was implemented in addition to the Direct Numerical Simulation (DNS) method used. This stability technique enabled the determination of which three-dimensional wavelengths would become unstable and was used to investigate the stability of the two and three dimensional flows and as an aid in the subsequent three-dimensional DNS simulations.

1.1 Research Problem Definition

The problem being considered here involves a circular cylinder being subjected to one or more modes of oscillation while surrounded by either an externally imposed flow or by a quiescent fluid. The surrounding fluid was considered to be incompressible and Newtonian. Simple harmonic forms of translational and rotational oscillation were used for all the modes of imposed oscillation considered in this thesis. The equations of motion detailing how the cylinder moves under the action of these forcing oscillations and the parameters affecting these oscillations are detailed in the following paragraphs and illustrated in the schematic of figure 1.1.

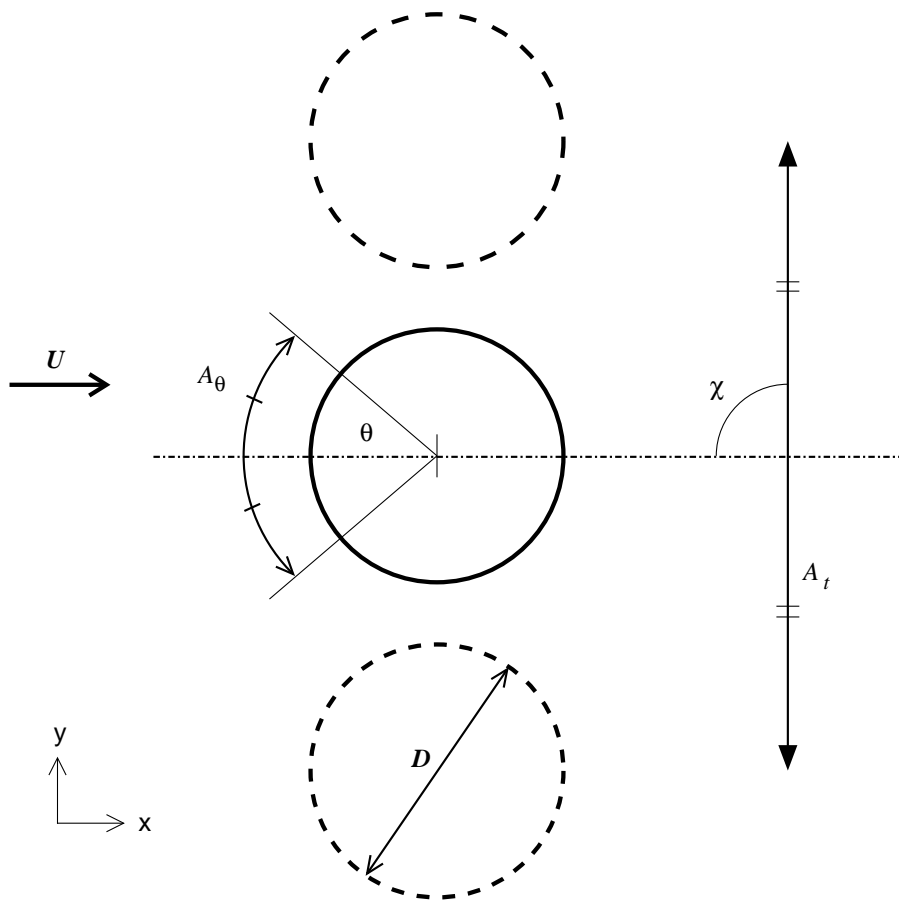


Figure 1.1: Schematic showing the two-dimensional problem geometry and important parameters relevant to the forcing oscillations.

For a cylinder subjected to a combined rotary and translational oscillation there are five dimensionless parameters governing its motion. The rotational and translational oscillations each have two parameters which define the respective motions and an additional fifth parameter exists which is the phase angle between these harmonic motions.

The equation of motion for a cylinder of diameter D in rectilinear oscillation along

1.1. RESEARCH PROBLEM DEFINITION

the y -axis is described by:

$$y(t) = A_t \cos(2\pi f_t t) \quad (1.1)$$

where A_t is the amplitude of oscillation and f_t is the frequency of oscillation for a cylinder oscillating along the y -axis. The rotational oscillation of the cylinder about its axis is described by:

$$\theta(t) = A_\theta \cos(2\pi f_\theta t + \phi) \quad (1.2)$$

where A_θ is the oscillation amplitude and f_θ is the oscillation frequency. The angle, ϕ , represents the phase angle between the rotational and rectilinear oscillations.

The five dimensionless parameters controlling the oscillations are defined as follows. Two parameters determine the state of the rectilinear oscillation in a fluid of kinematic viscosity ν . These are the Keulegan–Carpenter number

$$KC = \frac{2\pi A_t}{D} \quad (1.3)$$

and the Stokes number.

$$\beta = \frac{f_t D^2}{\nu} \quad (1.4)$$

The Keulegan–Carpenter number was introduced by Keulegan and Carpenter (1958) who found that the average values of the drag coefficients of a vertical cylinder subjected to a standing wave were functions of this parameter. The Stokes number is originally derived from Stokes's work on a vibrating string at very low Reynolds numbers, although recent literature attributes the use of this nomenclature to Sarpkaya (1986). An alternative to either of these parameters is the Reynolds number, $Re_t = KC\beta$, although this is less common in the published literature than the use of KC and β .

In the same manner, two parameters determine the state of the rotational oscillation. Previous research into rotary oscillations, such as that of Taneda (1978) or Tokumaru and Dimotakis (1991), have involved a freestream flow of constant velocity which was used to nondimensionalise the frequency of oscillation. This is not applicable to the situation where a quiescent fluid is present and therefore a convention similar to that used above for the rectilinear oscillation was settled upon. The parameter adopted to nondimensionalise the frequency of rotary oscillation is:

$$\beta_\theta = \frac{f_\theta D^2}{\nu} \quad (1.5)$$

The amplitude of the rotary oscillation, A_θ , was used as the fourth governing parameter and required no nondimensionalisation as it is an angle. This is inline with the convention used by Taneda (1978) who also used this as a governing parameter. The fifth parameter is that of the phase angle, ϕ , between the two harmonic motions.

The spanwise length of the cylinder projects into the third dimension (the z -axis) and

1.1. RESEARCH PROBLEM DEFINITION

is considered to be infinite in the numerical simulations to be discussed, although when results are compared with experimental results the impact of a finite spanwise length will be discussed as appropriate. While the majority of the investigation comprises rectilinear oscillations in a quiescent fluid, in some cases a cross flow can occur. In these cases the angle, χ , between the direction of the cross-flow and axis of the rectilinear oscillation becomes a relevant parameter. In this thesis the direction of an external flow will be taken as being from the left (with reference to figure 1.1) or along the x -axis. Rectilinear oscillations that are at right angles ($\chi = 90$) to this are defined as translational oscillations while those with zero angle ($\chi = 0$) are defined as inline.

It should be noted that the aspect of rectilinear oscillation of a cylinder in fluid, either in a quiescent fluid or in a cross-flow, has received a great deal of attention in the published literature. Largely this has been motivated by application to marine environments at high β numbers while at lower β numbers there has been considerable interest in the way in which vortices are created and shed. In the low (KC, β)-space a number of regimes have been identified, typically through experimental visualisation, by their two- and three-dimensional spatial and temporal characteristics of particle shedding. However little attention has been paid to why the transitions between these regimes occur, nor to the nature of these transitions. Additionally most of the previous research has been either experimental or two-dimensional numerical simulations. In contrast, the combined rotational and translational oscillation of a cylinder has received very little attention. In a two-dimensional simulation, Blackburn, Elston and Sheridan (1999) have shown that a cylinder subjected to this form of motion can produce a net thrust. However, to date, no three-dimensional simulations or experimental research has investigated this result.

The investigation is composed of two components:

1. The principle focus is an investigation of the primary two- and three-dimensional transitions for a cylinder performing rectilinear oscillation in a quiescent fluid. The investigation will focus upon identifying the type of transition occurring and in the event of a three-dimensional transition, determine the critical wavenumbers of the instability. To facilitate this a Floquet stability analysis technique is implemented in order to perform a linear stability analysis of the underlying periodic flow.
2. The mechanism resulting in the combined rotational and rectilinear oscillation of a circular cylinder producing a time-averaged thrust is examined. Additionally the influence of rotational oscillation on the near wake structure and the time-averaged thrust is investigated.

A spectral element method is used for the DNS computations. A spectral element spatial discretisation is applied for three-dimensional simulations in the x - y plane while along the z -axis a Fourier discretisation is employed. The technique implemented uses a

1.1. RESEARCH PROBLEM DEFINITION

fixed computational grid attached to the cylinder which does not deform to allow cylinder motion, instead it moves with the cylinder. The consequence of this is that the force experienced by the cylinder is different than the force it would experience if it had been fixed and the fluid oscillated about it. The Floquet stability analysis technique is implemented using the spectral element technique to provide the periodic flows whose stability is to be examined.

1.2. STRUCTURE OF THE THESIS

1.2 Structure of the Thesis

The thesis is structured as follows:

Chapter 2: A review of the relevant literature is conducted in order to assess the current state of knowledge, and to highlight unanswered questions and gaps in the existing research.

Chapter 3: The computational method used to simulate the nonlinear flows is outlined. A spectral element discretisation is used for two-dimensional flow simulations. In the three-dimensional simulations the same spectral element discretisation is employed in a two-dimensional plane while in the direction perpendicular to this plane a Fourier discretisation is employed.

Chapter 4: A core component of the research presented in this thesis is the use of linear stability analysis. In this chapter the technique and details of implementation of Floquet stability analysis are described.

Chapter 5: An investigation of the flow generated at very low amplitudes and frequencies of rectilinear oscillation is made. This chapter serves to illustrate the properties of the symmetric base flows and to define the symmetries present in this base flow state.

Chapter 6: The location, in a restricted two-dimensional space, of the onset of a bifurcation from the symmetric base flow outlined in the previous chapter is determined. The nature of the resultant states are explored using nonlinear DNS and Floquet analysis.

Chapter 7: The location, in a full three-dimensional space, of the onset of a bifurcation from two-dimensional symmetric base flows or flows that have broken two-dimensional symmetry are determined. The nature of the resultant states are explored using nonlinear DNS and Floquet analysis.

Chapter 8: The ‘swimming’ cylinder problem of a cylinder in combined rectilinear and oscillatory motion is examined briefly. The mechanism by which a force is generated is explored and the impact of the various parameters controlling the motion of the resultant flow is investigated.

Chapter 9: The results obtained in the previous chapters are summarised and potential future directions for research in this area are discussed.

Appendix A: A bibliography that contains all the references cited throughout the body of this thesis.

Chapter 2

Literature Review

In the following sections previous research into aspects of a cylinder oscillating in a fluid are examined. In particular two specific phenomena that, in part, provided the motivation for this research will be examined in greater detail. The first of these phenomena arises from the research of Honji (1981), Williamson (1985) and Tatsuno and Bearman (1990) who collectively observed that the rectilinear oscillation of a circular cylinder at low amplitudes and frequencies of oscillation in a quiescent fluid, or equivalently a fixed cylinder in sinusoidally oscillating flow, can generate a set of intriguing flow structures. Tatsuno and Bearman (1990) defined a number of unique regimes, on the basis of the distinctive flow structures shed from the cylinder, that were observed to occur over a very small range of Keulegan–Carpenter and Stokes numbers.

The second phenomenon of interest is observed when a harmonic rotational oscillation is imposed upon the cylinder in addition to the aforementioned rectilinear motion. It has been computationally shown by Blackburn, Elston and Sheridan (1999) that, for particular phase angles between the two forms of oscillations, a net thrust can be produced by the cylinder which acts upon the surrounding fluid and results in a time-averaged flow past the cylinder. This motion combination has also been identified, see for example Lighthill (1986), as being the propulsion mechanism used by the fastest deep sea marine animals. These animals, a small sample of which includes tuna, swordfish, sharks, whales and dolphins, utilise a form of tailfin motion identified as *carangiform* motion that in its simplest form can be related back to a bluff body performing translational and rotary oscillation. Although in carangiform motion, the phase angle between the rotational and translational motions is the reverse of that found to produce a thrust by Blackburn, Elston and Sheridan (1999) with a circular cylinder.

In the following sections previous work on cylinders oscillating in either a rotational or translational motion in a fluid will be examined. As this combination of oscillations has been shown to produce a net external flow, studies of forced oscillations in both quiescent and external flows will be examined. Initially we start by reviewing a stationary cylinder

2.1. STATIONARY CYLINDER IN A FREE STREAM

with no oscillation in a free stream and then review the influence of the addition of either oscillatory motion types with or without the free stream presence.

2.1 Stationary Cylinder in a Free Stream

Steady flow past a circular cylinder in an infinite medium has been one of the most extensively studied problems of fluid dynamics. One of the most notable and historically significant of these studies was that by Strouhal (1878) who examined the Aeolian tones produced by wires vibrating in the wind. His observations permitted him to conclude that the dynamics of this experiment were characterised by a relationship between the frequency of sound produced by the wire and the fluid velocity past the wire. In a similar manner the fluid dynamics of flow past a fixed cylinder have been characterised by a number of parameters, of which the most critical is the Reynolds number. This defining parameter, which relates the flow inertia to the viscous effects on a body, has been used by many researchers as a means of reducing and compacting their observations and results to a common form. In the case of the fixed cylinder in a free stream, the location of the major regimes of vortex shedding and the critical transition points between these regimes are typically characterised in terms of the Reynolds number.

The regimes can be distinguished through a number of qualitative and quantitative means, the most common of which are plots of the base pressure coefficient C_{pb} , or Strouhal number St , as a function of Reynolds number. In figure 2.1 measurements of the base pressure coefficient are plotted as function of the Reynolds number over the range $10 - 1000$ in order to illustrate the four regimes that occur over this Reynolds number range and to serve as a basis for further discussion. There exist a substantial number of regimes above $Re = 1000$, however these are beyond the domain of interest of this investigation and will not be considered here. The values quoted in Figure 2.1 and in the following discussion for the locations of the Regime transitions are derived from Barkley and Henderson (1996). These are numerically derived values and the variation of these from experimentally derived values, such as those cited in the review of Williamson (1996b), can in some cases be ascribed to experimental aspects such as roughness, turbulence levels, cylinder aspect ratio and blockage. However this is insufficient to completely describe the variance and in the following sections these regimes and the discrepancies between the numerical and experimental transition locations will be examined in more detail.

2.1.1 Laminar Steady Regime ($Re < 46$)

In the Reynolds number range $0 < Re < 46$ a steady two-dimensional recirculation region forms behind the cylinder, see Figure 2.2. This wake region consists of two vortices symmetrically placed on either side of the wake centreline, which together form a sym-

2.1. STATIONARY CYLINDER IN A FREE STREAM

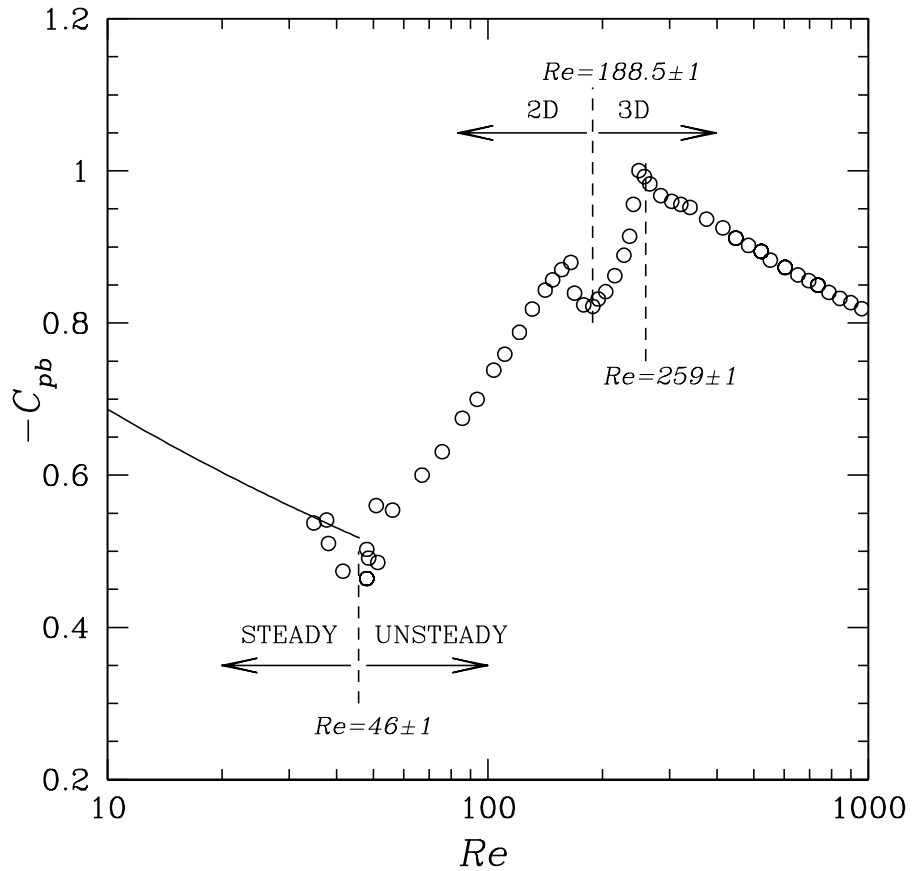


Figure 2.1: Variation of base suction coefficient ($-C_{pb}$) over the Reynolds number range $10 - 1000$. Data is obtained from the experiments of Williamson and Roshko (1990), \circ , the numerical computations of Henderson (1995), —, and the numerical analysis of Barkley and Henderson (1996), - - -.

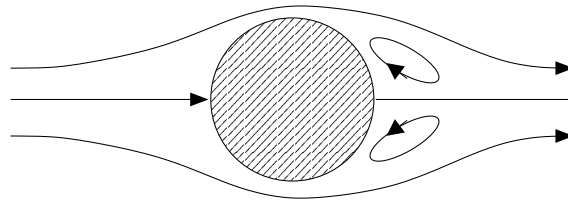


Figure 2.2: Streamlines of fluid flow in the Laminar Steady Regime.

metric recirculation region. Williamson (1996b) notes that the length of this region has been experimentally (Taneda (1956); Gerrard (1978); Coutanceau and Bouard (1977)) and numerically (Dennis and Chang (1970)) shown to increase as the Reynolds number increases.

2.1.2 Primary Wake Instability ($Re \approx 46$)

As the Reynolds number is further increased it exceeds a critical value at which point an instability has been shown by Taneda (1956) and Gerrard (1978) to manifest itself in the form of sinuous waves which propagate along the boundary of the wake recirculation in the downstream direction. This primary instability of the laminar steady regime has been established by the numerical results of Jackson (1987) and the experimental results of Provansal, Mathis and Boyer (1987) to be at $Re \approx 46$. At this point the flow is observed to undergo a supercritical Hopf bifurcation and the flow transitions to a two-dimensional oscillatory flow. Provansal et al. (1987) found that the von Kármán vortex street, see figure 2.3, that forms is the saturated end-product of this instability. They also established that the shedding frequency in the saturated state, for Reynolds numbers close to the critical Reynolds number (Re_{crit}), matches that obtained using linear stability theory. This result was achieved using a Stuart-Landau nonlinear model equation for the amplitude of wake oscillations. The Stuart-Landau equation for the complex amplitude of the wake oscillation is shown in equation 2.1, where σ and λ are complex coefficients.

$$dA/dt = \sigma A - \lambda |A|^2 A \quad (2.1)$$

In a Hopf bifurcation, the parameter σ can be expanded in powers of $(Re - Re_{crit})$. Provansal et al. (1987) found that by using the leading linear term of this expansion while searching for a steady state solution ($dA/dt = 0$) they could obtain a relationship that matched the results of their vortex shedding experiments.

2.1.3 Laminar Vortex Shedding Regime ($46 < Re < 188.5$)

As a consequence of the Hopf bifurcation (*the primary instability*) the wake in this regime oscillates periodically. As the Reynolds number is further increased within this regime, the amplitude of these oscillations increase and vortices are released periodically into the wake to form the classical von Kármán vortex street as shown in Figure 2.3. In an ideal case the cylinder is of infinite spanwise length, however in any laboratory experiment the cylinder is of a finite length and the experiment's spanwise boundary conditions have been shown to exert considerable influence over the flow. Williamson (1996b) observes that if the experimental spanwise boundary conditions are carefully manipulated then the flow is periodic and vortex shedding is parallel to the cylinder. Oblique forms of vortex shedding, where the vortex shedding is not parallel to the cylinder, can result in non-periodic shedding. However, this form of shedding will not be considered in this review because the end conditions are considered to be infinite in the numerical simulations to be presented.

The advent of vortex shedding into the flow results in the loss of the symmetry about

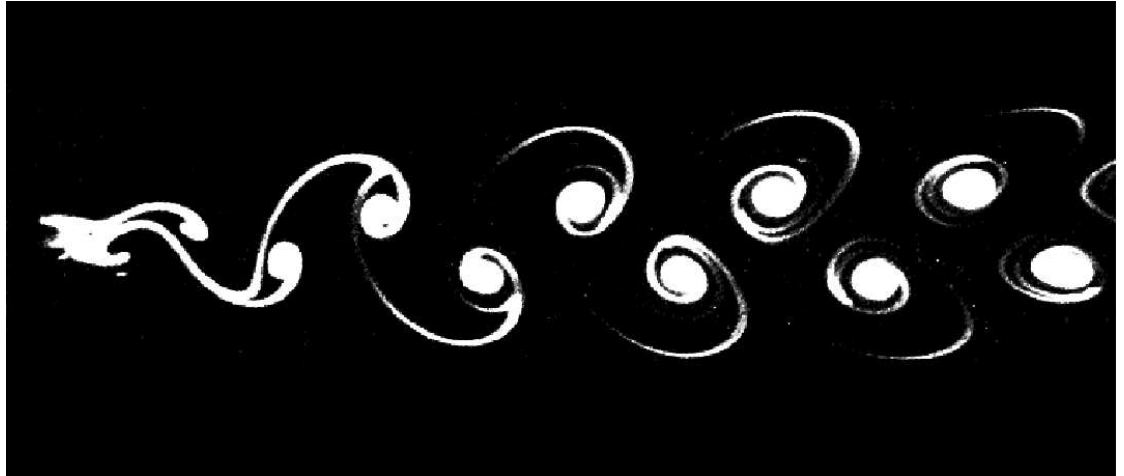


Figure 2.3: Kármán vortex street behind a circular cylinder at $Re = 105$. The image shows streaklines produced by electrolytic precipitation in water. *Photograph by Sadatoshi Taneda.* Reproduced from Van Dyke (1982).

the wake centreline, a dominant feature of the Laminar steady regime, however it retains the same form of symmetry in the spanwise direction (a two-dimensional flow). A feature of the primary instability is the inception of periodic shedding of vortices alternately from either side of the cylinder which in turn results in a periodic force being experienced by the cylinder. This force has been found to have components in the direction normal to the free stream, which oscillates at the shedding frequency of the vortices, as noted in the review of Bearman (1984), and a component inline with the stream, which oscillates at twice the shedding frequency, as noted in the review of Sarpkaya and Isaacson (1981).

2.1.4 Secondary Instability ($Re \approx 188.5$)

The transition from the Laminar vortex shedding regime is first observed in experiments as a sharp discontinuity of the Strouhal number, as shown in figure 2.4, where the Strouhal number can be seen to drop rapidly at $Re \approx 180$. This rapid experimental transition is characterised as the secondary instability of steady flow past a fixed circular cylinder. Williamson (1996b) observes that the upper-limit of the previous laminar vortex shedding regime has been found to vary considerably in experiments, from $Re = 140 - 194$. This large variation in the experimentally measured point of transition was ascribed by Williamson (1996b) to be a consequence of experimental sources of perturbation to the ideal flow. Cylinder roughness, free-stream turbulence amplitude, blockage and end effects are some of the perturbation sources cited which tended to have the effect of reducing the point of transition to a lower Reynolds number.

Barkley and Henderson (1996) numerically investigated the secondary instability via numerical techniques, using a Floquet stability analysis, with the objective of quantifying

2.1. STATIONARY CYLINDER IN A FREE STREAM

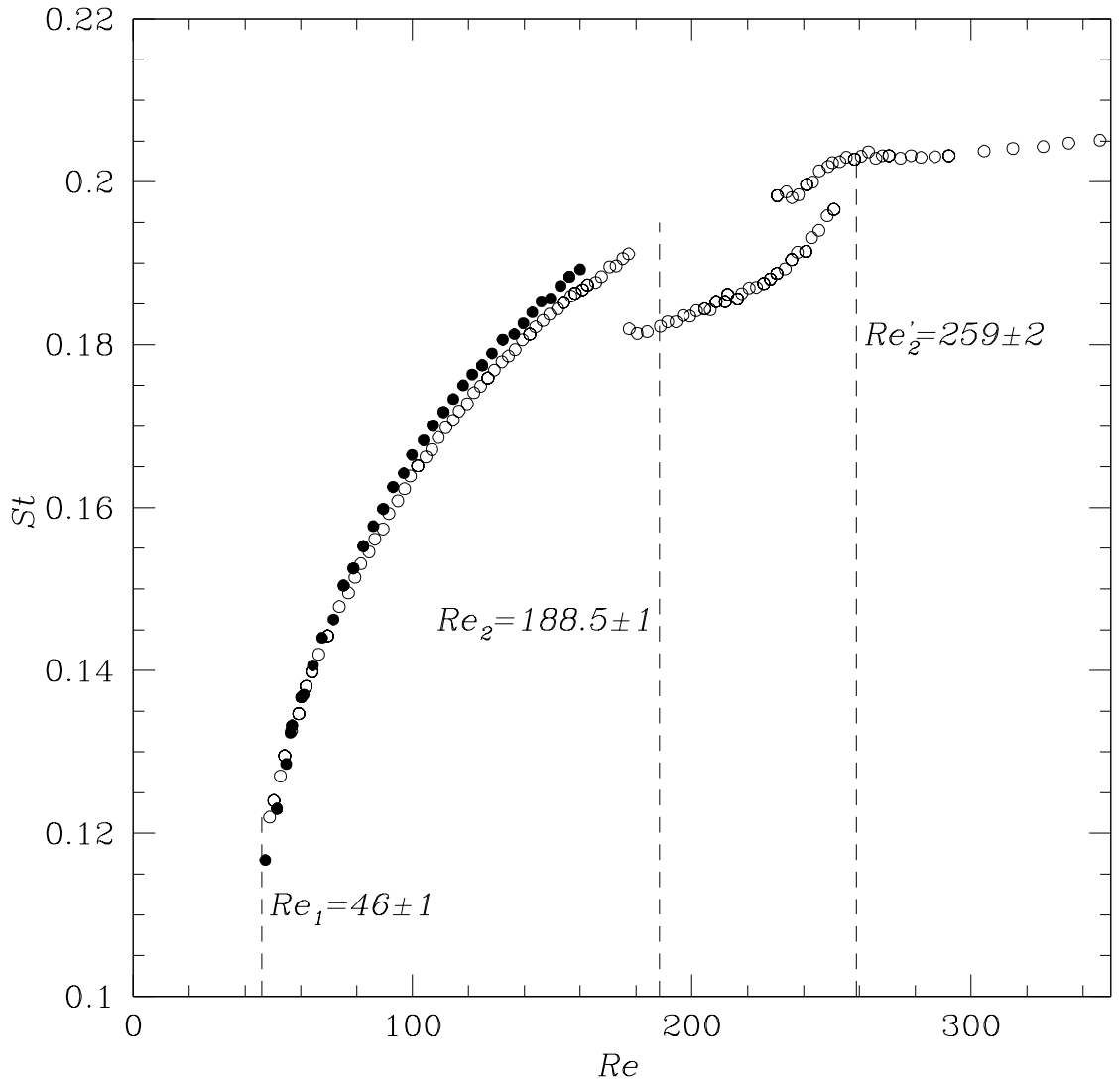


Figure 2.4: Variation of Strouhal number with Reynolds number for the cylinder wake. Shown are experimental results: \circ , Williamson (1989); \bullet , Hammache and Gharib (1991) and numerical results: $+$, Barkley and Henderson (1996). Wake instabilities up to $Re = 300$ are labelled: Re_1 (the primary instability), Re_2 (the secondary instability) and Re'_2 (the trinary instability). Reproduced from Barkley and Henderson (1996).

the nature and location of the transitions to three-dimensionality. Their results placed the secondary instability transition location at $Re = 188.5 \pm 1.0$, as shown in Figure 2.4. This value for the location of the secondary instability is at the upper end of the range of experimentally achieved values. The discrepancy between the experimental values and their numerically derived counterparts was explained as the consequence of three factors. The first of these was that of experimental noise which, as stated earlier, has the effect of reducing the transition location in Re . Secondly, the nonlinear bifurcation at this Re was found to be weakly subcritical by Henderson and Barkley (1996). A consequence

2.1. STATIONARY CYLINDER IN A FREE STREAM

of the subcritical nature of the bifurcation results in a hysteresis occurring, thus making the location of the transition dependent on whether Re is increasing or decreasing at this point. This has since been verified experimentally by Williamson (1988) and Leweke and Provansal (1995). Additionally, this subcriticality makes the critical point physically unreachable as any finite amplitude disturbance will cause the flow to transition to the upper-branch of the hysteresis. However, the hysteresis was considered to only influence the transition for a smaller range of Reynolds numbers, that being from 180 to 190. The third complication is due to the means of experimentally determining the point of transition. Typically, the experimental point at which the transition is stated to occur is when a sharp drop in shedding frequency is measured. This measure of instability which utilises the change in shedding frequency is in sharp contrast to the result obtained numerically. The numerical method of Floquet instability analysis predicted a real and positive leading Floquet multiplier. A real multiplier introduces no new temporal frequency into the flow and thus does not predict a change in frequency. It is suggested that the drop in shedding frequency is a result of strongly nonlinear phenomena in the near vicinity of the transition, which the Floquet method is unable to model. In further defence of their results Barkley and Henderson (1996) point out that this inability of linear theory to predict this nonlinear phenomena does not negate the value of their research as the information derived can provide important information about the structures at or near the onset of the instability.

2.1.5 3-D Wake Transition Regime ($188.5 < Re < 259$)

Williamson (1988) observed at the onset of this regime the formation of regular three-dimensional flow structures, which he labeled as a mode 'A' structure. This structure, which has been demonstrated experimentally in Williamson (1988), and again in more detail in Williamson (1996a), is characterised by a wavy deformation of the primary vortices and by the presence of streamwise vortex pairs which form vortex loops. Subsequent numerical simulations by Thompson, Hourigan and Sheridan (1996) confirmed the presence of these structures and compared favourably with the experimental results provided by Williamson (1996b) shown in Figure 2.5. The wavelength between the streamwise vortex pairs was determined experimentally by Williamson (1996b) to be $\lambda = 4.01D$ and again this compares favourably with the Floquet analysis of Barkley and Henderson (1996) which yielded values of $3.96D \pm 0.02$ for the wavelength of mode A.

Just beyond the onset of the mode A instability Henderson (1997) found that the flow was chaotic. This transition to chaos was attributed as being due to the broad-band nature of the mode A instability and a subsequent competition between the global modes arising from this instability. It was noted that the regular flow patterns that are a consequence of the modes A and B appear only as transients or when the spanwise boundaries conditions are manipulated to achieve spanwise periodicity.

2.1. STATIONARY CYLINDER IN A FREE STREAM

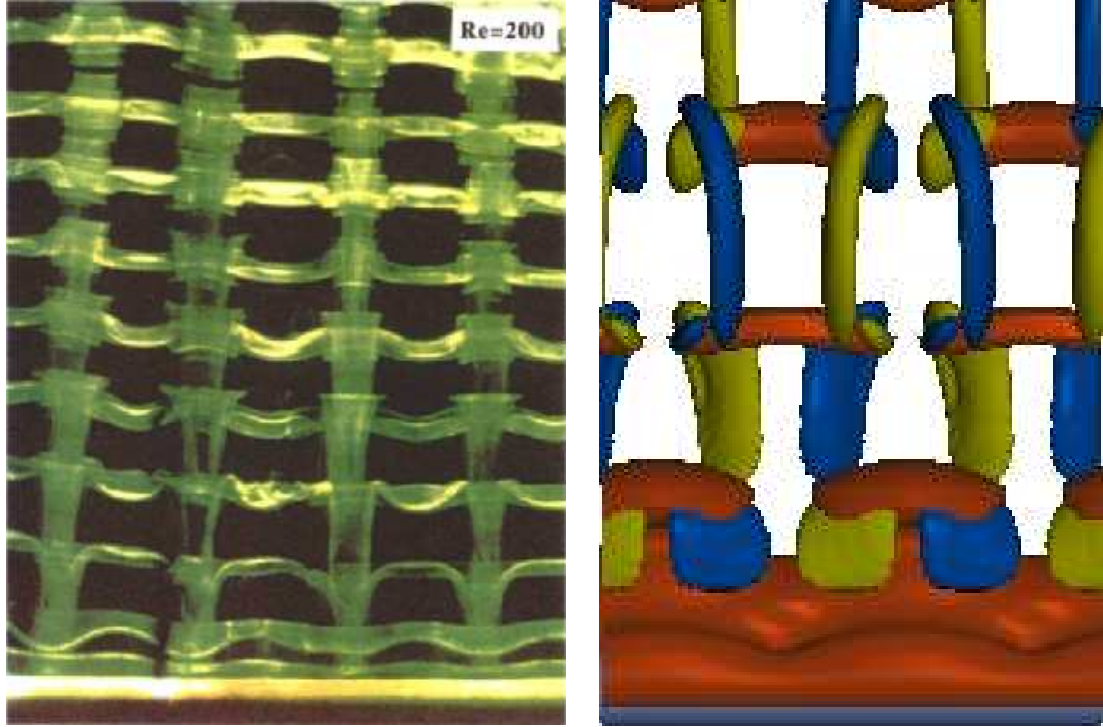


Figure 2.5: Mode A 3-D instabilities. (a) The left image shows a visualisation at $Re = 200$ obtained experimentally using fluorescein dye and laser light. Reproduced from Williamson (1996b). (b) Isosurfaces of vorticity and pressure at $Re = 210$. Shown are the horizontally aligned pressure isosurfaces (red) and vertically aligned isosurfaces of positive and negative vorticity. Reproduced from Thompson et al. (1995). The two images are scaled differently. While a direct comparison between the two images is not possible, due to the different means of producing these images, it can be seen that the experimental and computational results are consistent.

The upper boundary of this regime is delineated by a second discontinuous change in the shedding frequency, as shown in Figure 2.4. At this location a second form of shedding was observed to dominate the flow. This form of shedding, labeled as mode B shedding by Williamson (1988) and illustrated in Figure 2.6, is comprised of finer scale streamwise vortices than that of mode A and shows less spanwise deformation of the primary vortices. The emergence of this regime is observed to occur experimentally over a range of Reynolds numbers of approximately 230 – 250 and can be seen as the second discontinuity on a St - Re plot (Figure 2.4). Barkley and Henderson (1996) have found that the linear transition to mode B occurs at $Re = 259$ which is clearly not in accord with the experimental results. Barkley and Henderson (1996) speculated that this discrepancy arises for a number of reasons. At the critical point of transition to Mode B the two-dimensional wake used as the basis for their linear analysis, is already unstable to Mode A. Consequently it was likely that any bifurcation at this point would consist of both mode A and B instabilities. The nonlinear interactions in this flow were beyond the scope of the linear approximations in the Floquet method used and therefore it was not possible to

2.1. STATIONARY CYLINDER IN A FREE STREAM

explain why Mode B structures appeared in experiments before the critical point predicted by linear analysis.

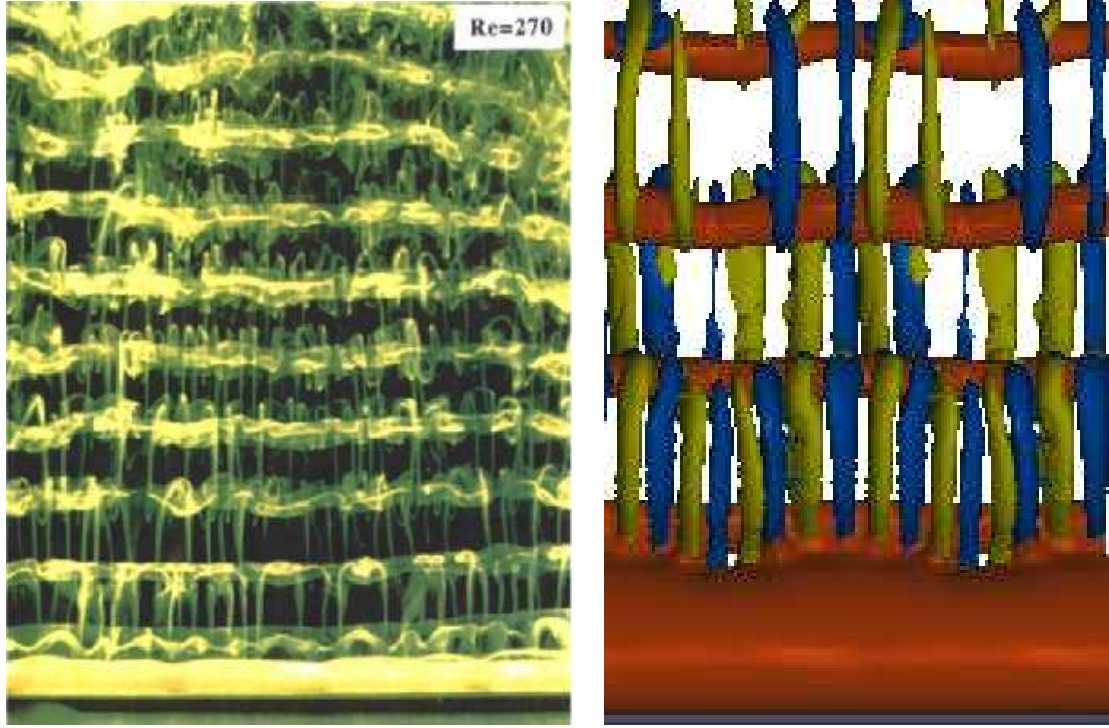


Figure 2.6: Mode B 3-D instabilities. (a) The left image shows a visualisation at $R = 270$ obtained experimentally using fluorescein dye and laser light. Reproduced from Williamson (1996b). (b) Isosurfaces of vorticity and pressure at $Re = 250$. Shown are the horizontally aligned pressure isosurfaces (red) and vertically aligned isosurfaces of positive and negative vorticity. Reproduced from Thompson et al. (1995). The two images are scaled differently.

In contrast to the transition to mode A, the transition to mode B is not hysteretic and instead involves a transfer of energy from mode A to mode B as Re is increased. Although the transfer of energy between these two modes is gradual, Williamson (1996a) asserts that during the transition phase there is an intermittent swapping between the modes, rather than the coexistence of both modes simultaneously. Barkley, Tuckerman and Golubitsky (2000) theoretical examined the transition scenario between modes A and B and presented a scenario which explained why mode B (a supercritical bifurcation) was observed before the linearly predicted point of instability at $Re \approx 259$ and the non-hysteretic transition from mode A to B where a mixed mode state is observed to occur. At $Re \approx 230$ a mix-mode branch appears in which both modes A and B are unstable. With increasing Re the mode B component of this state dominates the flow until at $Re \approx 265$ this branch was found to terminate at the point where it intersects the pure mode B branch which forms at $Re = 259$. Figure 2.7 shows the critical wavelengths for instability of these two modes found via the Floquet analysis of Barkley and Henderson (1996). Experimental measurements of the Mode B shedding wavelength by Williamson (1996a), Wu,

2.2. FORCED CYLINDER VIBRATION IN A FREE STREAM

Sheridan, Soria and Welsh (1994) and Mansy, Yang and Williams (1994) have yielded a wavelength of $\lambda/D \approx 1.0$ which is consistent with the value of $\lambda/D = 0.82$ calculated by Barkley and Henderson (1996).

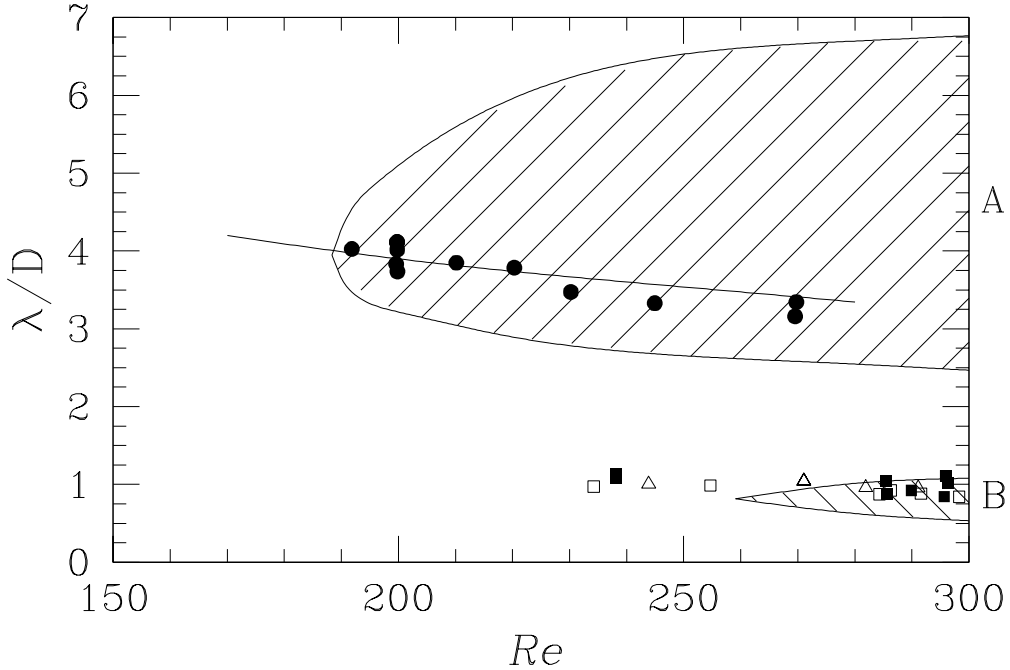


Figure 2.7: Spanwise instability wavelengths for mode A and B versus Re . Two distinct wavelengths for the mode A and B instabilities are observed. The shaded bands of unstable wavenumbers are from the Floquet analysis of Barkley and Henderson (1996) with the solid line providing an indication of the wavelength with the largest linear growth rate. Also shown are the dominant spanwise wavelengths observed in experiments: ■, Williamson (1987); □, Wu et al. (1994); △, Mansy et al. (1994); ●, Williamson (1996a).

2.1.6 Fine Scale 3-D Wake Regime ($259 < Re < 1000$)

This regime initially consists of mode B shedding. Subsequent increases in Re towards the limits of our consideration ($Re = 1000$) result in the flow becoming increasingly disordered, leading to a reduction in two-dimensional Reynolds stresses and an increasing length of the formation region.

2.2 Forced Cylinder Vibration in a Free Stream

The study of vortex-induced vibrations (VIV) is important to a large number of disciplines such as fluid mechanics, structural vibrations, acoustics, offshore engineering, heat

2.2. FORCED CYLINDER VIBRATION IN A FREE STREAM

exchanger design, bridge design and aeronautical engineering. Accordingly, substantial research time and publications have been devoted to this phenomenon. The approaches to studying and understanding this problem have tended to fall into two categories; the study of the response of an elastically mounted cylinder in a free stream or of a cylinder that has been subjected to forced rectilinear oscillations in a free stream. This review will primarily focus on the later approach, as it is the most relevant to the current investigation where the motion of the cylinder is proscribed. In forced rectilinear oscillations the cylinder axis is translating along a linear path at some orientation relative to the incident flow. Here we primarily consider two particular orientations relative to the free-stream: transverse oscillation where the direction of cylinder oscillation is at right angles to the incident flow; and inline oscillation where the direction of cylinder oscillation is aligned with the free stream. Other orientations will only be briefly touched upon.

2.2.1 Transverse Oscillations

The large volume of studies into a cylinder in simple harmonic cross-flow oscillation has identified a number of significant features of the fluid-cylinder interaction. Foremost amongst these are:

- The primary Lock-In region.
- The shedding of distinctive vortex structures.
- Sensitivity of the timing of vortex formation within the Lock-In region.

These features are reviewed in the following sections.

2.2.1.1 Primary Lock-In Region

A significant feature of the fluid-structure interaction for a cylinder in transverse oscillation is the ability of the cylinder to “capture” the vortex shedding frequency (f_v) so that it oscillates at the cylinder oscillation frequency (f_t) instead of the natural frequency of shedding (f_n) for a fixed cylinder. At very small amplitudes this phenomenon has been demonstrated to occur when the frequency ratio f_t/f_n is near 1.0. Subsequent increases of the amplitude of oscillation has been shown to increase the envelope of frequencies over which the primary lock-in regime will occur. A lock-in envelope derived from results presented in the reviews of Blevins (1977) and Sarpkaya (2004) can be seen in figure 2.8 which shows the boundaries of this region for low- Re experiments. The comparison between the results of Koopmann (1967) and Cheng and Moretti (1991) illustrate that increasing the Reynolds number results in a widening of the lock-in envelope. In the cases shown, the central frequency of the lock-in envelope is tilted towards the lower frequencies (< 1). Additionally, the envelope of frequencies found by Cheng and Moretti (1991)

2.2. FORCED CYLINDER VIBRATION IN A FREE STREAM

exhibits an onion-shaped region. According to Sarpkaya (2004), the Reynolds number has a strong influence on the upper frequency lock-in boundary.

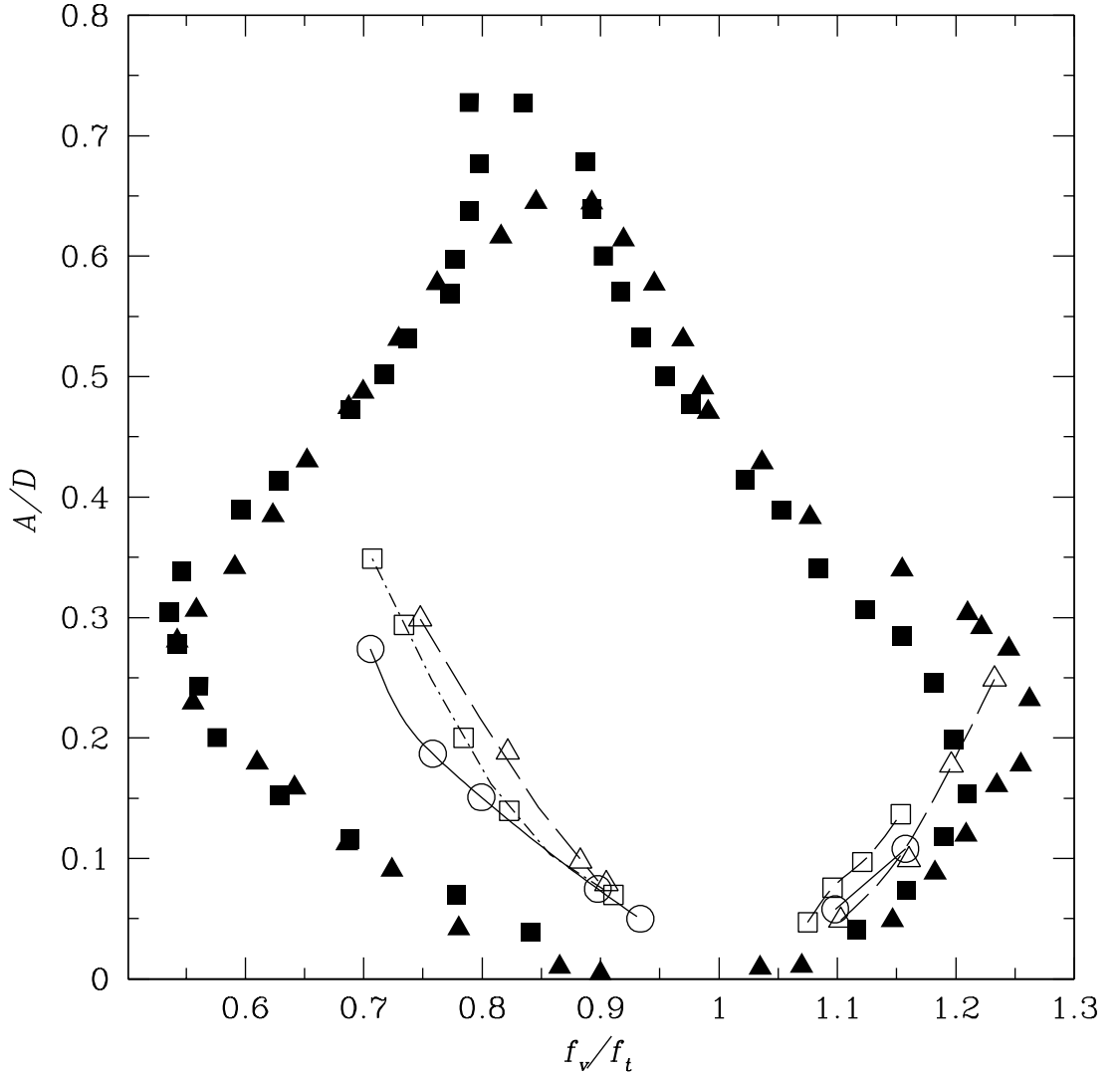


Figure 2.8: Primary Lock-In regime. Shown are the boundaries of the lock-in regime as a function of the frequency ratio between the excitation and natural shedding frequency and the non-dimensionalised amplitude of oscillation. Low Reynolds number results from Koopmann (1967) are at: \triangle , $Re = 100$; \square , $Re = 200$ and O , $Re = 300$. The experimental results of Cheng and Moretti (1991) were obtained at Reynolds numbers of 1500, \blacksquare , and 1650, \blacktriangle .

As the amplitude of oscillation approaches zero the lock-in envelope narrows such that f_t/f_n approaches 1.0. The results of Koopmann (1967), shown in Figure 2.8, have a minimum amplitude at which lock-in was found to occur, $A/D \approx 0.05$. However, the results of Cheng and Moretti (1991), also presented in Figure 2.8, show that much lower values of A/D in the lock-in regime can be achieved. Blackburn and Henderson (1999) suggested that the minimum amplitude was associated with presence of oblique,

2.2. FORCED CYLINDER VIBRATION IN A FREE STREAM

instead of parallel, vortex shedding for the stationary circular cylinder. Further it was speculated that it is likely for three-dimensionally unstable flows that there does exist a limiting minimum amplitude for lock-in to occur in experiments due to the perturbation imposed by the cylinder on the flow being insufficient to control the turbulent wake.

2.2.1.2 Vortex Shedding Structures

Williamson and Roshko (1988) visualised the vortex wake patterns for a cylinder subjected to harmonic transverse motion in a uniform cross-flow over a Reynolds number range 300-1000. The non-dimensionalised oscillation parameters of amplitude, A/D , and wavelength, λ/D , were used to characterise their study, where $\lambda = UT_e$ is equal to the product of the free-stream velocity, U , and the period of cylinder oscillation T_e . The parameters were varied over the range $0 < A/D < 5.0$ and $0 < \lambda/D < 15.0$. A number of different regimes were observed where each regime was characterised by the number of single vortices (S) or vortex pairs (P) formed over each cycle of vortex shedding. Their results can be seen in Figure 2.9, which shows the modes in the vicinity of the lock-in regime. The classical antisymmetric von Kármán vortex street which sheds two single vortices per cylinder oscillation is thus labelled as a '2S' mode using this notation.

Blevins (1977) showed that lock-in increases the span-wise correlation of vortex shedding along the cylinder axis. Figure 2.10 shows the effects that cylinder oscillation can have on the span-wise correlation, where a value of 1.0 corresponds to two-dimensional flow.

2.2.1.3 Vortex Shedding Timing in the Lock-In Regime

Within the lock-in regime it has been shown that the timing of vortex formation and release with respect to the cylinder motion is sensitive to the frequency of oscillation by a number of studies including those of Carberry, Sheridan and Rockwell (2001), Williamson and Roshko (1988) and Ongoren and Rockwell (1988a). As the ratio f_t/f_n is increased through $f_t/f_n \approx 1$ a simultaneous jump in the amplitude and phase of the lift force is observed. Ongoren and Rockwell (1988a) demonstrated, through a set of flow visualisations, that the jump in phase angle was matched by a switch in the timing of vortex shedding. Williamson and Roshko (1988) made the deduction that this phase angle jump within the lock-in regime corresponds to a change in the vortex shedding mode, from the 2S to the 2P mode, i.e.. see figure 2.9. The numerical computations of Blackburn and Henderson (1999) have also found that the jump in the lift force coincided with the change in the vortex shedding structure. It has been established that the mechanical energy, E , transferred from the fluid to the cylinder is influenced by the phase angle, ϕ , between the cylinder displacement and the fundamental harmonic of the lift force acting on the cylinder. When energy is being transferred from the fluid to the cylinder, E is

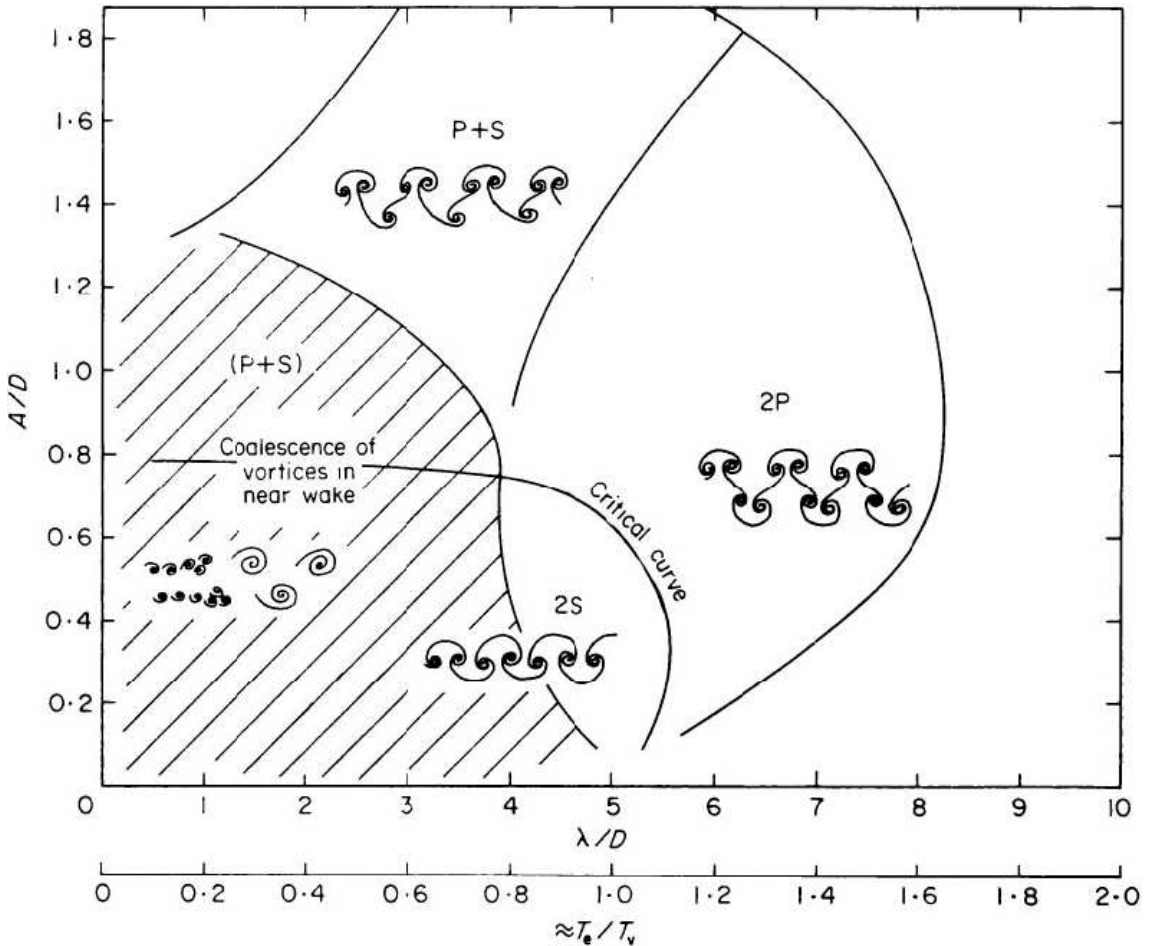


Figure 2.9: Map of vortex synchronisation patterns near the fundamental lock-in region. The critical curve marks the transition from one mode of vortex formation to another. Reproduced from Williamson and Roshko (1988).

positive and the phase angle is found to lie in the range $0 - 180^\circ$.

2.2.2 Inline and Oblique Oscillations

The study of forced oscillations at angles, χ , with respect to the freestream that are not transverse ($0^\circ \leq \chi < 90^\circ$) have received considerably less attention than the transverse case. Primarily this appears to have occurred because the forces arising from transverse oscillations are substantial greater than those arising from inline oscillations. Additionally, studies of cylinders, see e.g. Blackburn and Karniadakis (1993) and the review of Williamson and Govardhan (2004), where the cylinder was permitted to freely oscillate in both the inline and transverse directions, have observed that the cylinder generally performs a figure-eight trajectory and that permitting inline motion results in little influence on the cylinder response, the forces experienced and vortex wake modes of the cylinder. Although Jauvtis and Williamson (2003, 2004) have observed significant alteration of

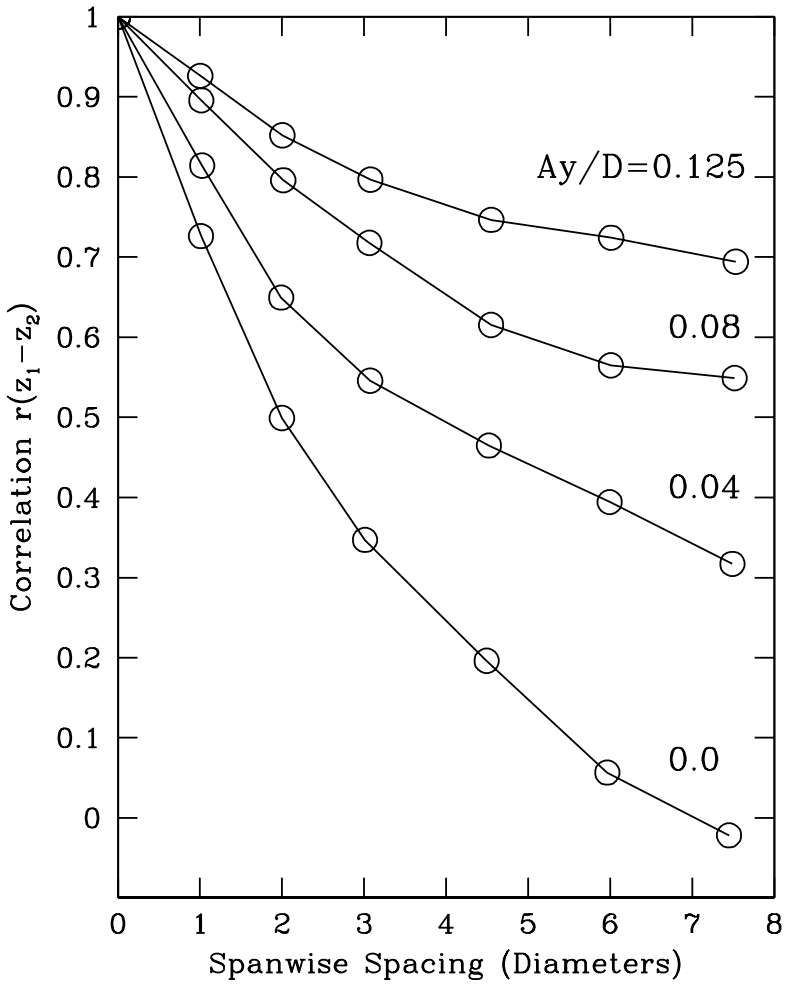


Figure 2.10: Span-wise correlation of vortex shedding for a rigid cylinder during lock-in. Reproduced from Blevins (1977).

the fluid-structure interactions when the mass ratio between the cylinder and surrounding fluid is reduced below 6. In this scenario, a new response branch was observed with much larger amplitudes of inline oscillation and a vortex shedding mode that resulted in a triplet of vortices being formed in each half-cycle.

Ongoren and Rockwell (1988b) presented hydrogen bubble visualisations of a circular cylinder subjected to forced oscillations at angles to the cross-flow ranging from the inline case, $\chi = 0^\circ$, to the transverse case, $\chi = 90^\circ$. They observed the formation of five distinct vortex shedding modes. These modes could further be classified as having symmetric, denoted as SY, or antisymmetric, denoted as AY, vortex formation, where the axis of symmetry is taken with respect to the freestream direction. Only one symmetric mode, SY-I, was observed and this occurs when a pair of vortices is shed in phase symmetrically from both sides of the cylinder. Only one pair is shed per oscillation and using the notation of Williamson and Roshko (1988) this would be described as a P mode of

2.3. ROTATIONAL OSCILLATION IN A FREE STREAM

shedding. This mode can only occur when there is a symmetrical perturbation to the flow imparted by the cylinder motion and thus only occurs for $\chi \neq 90^\circ$. There are four forms of the antisymmetric modes, AY-I to AY-IV, of which three of these, AY-II to AY-IV, are a consequence of the symmetric perturbation to the flow by the cylinder motion that only occurs for $0^\circ \leq \chi < 90^\circ$. The first of the antisymmetric modes, mode AY-I, involves the alternate shedding of two out of phase single vortices per oscillation from either side of the cylinder to form the classical von Kármán street (a 2S mode). The other antisymmetric modes AY-II to AY-IV are shed at double the period of the primary antisymmetric mode, AY-I, and the symmetric mode, SY, which have the same period of shedding. Mode AY-II is essentially the same as mode AY-I except that the period has doubled. In the remaining modes one (AY-III) or both (AY-IV) of the single vortices shed are replaced by a pair of counter-rotating vortices. Griffin and Ramberg (1976) in an inline study only, $\chi = 0^\circ$, experimentally visualised two modes of vortex shedding. These modes correspond to the symmetric, SY, and antisymmetric, AY-I, observed by Ongoren and Rockwell (1988b).

Griffin and Ramberg (1976) and Ongoren and Rockwell (1988b) found the lock-in region for inline oscillations was centered at a frequency which is double the Strouhal frequency of shedding, $2f_s$, as compared to the lock-in region for transverse oscillations which is centered at the Strouhal frequency. Ongoren and Rockwell (1988b) also found that lock-in was possible for all the modes they observed. When the vortex shedding was not synchronised to the oscillation frequency a competition between the symmetrical and antisymmetrical modes was observed. It was found that the near-wake structure locks on to each mode for a number of cycles and then abruptly switches to the next mode.

2.3 Rotational Oscillation in a Free Stream

It has long been known that the steady rotation of a cylinder placed in a free-stream introduces a net circulation into the fluid and produces a time-averaged force normal to the flow direction, in a phenomenon known as the Magnus effect. In contrast, the effects of rotary oscillation upon the wake structures and forces experienced by the cylinder are less well established. A series of visual observations by Taneda (1978) demonstrated that the wake structure can be substantially altered by rotary oscillation. Taneda (1978) performed a series of visualisations, using aluminium dust and electrolytic precipitation techniques, for the Reynolds number range 30 to 300 and Strouhal numbers between 0 and 55. By altering the frequency and amplitude of rotary oscillation he was able to determine a critical value of the Strouhal number where the dead water region behind the cylinder vanishes. In these experiments the Strouhal number was based on oscillation frequency, St_f (f = frequency of rotary oscillation) instead of the classical shedding frequency. The critical Strouhal number, St_c , was found to vary inversely with the oscillation amplitude but was

2.3. ROTATIONAL OSCILLATION IN A FREE STREAM

independent of the Reynolds number over the range of values considered. Increasing St_f from 0 was found to cause the separation points to move rearward until St_c was attained. At this point the recirculation region of the wake vanished and the wake was found to be narrow with no reverse flow. At values of St_f greater than St_c , the streamlines were found to converge at the back of the cylinder and approach a potential flow solution. Figure 2.11 shows clearly the effects mentioned for $St_f = 0$ and $St_f = 3.4$, where $St_c = 2.8$.

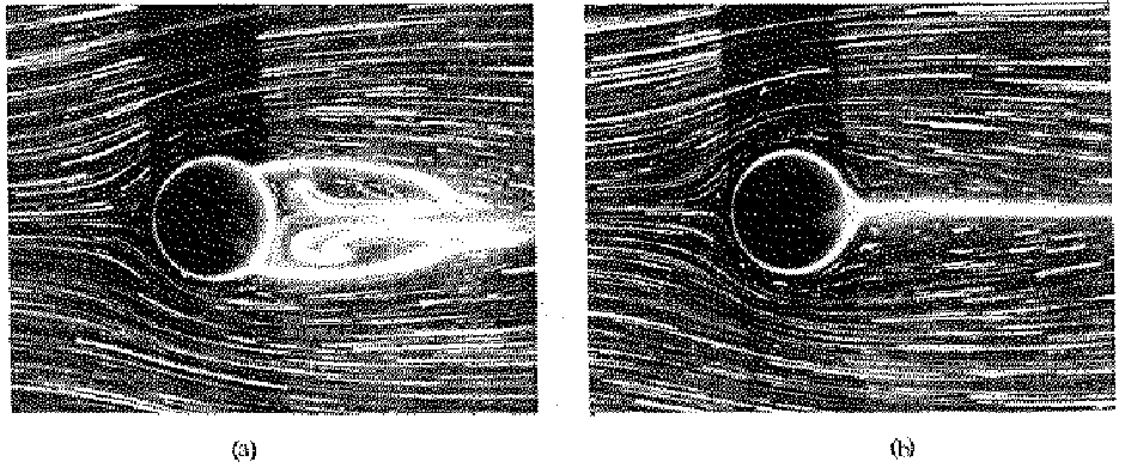


Figure 2.11: Streamline and streak-line patterns at $Re = 33.7$, $D = 1.0\text{cm}$, $\theta = 45^\circ$. (a) $St_f = 0$, (b) $St_f = 3.4$. At a critical frequency of oscillation the wake region behind the cylinder is much reduced. *Reproduced from Taneda (1978).*

Experiments at a higher Reynolds number of 1.5×10^4 by Tokumaru and Dimotakis (1991) have yielded related results. At this Reynolds number the rotational frequency (forcing Strouhal number, St_f) and the normalized peak rotation rate of Ω_1 were varied, where the rotation rate, $\Omega(t)$, is defined as

$$\Omega(t) = \frac{\dot{\theta}D}{2U_\infty} = \Omega_1 \sin(\omega t) \quad (2.2)$$

and $\dot{\theta}$ is the angular velocity of the cylinder. The drag coefficient, C_d , and the wake displacement thickness were evaluated at a single location, $4.5D$ downstream of the cylinder. The results showed that the wake displacement thickness could be made substantially larger or smaller than in the unforced case by altering the rotary motion of the cylinder. It was found that the minimum wake displacement area occurred in the neighbourhood of $St_f = 1$ and $\Omega_1 = 3$, where it was half the value for the unforced case. The cylinder wake-mean velocity profiles in figure 2.12 clearly demonstrate the influence of the rotational frequency. The minimum C_d was found to approximately coincide with the minimum wake area. The rate of rotation affected the number of vortices shed per cycle and four distinct modes of vortex shedding per cycle were identified. It was concluded

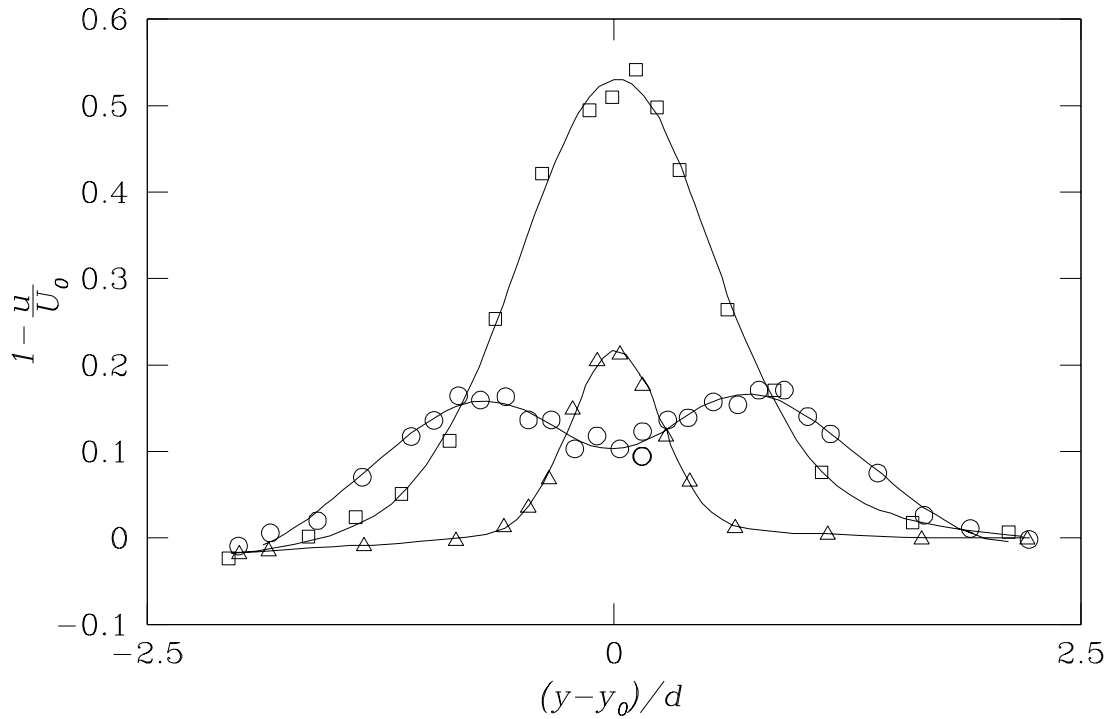


Figure 2.12: Cylinder wake mean velocity profiles, measured at midspan ($\Omega_1 = 2$): \square , unforced; \bigcirc , $S_f \approx 0.2$; \triangle , $St_f \approx 1$. (Tokumaru & Dimotakis, 1991)

that when the forcing frequency is similar to the natural vortex shedding frequency, the greatest control can be exerted over the wake. In both studies there was no net circulation introduced by the rotary oscillation and consequentially there was no time-mean lift generated.

2.4 Rectilinear Oscillation in Quiescent Fluid

Sinusoidally oscillating flow about a circular cylinder has been extensively researched in the past century due to its application in physical situations such as the forces experienced by man-made structures in a marine environment. However, most of the research into these applications involves flow with much higher Keulegan-Carpenter and Stokes numbers and consequentially is not considered here. Of primary interest to the current investigation are the flow visualisation studies of Honji (1981), Williamson (1985) and Tatsuno and Bearman (1990).

It is well established that a two-dimensional secondary streaming flow about a cylinder is induced when a cylinder is in oscillatory rectilinear motion relative to the surrounding fluid. The resulting secondary flow is symmetrical about the axis of oscillation and has been visualised by many studies (e.g. the visualisations of Schlichting (1932) and later

2.4. RECTILINEAR OSCILLATION IN QUIESCENT FLUID

by M. Tatsuno as shown in figure 2.13). When the Keulegan–Carpenter or Stokes number exceeds a critical value the flow is altered by the formation and subsequent separation of vortices on the cylinder surface, leading to a loss of this symmetry and the formation of three-dimensional flow.

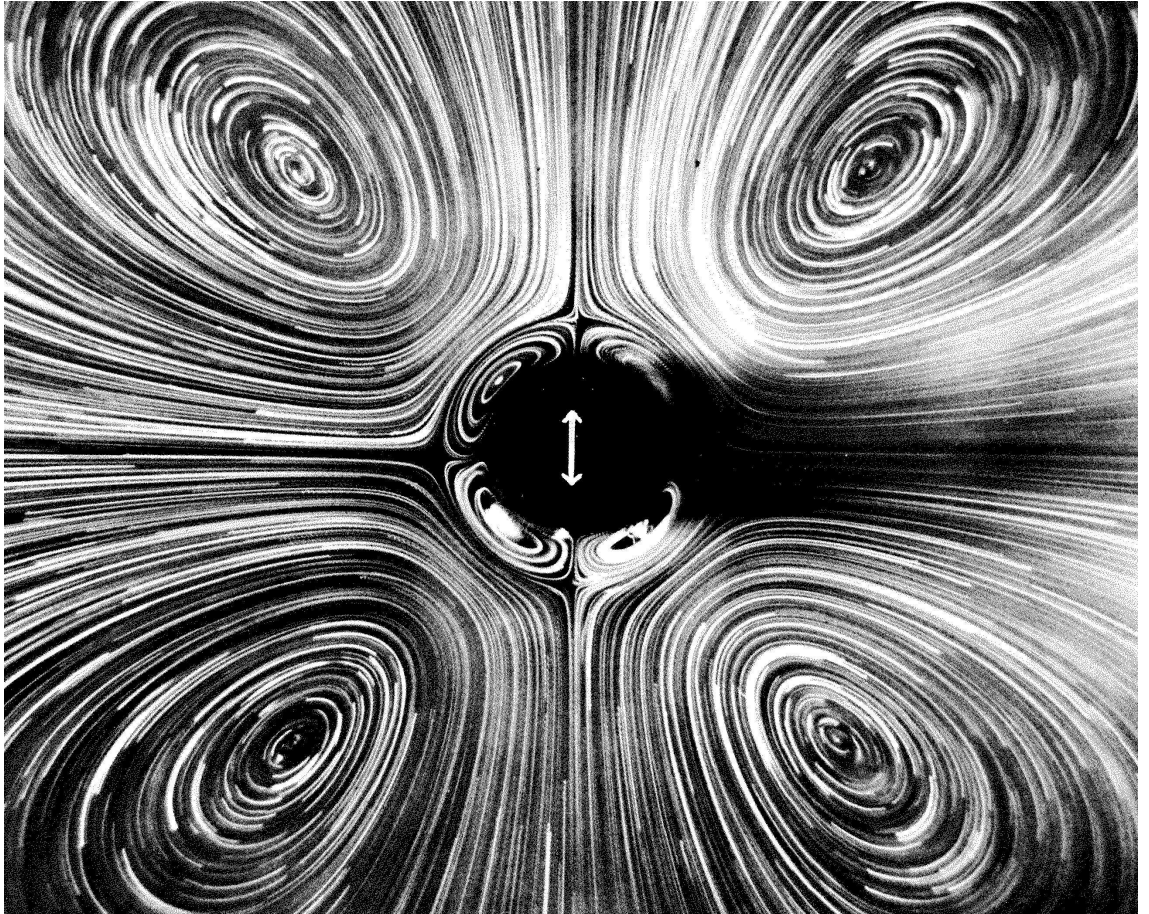


Figure 2.13: Secondary streaming induced by an oscillating cylinder. This image was produced by illuminating glass beads with a stroboscope. The image was taken at an oscillation amplitude of $A/D = 0.085$ and at $Re = 70$ (based on frequency). Reproduced from Van Dyke (1982). *Photograph by Masakazu Tatsuno.*

Williamson (1985) investigated the behaviour of vortices shed from a cylinder in sinusoidal flow using a combination of two dimensional flow visualisations and force measurements for $KC < 60$ and two β values of 255 and 730. Using two-dimensional visualisations of the repeatable patterns produced on the water tank surface a set of flow regimes were identified as a function of KC . This regime map, reproduced in figure 2.14, identifies each regime according to the number of vortices shed in each half-cycle and the corresponding lift force fluctuations per oscillation.

The regular lift force fluctuations were shown to be directly related to the repeatable vortex shedding patterns observed in the cylinder wake. It was found that the lift force

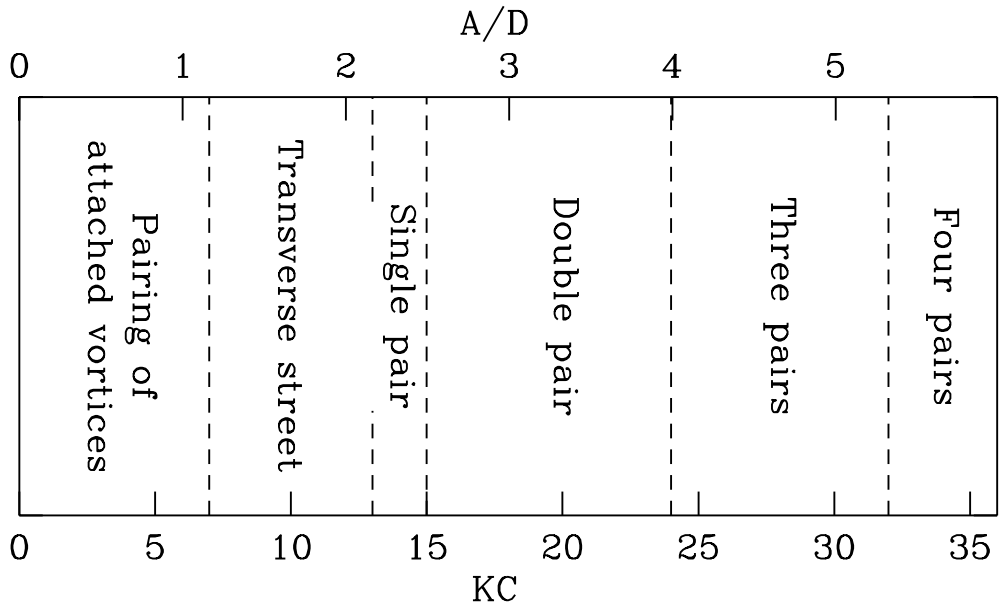


Figure 2.14: An approximate guide to the flow patterns produced from an oscillating cylinder as a function of the Keulegan–Carpenter number. Annotations describe the number of vortices shed per oscillation half-cycle. Regimes are based on observations conducted for β values of 255 and 730. Reproduced from Williamson (1985).

fluctuation frequency was a multiple of the forcing frequency and that this was directly tied to the shedding of a specific number of vortices in each half-cycle. In each of the regimes identified in figure 2.14 a specific number of vortices was shed in each half-cycle. The subsequent pairing of vortices shed in the present half-cycle with those of the preceding half-cycle was identified as being a core feature leading to the formation of the repeatable vortex patterns. In the first regime identified ($0 < KC < 7$) a pair of attached vortices are formed in the wake in each half-cycle. These are shed from the cylinder as it reverses direction and are symmetrical about the axis of oscillation up to $KC \approx 4$ where it was observed that the vortices formed are no longer equal in magnitude and are not shed at the time of cylinder reversal. This led to the detection of a lift force varying with the oscillation frequency. This regime should reasonably be sub-divided into two sub-regimes which are distinguished by the breaking of the symmetry about the oscillation axis.

In the transverse street/single pair regime ($7 < KC < 15$), see figure 2.15, a single vortex is shed per half-cycle which pairs up with the shed vortex from the previous half-cycle. A series of cycles results in a number of pairs being formed and shed on the same side of the cylinder. These pairs form a transverse street which convect away from the cylinder. In the lower end of the range ($7 < KC < 13$) the direction of the street was observed to be approximately perpendicular to the oscillation axis, as shown in figure

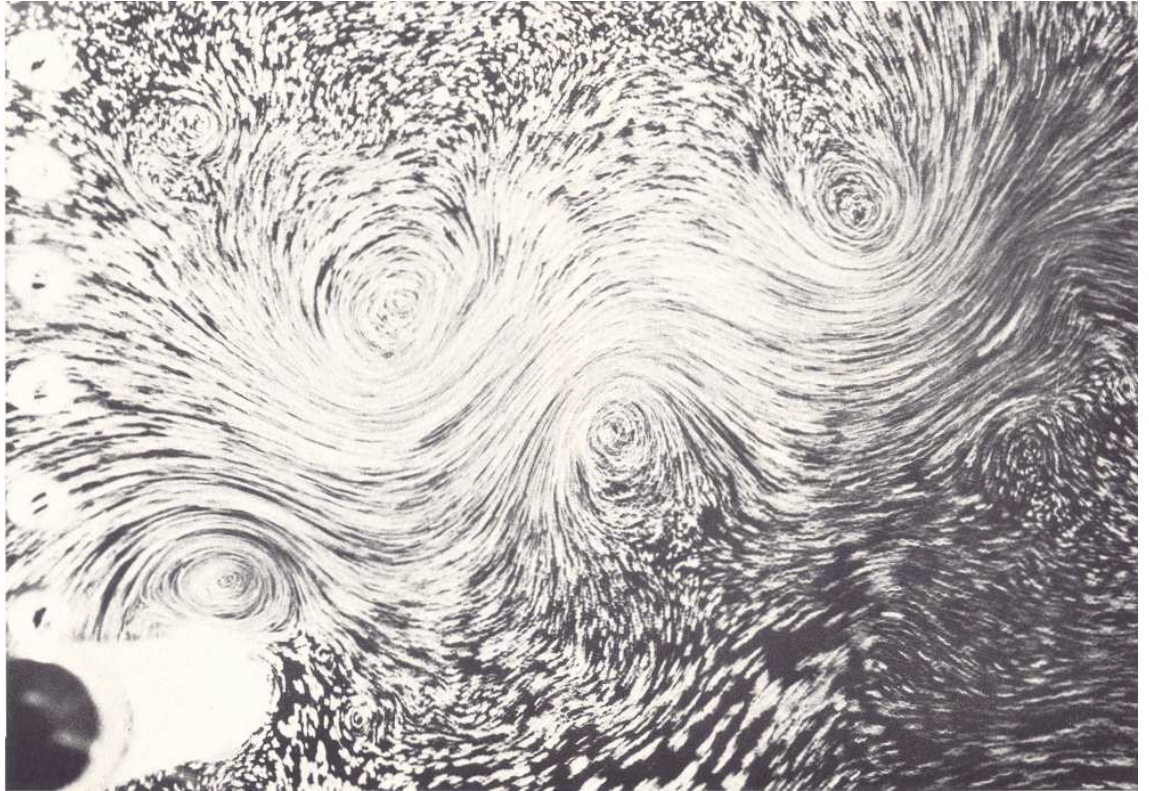


Figure 2.15: Transverse street wake for $KC = 12.0$. The cylinder is approaching its lowest point of its oscillation. This regime is delineated by the distinctive trail of vortices which convects away at around 90° to the oscillation axis. Reproduced from Williamson (1985).

2.15, while in the upper end of the range ($13 < KC < 15$) the direction of the street was observed to be at an angle of approximately 45° to the oscillation axis. Initial conditions were thought to determine which side of the cylinder that the street formed on, although it was also observed that the shedding could intermittently change sides. Higher regimes (Double pair, Three pairs and Four pairs) were distinguished by the formation of more vortices per cylinder oscillation cycle. In each case the process of pairing of the shed vortices was fundamental to the pattern formed.

Williamson's (1985) visualisations lent a good deal of insight into the flow dynamics despite the inherent limitation due to their two dimensional nature. A prior study by Honji (1981) produced visualisations of the three-dimensional structures that can arise in the same (KC, β) parameter space. Honji visualised the flow around a transversely oscillating cylinder in a quiescent fluid, for Stokes numbers in the range 68.8 to 700 and Keulegan–Carpenter numbers less than 7.5, and produced excellent visualisations of a three-dimensional flow instability. The presence of mushroom shaped vortices was observed, in a plane normal to the direction of cylinder motion, which were arranged alternately along each side of the cylinder span in a double row. These vortices were

2.4. RECTILINEAR OSCILLATION IN QUIESCENT FLUID

convected away from the cylinder by the induced flow to form equally spaced chains of dye. Each chain of dye retained its mushroom like form for a number of diameters away from the cylinder. The spanwise streak spacing was found to only weakly depend on the Stokes number and increased as the Keulegan–Carpenter number was increased. Honji (1981) also found that for Keulegan–Carpenter numbers above a second critical line “no clear streaked flow forms” which he attributed to the onset of turbulence. These structures were named the ‘Honji Instability’ by Sarpkaya (1986) although Honji simply referred to the patterns formed as ‘streaked flow’. Honji suggested that the instability mechanism leading to this flow pattern was ‘a kind of centrifugal one’. While Honji does not explicitly state that this was a Taylor–Görtler instability, it is probable that he was referring to this form of instability, which arises from the centrifugal forces induced by the curvature of the boundary layer.

Hall (1984) performed a theoretical stability analysis of the two-dimensional flow induced by a transversely oscillating cylinder in a viscous fluid. Using the assumption of a large oscillation frequency ($\beta \gg 0$) Hall derived an equation for the critical Keulegan–Carpenter number, KC_{cr} , at which the two-dimensional flow became linearly unstable to spanwise perturbations. This equation may be written as (see Sarpkaya; 1986, 2002):

$$KC_{cr} = 5.78\beta^{-\frac{1}{4}}(1 + 0.21\beta^{-\frac{1}{4}} + \dots) \quad (2.3)$$

The curve where $KC = KC_{cr}$ is the curve of neutral stability and for $KC > KC_{cr}$ the flow was deemed linearly unstable to Taylor–Görtler vortices. This relationship appears to be in excellent agreement with the results of Honji (1981). However, as noted in Sarpkaya (2002), to date, the inception of three-dimensional instabilities due to streamwise vorticity has not been verified experimentally or numerically. Additional nonlinear analysis by Hall (1984) predicts the nature of the bifurcation to be subcritical, a result which was unexpected because in the classical Taylor problem the bifurcation is supercritical. In Sarpkaya’s (2002) investigation at much higher Stokes numbers ($\beta \leq 1.4 \times 10^6$) a set of correlations for the primary onset of a three-dimensional instability was provided:

$$KC_{cr} = 12.5\beta^{-2/5} \quad (2.4)$$

For a $\beta \approx 100$ this is in agreement with (2.3) and for $\beta > 100$ the value of KC_{cr} is less than Hall’s (1984) predictions. Hall (1984) provides a value for the dimensionless spanwise wavenumber at the high- β limit, permitting the derivation of this relationship:

$$\lambda_{cr}/D = 6.95\beta^{-1/2} \quad (2.5)$$

2.4. RECTILINEAR OSCILLATION IN QUIESCENT FLUID

The correlation provided in Sarpkaya's (2002) investigation is:

$$\lambda_{cr}/D = 22 \beta^{-3/5} \quad (2.6)$$

These equations agree at $\beta = 1.5 \times 10^5$.

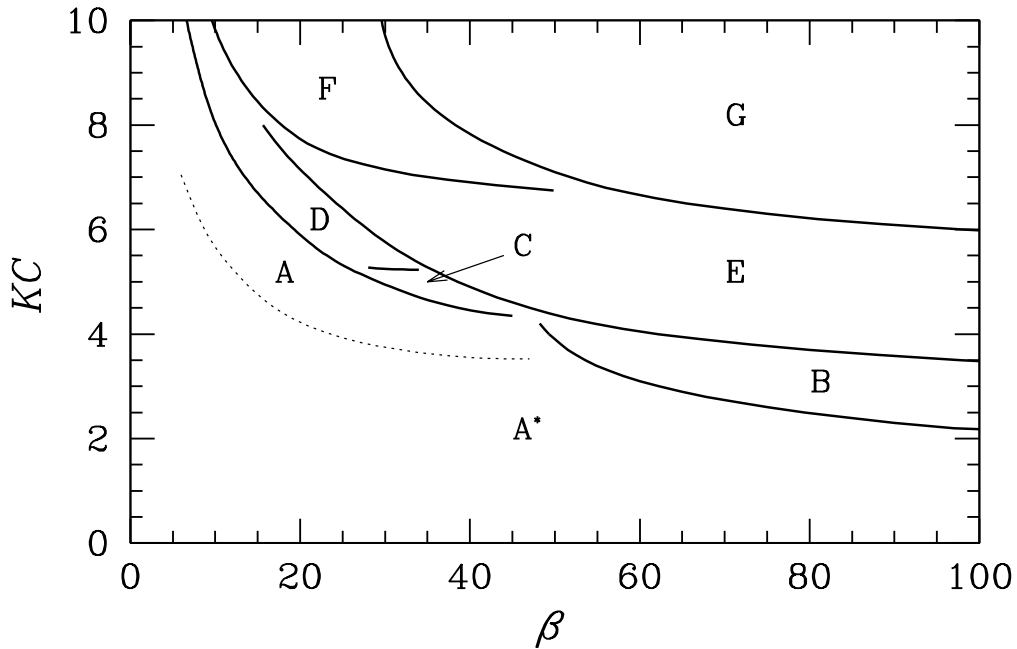


Figure 2.16: A classification of distinctive vortex shedding patterns into unique regimes. Regime B corresponds to the boundaries of the streaked flow regime found by Honji (1981). This map is a derivation of the original, found in Tatsuno and Bearman (1990), and does not display the experimental data points, only the interpolated regime boundaries.

A detailed visual study by Tatsuno and Bearman (1990) of the flow around an oscillating circular cylinder in the range $1.6 < KC < 15$ and $5 < \beta < 160$ identified a varied set of flow regimes. Like Williamson and Honji, they observed symmetrical flow separation and vortex development about the oscillation axis of the cylinder for very low Keulegan–Carpenter numbers. However, as the Keulegan–Carpenter number was increased, and eventually exceeded a critical value, the onset of an asymmetry in the vortex development and flow separation was observed. The consequence of this was shown to be the formation of a number of different regimes as evidenced by the visualisation of their unique two and three dimensional vortex shedding characteristics. A reduced version of the (KC, β) -space map they produced, which classified the unique flows identified into regimes, is shown in figure 2.16. These regimes appear to dovetail well with the observations of Honji (1981) and Williamson (1985). Honji's (1981) results were obtained for an overlapping region, $68.8 < \beta < 700$, within which Tatsuno and Bearman's (1990)

2.4. RECTILINEAR OSCILLATION IN QUIESCENT FLUID

observations closely agree. Williamson's (1985) results were obtained at a larger Stokes number, $\beta \approx 255$, and due to the two-dimensional limitation of Williamson's (1985) visualisations no observation of 'streaked flow' was made. However, the two-dimensional characteristics observed for $KC < 7$ resemble those identified by Honji (1981) and Tatsuno and Bearman (1990) for $\beta > 60$. A sample of the cross-sectional images that appeared in Tatsuno and Bearman (1988, 1990) illustrating these different regimes is shown in figure 2.17. The nomenclature introduced by Tatsuno and Bearman in labelling these regimes will be used for clarity from this point forward. Flows of regime A* were found to have no vortex shedding. They observed no flow along the span of the cylinder (i.e. two-dimensional flow) and found the flow to be symmetrical about the oscillation axis as shown in figure 2.17. Regime A is distinguished from A* due to the formation and shedding of vortices which was not observed in regime A*. In other respects it retains the same characteristics of regime A*. The boundary between these regimes was not explicitly delineated in the original diagram of Tatsuno and Bearman (1990) while in our reproduction, figure 2.16, it is shown as a dashed line. The lack of a distinct boundary was attributed by Tatsuno and Bearman to it being very difficult to determine the onset of vortex shedding and a consequence of the visual means used to evaluate this. In figure 2.17(A) the concentrations of dye that could be mistaken as the presence of vortices actually represent a periodic mass convection away from the cylinder. Tatsuno and Bearman stated that the vortices formed and shed in each half-cycle of cylinder motion are convected back towards the cylinder in the subsequent half-cycle and are then annihilated by mixing with vorticity in the boundary layer.

The flow of regime B was characterised by the presence of spanwise, periodic structures in the induced flow due to a three-dimensional instability. Both Honji (1981) and Tatsuno and Bearman (1990) visualised the formation of streaked flow, as illustrated in figures 2.18(a-c), which was formed and shed alternately along the cylinder span at regular intervals. It was concluded that these regular 'streaks' were due to pairs of contra-rotating longitudinal vortices being formed along the cylinder span and extending out into the flow in the direction of oscillation. The boundaries for this regime almost exactly match those identified by Honji (1981) for the formation of 'streaked flow'. Through measurements of the streak spacing, these vortices were found to have a spanwise wavelength ratio (λ/D) that increased as the Keulegan–Carpenter number is also increased. Despite the onset of a three-dimensional instability the spanwise average of the flow in regime B was found to preserve symmetry, as shown in figure 2.17(B)

The flow of regime C was found to be three-dimensional but appeared to have no periodic spanwise structure as shown in figures 2.18(d,e). In the cross-sectional plane the vortices initially shed from the cylinder were seen to roll up into large vortices, figure 2.17(C), and form a street of vortices similar to that of the von Kármán street, although in this case the sense of rotation of the vortices was opposite to that of the von Kármán

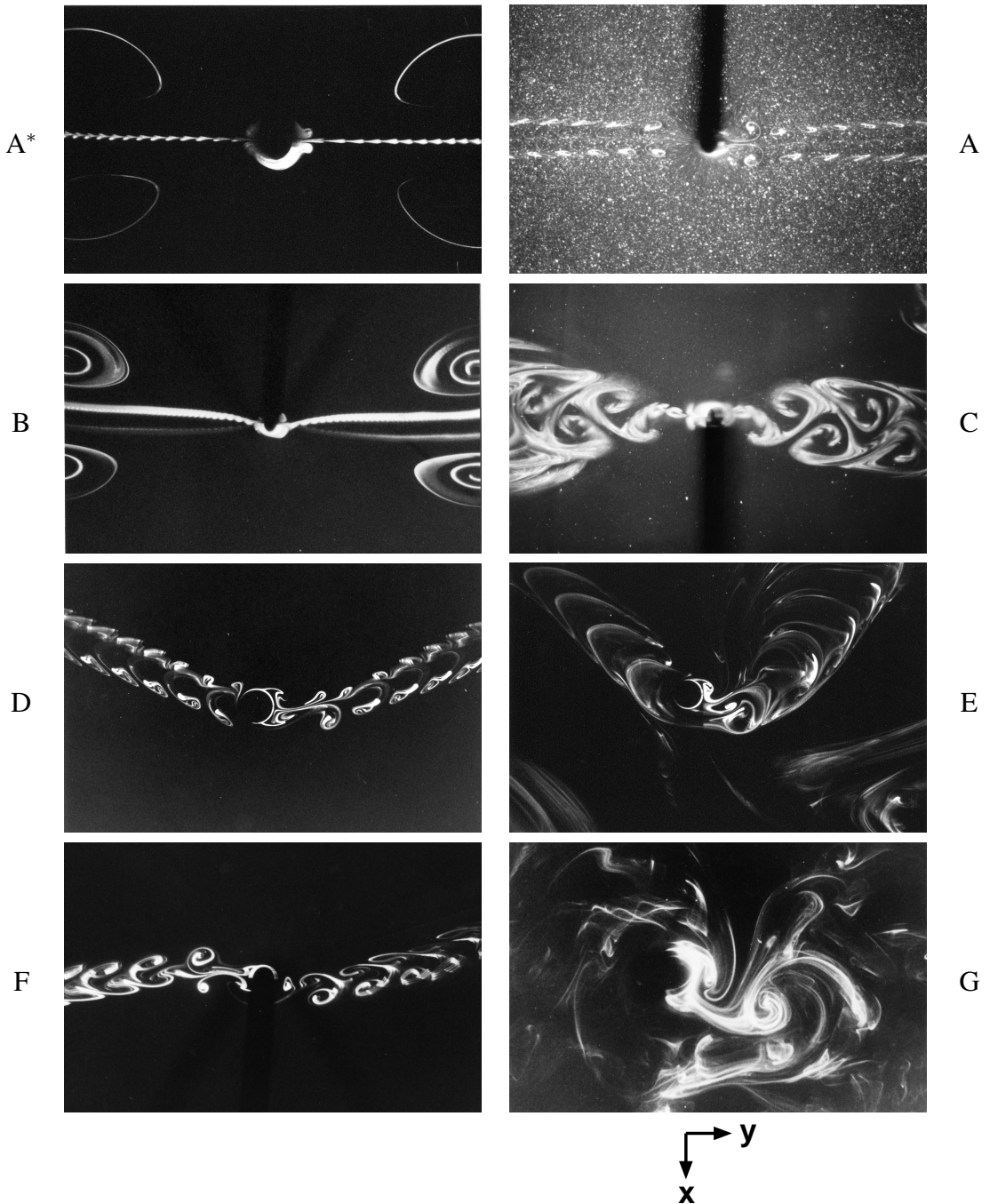


Figure 2.17: Two-dimensional visualisations of the vortex shedding patterns found for Regimes A*–G. The cylinder is shown oscillating along the horizontal axis of the page. The image for regime F appeared in Tatsuno and Bearman (1988), while the others are from Tatsuno and Bearman (1990); All images are reproduced with their permission.

2.4. RECTILINEAR OSCILLATION IN QUIESCENT FLUID

street, i.e. jet-like. It was noted that the large vortices are formed in succession for equal numbers of oscillation cycles, however it is unclear how many oscillation cycles are required for the formation of a large vortex.

Regime D flows were found to break a symmetry that characterised the previously discussed flows; in this regime the induced flow no longer convected along the axis of oscillation, as it did for regimes A*–C, but at an angle to the axis of oscillation as shown in figure 2.17(D). No mention was made of the actual angle to the oscillation axis that the flow initially convected along, however from the figures presented it can be estimated to be approximately 25° . This feature was attributed to an asymmetry in the development of a vortex pair in each half-cycle. While the resultant flow breaks symmetry about the axis of oscillation (the x -axis), it was observed that the time-periodic symmetry about the y -axis was retained, i.e. the flow was still synchronous with the cylinder oscillation. Along the span the formation of regular ‘tubes’ was found, see figure 2.18(f), within which the fluid was observed to be travelling faster than the surrounding fluid. The spanwise spacing between the tubes was found to be independent of KC and only weakly to decrease with increasing Stokes numbers.

The flow in regime E exhibited spatial patterns in the cross-section similar to that of regime D see figure 2.17(E), but it was found that the direction to which the flow convected intermittently changed direction between the $+x$ and $-x$ side of the cylinder. The irregular switching to either side is in contrast to regime D where the direction was fixed. Along the span there was evidence of some three-dimensional structures, see figure 2.18(g), although no periodic wavelength could be established. The structures that were present were found to be obscured by the switching of the flow convection direction.

Regime F exhibits a similar behaviour to regime D except that in this case the convections arms depart the near wake region at opposing angles with respect to the oscillation axis (see Figure 2.17(F)). Along the span, a periodic structure was found with pairs of counter rotating vortices observed to form at regular intervals along the span as shown in figure 2.18(h). The spacing between these structures was found to vary in the same manner as it did for its neighbouring regime, D.

A circulatory streaming motion around the cylinder was observed to occur in regime G, figure 2.17(G). Increases in KC or β within this region resulted in the onset of turbulent motion and the streaming flow generated by the cylinder motion was observed to irregularly change direction. No regular formation of structures along the span was observed.

Yang and Rockwell (2002) observed sinusoidal spanwise variations in the flow about a cylinder subjected to wave loading at a relatively low $KC = 4.5$. Along the span of the cylinder regular patterns of streamwise vorticity were observed. The spanwise wavelength between vorticity of like sign ranged from $1 \lesssim \lambda/D \lesssim 4.5$, which at this value of KC is compatible with the observations Tatsuno and Bearman (1990). At larger

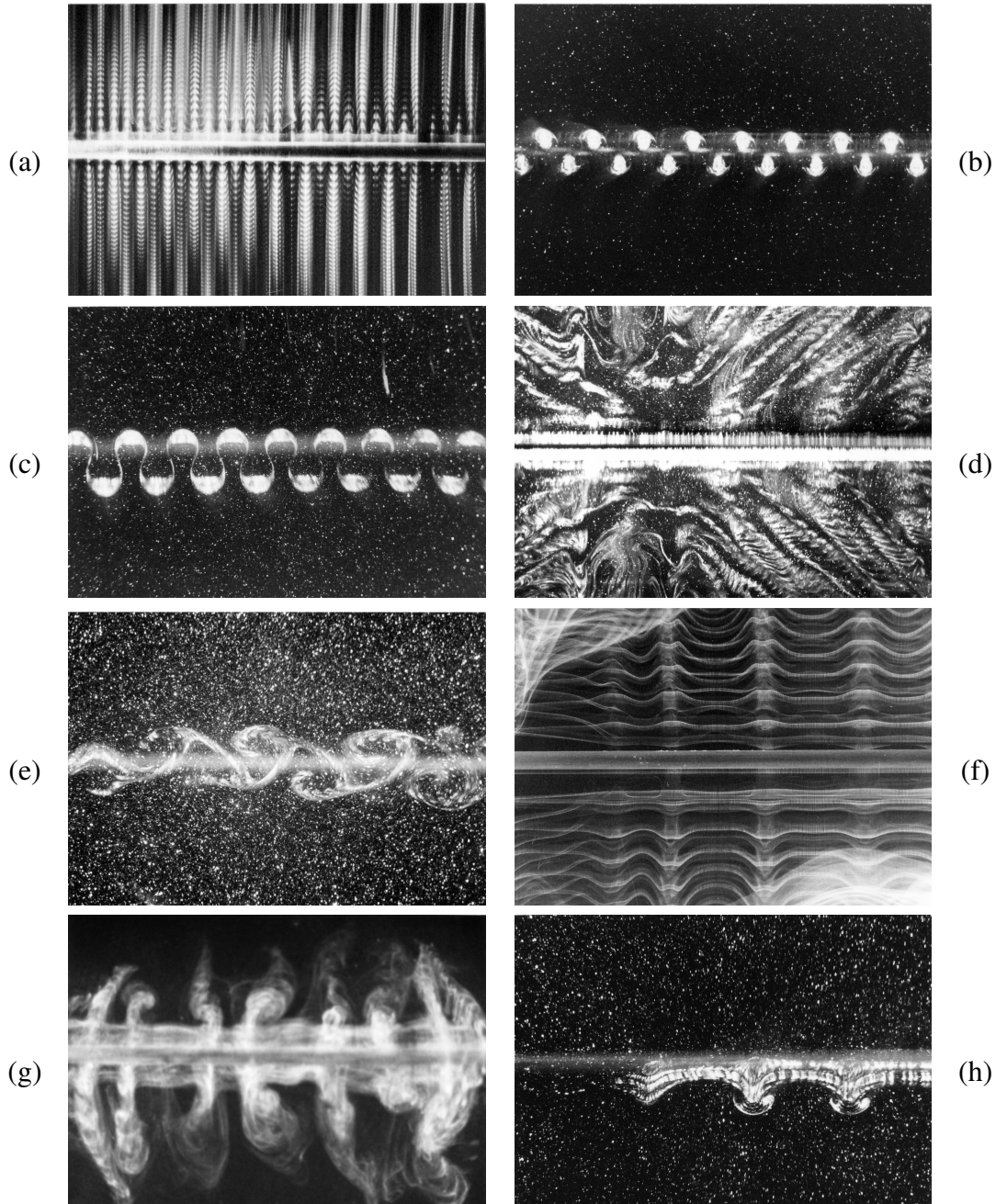


Figure 2.18: Visualisations of the three-dimensional structures observed in Regimes B to F. The images were produced using an electrostatic precipitation method and show the variation in the flow along the cylinder span. The span of the cylinder (z -axis) is orientated horizontally in all these images with the cylinder oscillating along the y -axis. Images (a), (d), (f), (g) and (h) are taken in the y - z plane while images (b), (c) and (e) are taken in the x - z plane. Presented are Regime B [(a), (b) & (c)], Regime C [(d) & (e)], Regime D [(f)], Regime E [(g)] and Regime F [(h)]. All the images appeared in Tatsuno and Bearman (1990) and are reproduced with their permission.

2.4. RECTILINEAR OSCILLATION IN QUIESCENT FLUID

values of KC (10 and 18) larger scale regular variations along the span were observed. These variations were of the order $10 \lesssim \lambda/D \lesssim 110$ which was greater than the distances between individual concentrations of streamwise vorticity.

Using a two-dimensional finite-difference numerical technique Justesen (1991) was able to predict the transverse street and other vortex shedding regimes, as found by Williamson (1985) and shown in figure 2.9. Despite this study being under-resolved in some regions of its parameter space, it was conducted for β in the range 196–1035 and KC between 0 and 26, and being restricted to two dimensions they were able to obtain good agreement between calculated drag and inertia coefficients and experimental data. The onset of an asymmetry in the flow was found to occur at $KC \approx \pi$ for $\beta = 196$ and to decrease slightly for higher Stokes numbers.

A comparison between LDA measurements and two-dimensional computations was performed by Dütsch, Durst, Becker and Lienhart (1998) for three regimes: A, F and E. In regime A they found good agreement between the velocity fields produced by both techniques. This was in accord with Tatsuno and Bearman's (1990) work which had previously established that this flow was two-dimensional. In regime F they found that the flow was asynchronous using both techniques. As a consequence of the formation of a vortex pair that was unequal in magnitude a vortex street was observed to form that convected away from the cylinder at an angle of approximately 27° . This again matches previous results, e.g. see figure 2.17(F), but is interesting because it was achieved by both LDA and two-dimensional computation suggesting that the breaking of symmetry about the oscillation axis and the asynchronous behaviour are largely two-dimensional phenomena. In the final regime studied, E, they presented vorticity contours which matched the flow fields generated by Tatsuno and Bearman (1990) in figure 2.17(E). However, they found that their simulations were stable after 15 cycles and that periodic shedding resulted. This is in direct contrast to Tatsuno and Bearman (1990) who observed an irregular switching of the direction of vorticity shedding between the $+x$ and $-x$ sides of the cylinder.

A finite-element study by Iliadis and Anagnostopoulos (1998) located a boundary in (KC, β) -space where the two-dimensional symmetric flow became asymmetric. Conducted over the range $KC \leq 15$ and $6 \leq \beta \leq 100$ it was in good agreement with the experimental boundaries presented in figure 2.16 for $\beta > 40$, but in the low Stokes number region the match was poorer. At a low Stokes number (regime D) their vorticity contours match experimental visualisations both in their spatial and temporal (synchronous) nature. Investigations of flows that lay in regimes E and F yielded results that showed no intermittent switching of the shedding direction as found in experiments. This led them to conclude that the switching of flow direction is associated with the three-dimensional nature of the flow.

Three-dimensional numerical investigations of this parameter space have been more sparse. An investigation into the onset of three-dimensionality by Zhang and Dalton

2.4. RECTILINEAR OSCILLATION IN QUIESCENT FLUID

(1999) using a numerical technique at $\beta = 196$ yielded a set of results that agreed with experimental results. The onset of three-dimensionality was observed for $KC = 2$ and separation was subsequently observed to occur at $KC = 3.2$ before the flow became chaotic at $KC = 4$. Nehari, Armenio and Ballio (2004) examined two three-dimensional states, both at $\beta = 20$; one at $KC = 6.5$ (Regime D) and the other at $KC = 8.5$ (Regime F). They found that in both cases irregular switching of the vortex streets between the $+x$ and $-x$ directions was observed. This behaviour was able to be reproduced using purely two-dimensional simulations and therefore it was concluded that this is related to a two-dimensional instability, a finding in direct contrast to that of Iliadis and Anagnostopoulos (1998). It was noted that three-dimensionality appears after the underlying two-dimensional symmetry has been broken. It was speculated that this switching of vortex shedding direction in combination with the onset of three-dimensionality would contribute to the formation of the sinuous S-mode witnessed in Yang and Rockwell (2002).

2.5 Combined Rotational and Rectilinear Oscillation

To date no detailed studies into the effects of combining an oscillatory rotational and translational motion of a circular cylinder in either quiescent fluid or in external flow are known. However, a similar form of motion is observed in nature and recent research into this is discussed in §2.5.1. A set of preliminary studies into the effect of combining rotational and rectilinear oscillations of a circular cylinder by Elston (1997); Blackburn et al. (1998, 1999) have demonstrated a number of interesting results.

In a series of two-dimensional numerical simulations it was shown that this combination of motions was able to produce a variety of flows, as shown in figure 2.19. In these simulations the phase angle, α , between the two motions was found to have a significant effect upon the near wake structure. In the results shown, the computational domain has periodic boundaries and for the $\alpha = 45.0^\circ$, 67.5° and 90.0° this permitted vortex pairs to leave the domain and reenter on the opposite side. The phase angle between the motions seems to influence the degree to which cross-annihilation of vorticity occurs and the distance from the cylinder at which vorticity persists.

A further consequence of the phase angle is the ability of the cylinder's motion to result in net force being exerted upon the surrounding flow. Of particular interest are the $\alpha = 0^\circ$ and 157.5° cases. In these cases a net force was found to act on the surrounding fluid at an angle perpendicular to the oscillation axis. Further investigation by Blackburn, Elston and Sheridan (1999) of the solitary jet of fluid produced in a direction normal to the translational axis for the $\alpha = 0^\circ$ yielded interesting results. Two scenarios were examined for this case: firstly where the cylinder was held fixed in the horizontal plane and secondly where the cylinder was permitted to freely move in the horizontal plane. The translational oscillation had the parameters $KC = \pi$ and $\beta = 90$ which was shown to result in a regime B flow with no rotary oscillation present. The frequency of the rotary oscillation was set to be synchronous with the translational oscillation and the amplitude of oscillation was one radian.

For the first scenario where the cylinder was fixed in the horizontal direction, see figure 2.20, a streaming flow along this axis is apparent in the vorticity contours. A corresponding simulation of particles being shed from the cylinder surface further illustrates the jet that results. A wake velocity profile at $x/D = 2.0$ downstream revealed this jet to have a double-peaked nature as suggested by the particle transport map. In the second scenario, where the cylinder was allowed to move in response to the forces exerted by the jet, a terminal velocity approximately $1/3$ of the magnitude of the maximum translational velocity was achieved. The instantaneous vorticity contour and particle transport maps are shown in figure 2.21. In these maps the high-speed pulsating nature of the jet is shown as discrete 'puffs' of particles.

The mechanism by which a thrust is generated was only briefly touched upon in Black-

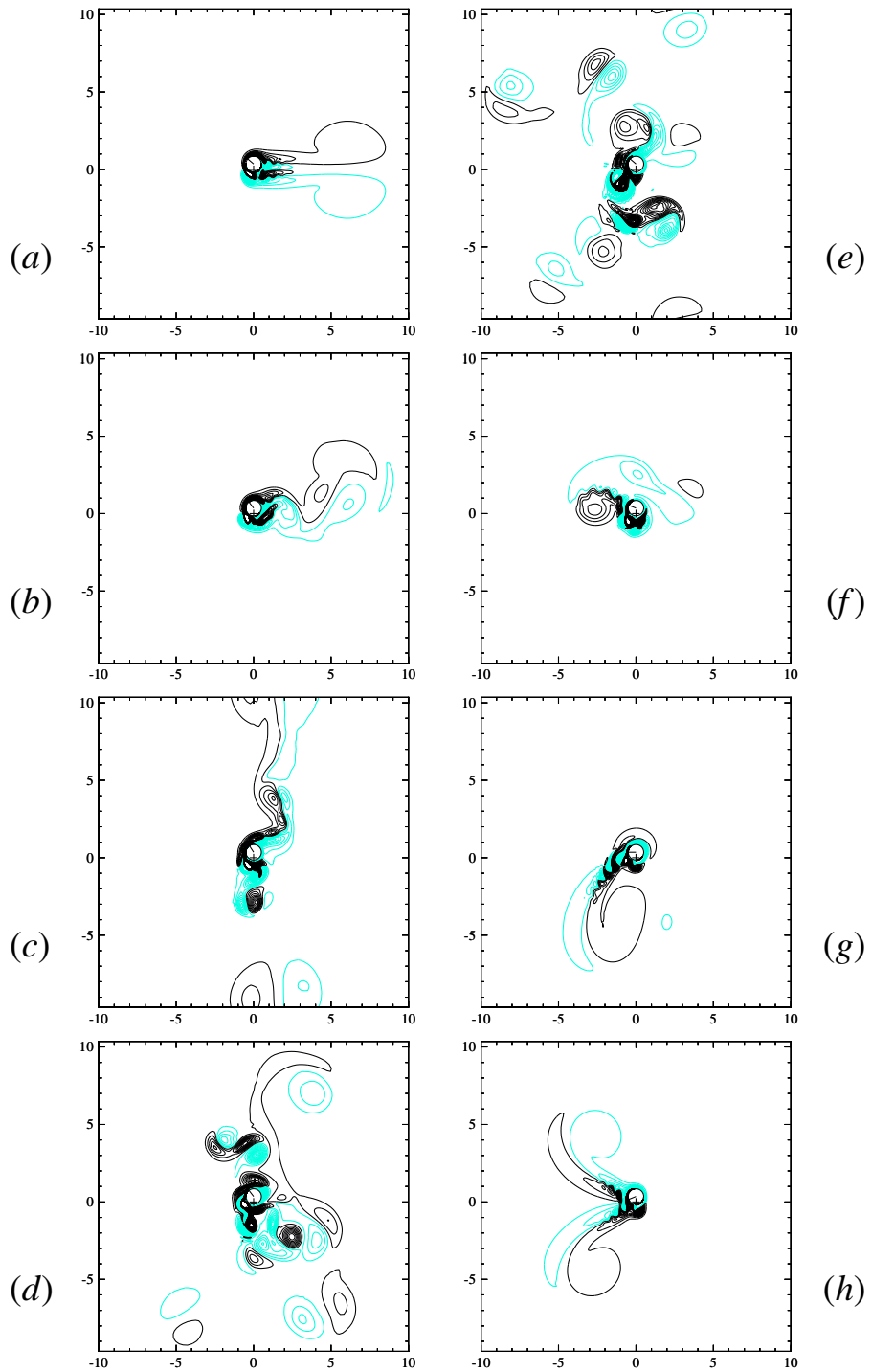


Figure 2.19: Instantaneous vorticity contours for a cylinder with both translational and rotational oscillation, shown at $t/T = 45.75$ for a range of phase angles: (a), $\alpha = 0^\circ$; (b), $\alpha = 22.5^\circ$; (c), $\alpha = 45^\circ$; (d), $\alpha = 67.5^\circ$; (e), $\alpha = 90^\circ$; (f), $\alpha = 112.5^\circ$; (g), $\alpha = 135^\circ$; (h), $\alpha = 157.5^\circ$. Reproduced from Blackburn et al. (1998).

burn et al. (1999). In figures 2.20(a) and 2.20(b) it can be seen that the vorticity on the left side of the cylinder is greater in magnitude than that of the right side, this is consis-

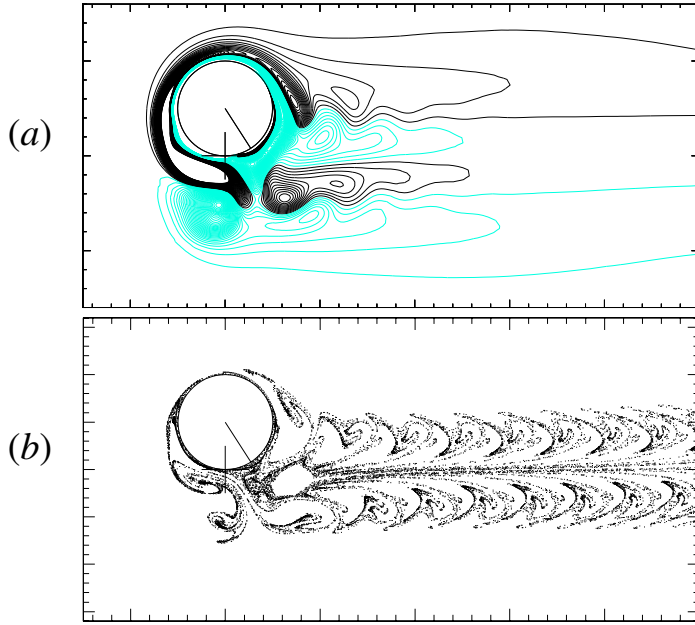


Figure 2.20: Flows produced by a cylinder with oscillatory translation and rotation: (a) instantaneous vorticity contours; (b) fluid particle transport. The cylinder is at its maximum vertical position and most negative angular displacement at the instant shown. The rest position of the cylinder is indicated by cross-hairs, and the radial line shows the radial displacement of the cylinder from the horizontal. Reproduced from Blackburn et al. (1999)

tent with the fact that the surface-tangential component of cylinder acceleration is always larger on the left face of the cylinder due to the particular combination of translational and rotational oscillation employed. It is speculated that a simplified explanation for the thrust produced by this motion combination is due to the pressure difference across the cylinder. This can be explained by applying Bernouilli's equation at the cylinder's surface. If we consider two points placed on opposite sides of the cylinder (denoted left(L) and right(R)) and neglect the effect of gravity then Bernouilli's equation becomes:

$$\frac{1}{2}(V_L^2 - V_R^2) = \frac{1}{\rho}(P_R - P_L). \quad (2.7)$$

where P is pressure and V is velocity. For the specified combination of motion it is known that the left face has a greater tangential velocity than the right face and therefore $P_R > P_L$ leading to a thrust in the left direction, as observed.

To date, no three-dimensional numerical simulations of this flow have been performed. This potentially could have a significant impact upon the thrust observed as the flow for a cylinder in purely translational motion at this point in the (KC, β) -parameter space has been proven to be three-dimensional. Additionally while these simulations have been implemented with all possible care and testing, no physical experiments exist which

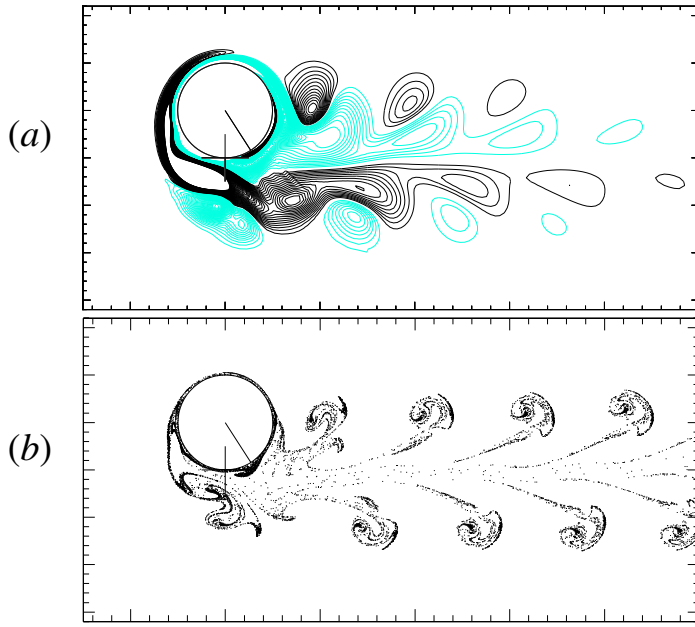


Figure 2.21: Flows produced by a cylinder with oscillatory translation and rotation with no restraints applied in the horizontal direction: (a) instantaneous vorticity contours; (b) fluid particle transport. The cylinder is moving at terminal speed in the $-x$ direction. Reproduced from Blackburn et al. (1999).

confirm that these effects occur. On the other hand, there does exist a similar motion in nature, that is a combination of rotational and translational motion, which is used as a propulsion mechanism. This motion will be discussed in the following section.

2.5.1 Carangiform Motion

In the animal kingdom, the process of evolution has led to highly efficient methods of propulsion being developed. Of particular relevance to the combined motion outlined in §2.5 is the means of propulsion developed by animals of three distinct groups, that include all of the fastest, continuously swimming animals in the ocean. These animals, such as tuna, marlin, sharks, whales and dolphins, all have an identical means of propulsion which is based upon their fins (or tails) being given a characteristic combination of rectilinear and rotational oscillation. This mode of oscillation, which is called *Carangiform* motion, utilizes a twist of the animals' wing-like surface at the extreme ends of the fins rectilinear oscillation (Lighthill; 1986).

In comparison, the results for the circular cylinder have the change in rotational velocity at the midpoint of the cylinders translation. The propulsive jet that is produced from carangiform motion occurs when the oscillations are phase-locked and in phase, in contrast to the preliminary results for the swimming cylinder, which occurred when the translational and rotational oscillations were in anti-phase (Blackburn et al.; 1999). It has been suggested that this disparity in the phase angle between carangiform motion and the numerical results could be linked to the features which act to influence and control the fin's wake. The magnitude of thrust from the fin is also much larger than that from the oscillating cylinder, but it is likely that much of the thrust comes from the aerodynamic shape of the fin. It is possible that the oscillatory motion of the fin could serve as a drag reduction mechanism.

Experimental research into thrust producing oscillating foils has tended to focus on marine propulsion and has correspondingly been conducted at much higher Reynolds numbers than the present study, i.e. Triantafyllou, Triantafyllou and Yue (2000). A study into oscillating foils by Anderson, Streitlien, Barrett and Triantafyllou (1998) has found that high efficiency is associated with the formation of a reverse Kármán street (e.g. see figure 2.21) and that the phase angle between the transverse oscillation and angular motion is the critical parameter affecting the vorticity formation and propulsion efficiency.

2.6 Summary

Translational oscillation of a cylinder in both a free-stream and in quiescent fluids has been well researched. A ‘Lock-In’ region has been identified for cylinders oscillating in a free-stream. The boundaries of the region vary depending upon the Reynolds number of the incident flow and the amplitude and frequency of the oscillation. Within the Lock-In region the frequency of vortex shedding is captured by the cylinder oscillation frequency and a number of forcing and wake structure events are observed to occur. For a cylinder oscillating in a quiescent fluid, a number of different wake regimes have been identified by Williamson (1985) that are selected on the basis of the cylinder’s amplitude of oscillation. The effects of rotational oscillation of a cylinder in a uniform stream have been less well documented, but recent research has shown how the rotary oscillation of a cylinder can dramatically increase or decrease a cylinders wake and alter the normal pattern of vortex shedding.

At low amplitudes and frequencies of rectilinear oscillation in a quiescent fluid the resulting flow has been observed to form a number of unique flow structures that quickly transition to different forms of flow structures for relatively small changes in the controlling parameters. Little investigation has occurred into these transitions with the majority of the existing research consisting of experimental visualisations. Some limited numerical computations have been performed although these have been two-dimensional (in the x - y plane) and haven’t explained the nature of these transitions. The rectilinear oscillation when combined with a rotational oscillation has been shown numerically to produce a time-averaged net force perpendicular to the direction of rectilinear oscillation. A hypothesis has been proposed that this is due to a pressure variation across the cylinder diameter caused by the phase-locked oscillations, however no research has confirmed this.

Chapter 3

Numerical Method: Spectral Element Method

In this chapter the high order numerical method used for direct numerical simulation of the incompressible, unsteady Navier–Stokes equations is outlined. The chosen method, a spectral element method, is used for both direct analysis of the flows to be studied and to produce the periodic flows used in Floquet analysis, as will be discussed later in chapter §4. The source code for this method was obtained from H. M. Blackburn¹ and has been used extensively, with modifications for different geometries and coordinate systems, to produce a number of publications, of which a small selection includes Blackburn et al. (1999); Blackburn and Henderson (1999); Blackburn and Lopez (2002, 2003). In the implementation used here the incompressible Navier–Stokes equations are solved in an accelerating reference frame attached to the cylinder.

The form of the nonlinear equations modelled by this code is presented in §3.1. In the subsequent section, §3.2, the numerical techniques used for spatial and temporal discretisation are examined. Throughout the results to be presented a number of variables are calculated via post-processing of the primitive variables (u, v, w) , i.e. vorticity; the means by which these are calculated are discussed in §3.3. Finally, in §3.4 the choice of domain extent, the elemental discretisation and the timestep for the simulations are discussed.

¹CSIRO Manufacturing and Infrastructure Technology, Australia

3.1 Governing Flow Equations

Considered in this study are Newtonian, unsteady, incompressible flows with constant properties governed by the Navier–Stokes equations expressed in the form:

$$\frac{\partial \mathbf{u}}{\partial t} = -\nabla P + \mathbf{N}(\mathbf{u}) + \nu \nabla^2 \mathbf{u} \quad (3.1a)$$

$$\nabla \cdot \mathbf{u} = 0 \quad \text{in } \Omega \quad (3.1b)$$

where $\mathbf{u} \equiv (u, v, w)$, $P = p/\rho$, p is the kinematic pressure and Ω is the computational domain. On the cylinder boundaries a no-slip velocity condition, $\mathbf{u} = 0$, is applied while at the outer boundaries a prescribed velocity condition is applied that takes into account the moving frame of reference, as will be described in §3.1.1.

The nonlinear advection term, $\mathbf{N}(\mathbf{u})$, can be represented in one of three forms:

$$\mathbf{N}(\mathbf{u}) = -(\mathbf{u} \cdot \nabla) \mathbf{u} \quad (3.2a)$$

$$= -\frac{1}{2}[(\mathbf{u} \cdot \nabla) \mathbf{u} + \nabla \cdot (\mathbf{u} \mathbf{u})] \quad (3.2b)$$

$$= -\frac{1}{2}\nabla(\mathbf{u} \cdot \mathbf{u}) - \mathbf{u} \times \nabla \times \mathbf{u} \quad (3.2c)$$

These are known as the *convective* form, *skew-symmetric* form and *rotational* form, respectively. While these three forms are equivalent in a continuum treatment they behave differently in discrete implementations. As noted in Henderson and Karniadakis (1995), the skew-symmetric form (3.2b) has been shown to be better at minimizing aliasing errors and will be used herein.

3.1.1 Moving Frame of Reference

The problem being considered here deals with a cylinder in relative rectilinear motion to the surrounding fluid. Computationally there are three general techniques of dealing with this. One technique is to have a computational grid which deforms to allow cylinder motion. This technique has the substantial disadvantage of not permitting the use of optimised solvers which have been developed for static meshes. The second technique is to attach the coordinate system to the body and impose an oscillating inflow and outflow on the outer boundaries. A third technique is to attach the coordinate system to the body, and solve the governing equations in a moving frame of reference. The second and third options utilise fixed computational meshes and therefore permit the use of optimised solvers. Although both the second and third options are simply a change in the frame of reference, the third technique is the technique that is used here because of the later desire to study the forces experienced by the cylinder.

In order to accommodate the externally applied motion of the cylinder, the Navier–

3.1. GOVERNING FLOW EQUATIONS

Stokes equations (3.1) are solved in a moving reference frame attached to the cylinder as described in Blackburn and Henderson (1996). Consequently, the governing equations and the boundary conditions outlined in §3.1 require some modification.

When the reference frame in which the Navier–Stokes equations are being solved has a rectilinear acceleration, \mathbf{a} , then (3.1) becomes:

$$\frac{\partial \mathbf{u}}{\partial t} = -\nabla P + \mathbf{N}(\mathbf{u}) + \nu \nabla^2 \mathbf{u} - \mathbf{a} \quad (3.3a)$$

$$\nabla \cdot \mathbf{u} = 0. \quad (3.3b)$$

The prescribed velocity boundary conditions become:

$$\mathbf{u} = \mathbf{U}_p - \mathbf{v}, \quad (3.4)$$

where \mathbf{v} is the velocity of the reference frame and \mathbf{U}_p is the prescribed value, in this case $\mathbf{U}_p = 0$. The pressure boundary condition is obtained by taking the normal component of (3.3a) to make

$$\frac{\partial P}{\partial n} = \mathbf{n} \cdot [\mathbf{N}(\mathbf{u}) - \nu \nabla \times \nabla \times \mathbf{u} - \frac{\partial \mathbf{u}}{\partial t} - \mathbf{a}]. \quad (3.5)$$

The form of the viscous term is obtained from $\nu \nabla^2 \mathbf{u}$ using the vector identity $\nabla \times \nabla \times \mathbf{u} = \nabla \nabla \cdot \mathbf{u} - \nabla^2 \mathbf{u}$ and incorporating in the incompressibility constraint $\nabla \cdot \mathbf{u} = 0$.

On the cylinder boundary (a solid wall) $\partial \mathbf{u} / \partial t = 0$ and therefore (3.5) becomes

$$\frac{\partial P}{\partial n} = \mathbf{n} \cdot [\mathbf{N}(\mathbf{u}) - \nu \nabla \times \nabla \times \mathbf{u} - \mathbf{a}], \quad (3.6)$$

while on prescribed velocity boundaries $\partial \mathbf{u} / \partial t = -\mathbf{a}$ and (3.5) becomes

$$\frac{\partial P}{\partial n} = \mathbf{n} \cdot [\mathbf{N}(\mathbf{u}) - \nu \nabla \times \nabla \times \mathbf{u}]. \quad (3.7)$$

3.2 Spectral Element Method

Spectral element methods combine the advantages of high-order methods, which offer fast convergence and small numerical errors, and finite element methods, which provide the ability to simulate more complex geometries and localise mesh refinement. In the method implemented here the domain to be investigated is broken up into elements and within each element it is spatially evaluated using Gauss–Lobatto–Legendre (GLL) polynomial interpolants in the x – y plane and Fourier expansions along the spanwise z -axis, as described in §3.2.2. Details of the high-order time-splitting scheme used to integrate 3.3 are described in §3.2.1.

3.2.1 Temporal Discretisation

A second-order time splitting scheme, as advanced by Karniadakis, Israeli and Orszag (1991), was used for the temporal discretisation. With this scheme a discrete set of times is introduced, $t_n \equiv n\Delta t$, and a semi-discrete approximation to the velocity is introduced $\mathbf{u}^n \equiv \mathbf{u}(\mathbf{x}, t_n)$ (full spatial discretisation will be considered in the subsequent section §3.2.2). Using this semi-discrete approximation the momentum equation (3.3) is integrated over a single time step to obtain:

$$\mathbf{u}(t + \Delta t) = \mathbf{u}(t) + \int_t^{t+\Delta t} [\mathbf{N}(\mathbf{u}) - \nabla P + \nu \nabla^2 \mathbf{u} - \mathbf{a}] dt. \quad (3.8)$$

This equation can then be broken up into discrete substeps which treat the advection, diffusion and pressure/mass conservation terms of the momentum equation separately.

$$\mathbf{u}^{(1)} - \mathbf{u}^n = \int_t^{t+\Delta t} [\mathbf{N}(\mathbf{u}) - \mathbf{a}] dt \quad (3.9a)$$

$$\mathbf{u}^{(2)} - \mathbf{u}^{(1)} = \int_t^{t+\Delta t} -\nabla P dt \quad (3.9b)$$

$$\mathbf{u}^{n+1} - \mathbf{u}^{(2)} = \int_t^{t+\Delta t} \nu \nabla^2 \mathbf{u} dt, \quad (3.9c)$$

where $\mathbf{u}^{(1)}$ and $\mathbf{u}^{(2)}$ are intermediate velocity fields introduced to facilitate the decoupling of the pressure, advection and diffusion terms so that different integration methods can be used for each.

A high-order multi-step integration scheme is used to increase the time accuracy of the integration in (3.9) to $O(\Delta t^J)$. Derivatives in time are approximated to order J with a backward difference of the form:

$$\frac{\partial \mathbf{u}}{\partial t} \approx \Delta t (\gamma_0 \mathbf{u}^{n+1} - \sum_{q=0}^{J-1} \alpha_q \mathbf{u}^{n-q}), \quad (3.10)$$

3.2. SPECTRAL ELEMENT METHOD

J	γ_0	α_0	α_1	α_2	β_0	β_1	β_2
1	1	1			1		
2	3/2	2	-1/2		2	-1	
3	11/6	3	-3/2	1/3	3	-3	1

Table 3.1: Integration coefficients for a stiffly-stable multi-step scheme of order J .

where $\gamma_0 = \sum \alpha_q$ for consistency. Integration of the reference frame acceleration and the nonlinear term in (3.9a) is accomplished via explicit extrapolation, again of order J , where the weights used for the calculation of the integration and time derivatives are outlined in Table 3.1.

$$\int_{t_n}^{t_{n+1}} [\mathbf{N}(\mathbf{u}) - \mathbf{a}] dt \approx \Delta t \sum_{q=0}^{J-1} \beta_q [\mathbf{N}(\mathbf{u}^{n-q}) - \mathbf{a}^{(n-q)}], \quad (3.11)$$

where $\sum \beta_q = 1$.

The incompressibility constraint (3.3b) is incorporated into the second substep of the timesplitting scheme (3.9b) when the assumption is made that $\mathbf{u}^{(2)}$ satisfies this condition. An additional assumption is also made that $\mathbf{u}^{(2)}$ satisfies the Dirichlet boundary conditions in a direction normal to the boundary ($\mathbf{n} \cdot \mathbf{u}^{(2)} = \mathbf{n} \cdot \mathbf{u}^{n+1}$). In (3.9b) the pressure integral is replaced with:

$$\nabla \tilde{p} \equiv \frac{1}{\Delta t} \int_{t_n}^{t_{n+1}} \frac{1}{\rho} \nabla P dt \quad (3.12)$$

and then a separately solveable Poisson equation for the pressure can be derived by incorporating in the above assumptions.

$$\nabla^2 \tilde{p} = \frac{1}{\Delta t} (\nabla \cdot \mathbf{u}^{(1)}) \quad (3.13)$$

The field \tilde{p} couples the momentum and continuity equations. The Neumann boundary conditions for \tilde{p} are obtained by taking the normal component of (3.3a) such that:

$$\frac{\partial \tilde{p}}{\partial n} = \mathbf{n} \cdot [\mathbf{N}(\mathbf{u}^n) - \nu \nabla \times \nabla \times \mathbf{u}^n]. \quad (3.14)$$

On the cylinder boundary the pressure boundary condition is,

$$\frac{\partial \tilde{p}}{\partial n} = \mathbf{n} \cdot [\mathbf{N}(\mathbf{u}) - \nu \nabla \times \nabla \times \mathbf{u} - \mathbf{a}]. \quad (3.15)$$

These boundary conditions, introduced by Karniadakis et al. (1991), minimize the effect of numerical errors introduced by the time-splitting method.

3.2. SPECTRAL ELEMENT METHOD

The linear terms in the third sub-step (3.9c) are approximated implicitly in time

$$\int_{t_n}^{t_{n+1}} \nu \nabla^2 \mathbf{u} dt \approx \Delta t \sum_{q=0}^{J-1} \gamma_0 \nu \nabla^2 \mathbf{u}^{(n+1-q)}. \quad (3.16)$$

After incorporating in the above modifications the sub-steps are now:

$$\mathbf{u}^{(1)} - \sum_{q=0}^{J-1} \alpha_q \mathbf{u}^{n-q} = \Delta t \sum_{q=0}^{J-1} \beta_q [\mathbf{N}(\mathbf{u}^{n-q}) - \mathbf{a}^{(n-q)}] \quad (3.17a)$$

$$\nabla^2 \tilde{p} = \frac{1}{\Delta t} (\nabla \cdot \mathbf{u}^{(1)}) \quad (3.17b)$$

$$\mathbf{u}^{(2)} - \mathbf{u}^{(1)} = - \Delta t \nabla \tilde{p} \quad (3.17c)$$

$$\gamma_0 \mathbf{u}^{n+1} - \mathbf{u}^{(2)} = \Delta t \sum_{q=0}^{J-1} \gamma_0 \nu \nabla^2 \mathbf{u}^{(n+1-q)} \quad (3.17d)$$

These equations comprise the fully three-dimensional semi-discrete equations required to integrate the Navier–Stokes equations. In order to solve these equations the following are required for each time step: the solution to one Poisson equation for the pressure, the solution to a Helmholtz equation for the diffusion in each direction and a number of spatial derivatives. The evaluation of these equations and derivatives requires knowledge of the spatial discretisation and this will be discussed in the following section.

3.2.2 Spatial Discretisation

Spatial discretisation of the computational domain is solved in two parts: in the x – y plane the domain is broken up into quadrilateral elements within which a high order interpolant is utilised; along the cylinder span, the z -axis, a Fourier decomposition is employed. The treatment of these, which is only briefly outlined here, is further described in detail in (amongst others) Blackburn and Lopez (2003), Henderson and Karniadakis (1995), Karniadakis et al. (1991), Karniadakis (1990) and Karniadakis and Sherwin (1999). We will first consider the solution of an elliptic problem in Cartesian coordinates on a fully two-dimensional domain and then subsequently extend it to the case where a Fourier expansion is used in the z -direction.

3.2.2.1 Two-Dimensional Spectral Element Discretisation

In this section the Galerkin formulation for the solution of an elliptic problem on a two-dimensional domain is outlined. The Helmholtz elliptic problem can be stated in *strong* form as: given $b \in \Re$ and smooth functions $c : \Omega \rightarrow \Re$, $g : \Gamma_g \rightarrow \Re$, and $h : \Gamma_h \rightarrow \Re$, find u such that

$$\nabla^2 u - b^2 u + c = 0 \quad \text{in } \Omega \quad (3.18)$$

3.2. SPECTRAL ELEMENT METHOD

subject to the boundary conditions

$$u = g \quad \text{on } \Gamma_g, \quad (3.19a)$$

$$\mathbf{n} \cdot \nabla u = h \quad \text{on } \Gamma_h \quad (3.19b)$$

where Ω is the unit domain $-1 \leq x, y \leq 1$. If $b = 0$ then this equation is called Poisson's equation while if both b and c are 0 then this is known as Laplace's equation. For the solution of our semi-discrete equations (3.17) we need to solve both Helmholtz and Poisson equations.

With spectral element methods the above *strong* form is rewritten into a weaker formulation that is more readily solved. This is achieved by defining a residual function, R , and a set of weighting functions, w , such that

$$R(u) = \int_{\Omega} w(\nabla^2 u - b^2 u + c) d\Omega. \quad (3.20)$$

Setting $R(u) = 0$ and integrating this equation once by parts results in the variational form of the problem:

$$a(u, w) = (c, w) + (h, w)_{\Gamma_h} \quad (3.21)$$

where the following symmetric bilinear forms have been used:

$$a(u, w) = \int_{\Omega} (\nabla u \nabla w + b^2 u w) d\Omega \quad (3.22)$$

$$(c, w) = \int_{\Omega} c w d\Omega. \quad (3.23)$$

Integrating by parts has resulted in the requirement that the trial, u , and test, w , functions both have square integrable first derivatives and that both sets of functions belong to the Sobolev space H^1 . In addition the symmetry of the equation leads to less computational effort later. The sets of trial and test functions are defined as:

$$\begin{aligned} S &= \{u \mid u \in H^1, u = g \quad \text{on } \Gamma_g\} \\ V &= \{w \mid w \in H^1, w = 0 \quad \text{on } \Gamma_h\}. \end{aligned} \quad (3.24)$$

The space H^1 has two properties central to the use of a Galerkin approximation. Firstly it is a ‘linear space’ and secondly, it is ‘infinite-dimensional’. The ‘linear space’ property simply means that linear combinations of members of H^1 are also members of H^1 . The space is ‘infinite-dimensional’ in that it is required to specify an infinite number of parameters in order to define a unique function within the space. The Galerkin approximation represents the infinite dimensional space using a finite collection of n basis functions

3.2. SPECTRAL ELEMENT METHOD

$(\phi_1, \phi_2, \dots, \phi_n)$ to represent the members of S and V such that

$$u_n = \sum_{p=1}^n \alpha_p \phi_p \quad (3.25)$$

$$w_n = \sum_{p=1}^n \beta_p \phi_p. \quad (3.26)$$

When these are inserted into the variational statement of the problem (3.21) the following form can be arrived at

$$\sum_{p=1}^n \beta_p \left(\sum_{j=1}^n K_{pj} \alpha_j - F_p \right) = 0 \quad (3.27)$$

where,

$$K_{pj} = a(\phi_p, \phi_j) \quad \text{and} \quad (3.28)$$

$$F_p = (\phi_p, c) + (h, \phi_p)_{\Gamma_h} \quad (3.29)$$

As the choice of β_p is arbitrary the result problem becomes the matrix problem $\mathbf{K}\alpha = \mathbf{F}$ where α is the vector of coefficients α_p .

What remains now is to select an appropriate set of basis functions, ϕ_n . Details of the properties required by these functions can be found in most textbooks, such as Hughes (1987) or Becker, Carey and Oden (1981). In the implementation used in this thesis, Gauss-Lobatto-Legendre (GLL) quadrature points are used in conjunction with a set of GLL polynomial interpolants as the basis for the numerical solution. The GLL quadrature points used are the roots of the equation

$$(1 - \xi^2) L'_N(\xi) = 0 \quad \text{with} \quad -1 \leq \xi \leq 1, \quad (3.30)$$

where L_N is the Legendre polynomial of degree N . The GLL interpolants can be written as

$$\phi_i(\xi) = -\frac{(1 - \xi^2) L'_N(\xi)}{N(N + 1)L_N(\xi_i)(\xi - \xi_i)}. \quad (3.31)$$

These interpolants have been found to converge exponentially fast and the polynomials, quadrature points and weights can be numerically generated using recursive algorithms that are stable for $N \lesssim 100$. The number of basis functions used for construction of the test and weighting functions is known as the polynomial order (or degree) of the solution. Substitution of the basis functions and their coefficients into the variational equation results in a matrix system that can be solved to determine the coefficients of the basis functions. Selection of the polynomial order required to accurately model the flow dynamics

3.2. SPECTRAL ELEMENT METHOD

is achieved through convergence tests which are detailed in a later section §3.4.

3.2.2.2 Three-Dimensional Fourier Discretisation

In the cases where a three-dimensional direct numerical simulation was required a Fourier expansion in the spanwise z -direction was employed. The velocity vector, $\mathbf{u}(x, y, z, t)$, is projected onto a Fourier basis in z using

$$\hat{\mathbf{u}}_q(x, y, t) = \frac{1}{L_z} \int_0^{L_z} \mathbf{u}(x, y, z, t) e^{-i(2\pi/L_z)qz} dz, \quad (3.32)$$

where q is an integer and represents the Fourier mode number, $i = \sqrt{-1}$ and L_z is a spatial length scale. A scaled wavenumber is defined as $k_q = (2\pi/L_z)q$. This projection is reconstructed using the Fourier series

$$\mathbf{u}(x, y, z, t) = \sum_{q=-\infty}^{\infty} \hat{\mathbf{u}}_q(x, y, t) e^{ik_q z}. \quad (3.33)$$

Naturally, for an infinite spectrum of wavenumbers, k , this is an exact projection and reconstruction. However, an infinite spectrum of wavenumbers is not feasible in practice, nor desirable as typically only a certain range of wavenumbers contain energy and therefore need to be simulated. The number of wavenumbers considered is consequently restricted to a finite number based upon the required accuracy. Use of a Fourier basis has altered the problem from a three-dimensional one to a set of two-dimensional problems which are coupled through the nonlinear term. Computationally this is convenient for parallel computing as communication between the Fourier modes is only required during evaluation of the nonlinear term. Additionally as the flow is real, the Fourier modes are symmetric, $\hat{\mathbf{u}}_{-q} = \hat{\mathbf{u}}_q$, and only the half the spectrum of modes is required ($q \geq 0$). The selection of the wavenumber range, M , can be determined through the use of either a resolution study or a linear stability analysis to determine the unstable wavelengths.

3.3 Post Processing

A number of variables are calculated from the primitive variables (u, v, w), either after a set number of iterations or at the end of a computation, for the purpose of diagnostics or to obtain derived variables. We present here the means by which force acting on the cylinder (§3.3.1), vorticity (§3.3.2) and spanwise energy (§3.3.3) are calculated from these.

3.3.1 Force Calculation

The total force acting on the cylinder surface is due to the viscous and pressure force components. The spectral element method has the conceptual advantage that the velocity and pressure fields are continuous, so that the corresponding forces can be computed by direct integration of an appropriate quantity over the surface of the cylinder. The pressure and viscous forces per unit spanwise length are given by:

$$\mathbf{f}_p = \oint p \mathbf{n} \, ds \quad (3.34)$$

$$\mathbf{f}_v = - \oint \mu \mathbf{n} \cdot [\nabla \mathbf{u} + (\nabla \mathbf{u})^T] \, ds \quad (3.35)$$

$$\mathbf{f}_T = \mathbf{f}_p + \mathbf{f}_v \quad (3.36)$$

where \mathbf{n} is the unit outward normal of the fluid domain and the integration is performed around the circumference of the cylinder, again using GLL quadrature.

3.3.2 Vorticity Calculation

The vorticity contours and isosurfaces presented in this study were produced through post-processing of the velocity vectors. The following equation was used to add the three components of vorticity to the data set containing the velocity vectors. This was sufficient to permit visualisation of the vorticity fields.

$$\xi = \nabla \times \mathbf{u} \quad (3.37a)$$

$$= \mathbf{i}\omega_x + \mathbf{j}\omega_y + \mathbf{k}\omega_z \quad (3.37b)$$

$$= \mathbf{i}\left(\frac{\partial w}{\partial y} - \frac{\partial v}{\partial z}\right) + \mathbf{j}\left(\frac{\partial u}{\partial z} - \frac{\partial w}{\partial x}\right) + \mathbf{k}\left(\frac{\partial v}{\partial x} - \frac{\partial u}{\partial y}\right) \quad (3.37c)$$

3.3. POST PROCESSING

3.3.3 Energy Calculation

As outlined in Blackburn and Lopez (2002) the normalised amount of kinetic energy in each Fourier mode k is

$$E_k = \frac{1}{2AU_{max}^2} \int_A \hat{\mathbf{u}}_k \cdot \hat{\mathbf{u}}_k^* dA \quad (3.38)$$

where A is the area of the two-dimensional cross-section. This measure can be used to determine the number of spanwise wavenumbers needed to model the computational domain to the required accuracy.

3.4 Validation

The technique outlined in this chapter has been previously implemented and validated, e.g. in a two-dimensional subspace in Blackburn and Henderson (1999) and with Fourier expansions along the z -axis in Blackburn and Karniadakis (1993). Temporal accuracy was achieved using second-order time integration and sufficiently small timesteps so that the results are independent of step size. Consequently the following validation tests are not focused upon testing this implementation but in choosing the geometries and parameters required to accurately model the scenarios outlined in §1.1. In the following sections the choice of domain extent, the elemental geometry, the GLL interpolant order and the timestep are examined.

3.4.1 Mesh Selection

The following selection of the domain extent, the number of elements and interpolant order are based on accurately modelling a cylinder undergoing simple-harmonic rectilinear oscillations in a two-dimensional subspace. It is for this problem that the majority of research presented in this thesis has been performed. Meshes required for other problem scenarios, such as the swimming cylinder, will be presented and validated as required. The following meshes use two-dimensional distorted quadrilateral elements as their fundamental building block. In the following sections we investigate firstly the impact of the domain extent and secondly the impact of the GLL interpolant order.

3.4.1.1 Temporal Resolution

In all the simulations presented in this study second-order time integration was employed and the time step, Δt , was selected to satisfy the required accuracy. The selection of a suitable timestep is dependent upon the mesh and the polynomial order used for this mesh. Presented here is a resolution study for the mesh/polynomial combination that was used predominantly throughout this thesis. The details of the selection of the mesh and polynomial order used in this study are considered in the subsequent sections.

In Table 3.2 the variation of the coefficient of force along the axis of oscillation is presented as a function of the number of timesteps per period of oscillation. In the three separate locations in (KC, β) -space shown the peak coefficient of force was found to vary little across the range of timesteps considered. The timestep was chosen to be 3000 timesteps per period which achieves an accuracy of four decimal places.

3.4. VALIDATION

Steps per Period	(KC, β)		
	(2.5, 100)	(8, 10.0)	(8, 11.0)
1000	9.69562	5.66330	5.10862
1500	9.69567	5.66183	5.11440
2000	9.69570	5.66298	5.11479
2500	9.69572	5.66270	5.11467
3000	9.69572	5.66290	5.11481
3500	9.69574	5.66288	5.11504
4000	9.69574	5.66288	5.11504
4500	9.69577	5.66293	5.11494
5000	9.69577	5.66288	5.11504
5500	9.69577	5.66295	5.11508
6000	9.69580	5.66288	5.11506
6500	9.69580	5.66295	5.11502

Table 3.2: Variation of the peak coefficient of force \hat{C}_{f_y} per unit length along the y -axis as a function of the number of timesteps per period of oscillation, T . Simulations were conducted on the $40D \times 40D$ mesh with a interpolant order of $N_p = 8$.

3.4.1.2 Domain Size Resolution

The extent of the domain surrounding the oscillating cylinder could potentially impact upon the results. In the previous experiments of Honji (1981) and Tatsuno and Bearman (1990) different sized domains were employed, however their results agreed within a reasonable margin of experimental error. As a result it is difficult to draw any conclusion from their domains about the optimum domain size and any potential impact this may have. In the initial numerical study of this problem by Elston (1997) a $20D \times 20D$ mesh was used, see figure 3.1(a), for two-dimensional modelling of regime B. The vorticity contours generated appeared to be in excellent agreement with the flows visualised in Tatsuno and Bearman (1990).

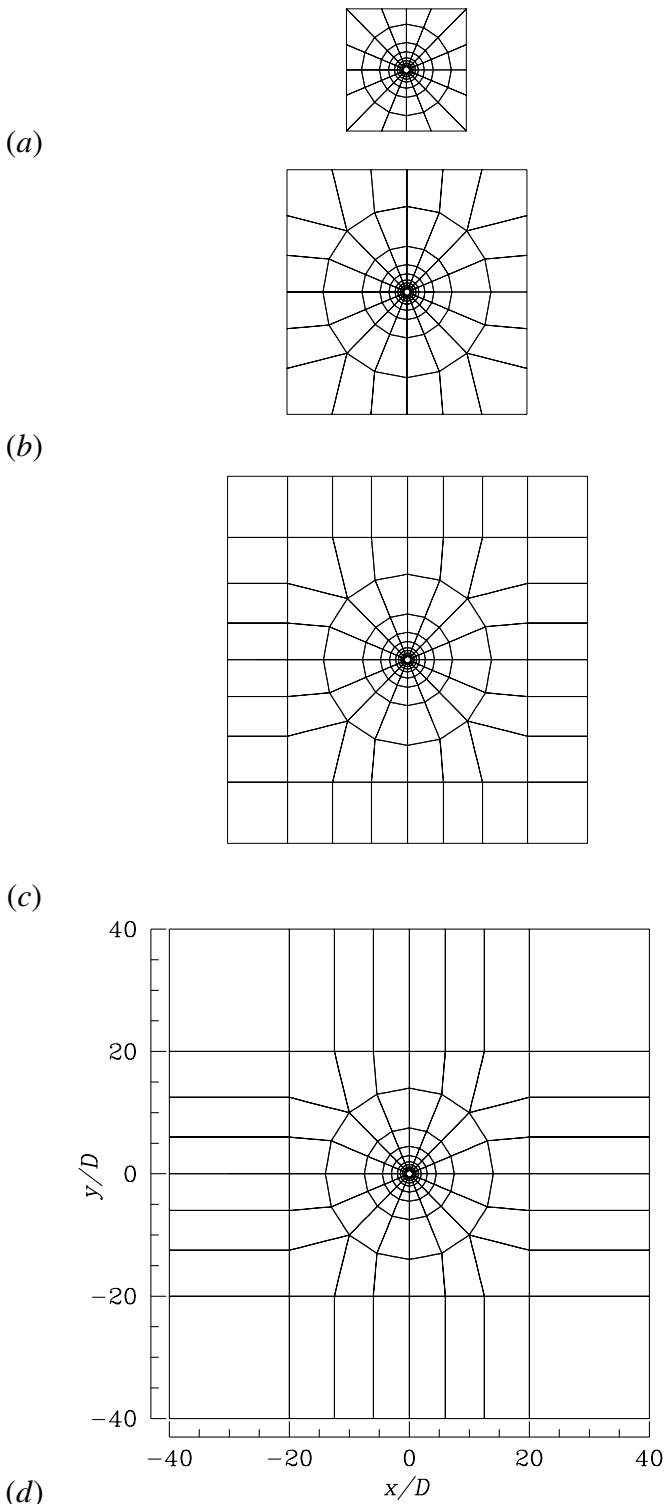


Figure 3.1: Outlines of (a), 144-element $20D \times 20D$ domain; (b), 164-element $40D \times 40D$ domain; (c), 192-element $30D \times 30D$ domain; (d), 192-element $80D \times 80D$ domain. All meshes are shown scaled to a common cylinder diameter and relative to each other. The horizontal and vertical axis's, where not shown, are x/D and y/D respectively, with the reference point co-located with the center of the cylinder.

3.4. VALIDATION

To determine the impact of the domain size upon the flow dynamics a number of meshes of differing size were examined. The diagnostic used to determine the influence of the domain extent was the peak coefficient of force \hat{C}_f exerted along the y -axis on the cylinder.

$$\hat{C}_{fy} = \frac{2\hat{f}_{ty}}{\rho U_{rms}^2 D} \quad (3.39)$$

where \hat{f}_{ty} is the peak total force acting on the cylinder in the y -direction (inline with the oscillation), and U_{rms} is the root mean square velocity. The results of an investigation of four different meshes, figures 3.1(a)–(d), which increased in domain extent from $20D \times 20D$ to $80D \times 80D$ are shown in Table 3.3. This series of meshes shares a common core section for $-8 < (x^2 + y^2)^{\frac{1}{2}} < 8$. The meshes shown have additional elements added around this core section to increase the domain extent to the desired size. A preliminary study in Elston (1997) has indicated that, at the chosen point in (KC, β) -space, ($KC = 2.5$, $\beta = 100$), an interpolant order of $N_p = 8$ was sufficient to resolve the flow dynamics.

The results in Table 3.3 indicate that the range of domain extents considered had very little impact upon the peak force coefficient with only a 0.40% variation occurring across the entire series. The $40D \times 40D$ domain was subsequently chosen for the simulations of a cylinder in simple-harmonic rectilinear motion as it is of the same order of domain as the physical domain used by Tatsuno and Bearman (1990) and the peak coefficient of force has converged to four-figure accuracy. Subsequent increases in the domain extent resulted in less than a 0.1% decrease in the peak force coefficient.

Domain size	$20D \times 20D$	$40D \times 40D$	$60D \times 60D$	$80D \times 80D$
N_{el}	144	164	192	192
\hat{C}_f	9.717	9.687	9.682	9.678

Table 3.3: Peak coefficients of y -component force per unit length for different domain sizes and number of elements, N_{el} , with the order of the tensor-product interpolant function employed within each element held constant at $N_p = 8$. Each simulation was performed at ($\beta = 100$, $KC = 2.5$) and allowed to reach a periodic state.

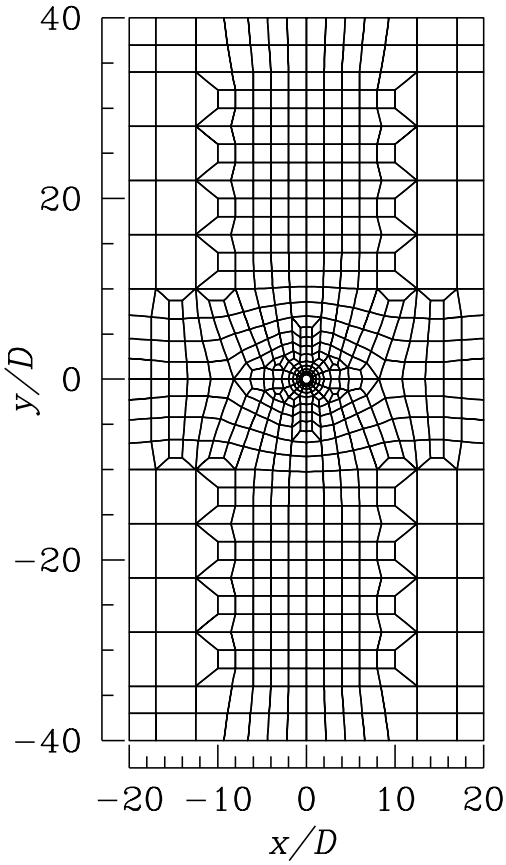


Figure 3.2: Outline of the 700-element $40D \times 80D$ domain used for a small proportion of the results presented here.

3.4.1.3 Spatial Order Resolution

The order of the tensor-product interpolant used was determined through an investigation at a number of locations in (KC, β) -space using the chosen $40D \times 40D$ mesh. Additionally a 700 element, $40D \times 80D$ mesh which was required for Floquet analysis was also investigated. For tests in (KC, β) -space where the resulting flow would have broken K_x symmetry, a half mesh was created which was simply the full mesh sliced in half at $x = 0$. At the mesh boundary $x = 0$, symmetry boundary conditions were employed so that all the simulations were consistent and K_x symmetry was enforced. The symmetry boundary conditions are:

$$\begin{aligned} u &= 0 \\ \frac{\partial v}{\partial n} &= 0 \end{aligned} \tag{3.40}$$

with a high-order boundary condition imposed on the pressure field.

The results of a convergence study into the interpolant orders using the $40D \times 40D$ and $40D \times 80D$ mesh are shown in Table 3.4. An interpolant order of 8 was chosen for

3.4. VALIDATION

$(\beta, KC) \setminus N_p$	6	8	10	12
(a) (12.5, 8)	5.433	5.434	5.434	5.434
	6.080	6.080	6.080	6.080
	9.687	9.687	9.687	9.686
(b) (12.5, 8)	5.420	5.420	5.420	5.420
	9.682	9.682	9.681	9.681

Table 3.4: N_p -convergence results for peak coefficients of y -component force per unit length, \hat{C}_f , obtained using (a) the 164-element $40D \times 40D$ mesh, and (b) the 700-element $40D \times 80D$ mesh. Simulations at ($\beta = 12.5$, $KC = 8$) conducted with enforced K_x symmetry.

use with the $40D \times 40D$ mesh and an order of 10 for the $40D \times 80D$ mesh. The choice of these interpolant orders was sufficient to enable four-figure accuracy with each of the meshes.

3.5 Chapter Summary

In this chapter the technique used to directly model fluid flows of the types outlined in §1.1 has been outlined. The spectral element method was briefly introduced and the means by which spatial and temporal discretisation has been accomplished with this method was covered. Critical to the accuracy of this method is the selection of the tensor-product interpolant order and spatial extent of the meshes. The convergence studies presented show the impact of the spatial extent and interpolant order for the case of a cylinder in simple-harmonic rectilinear motion. The choice of interpolant order and domain for the ‘swimming’ cylinder problem is considered later in chapter 8.

Chapter 4

Numerical Methods: Floquet Stability Analysis

The implementation of the Floquet analysis technique is outlined in this chapter. This technique examines the linear stability characteristics of a periodic system to infinitesimal perturbations. It has been used in a number of recent research publications, such as that of Barkley and Henderson (1996) where it was used to identify the three-dimensional modes ‘A’ and ‘B’ of the oscillating wake behind a circular cylinder and further, to accurately determine the onset of these modes as a function of Re . In contrast to that application where the periodicity of the base flows is the result of a Hopf bifurcation and the flows are autonomous, the flows studied here involve periodicity due to an external forced oscillation of the cylinder.

Additionally, while previous investigations have focused on using this technique to determine the susceptibility of two-dimensional periodic flows to three-dimensional disturbances, in this investigation it is also applied to determining the susceptibility of two-dimensional periodic flows to two-dimensional perturbations. Outlined in the following sections are the process of linearisation of the Navier–Stokes equations (§4.1), the technique of linear stability analysis of steady state flows (§4.2) and finally the Floquet analysis technique (§4.3).

An implementation of the Floquet stability analysis technique was obtained from D. Barkley, which the author is led to believe was employed in the research resulting in the recent publication of Barkley and Henderson (1996). This implementation required mating with the DNS technique outlined in the previous chapter. Additionally, alterations to the DNS implementation were required to solve the linearised Navier–Stokes equations. Consequently, the last section of this chapter (§4.4) outlines the tests the code was subjected to during its development and validation.

4.1 Linearised Navier–Stokes Formulation

The incompressible Navier–Stokes equations, (3.1), are linearised by assuming that the flow, $\mathbf{u}(x, y, z, t)$, at the onset of an infinitesimal perturbation, is the linear sum of a three-dimensional perturbation, $\mathbf{u}'(x, y, z, t)$ and a two-dimensional base flow, $\mathbf{U}(x, y, t)$, such that:

$$\mathbf{u} = \mathbf{U} + \mathbf{u}' \quad (4.1)$$

$$p = P + p'. \quad (4.2)$$

In this implementation the perturbation is, at times, restricted to a two-dimensional subspace in the x - y plane. However, in this description of the technique the full three-dimensional implementation is discussed. Insertion of these terms into the Navier–Stokes equations (3.1) results in the linearised Navier–Stokes equations for the evolution of the perturbation once terms that satisfy the Navier–Stokes equations for the base flow are removed, and assuming that the perturbation is infinitesimally small $|\mathbf{u}'|, |p'| \ll 1$:

$$\frac{\partial \mathbf{u}'}{\partial t} = -\frac{1}{\rho} \nabla p' - (\mathbf{u}' \cdot \nabla) \mathbf{U} + (\mathbf{U} \cdot \nabla) \mathbf{u}' + \nu \nabla^2 \mathbf{u}' \quad (4.3a)$$

$$\nabla \cdot \mathbf{u}' = 0. \quad (4.3b)$$

The linearised advection terms are written in convective form here instead of the skew-symmetric formulation used for this term in the fully nonlinear implementation (3.2). Wilhelm and Kleiser (2001) have shown that use of the linearised skew-symmetric formulation results in numerical instability and during the development of this Floquet solver, before becoming aware of this, the author also observed this to be the case. The boundary conditions on the perturbed velocity are: $\mathbf{u}' = 0$ on both the outer walls and on the cylinder surface. These equations can be rewritten more compactly in the ‘schematic’ form:

$$\partial_t \mathbf{u}' = (N_U + L) \mathbf{u}' \quad (4.4)$$

where the operator N_U is the T -periodic linear operator $(\mathbf{u}' \cdot \nabla) \mathbf{U} + (\mathbf{U} \cdot \nabla) \mathbf{u}'$. The linear operator L corresponds to the viscous diffusion term. The pressure is set to the solution of a Poisson equation that has the divergence of the advection terms as forcing. These terms were calculated using the spatial discretisation and time-stepping discussed in the previous chapter §3. The entire operator $(N_U + L)$ is T -periodic because the linearised advection term is.

4.2 Stability Analysis of Steady-State Flows

A number of techniques are available to examine the linear stability of U when it is a steady state flow. The method implemented here is a version of the exponential power method, as described in Tuckerman and Barkley (2000), that permits multiple solutions to be obtained and is outlined in the following section. When the base flow is steady, $\mathbf{U}(t) = \mathbf{U}$, and infinitesimal perturbations to this state evolve according to the linearised stability equations (4.4) then the stability of \mathbf{U} is governed by the eigenvalues, λ , of the operator $N_U + L$.

$$(N_U + L)\mathbf{u}' = \lambda\mathbf{u}' \quad (4.5)$$

A positive real component of any eigenvalue indicates an unstable mode and the corresponding eigenvector provides the form of the unstable perturbation to the base flow. The size of the matrices involved can rapidly become so large that a direct solution of the problem rapidly becomes unfeasible for all but the smallest and simplest problems. However, this can be overcome as only the leading eigenvalues of the spectrum are required, and their matching eigenvectors. This can be found using an iterative method, such as a variation of the power method. The basic power method produces a sequence of vectors by acting repeatedly upon an arbitrary initial vector, u_0 , with the operator $N_U + L$:

$$u_n = (N_U + L)^n u_0. \quad (4.6)$$

The sequence of vectors, u_n , eventually approaches the dominant eigenvector. As discussed in Tuckerman and Barkley (2000), two modifications are required to this technique to make it applicable to the linearised Navier–Stokes problem: firstly, to determine more than one eigenpair; and secondly to determine the leading eigenvalues (largest real part), as distinct from the dominant eigenvalues (largest magnitude).

To determine multiple eigenpairs to the eigensystems a variant of the Arnoldi method (Saad; 1992) is employed. In the technique implemented a Krylov subspace is formed from the sequence $u_0, (N_U + L)u_0, \dots, (N_U + L)^{K-1}u_0$, where K is both the order of the Krylov-space and the number of eigenpairs sought. The eigenpairs in this subspace are the dominant eigenpairs of the system.

The second change to the underlying power method is to convert the method to determine the leading eigenvalues, i.e. those with largest real part, instead of the dominant eigenvalues. In the exponential variation to the power method the solution to (4.4) is

$$u(t + \Delta t) = e^{\Delta t(N_U + L)}u(t). \quad (4.7)$$

The leading eigenvalues of the operator $N_U + L$ are the dominant ones of $e^{\Delta t(N_U + L)}$ for any positive Δt . By using the exponential version the leading eigenvalues will be obtained.

4.2. STABILITY ANALYSIS OF STEADY-STATE FLOWS

The final technique is a hybrid of the Arnoldi technique which obtains multiple eigenpairs of the system and the exponential power method which finds the leading eigenpairs of the system. The Krylov-space dimension used with this system is selected to accommodate all the leading eigenpairs of interest.

4.3 Floquet Analysis

Floquet analysis is employed when the underlying base flow, whose stability to infinitesimal perturbations is sought, is T -periodic instead of steady (time invariant) as outlined in the previous section. This requires modification to the exponential power method used for the steady-state analysis as the linear operator of (4.4) is no longer constant. The stability of this system is now determined by eigenvalues of the operator

$$B \equiv \exp \left(\int_{t_0}^{t_0+T} (N_U(t') + L) dt' \right). \quad (4.8)$$

The operator B evolves the perturbation, \mathbf{u}' , subject to the linearised Navier–Stokes equations, over a single period of time, T . As a consequence of the T -periodic nature of the base flow, it is essential to monitor the growth or decay of any perturbation to this system over an entire period of the base flow in order to determine its stability characteristics. The starting point, t_0 , becomes irrelevant as a result of monitoring the growth of the perturbation over an entire period of the base flow. The eigenvalues μ of B are known as Floquet multipliers. The trial solutions to (4.4) are now of the form:

$$u(t) = \tilde{u}(t \bmod T) e^{\sigma t} \quad (4.9)$$

where $\sigma = \log(\mu/T)$ is called a Floquet exponent and $\tilde{u}(t \bmod T) e^{\sigma t}$ is called a Floquet mode. The Floquet eigenfunctions, $\tilde{u}(t)$, are T -periodic however, they are only determined at an arbitrary starting phase, t_0 . Determining the stability now requires integrating the linearised stability equations over one full period and using the resultant vector as the vectors for the Krylov subspace. A requirement of this is that the base flow is now known for each Δt over one period. This is accomplished by storing a number of velocity fields equally spaced over one period of the base flow and reconstructing the base flow from this using a Fourier series. This is an ideal way to represent the base flow because it is known that it is periodic. The selection of the number of base flow fields required to accurately model the base flow is determined by calculating the spread of kinetic energy in each Fourier mode for increasing numbers of slices per period. In the simulations presented later it was found that 32 fields were sufficient, however 64 fields were used to provide accuracy.

4.3. FLOQUET ANALYSIS

The algorithm implemented by D. Barkley is outlined below, where LNS(u , T) specifies the evolution of the velocity field, u , over one period, T :

1. Set first vector of Krylov matrix of dimension kdim to initial condition.

2. Fill Krylov matrix:

```
for i = 2 to kdim  
    K[i] = LNS( K[i-1], T )
```

3. Iterate over Krylov matrix until converged or maximum iterations are reached.

(a) Roll matrix and add new vector:

```
for i = 1 to kdim  
    K[i-1] = K[i]  
    K[kdim] = LNS( K[kdim-1], T )
```

(b) Calculate eigenvalues of K :

- i. Perform Q R decomposition using MGS algorithm.
 - ii. Compute Hessenberg matrix, $H = Q * \text{LNS}() Q$
where $Q^* \text{LNS}() = R$
 - iii. Calculate eigenpairs of H , which are the Floquet multipliers
achieved using a standard linear package, i.e. LAPACK
 - iv. Determine residuals from eigenvectors of H as a measure of convergence.
-

4.4 Validation Tests

Two tests were used to validate the implementation of the iterative solver and Floquet method. These were chosen and performed in a specific order such that each successive test added an extra feature or layer of complexity to the previous test. The tests chosen all had previously published results with either quantitative or graphical data to compare the results with. The first test was a stability analysis of a steady state flow. In this the two-dimensional stability of a two-dimensional steady flow between two parallel walls (planar Poiseuille flow) was examined as a test of the iterative eigenvalue solver. In the second test the Floquet analysis technique was employed. In the second test the extra complexity of testing for three-dimensional instabilities of a two-dimensional periodic base flow was added. This was done by examining the stability characteristics of the two-dimensional periodic wake of a circular cylinder at $Re = 220$.

4.4. VALIDATION TESTS

4.4.1 Poiseuille Flow - A Steady State Problem

A well documented problem of interest is that of two-dimensional incompressible flow in a straight channel, otherwise known as plane Poiseuille flow. A number of studies, such as those of Orszag (1971) and Canuto, Hussaini, Quarteroni and Zang (1988), have focused on the linear stability of the time-invariant solution to this flow. In both of these works, quantitative results for the growth of the perturbations are presented as functions of the Reynolds number and the streamwise wavenumber, which makes these ideal cases for testing the iterative eigenvalue solver. The critical Reynolds number for growth of a perturbation has been found to be 5772.22 with a streamwise wavenumber of 1.02056 (Orszag; 1971).

The two-dimensional time-invariant velocity and pressure fields that forms between two walls placed at $y = -1$ and $y = +1$ are described in (4.10). The walls are impermeable and have non-slip boundary conditions. The Reynolds number is based upon half the channel height, h , and the centre-stream velocity such that $Re = 1/\nu$, where ν is the kinematic viscosity.

$$\begin{aligned} u(x, y, t) &= 1 - y^2 \\ v(x, y, t) &= 0 \\ p(x, y, t) &= -2\nu x \end{aligned} \tag{4.10}$$

A two-dimensional solution of the following form is assumed for the velocity field of the base and perturbation flows:

$$u(x, y, t) = U(x, y) + u'(x, y, t) \tag{4.11}$$

$$u(x, y, t) = (1 - y^2) + \varepsilon Re\{\phi(y)e^{i\alpha x - i\omega t}\} \tag{4.12}$$

where ε is the amplitude of the perturbation. A solution has been presented in Canuto et al. (1988), where results for one particular case are cited with the parameters $Re = 7500$ and a streamwise wavenumber of $\alpha = 1$. Using a domain of length $L_x = 2\pi/\alpha$ they calculated that the eigenfrequency of the growing mode was $\omega = \omega_r + i\omega_i$, where $\omega_r = 0.24989154$ and $\omega_i = 0.00223497$. Orszag (1971) reported values for a case at a slightly higher Reynolds number of 10000 with a streamwise wavenumber of 1.0 where an eigenfrequency of $\omega = 0.23752649 + 0.00373967i$ was found. Both of these cases were employed as tests of the solver.

The simulations were carried out using the mesh shown in figure 4.1 with interpolant orders of 8, 10, 12 and 14. The domain has length $L_x = 2\pi$ and has periodic boundary conditions applied at $x = -\pi$ and $x = +\pi$. The equilibrium solution (4.10) was imposed upon this mesh and used as the base flow, \mathbf{U} . A Krylov matrix with a dimension of 3 was

4.4. VALIDATION TESTS

GLL order (N_p)	$Re = 7500$		$Re = 10000$	
	Canuto et al. (1988)	Orszag (1971)	Canuto et al. (1988)	Orszag (1971)
Calculated	ω_r	ω_i	ω_r	ω_i
8	0.2498901	0.00223634	0.2375274	0.00374272
10	0.2498917	0.00223577	0.2375265	0.00373971
12	0.2498916	0.00223511	0.2375265	0.00373975
14	0.2498916	0.00223510	0.2375265	0.00373978

Table 4.1: Comparison of the eigenvalues produced by the linear solver with two sets of previously calculated values published in Canuto et al. (1988) and Orszag (1971). In both cases increasing the interpolant order improved the accuracy of the solution. With an interpolant order of $N_p = 10$ the eigenvalues were accurate to four significant figures.

used. The initial perturbation vector used was seeded with random numbers to excite all possible modal frequencies.

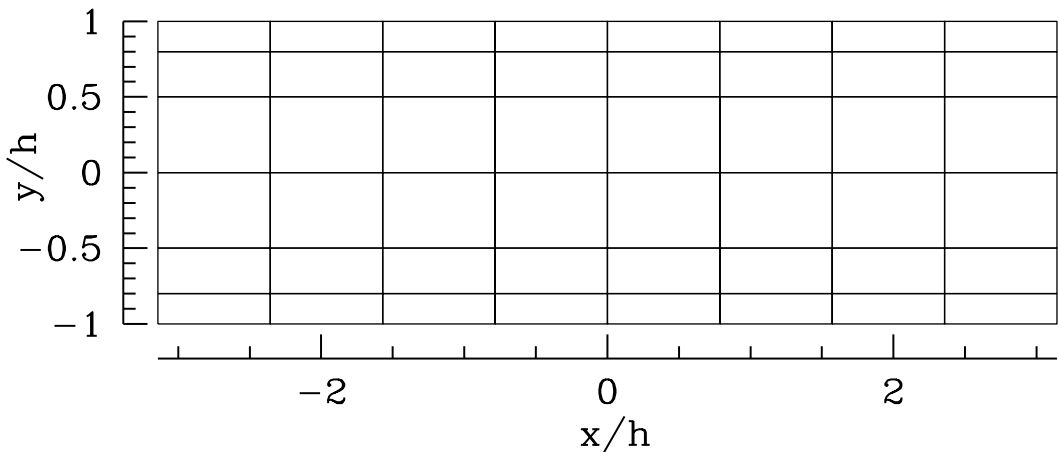


Figure 4.1: 24 element mesh used for simulations of Poiseuille flow. The upper and lower boundaries at $y = -1$ and $y = +1$ have non-slip boundary conditions applied on them while the boundaries at $x = -\pi$ and $x = +\pi$ are periodic with each other.

The results of the simulations for both of these cases are presented in Table 4.1. In both scenarios the iterative solver produced results that were accurate to three significant figures for a GLL interpolant order of 8. Increasing the interpolant order increased the accuracy slightly. The implementation of the linear eigensystem solver achieved the correct result with the required accuracy in this case.

4.4. VALIDATION TESTS

4.4.2 Circular Cylinder Wake - A Floquet Problem

This test case introduced the aspect of examining the linear stability of a two-dimensional periodic flow, as compared to the previous case which had a steady base flow. This test focuses on examining the three-dimensional stability of the two-dimensional periodic flow past a circular cylinder, which is known to bifurcate to a mode 'A' instability, as has been previously discussed extensively in §2.1. Barkley and Henderson (1996) have established a neutral stability curve, see figure 2.7, for the onset of three-dimensional structures in the periodic wake past a circular cylinder. In particular, Floquet multiplier magnitudes were presented as a function of the Reynolds number and the wavenumber, k . The focus here was to replicate one specific example of this, that of the series at $Re = 220$ with wavenumbers less than $k = 2.5$.

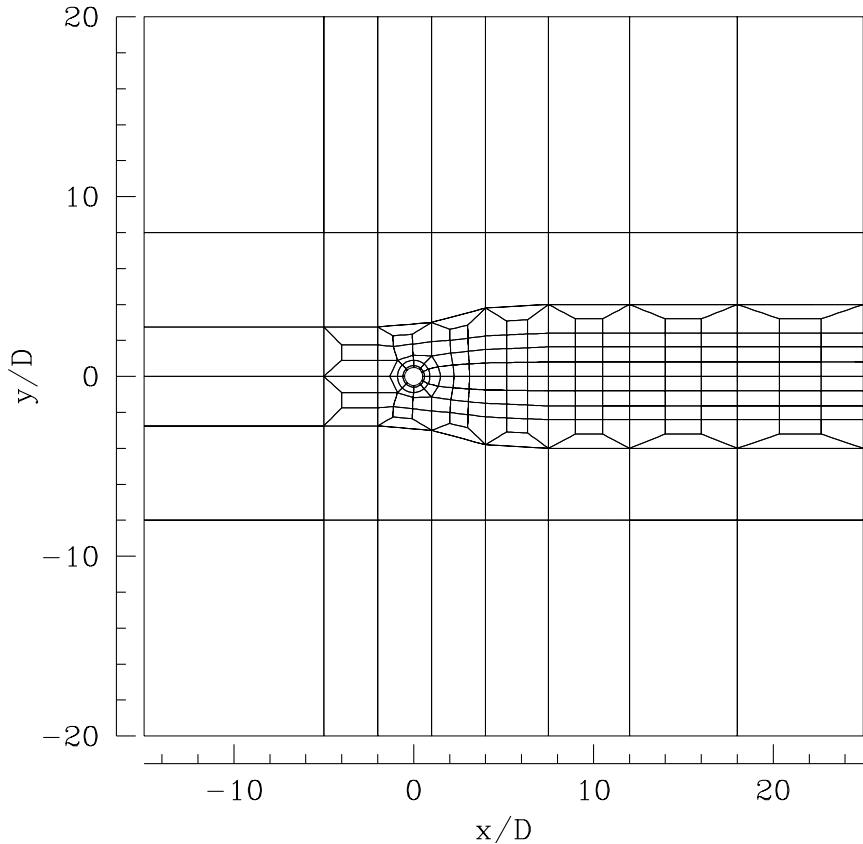


Figure 4.2: Spectral element mesh used for simulation of the periodic wake past a circular cylinder. The mesh contains 218 elements and is scaled by the reference length of the cylinder diameter, $D = 1$.

The spectral element mesh shown in figure 4.2 was used to simulate the periodic wake of the cylinder. On the inflow (left), upper and lower boundaries the velocity was prescribed as $u = 1$, $v = 0$, while on the outflow (right) boundary a standard Neumann boundary condition was implemented. No-slip boundary conditions were applied on the

4.4. VALIDATION TESTS

cylinder surface. A periodic base flow was generated by simulating the flow with DNS until a periodic state was reached. The periodic fields were stored by taking 32 equi-spaced in time snapshots of the fields over one period. This permitted the calculation of the base flow velocity fields at any time within the period using a Fourier reconstruction.

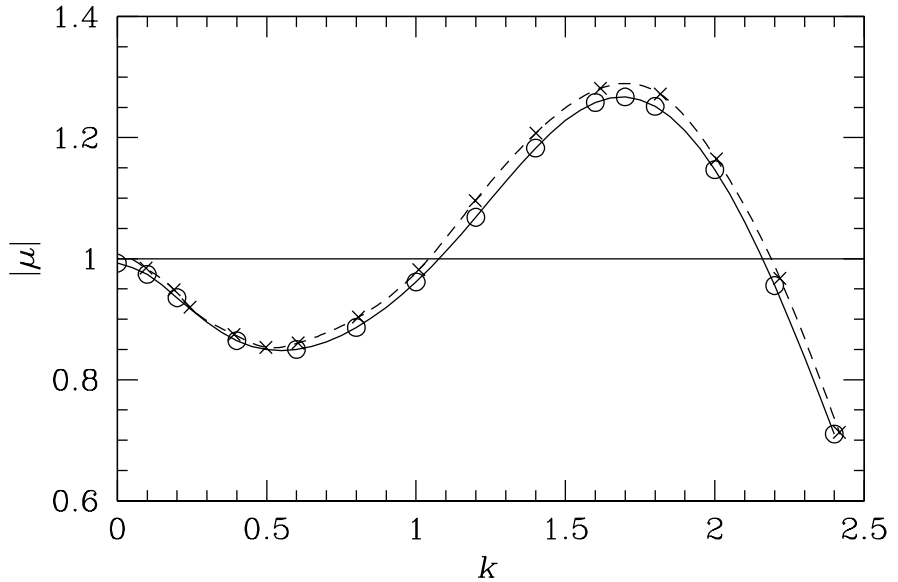


Figure 4.3: Floquet multiplier results for the three-dimensional stability of the periodic wake of a circular cylinder at $Re = 220$ as a function of spanwise wavenumber k . Shown are the results, \circ , and those of Barkley and Henderson (1996), \times . Values of the Floquet multiplier $|\mu| > 1$ indicate a point that is unstable.

The results of the Floquet analysis are reproduced alongside those of Barkley and Henderson (1996) in figure 4.3. The results are in reasonable agreement and the discrepancy could be due to a number of factors. These factors include, but are not limited too, the aspects of the domain sizes being different, the data of Barkley and Henderson (1996) being extracted from a reproduction and only a minimal study into the dependence of the GLL interpolant orders being conducted.

4.5 Chapter Summary

The Floquet analysis technique used to determine the stability of periodic systems to infinitesimal perturbations was outlined in this chapter. Its implementation was discussed and then validated through testing against a known steady flow problem and a Floquet problem. In both cases it was found to produce results that were quantitatively comparable to previously published results to within the desired accuracy.

Chapter 5

Rectilinear Oscillation: Symmetric Synchronised Flow

5.1 Introduction

It is well known that the flow produced by a cylinder in rectilinear oscillation at extremely low amplitudes and frequencies of oscillation is both symmetric about the oscillation axis and synchronised with the cylinder oscillation. A number of researchers (Honji; 1981; Williamson; 1985; Tatsuno and Bearman; 1990) have shown that small increases in either of these oscillation parameters can result in the formation of flow states with a different set of spatial and temporal symmetries. The bifurcations between these new states and the initially symmetric flow can break one or more of the symmetry properties that the initially symmetric flow possessed. The focus of this investigation will be on identifying the nature of the bifurcations occurring, the point of onset of the primary and secondary bifurcations that occur and, if the transition is three-dimensional (along the span), determining the critical three-dimensional wavenumbers of the bifurcation. Where not explicitly stated the use of the terminology ‘two-dimensional’ refers to the plane perpendicular to the span of the cylinder and implies that there is no spanwise variation of the flow.

In order to determine a transition from one state to another, the properties of the initial state need to be known accurately. In this chapter the spatial and temporal properties of the flow occurring for very low Keulegan–Carpenter and Stokes numbers are examined and classified according to the symmetry properties present. In subsequent chapters we investigate the transitions that occur when either or both of the control parameters are increased while the domain is either restricted to a two-dimensional subspace perpendicular to the cylinder span (chapter 6) or in a fully three-dimensional space where spanwise variations are taken into account (chapter 7).

In this chapter the properties of the stable flow will be established through an examination of the flows produced at a set of four points in (KC, β) -space that have been

5.1. INTRODUCTION

shown visually to lie in stable regions on a $KC-\beta$ plot. The regimes these points lie in, regimes A*, A and B, were identified visually by Tatsuno and Bearman (1990) as having synchronous and symmetric flow about the cylinders oscillation axis. It should be noted that flows of regime B have been shown to be three-dimensional, however as one component of the investigation is examining flows restricted to a two-dimensional subspace it is appropriate to identify its symmetry properties so that transitions from this initial state could be determined. From the examination of the flows produced in these four instances a set of properties will be established (§5.4) which are then used in later chapters to characterise the instability modes.

5.2 Two-Dimensional Base States

The objective of this section is to establish the properties of the symmetric and synchronous flows that will be known in later chapters as ‘base flows’. Through the experimental visualisations of Honji (1981) and Tatsuno and Bearman (1990) a number of properties of these stable flows have been identified. However, these have been experimental visualisations only and as the subsequent chapters are centered around a numerical stability analysis of these flows it is important to numerically duplicate these flows and to accurately define the properties that are lost or altered through a bifurcation arising from a change in the oscillations control parameters.

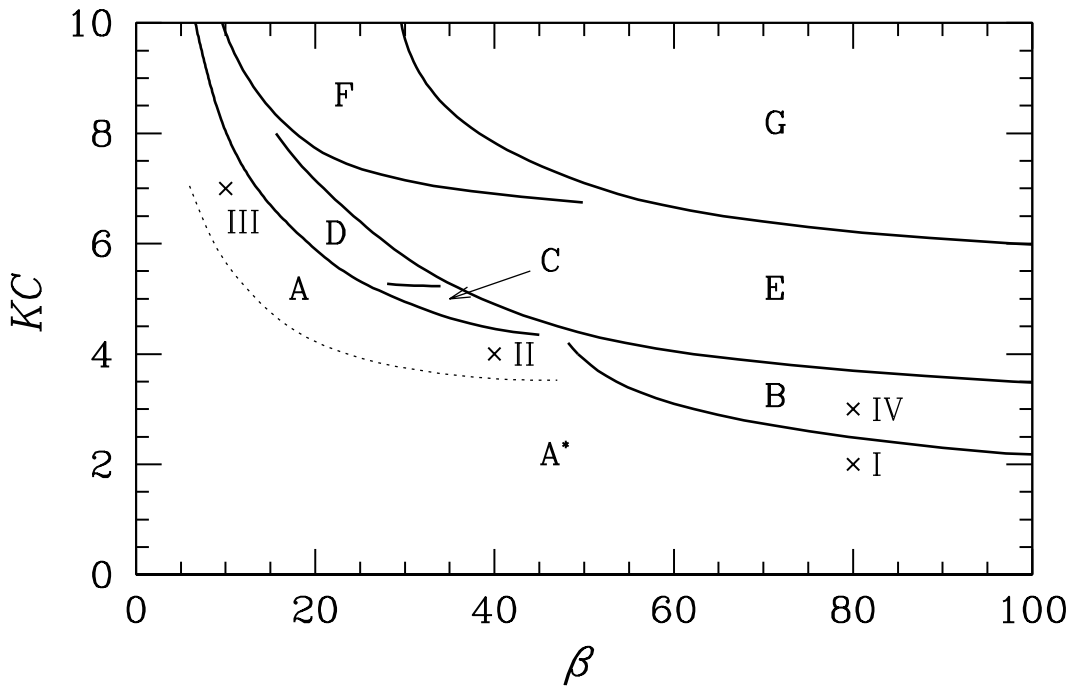


Figure 5.1: Map of vortex shedding regimes (A*-G), from Tatsuno and Bearman (1990), and the locations examined for their symmetry properties. Four points are shown where the symmetrical properties of the initial flow states are examined here. These points are located in (KC, β) -space at I: (2.0, 80.0), II: (4.0, 40.0), III: (7.0, 10.0) and IV: (3.0, 80.0). It should be noted that although three of the points, I–III, are located in regimes experimentally reported to be two-dimensional (no spanwise variation), the fourth point, IV, is located in a regime reported to be three-dimensional. This point was examined because in simulations restricted to a two-dimensional subspace this point is likely to preserve the symmetry characteristics observed in regimes A* and A.

In their experimental visualisations, Tatsuno and Bearman identified two regimes, A^* and A, in which symmetrical flow structures were observed to form about the cylinders oscillation axis. Images of these structures can be seen in figures 2.17(A^*) and 2.17(A). The formation of these structures was observed to be synchronised with the motion of

5.2. TWO-DIMENSIONAL BASE STATES

the cylinder. In both of these regimes, the formation of structures that varied along the cylinder span were not observed. Additionally, the formation of an induced flow that approached the cylinder from a direction perpendicular to the oscillation axis and departed the cylinder vicinity along the oscillation axis was noted to occur. The distinction between regimes A* and A lies in the assertion that in regime A* there was no vortex shedding while in regime A vortex shedding does occur. It is assumed, due to the visual nature of the study, that the determination of the presence of vortex shedding arises from the patterns formed by the particles and dye being shed from the surface of the cylinder, although it is noted that far from the cylinder the concentrations of dye do not represent vortices but instead mark periodic mass convection from the boundary layer of the cylinder. Due to the difficulty in determining the onset of vortex shedding the boundary between these regimes was not explicitly delineated, as was done for the boundaries between the other regimes identified.

In regime B the onset of a regular spanwise variation in the structures visualised was experimentally observed. It is clear from these visualisations that a bifurcation from the two-dimensional flows of regimes A* and A has occurred resulting in the formation of three-dimensional structures. However, when restricted to a two-dimensional subspace, flows in this regime retain the symmetry characteristics of regimes A* and A. The implication of this is that the onset of a two-dimensional transition occurs after regime B and therefore when determining the onset of two-dimensional subspace transitions it is important to know the symmetry characteristics of regime B when it is restricted to the two-dimensional subspace.

In the following sections four points located in regimes A*, A and B are selected and analysed with respect to their symmetry properties. The location of these four points is (as shown in figure 5.1):

I. $KC=2, \beta = 80.0$

II. $KC=4, \beta = 40.0$

III. $KC=7, \beta = 10.0$

IV. $KC=3, \beta = 80.0$

These points were selected on the basis of being representative of the regimes they lie in and also being near the boundary where a detailed transition study will occur in chapters 6 and 7.

5.2. TWO-DIMENSIONAL BASE STATES

5.2.1 Point I: $KC=2$, $\beta = 80.0$

The first point to be examined is at $KC=2$, $\beta = 80.0$, which using the regime map of Tatsuno and Bearman (1990), see figure 5.1, lies in regime A*. At this location a two-dimensional DNS was evolved until the flow has settled into a limit cycle. A number of measures were available to determine if the flow had reached an asymptotic state. These included examining the time traces of the velocity components at a number of points in the domain, or alternatively by calculating the forces experienced by the cylinder and it could be qualitatively derived by inspection of the vorticity contours over a period of oscillation. In the first instance the velocity variables (u, v) at four discrete locations in the domain were plotted against each other over a discrete period of time. In figure 5.2 these are plotted for one period of oscillation. In this case the four traces result in closed loops where the loop was terminated at the end of one period of motion. This indicates

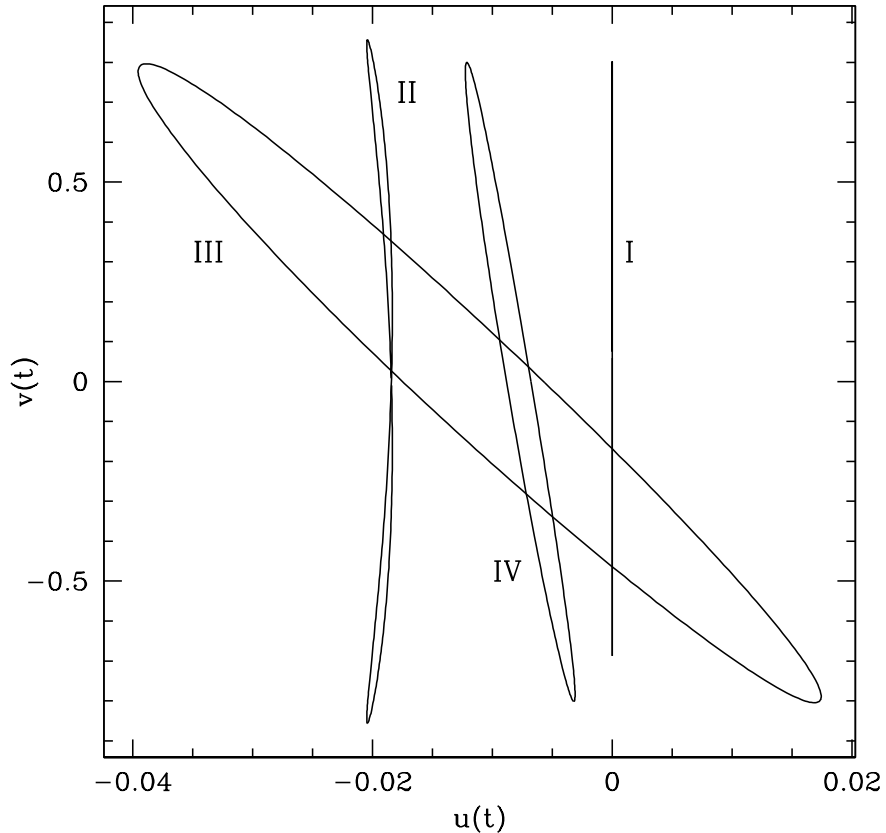


Figure 5.2: Plot of the u vs. v velocity components (relative to a fixed cylinder) over one period of motion at four discrete locations in the domain. The two-dimensional DNS simulation was carried out at $KC=2$, $\beta=80.0$. The plot at each location of an entire period forms a complete circuit indicating that the flow at this spatial location is periodic and synchronised with the forcing period. The four locations are (relative to the centre of the cylinder): I $x = 0.0D, y = 2.0D$, II $x = 2.0D, y = 0.0D$, III $x = 2.0D, y = 2.0D$ and IV $x = 5.0D, y = 5.0D$.

5.2. TWO-DIMENSIONAL BASE STATES

that the flow at these points in the domain is periodic and synchronised with the forcing period. When these traces were examined over one hundred periods the same limit cycles were found to occur. This demonstrates that at these spatial locations the flow has reached an asymptotic state. At later stages of the thesis these diagrams are not shown and the flow is simply referred to as having reached a limit cycle. Typically this was established by examining such limit cycles over at least one hundred periods of oscillation.

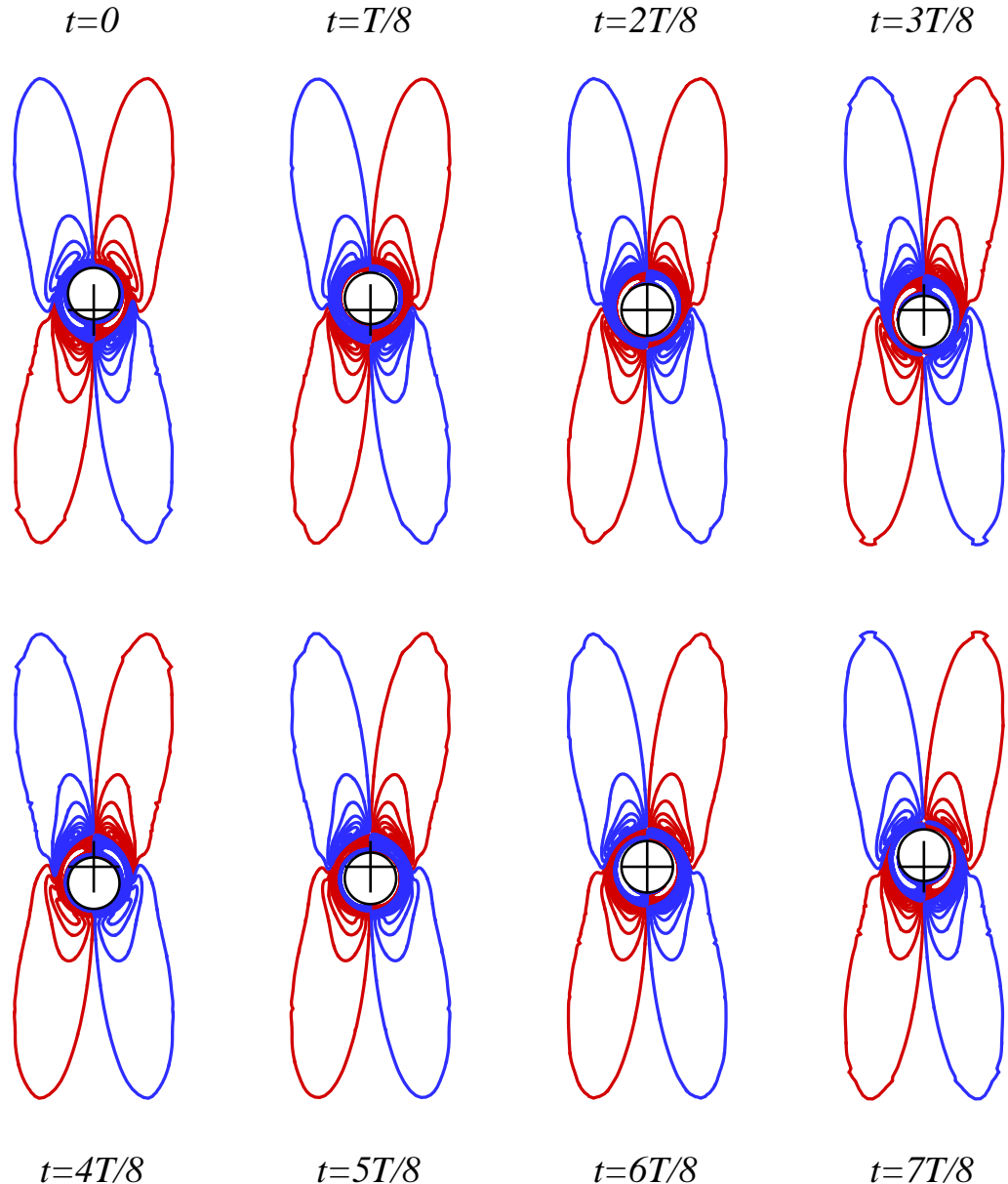


Figure 5.3: A sequence of instantaneous vorticity contours extracted over one motion period, T , at $KC=2$, $\beta=80.0$. Positive (anti-clockwise) and negative vorticity contours are denoted by red and blue colours respectively. The crosshairs denote the fixed point that the cylinder is oscillating about.

The sequence of eight images in figure 5.3 is of the instantaneous vorticity contours

5.2. TWO-DIMENSIONAL BASE STATES

generated over one period of motion. In these vorticity contours the symmetry of the flow about the axis of oscillation can be seen as an inverse reflection of the vorticity field about this axis. The synchronisation of the flow with the forcing frequency is also evident by comparing any single image with one half a period later. In these cases performing an inverse reflection about the x -axis of one set of vorticity contours will result in an set of vorticity contours that is identical to the flow state at a time $T/2$ later. An interesting aspect of these images is that the vorticity contours are all connected back to the near cylinder region and that there are no far field concentrations of vorticity. This is consistent with the lack of vorticity shedding observed by Tatsuno and Bearman (1990).

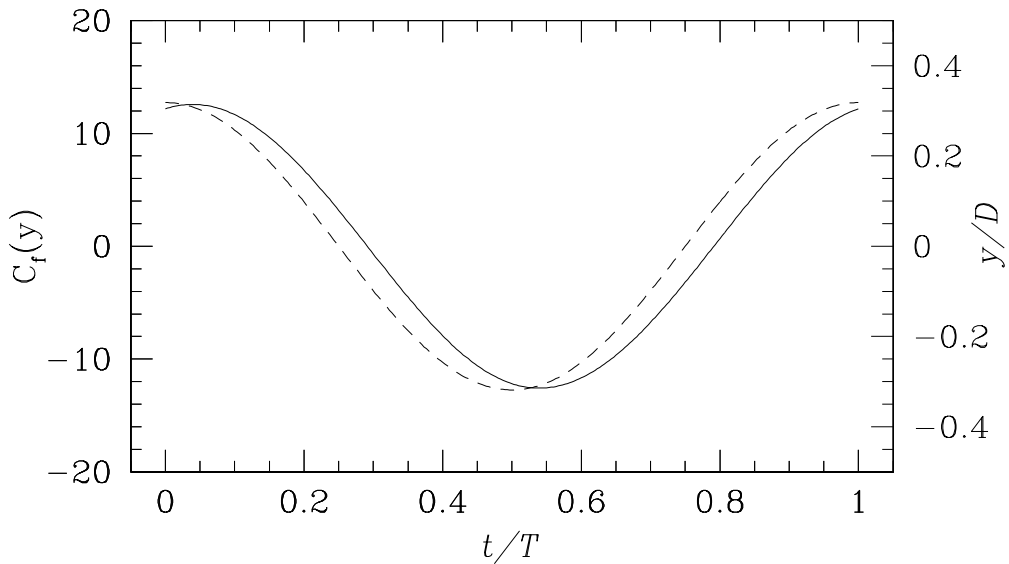


Figure 5.4: Plot of the coefficient of total y -force exerted on the cylinder over one period of cylinder motion. The simulation was carried out at $KC=2$, $\beta=80.0$. The force is non-dimensionalised with respect to the root mean square of the cylinders proscribed y -axis velocity. Also shown is the cylinders displacement (dashed line) over one period of motion.

When the forces experienced by the cylinder are examined in the x and y directions, the symmetry of the flow and its synchronisation with the forcing frequency of oscillation can be detected. In figure 5.4 a time trace of the coefficient of y force exerted on the cylinder over a single period is presented. The equivalent time trace of the x -force coefficient (not shown) shows the x force to be zero and constant over a period of oscillation. This is consistent with the flow being symmetrical about the oscillation axis and thus the x component of force resulting from the flow on one side of the cylinder is negated by the equal and opposite force experienced by the flow on the other side of the cylinder. An examination of the time-trace of y -force component, figure 5.4, over one period shows that there is a periodic variation of the force experienced by the cylinder. This force is synchronised

5.2. TWO-DIMENSIONAL BASE STATES

with the cylinder motion and its maxima occur just after the cylinder reaches the peak of the sinusoidal oscillation.

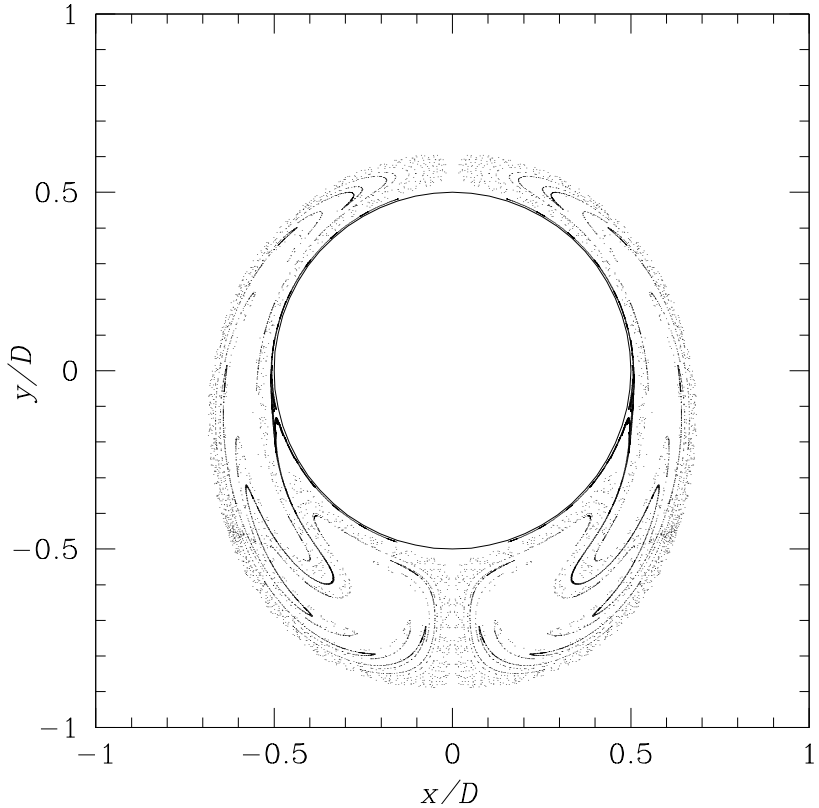


Figure 5.5: Particle shedding image. Over 15 periods of motion conducted at $KC=2$, $\beta=80.0$, with two-dimensional DNS, ten equally spaced points on the cylinder surface released massless particles into the surrounding fluid.

In figure 5.5 a particle-track plot of this symmetric and periodic flow is presented. This image was created by placing ten sources of massless particles equally around the cylinder circumference at a very small distance from the cylinder surface and evolving the flow using two-dimensional DNS. The particles were released into the surrounding fluid over 15 periods of motion. It is interesting to note that the particles all remained in the near vicinity of the cylinder. This appears to be in contrast to the result of Tatsuno and Bearman (1990) for this regime, see figure 2.17(A*), which shows a jet of particles moving away from the cylinder along the oscillation axis. However, their figures are at different Stokes numbers, $\beta=52.5$ in figure 2.17(A*), and the placement of the particle sources around the cylinder was at a set of discrete points in comparison to the experimental implementation which could influence the patterns formed. In figure 5.6 streamlines of the average flow over one oscillation are presented. The induced flow can be seen to form eight cells of rotating fluid. This images closely resembles the experimental visualisation of figure 2.13 which was produced at ($KC = 0.53$, $\beta = 132$).

The results of a three-dimensional Floquet analysis of this flow are shown in fig-

5.2. TWO-DIMENSIONAL BASE STATES

ure 5.7. In this instance no Floquet multiplier exceeded a magnitude of 1.0 for all the wavenumbers tested. This indicates that this flow is linearly stable to three-dimensional perturbations and agrees with the visualisations of Tatsuno and Bearman (1990) who also saw no evidence of three-dimensional spanwise structures in this regime.

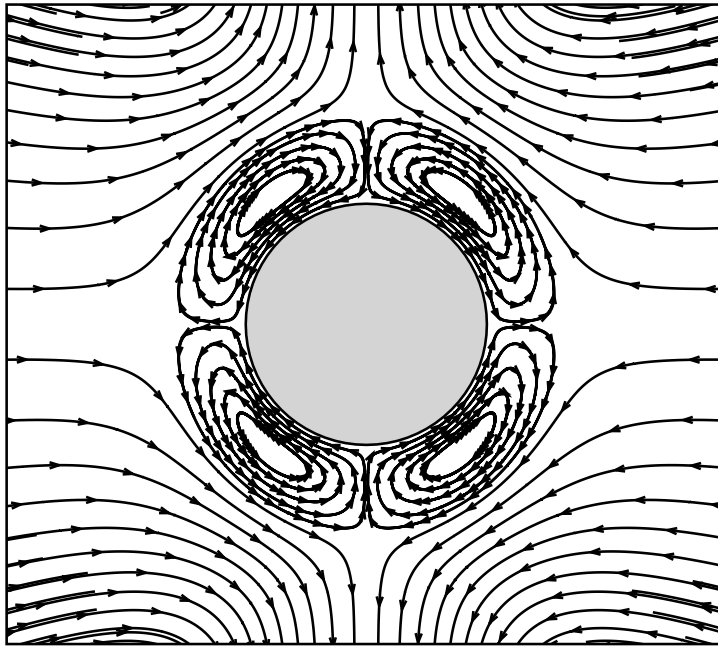


Figure 5.6: Streamlines of the secondary streaming induced by an oscillating cylinder. This image was produced from an average of the velocity fields over one period of oscillation at ($KC = 2$, $\beta = 80$). The cylinder is oscillating in the vertical direction.

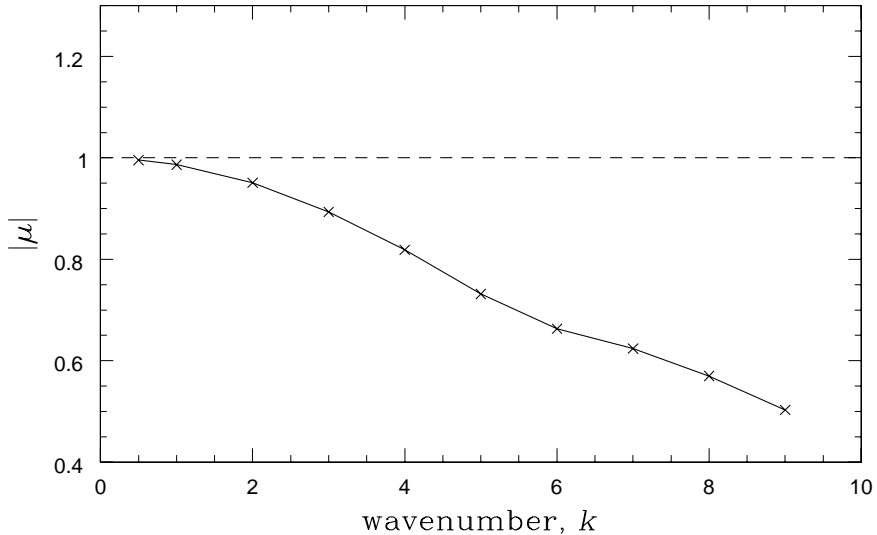


Figure 5.7: Results of a three-dimensional Floquet analysis conducted at $KC=2$, $\beta=80.0$ showing dependence of the dominant Floquet multiplier, μ , on spanwise wavenumber, k . The value $|\mu| = 1$ corresponds to the onset of instability. 64 time-slices were used in the construction of the stable, two-dimensional base flow.

5.2.2 Point II: $KC=4, \beta = 40.0$

The second point to be examined at $KC=4, \beta = 40.0$ lies in regime A. A two-dimensional DNS was evolved at this location until it was determined the simulation had reached an asymptotic state. That it had reached a periodic limit cycle was established by examining both the time traces of the velocity components at a set of locations and by examining the forces experienced by the cylinder over many oscillation periods.

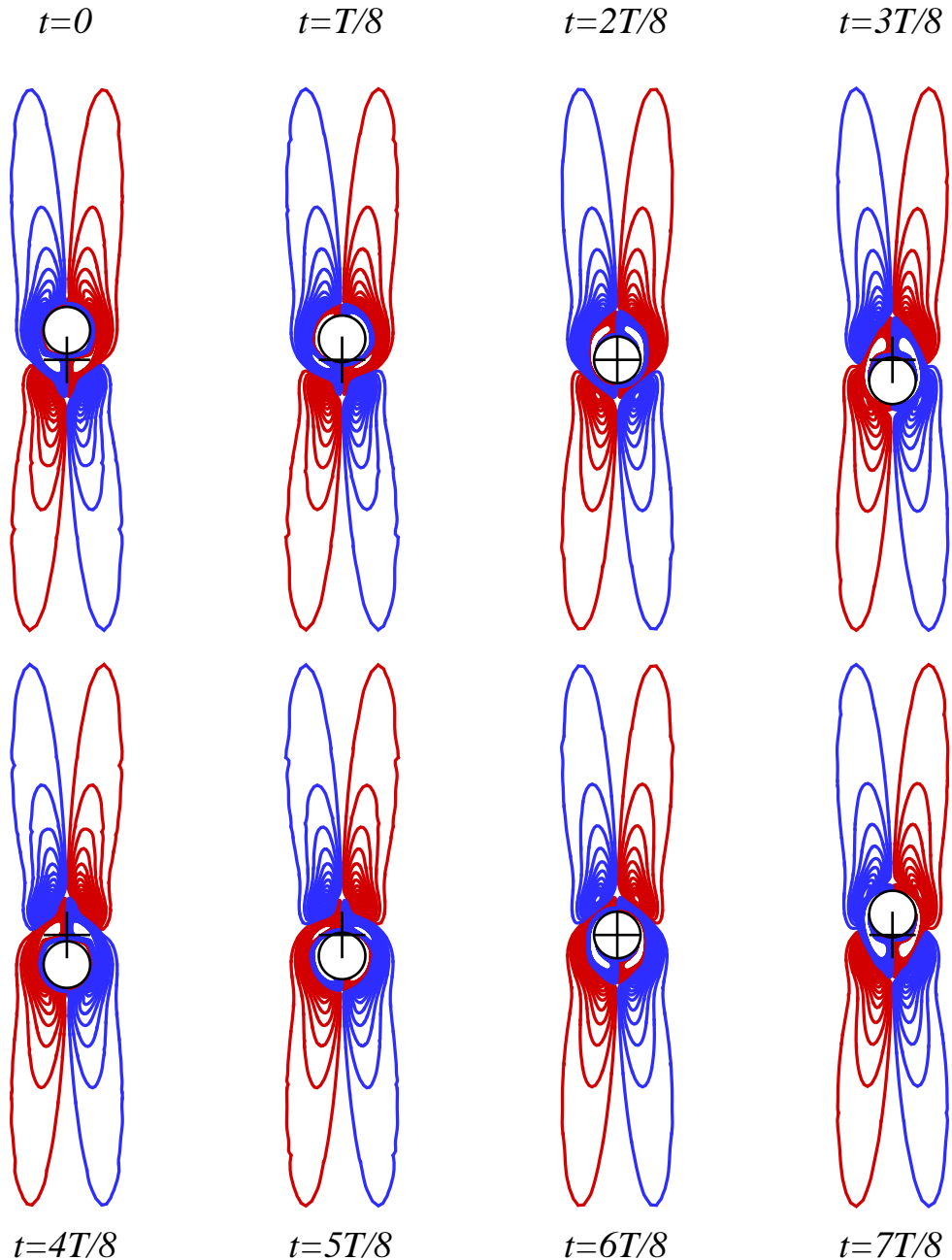


Figure 5.8: A sequence of instantaneous vorticity contours extracted over one motion period, T , at $KC=4, \beta=40.0$. Positive (anti-clockwise) and negative vorticity contours are denoted by red and blue colours respectively.

5.2. TWO-DIMENSIONAL BASE STATES

The sequence of eight images in figure 5.8 is of the vorticity contours generated over one period of motion. The flow can clearly be seen to be symmetric about the axis of oscillation as is visualised in the inverse symmetry of the vorticity contours about this axis. As with the previous case in §5.2.1 the synchronisation with the forcing period is also detected. This is seen by applying an inverse reflection about the x -axis of any image to obtain the image shown half a period later. No far field local concentrations of vorticity were detected for this case and all the vorticity contours connected back to the near cylinder region. Tatsuno and Bearman (1990) identified this location as belonging to regime A with its definitive characteristic, in relation to the flows of regime A*, being the presence of vortex shedding. These vorticity contours suggest that this location in (KC, β) -space should belong to regime A*.

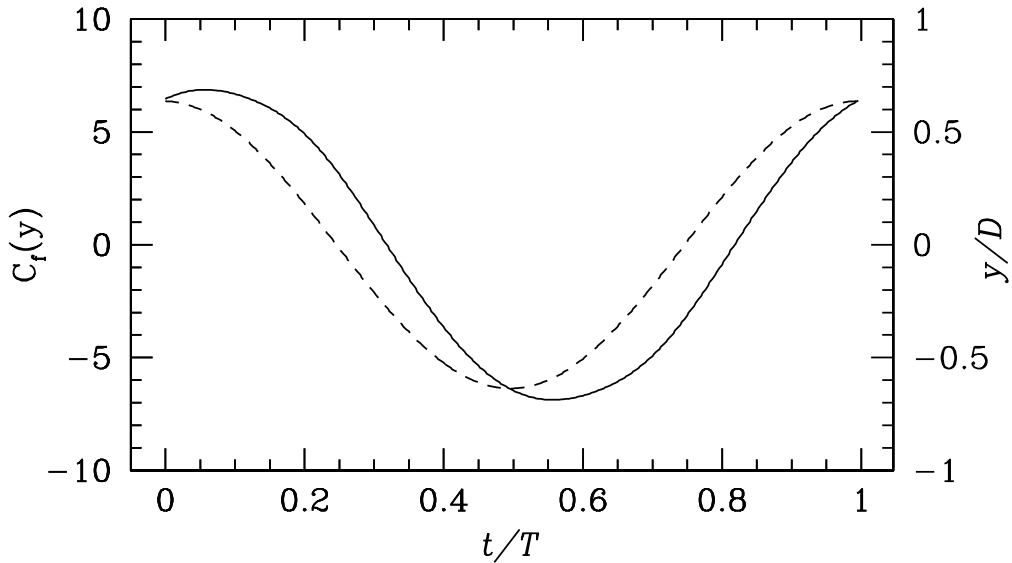


Figure 5.9: Plot of the coefficient of total y -force exerted on the cylinder over one period of cylinder motion. The simulation was carried out at $KC=4$, $\beta=40.0$. The force is non-dimensionalised with respect to the root mean square of the cylinders proscribed y -axis velocity. Also shown is the cylinders displacement (dashed line) over one period of motion.

The net force experienced by the cylinder in the x direction is zero and does not vary over an entire oscillation. This confirms that the simulation is symmetrical about the oscillation axis as the net x -component of force exerted on the cylinder is zero. Examination of the y -component of force exerted on the cylinder, see figure 5.9, shows a sinusoidal variation of the net force that is synchronised with the cylinder motion. The force exerted on the cylinder has a small phase lag to the displacement of the cylinder.

Examination of the particle track plot of figure 5.10 shows a jet of particles travelling away from the cylinder along the oscillation axis. It shows no discrete packets of particles

5.2. TWO-DIMENSIONAL BASE STATES

separating from the near cylinder region into the flow. It closely resembles the image of regime A* from Tatsumo and Bearman (1990), see figure 2.17(A*), which was obtained for $KC=3.14$, $\beta=52.8$. The vorticity contour plots in figure 5.8 also show no shedding of vorticity. However, this location is supposed to lie in a regime whose defining characteristic is the shedding of vorticity.

A three-dimensional Floquet analysis of this flow was conducted to verify that this flow has no structures that vary in the spanwise direction as observed by Tatsumo and Bearman (1990). The result, shown in figure 5.11, shows that no Floquet multipliers were of an absolute magnitude greater than 1.0 and consequently it can be concluded that this flow is two-dimensional.

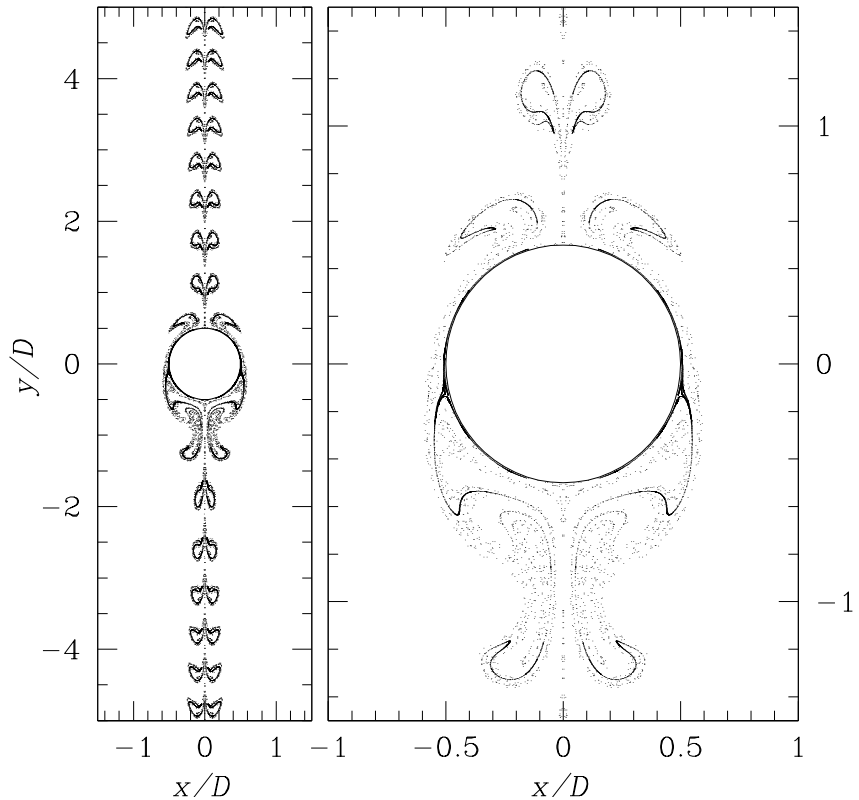


Figure 5.10: Particle shedding image. Over 15 periods of motion conducted at $KC=4$, $\beta=40.0$ with two-dimensional DNS, ten equally spaced points on the cylinder surface released massless particles into the surrounding fluid.

5.2.3 Point III: $KC=7$, $\beta=10.0$

The third point to be examined, like the previous point, lies in regime A. However it is at a much higher Keulegan–Carpenter number than the previous point and correspondingly its Stokes number is reduced to keep it within regime A. A two-dimensional DNS was

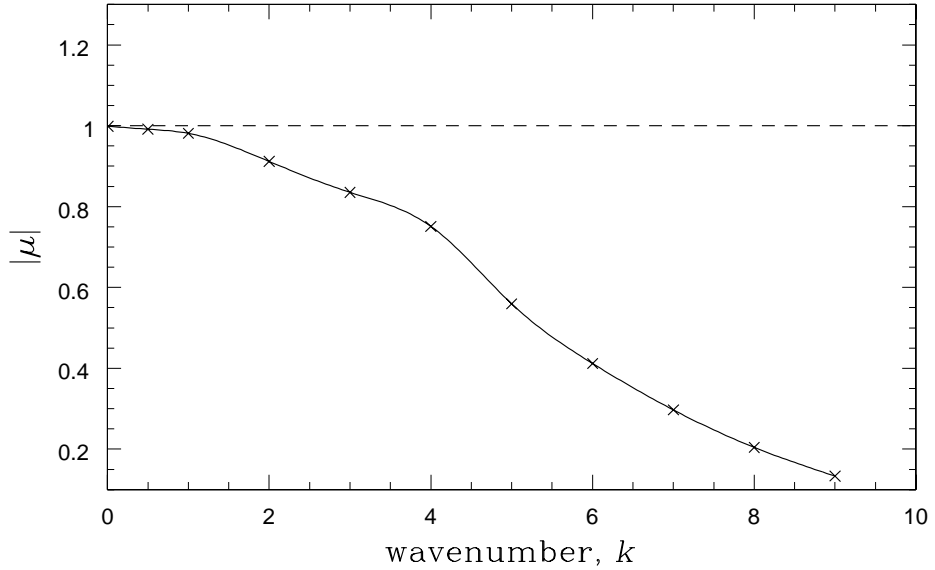


Figure 5.11: Results of a three-dimensional Floquet analysis conducted at $KC=4$, $\beta=40.0$ showing dependence of the dominant Floquet multiplier, μ , on spanwise wavenumber, k . The value $|\mu| = 1$ corresponds to the onset of instability. 64 time-slices were used in the construction of the stable, two-dimensional base flow.

evolved at this location until it was established that the flow had reached an asymptotic state.

The sequence of eight vorticity contour images presented in figure 5.12 was generated by taking eight equi-spaced in time snapshots of the flow over one period of cylinder motion and then subsequently calculating the vorticity fields. As with the previous cases the symmetry of the flow about the oscillation axis at any one instant is seen as an inverse reflection of the vorticity contours about the oscillation axis. The vorticity contours in this case are all connected back to the near cylinder region and no far field concentrations of vorticity have been found to exist. This would indicate the absence of vorticity shedding from the cylinder. A finding in contrast to the observations of Tatsuno and Bearman (1990) for a simulation at this location in (KC, β) -space.

The component of force acting along the oscillation axis can be seen, figure 5.13, to oscillate with the same period as the cylinder oscillation and with a small phase lag from the cylinders displacement. The component of force acting perpendicular to this axis is zero and remains constant over the period of oscillation. This indicates that the flow is symmetrical as the forces resulting from the vorticity in the flow is balanced across the oscillation axis.

Inspection of the particle track plot at this location, figure 5.14, shows a series of ‘puffs’ of particles being convected away from the cylinder by the induced flow. While these suggest the presence of vorticity shedding, especially given that their shape changes with distance from the cylinder, the vorticity contours show no sign of vorticity shedding.

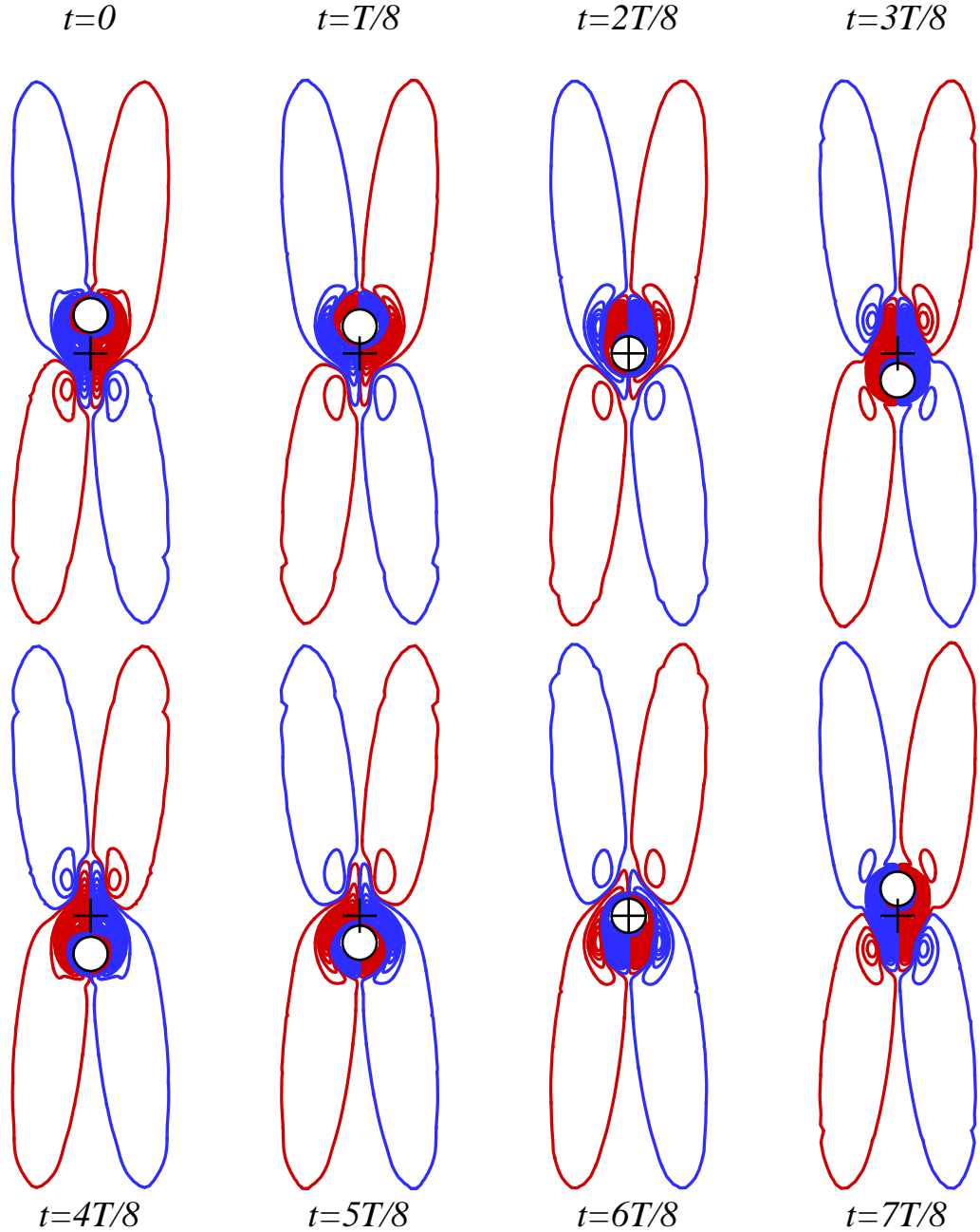


Figure 5.12: A sequence of instantaneous vorticity contours extracted over one motion period, T , at ($KC=7$, $\beta=10.0$). Positive (anti-clockwise) and negative vorticity contours are denoted by red and blue colours respectively.

The shape change of the ‘puffs’ of particles is instead due to the flow not being uniform and the corresponding velocity gradients in this region. As with the previous cases, the vorticity contours support the conclusion that there is an absence of vorticity shedding. A three-dimensional Floquet analysis at this location, shown in figure 5.15 shows no linearly unstable spanwise modes.

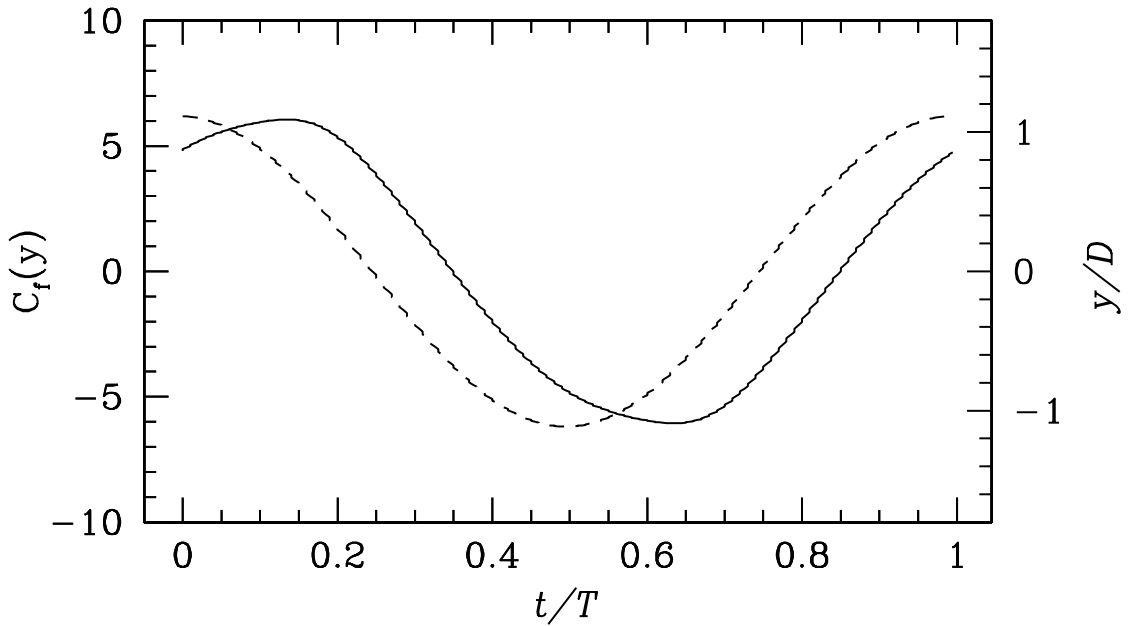


Figure 5.13: Plot of the coefficient of total y -force exerted on the cylinder over one period of cylinder motion. The simulation was carried out at $KC=7$, $\beta=10.0$. The force is non-dimensionalised with respect to the root mean square of the cylinders proscribed y -axis velocity. Also shown is the cylinders displacement (dashed line) over one period of motion.

5.2.4 Point IV: $KC=3$, $\beta = 80.0$

The fourth and final point to be examined is at $KC=3$, $\beta = 80.0$. The location of this point on the (KC,β) map of Tatsuno and Bearman (1990) places it within regime B. One of the defining characteristics of regime B is the presence of structures which regularly vary along the span of the cylinder. In this respect this case has broken a symmetry property and is no longer considered an initial state. However, as a component of this investigation involves restricting the domain to a two-dimensional subspace it is important to establish the properties of this location in the reduced space. Accordingly a two-dimensional DNS was conducted at this location and evolved until it was established through the examination of limit cycles that an asymptotic flow state had formed.

The sequence of eight vorticity contour images presented in figure 5.16 was generated by taking eight equi-spaced in time snapshots of the flow over one period of cylinder motion and then subsequently calculating the vorticity field. Experimental observations of the full three-dimensional flow do not show a symmetry about the oscillation axis when considered at a discrete spanwise location, however when two experimental images taken half a spanwise wavelength apart are superimposed the symmetry does appear to be present. In this two-dimensional simulation the vorticity contours resemble those of the previous cases where an inverse reflection of the vorticity contours about the oscillation axis was observed. In this case, like all the previous cases, the vorticity contours are all

5.2. TWO-DIMENSIONAL BASE STATES

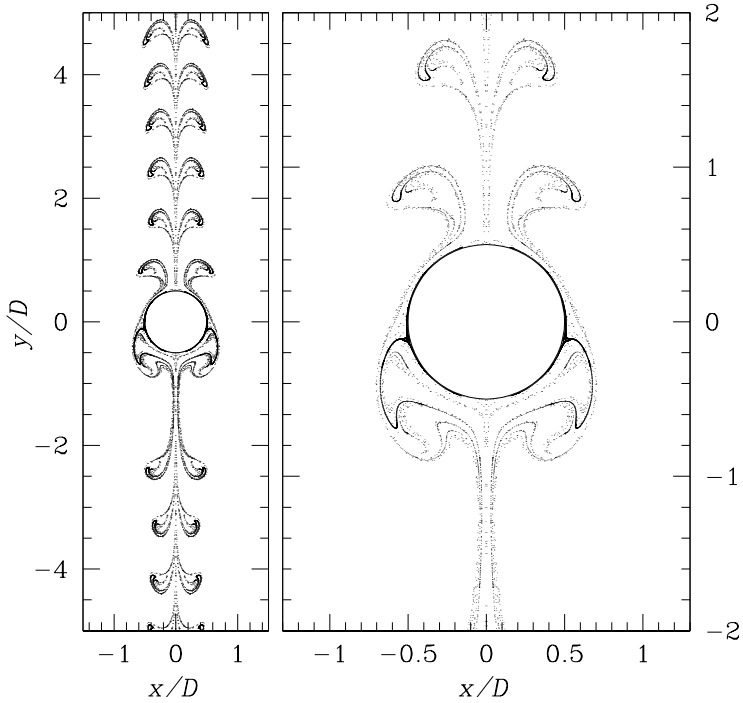


Figure 5.14: Particle shedding image. Over 15 periods of motion conducted at $KC=7$, $\beta=10.0$ with two-dimensional DNS, ten equally spaced points on the cylinder surface released massless particles into the surrounding fluid.

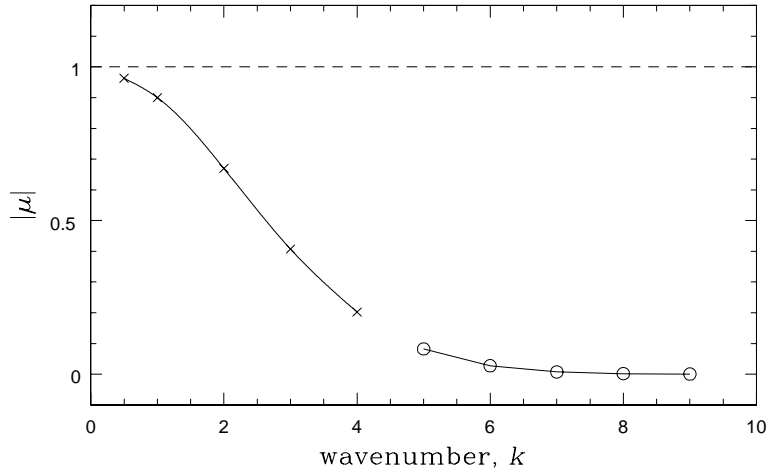


Figure 5.15: Results of a three-dimensional Floquet analysis conducted at $KC=7$, $\beta=10.0$ showing dependence of the dominant Floquet multiplier, μ , on spanwise wavenumber, k . The value $|\mu| = 1$ corresponds to the onset of instability. 64 time-slices were used in the construction of the stable, two-dimensional base flow.

connected back to the near cylinder region and no far field concentrations of vorticity are observed to occur.

Examination of the time traces of the force experienced by the cylinder reveals that the flow is symmetric about the oscillation axis and periodic. The x -component of force

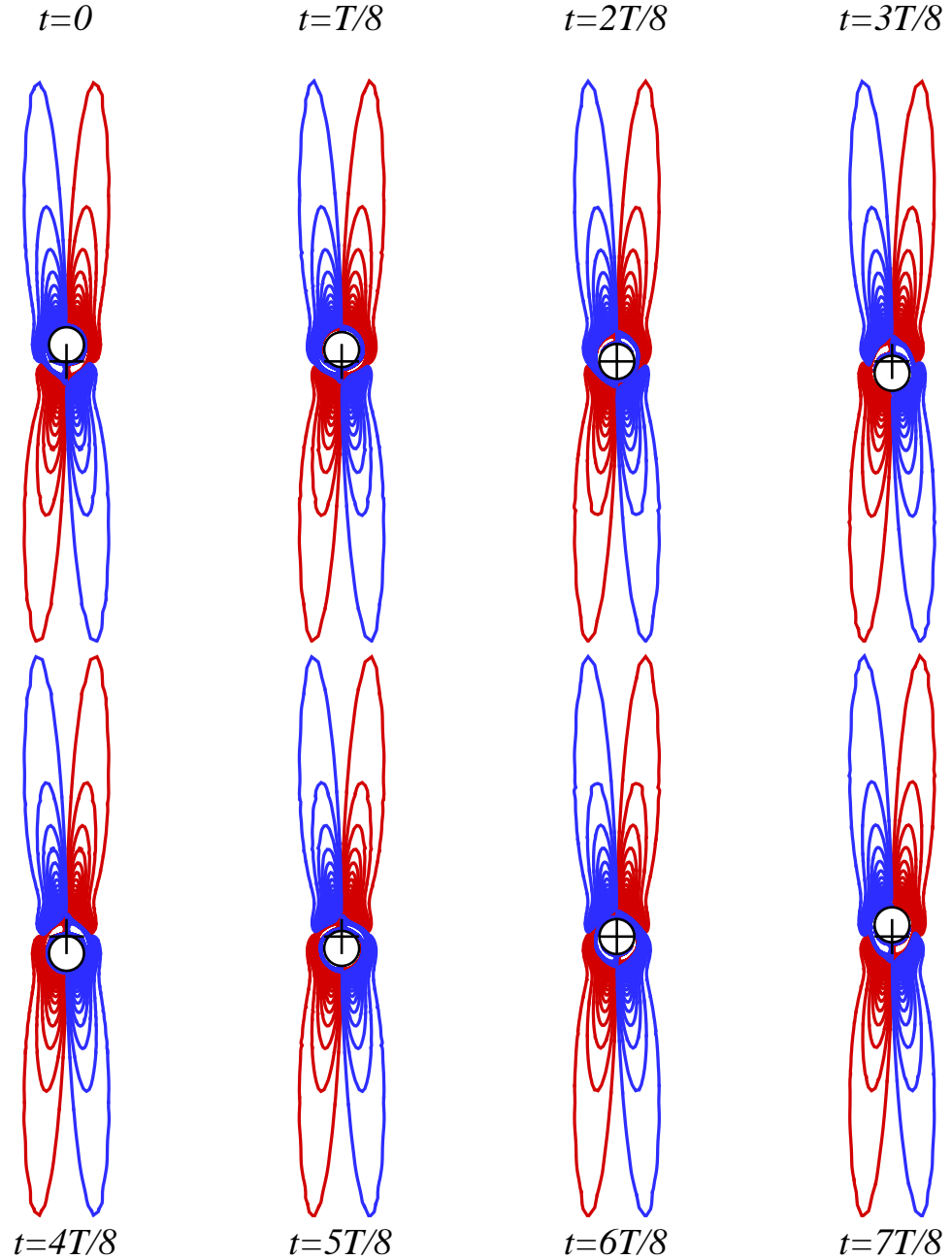


Figure 5.16: A sequence of instantaneous vorticity contours extracted over one motion period, T , at $KC=3$, $\beta=80.0$. Positive (anti-clockwise) and negative vorticity contours are denoted by red and blue colours respectively.

experienced by the cylinder remains zero over an entire period from which it can be concluded that the flow is symmetrical about the oscillation axis ($x=0$). The component of force inline with the oscillation, figure 5.17, shows a periodic variation that is synchronised with the period of oscillation. Additionally a small phase lag, with reference to the cylinders displacement, is also visible. It is concluded that the flow is symmetrical about the oscillation axis and synchronised with the oscillation in the case where the flow is

5.2. TWO-DIMENSIONAL BASE STATES

restricted to a two-dimensional subspace.

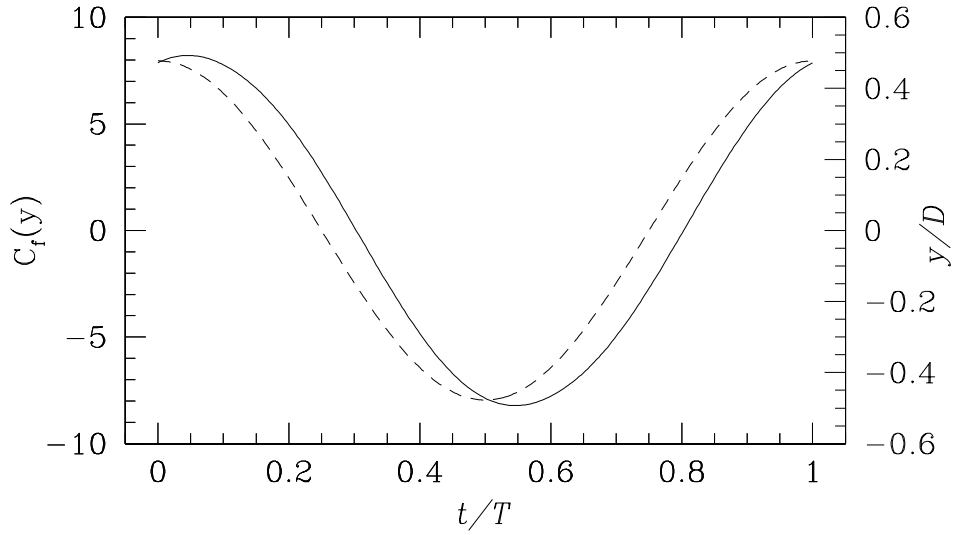


Figure 5.17: Plot of the coefficient of total y -force exerted on the cylinder over one period of cylinder motion. The simulation was carried out at $KC=3$, $\beta=80.0$. The force is non-dimensionalised with respect to the root mean square of the cylinders proscribed y -axis velocity. Also shown is the cylinders displacement (dashed line) over one period of motion.

In the interests of completeness the two-dimensional particle shedding plot for this location is shown in figure 5.18. However it must be noted that this flow is strongly three-dimensional and spanwise fluctuations along the span would definitely perturb the particle shedding diagram. It would appear that a particle shedding pattern similar to those of points II & III is formed. In combination with the matching vorticity contours it can be seen that the discrete ‘puffs’ of particles are not representative of vortex shedding figure but are instead formed in the near cylinder region and transported away from the cylinder by the induced flow. In figure 5.19 the Floquet analysis of this location clearly show that the flow is linearly unstable to mode with a wavenumber $\approx 5D$. The aspect of three-dimensionality will be considered in more detail in chapter 7.

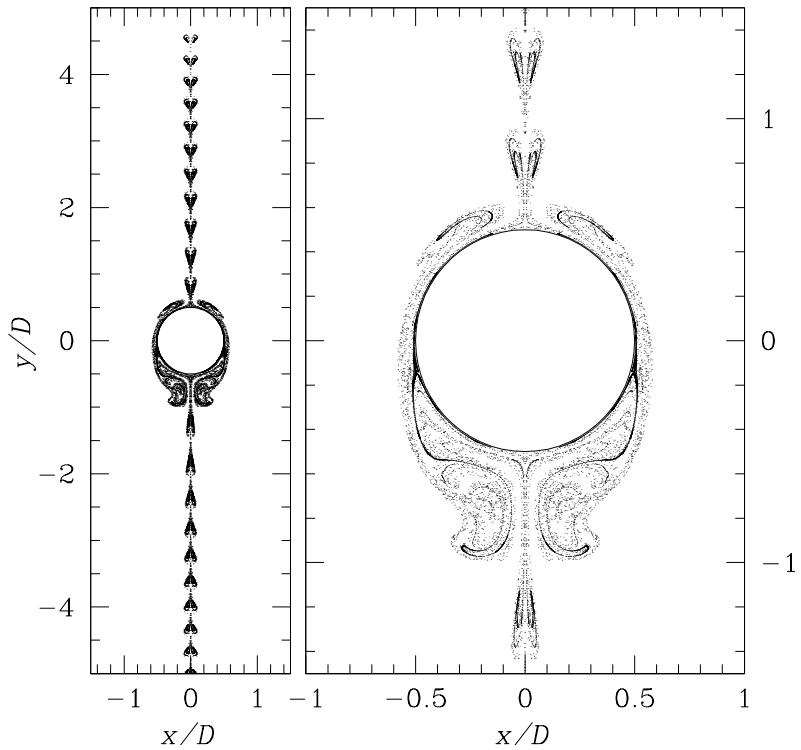


Figure 5.18: Particle shedding image. Over 15 periods of motion conducted at $KC=3$, $\beta=80.0$ with two-dimensional DNS, ten equally spaced points on the cylinder surface released massless particles into the surrounding fluid.

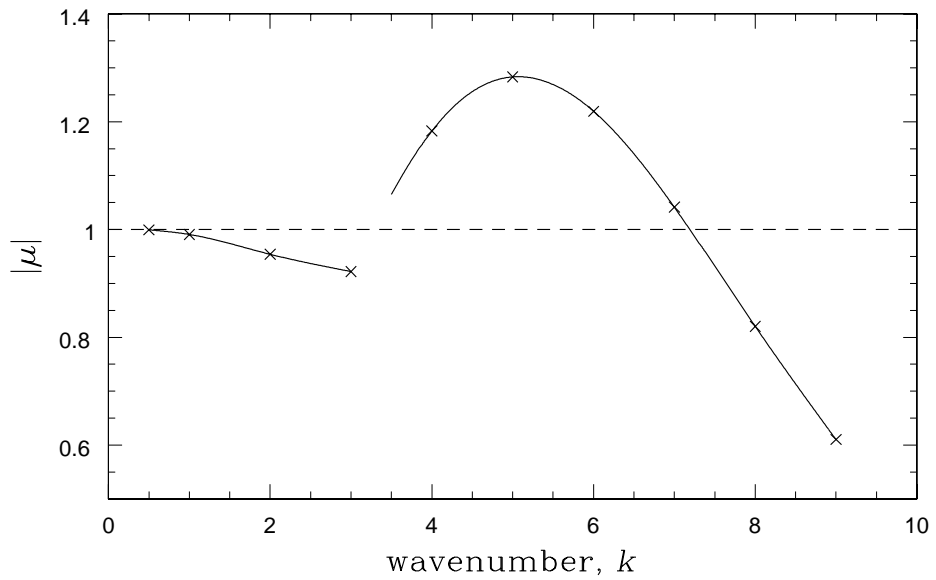


Figure 5.19: Results of a three-dimensional Floquet analysis conducted at $KC=3$, $\beta=80.0$ showing the dependence of the dominant Floquet multiplier, μ , on spanwise wavenumber, k . The value $|\mu| = 1$ corresponds to the onset of instability. 64 time-slices were used in the construction of the stable, two-dimensional base flow.

5.3 Discussion

In the previous sections four test locations have been examined in detail. These four points were chosen because they were representative of the regimes established by Tatsuno and Bearman (1990) and for being at a point in (KC, β) -space where a detailed study of the transitions that occur to this flow, as either of these parameters is increased, is later made. In examining these four points a number of common features in the flow were identified. These features are:

- *T*-Periodicity: All of the two-dimensional DNS presented eventually evolved into an asymptotic flow state that was synchronised with the period of cylinder motion, T . This feature was found to be present in the time-traces of the velocity at points in the domain, in the time-traces of the force experienced by the cylinder and visually in the sequence of vorticity contours presented over one period of motion.
- Spatial reflection about $x = 0$: In all of the cases examined a symmetry about the axis of cylinder oscillation (the y -axis) was observed. When presented in terms of vorticity contours this was shown as an inverse reflection of the z -component of vorticity about $x = 0$. This symmetry was also evident when the component of force experienced by the cylinder in a direction perpendicular to the motion was examined. In all the cases examined this net force was found to be zero and constant over a period of oscillation, indicating that the force experienced by either side of the cylinder about $x = 0$ was equal in magnitude and opposite in sign. This is consistent with a vorticity field that has an inverse reflection about $x = 0$.
- Spatio-Temporal reflection about $y = 0$: When the vorticity contours of the previous cases are examined an additional symmetry is observed that is dependent on both time and spatial location. When an image out of either of figures 5.3, 5.8, 5.12 or 5.16 is examined, it can clearly be seen in the vorticity contours that the flow state at $t = T/2$ is an inverse reflection about $y = 0$ of the flow state at $t = 0$.
- Spanwise Symmetry: For each of the previous cases a three-dimensional Floquet stability analysis was conducted. In only one case, as expected for the case $KC = 3, \beta = 80.0$, was an unstable spanwise mode detected. This corresponds with the previous experimental visualisations of Honji (1981) and Tatsuno and Bearman (1990). In the other three cases considered no spanwise linearly unstable modes were detected. This is supported by the existing experimental visualisations where regimes A* and A showed no variation along the span.

These four properties are the essential characteristics that define the initial state known as the ‘base flow’. When restricted to the $x-y$ plane (conventionally referred to as the two-dimensional flow throughout this thesis) which is perpendicular to the cylinder span, only

5.3. DISCUSSION

three of these properties are applicable and in this case all four test cases can be considered as ‘base flows’. However, when considered in a fully three-dimensional space, the flow at $KC = 3, \beta = 80.0$ is clearly three-dimensional and the spanwise symmetry property of the flow has been altered from being constant along the span to having a regular variation along the span. Clearly this indicates that there is a transition occurring between the point at $KC = 2, \beta = 80.0$ and this point. However, in a restricted two-dimensional subspace this point satisfies all the properties of the base flow and will be used as such.

In the investigation of Tatsuno and Bearman (1990) the defining visual characteristic separating flows of regime A* from those of A was the presence of vortex shedding. However, due to an acknowledged difficulty in determining the onset of vortex shedding, the boundary was not delineated in their map of the flow regimes. In the figures of the vorticity contours presented in this chapter no evidence is seen of any concentrations of vorticity separating from the near cylinder region. Other than a stretching of vorticity contours along the oscillation axis, due to the increased amplitudes of oscillation, the vorticity diagrams presented are all very similar. In the numerical two-dimensional results there is only one distinguishable difference between flows in either regime. The difference that was detected was the contrast between the particle shedding image of regime A* and the experimental visualisation of figure 2.17(A*). In this case the particles were observed to remain in the near vicinity of the cylinder. It is suggested that the figure presented in Tatsuno and Bearman (1990) for regime A* belongs instead to regime A and that an experimental image where the dye or particles remain in the cylinder vicinity is a more appropriate image for this regime.

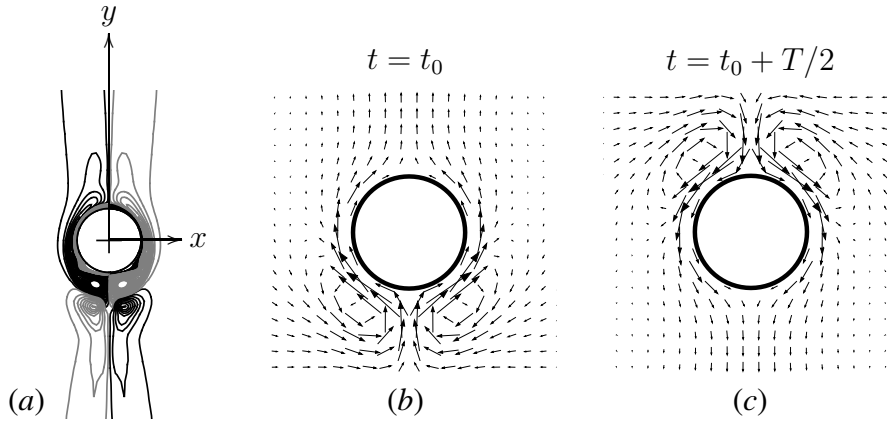


Figure 5.20: Two-dimensional symmetric base flows at low KC and β . Panel (a) illustrates the coordinate system (the spanwise, z , coordinate is normal to the (x, y) plane), and contours of positive (black) and negative (grey) vorticity, which have symmetry (5.6). Panels (b) and (c) illustrate the spatial (K_x) and spatio-temporal (H_1, H_2) symmetries of the base flow velocity.

5.4 Symmetry Definitions

In the previous sections the characteristics common to the symmetric and periodic base flow were highlighted and qualitatively discussed. To enable a concise means of establishing exactly which symmetry property has broken through a bifurcation, in this section these spatial and/or temporal properties are formally defined. In the previous section four characteristics of the two-dimensional symmetric state were established:

1. T -periodic flow.
2. A reflection symmetry about the axis of oscillation, $x = 0$.
3. A $T/2$ reflection symmetry about $y = 0$
4. A spanwise invariance of the flow.

With the coordinate system fixed to the cylinder axis, as shown in figure 5.20, the two spatial symmetries for the velocity fields of the base flow can be written as

$$x\text{-reflection: } K_x(u, v, w)(x, y, z, t) = (-u, v, w)(-x, y, z, t), \quad (5.1)$$

$$z\text{-translation: } R_\alpha(u, v, w)(x, y, z, t) = (u, v, w)(x, y, z + \alpha, t), \quad (5.2)$$

$$z\text{-reflection: } K_z(u, v, w)(x, y, z, t) = (u, v, -w)(x, y, -z, t), \quad (5.3)$$

With some advance knowledge from the visualisations of Tatsuno and Bearman (1990), about the way in which the flow states change, the spatio-temporal symmetries can be

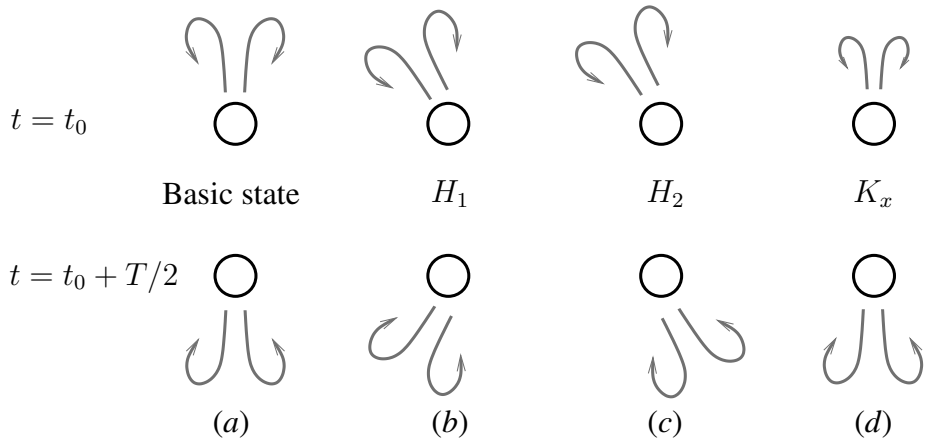


Figure 5.21: Schematics illustrating representative ways in which the two-dimensional symmetries of the basic state can be broken. The basic state, (a), has the three symmetries K_x , H_1 , H_2 , while in (b–d), two out of three break, and the outcomes are labelled with their remaining symmetry.

written accordingly. The $T/2$ reflection symmetry about $y = 0$ and the T -periodicity are written as two spatio-temporal symmetry forms:

$$H_1(u, v, w)(x, y, z, t) = (u, -v, w)(x, -y, z, t + T/2), \quad (5.4)$$

$$H_2(u, v, w)(x, y, z, t) = (-u, -v, w)(-x, -y, z, t + T/2). \quad (5.5)$$

These two forms together define the spatio–temporal symmetry observed in the initial flow state. The first symmetry listed previously, that of the T -periodic flow, is a subset of (5.4) and (5.5) and is broken when both the H_1 and H_2 symmetries are broken. All the symmetries listed are written with three velocity components because the flow instabilities may be three-dimensional. In figure 5.21 the ways in which the two-dimensional symmetry can be broken are illustrated in schematic form. The reflection symmetry, K_x , when applied twice returns the original starting point.

The symmetry equations corresponding to 5.1, 5.4 and 5.5 for the two-dimensional base flow expressed in terms of the z -component of vorticity are:

$$\xi(x, y, z, t) = -\xi(-x, y, z, t), \quad (5.6)$$

$$\xi(x, y, z, t) = -\xi(x, -y, z, t + T/2), \quad (5.7)$$

$$\xi(x, y, z, t) = \xi(-x, -y, z, t + T/2). \quad (5.8)$$

5.5 Summary

In this chapter the symmetry properties of the base flow have been established. Two-dimensional DNS's were run for a number of cases that had been shown experimentally to be symmetric and periodic. These cases were evolved until they reached a terminal state, which in all cases was a periodic limiting state. A number of measures were used to establish the properties of the base flow which included monitoring the time-traces of the velocities at spatial locations in the domain, monitoring the forces on the cylinder decomposed into directions along and perpendicular to the oscillation axis, examining the vorticity field over a period of cylinder motion and examining the particle shedding plots. From this information regarding the flow properties at these four locations the symmetry properties of the base flow were defined.

An interesting feature that was also clarified was the absence of vorticity shedding observed in regime A. Tatsuno and Bearman (1990) delineated the difference between regimes A^* and A as the presence of vorticity shedding in regime A. In the observation of flows in both regimes, no far field concentrations of vorticity were observed to occur and it is concluded that there is no difference between the flows of either regime in terms of the vorticity contours. One noticeable difference that was observed was that the particles shed for low Keulegan–Carpenter numbers remained in the near cylinder region. The difference between regimes A^* and A might better be defined by the breakdown of the flow cells seen in figure 5.6 so that particles shed from the cylinder surface are transported away from the cylinder.

Chapter 6

Rectilinear Oscillation: Symmetry Breaking in a Two-Dimensional Subspace

In chapter 5 the properties of the stable, symmetric flow generated by a rigid cylinder with rectilinear oscillation in the plane normal to the cylinder span were examined. It was found that this flow, the ‘base flow’, possessed five distinct symmetries that can be summarised as:

1. K_x : a spatial reflection in $x = 0$,
2. H_1 : a spatio-temporal symmetry about y ,
3. H_2 : a second spatio-temporal symmetry about y ,
4. K_z : a spatial reflection in z ,
5. R_α : a spatial translation along z .

At this stage of the study the domain of investigation is restricted to the two-dimensional plane perpendicular to the cylinder span for this chapter. A consequence of this is that only the symmetries K_x , H_1 and H_2 can be broken.

In this chapter the transitions that occur in this two-dimensional subspace are investigated using a combination of Floquet analysis and DNS. In particular the focus is on the nature of these transitions and the symmetries that are broken by the different types of transitions. Although the principal focus is on the first transition (the primary transition) from the base flow, subsequent two-dimensional transitions are also briefly examined.

In the following sections Floquet analysis is employed firstly to isolate the curve of marginal stability in (KC, β) -space (§6.1) and secondly to identify the nature of the resultant transition. The two transitions that are identified, corresponding to either a real

Floquet multiplier or a pair of complex-conjugate multipliers crossing the unit circle, are explored in sections §6.2 and §6.3 respectively. In both of these sections the spatial and temporal characteristics of the flow is examined from the perspective of both the linearised and the non-linear dynamics of the system. In §6.4 the nature of the subsequent transitions is briefly explored and finally in §6.5 these results are discussed and summarised.

6.1 Curve of Marginal Stability

The critical curve which denotes the marginal stability of the base flow was identified using Floquet analysis to find the point at which the magnitude of the Floquet multiplier, $|\mu|$, was equal to unity. The procedure used to determine a single point on the critical curve is as follows: at any chosen location in (KC, β) -space a two-dimensional base flow is generated using DNS. This is performed on half the computational domain, $x \geq 0$, with symmetry boundary conditions enforced on the line of bisection of the full domain, at $x = 0$, to ensure that the resultant base flow is symmetric about the axis of oscillation. Once a time-periodic flow has evolved on this half domain, it is then projected onto the full domain using a reflection about $x = 0$. 64 equi-spaced in time snapshots of the velocity fields were stored over one period, which could then be used to recreate the base flow velocity vectors, via a Fourier reconstruction, at any time t . A Floquet stability analysis was then performed on this base flow with the initial perturbation vector set to a small level of noise. Alternatively the initial perturbation vector can be set to a previously calculated field, however no difference in the resultant instability was observed between starting from a previous solution or from noise, except in the computational time required. At each new location in (KC, β) -space to be tested the first perturbation vector was set to noise. Owing to computational limits, only a certain number of iterations could be performed per simulation. Consequently, in order to achieve the desired accuracy, a simulation was often run multiple times, each time restarting from the solution of the previous simulation. Through a series of these simulations, usually at either a fixed Keulegan–Carpenter or Stokes number, the critical point in (KC, β) -space where a unity Floquet multiplier, $|\mu| = 1$, exists was identified. Using both bisection and extrapolation techniques new locations in the (KC, β) -space were selected for testing. In the results presented the critical values of KC and β were determined to within ± 0.05 in both control-parameters, which typically required 5 – 15 individual locations to be tested.

In some cases extrapolation was required because of difficulties in resolving the stable component, $|\mu| < 1$, of the multiplier branches. This difficulty arises because a multiplier with a magnitude just less than unity is being detected as the dominant multiplier for the analysis in stable regions. This ‘unity’ multiplier is a consequence of the base flow being driven in simple harmonic motion over much of the domain. Iooss and Joseph (1990, § VII.6.2) argue that for a set of autonomous ODEs, a neutrally stable multiplier $\mu = +1$ exists for a solution in simple harmonic motion. While a simple harmonic motion can arise as the solution of a set of autonomous ODEs, in this case the flow is driven, not autonomous. However, the flow in this case is in simple harmonic motion over much of the domain and therefore a multiplier arises just less than unity. An unfortunate implication of the presence of this spurious multiplier was the inability to accurately resolve the multiplier branches when their values were below one. Consequently, in most cases,

6.1. CURVE OF MARGINAL STABILITY

stable base flows beyond the point of instability onset were required. Additionally the technique of bisection to locate the critical point in (KC, β) -space could not always be employed as values of the multiplier below one were not achievable. In the case of the primary transition this difficulty was managed by using a base flow that is solved in a half-domain, $x \geq 0$, and enforcing the symmetry of the flow at $x = 0$. However, this difficulty presented an insurmountable obstacle in determining subsequent instabilities as the ‘base flows’ no longer had the same symmetry characteristics that could be enforced by means such as using a symmetry boundary condition and a half domain. The alternative of detecting a multiplier branch before it becomes unstable and watching it increase through $|\mu| = 1$ as the control parameters are varied was not possible due to the inability to resolve stable branches, $|\mu| < 1$.

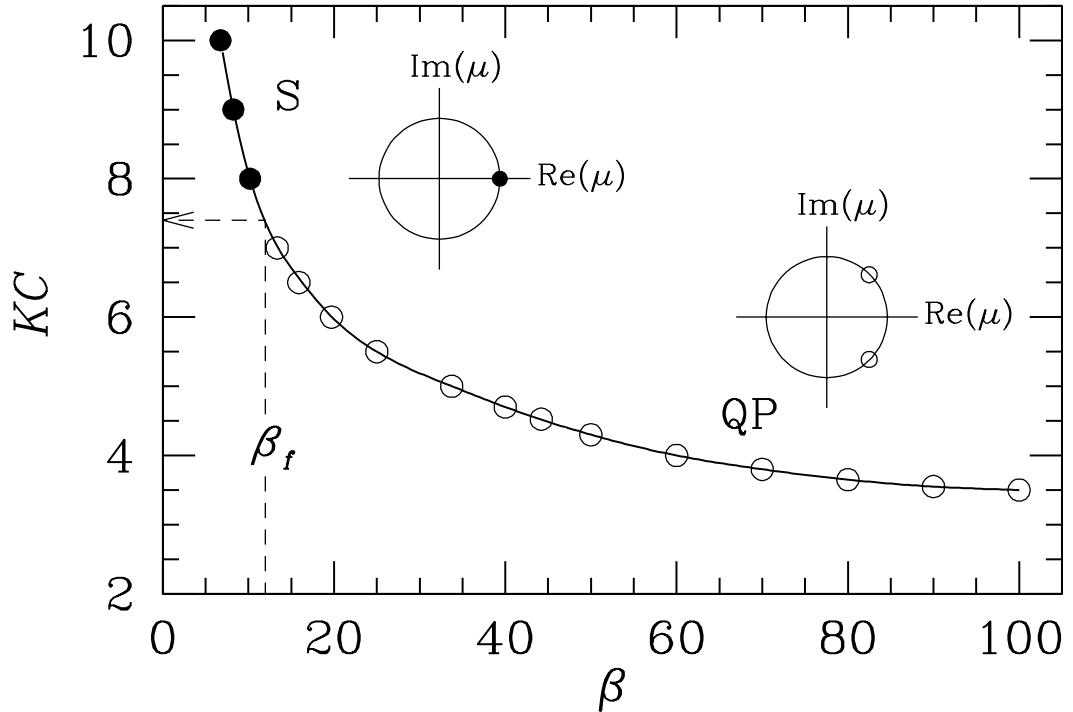


Figure 6.1: Curve of marginal stability for the primary transition in a two-dimensional subspace. The curve shown denotes the points at which real or a pair of complex-conjugate critical Floquet multipliers were found in the (KC, β) control space, with the insets illustrating the placement of critical multipliers on the unit circle in the complex domain. The dashed lines indicate the approximate values of β_f and KC_f at which the critical multiplier switches between a real and a pair of complex-conjugate multipliers.

In figure 6.1 the curve of marginal stability is shown for the range of control-space parameters investigated ($KC \leq 10$, $\beta \leq 100$). Two types of the three possible forms of the critical Floquet multiplier occur along this curve. In the upper Keulegan–Carpenter number, low Stokes number region, denoted by the letter ‘S’, a real positive critical Flo-

6.1. CURVE OF MARGINAL STABILITY

quet multiplier, $\mu_c = +1$, occurs which indicates an unstable mode that is synchronous with the base flow. Further along the curve, with increasing Stokes numbers, a pair of complex multipliers arise, $\mu_c = \exp \pm i\theta$, marking the manifestation of an unstable mode in the flow that, in addition to the spatial consequences, introduces a new temporal period. This new secondary period, T_s , if incommensurate with the period of oscillation, T , results in a quasi-periodic variation of the flow. The regime that arises from this mode is denoted as ‘QP’ in figure 6.1. The third possible form of a critical Floquet multiplier is the case where a real negative multiplier occurs, $\mu_c = -1$, corresponding to period doubling. This form is not found at any point on the critical curve. The point at which the real and complex branches of the critical multiplier curve meet is denoted as the ‘freezing point’ and is indicated by the variables KC_f and β_f . The exact values at which this point occurs are discussed in the following paragraphs.

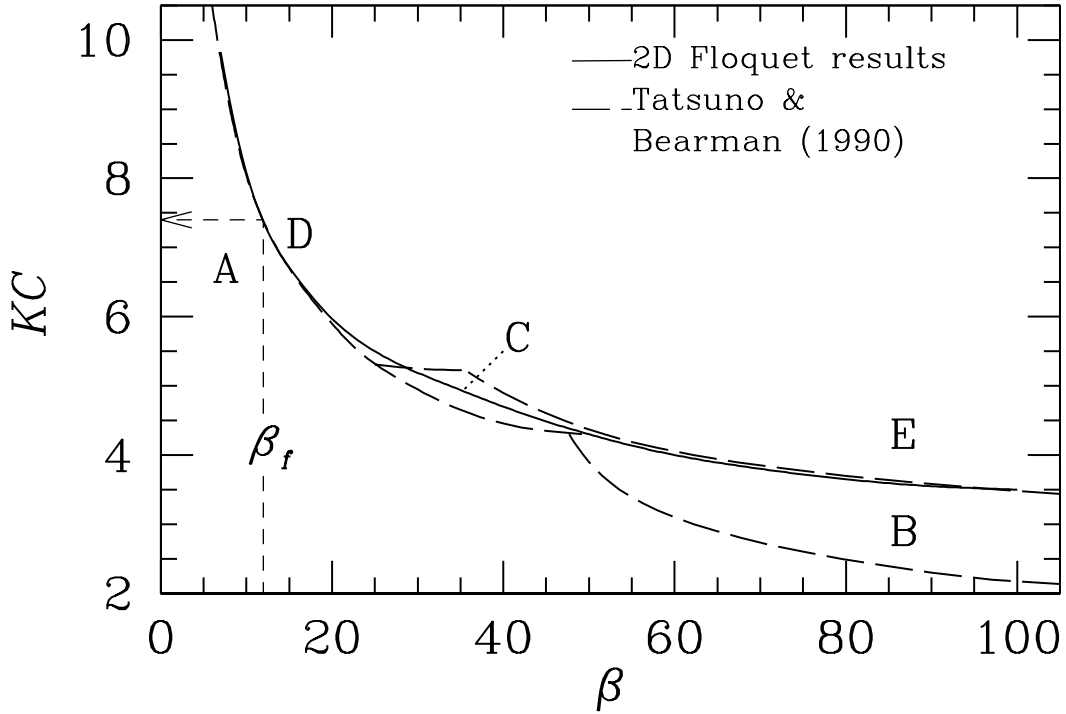


Figure 6.2: Curve of marginal stability for the primary transition in a two-dimensional subspace shown with the experimental regimes of Tatsuno and Bearman (1990). The dashed lines indicate the approximate position at which the critical multiplier switches between real and complex-conjugate pair multipliers.

Figure 6.2 shows the critical curve plotted alongside a selection of the nearest experimental regime boundaries of Tatsuno and Bearman (1990). The results of this study are in excellent agreement with a selection of Tatsuno and Bearman’s boundaries. In particular the boundaries denoting the transitions between regimes A-D and B-E match the critical curve very closely in the limits $KC \rightarrow 10$, $\beta \rightarrow \infty$ respectively. This is despite the fact

6.1. CURVE OF MARGINAL STABILITY

that the calculations in this chapter are restricted to a two-dimensional subspace and do not take into account spanwise variations which are plainly evident in Tatsuno and Bearman's images of regimes B, D and E. The correlation between the critical curve and the regime boundaries in the neighbourhood of regime C is not as close. This discrepancy is not large and, as will be shown in a later section, the flow dynamics reported by Tatsuno and Bearman (1990) match those predicted by the two-dimensional Floquet analysis and DNS computations. It must also be noted that Tatsuno and Bearman's boundaries are derived by interpolating between a discrete set of experimentally derived points and, as such, some error in these boundaries may be expected. In the results presented here the points between which the critical point was established to lie in (KC, β) -space were located 0.05 apart in either KC or β .

Along the critical curve a transition occurs from real to complex-conjugate pair multipliers at the 'freezing point', (KC_f, β_f) . This point signifies the location at which a quasi-periodic mode 'freezes' into a synchronous one. In figure 6.3(a) the phase angles along the critical curve are shown and it can be seen that the freezing point occurs approximately at $\beta_f \approx 12$ and, using figure 6.1, $KC_f \approx 7.4$. At this stage it is interesting to note that this point occurs not at an intersection of the boundaries between the three-dimensional flow regimes but instead in the middle of the boundary denoting the transition between the flows of regimes A and D. As a complex-conjugate multiplier gives rise to a quasi-periodic mode it is expected that the resultant flow would be quasi-periodic, instead, experimentally the formation of the synchronous regime D is observed to occur for locations beyond the marginal curve both above and below the freezing point with respect to KC . In section §6.4 this apparent inconsistency is examined, but for now, note that the change from regime S to QP is only defined very close to the marginal stability curve.

As mentioned previously complex-conjugate pair multipliers having a magnitude greater than unity signify the growth of a mode with a period that is distinct from the period of cylinder oscillation. This secondary period, T_s , is related to the phase angle of the multipliers such that:

$$\frac{T_s}{T} = \frac{2\pi}{\theta}. \quad (6.1)$$

However, this relationship only holds if $\theta < 2\pi$ which is the case here. In figure 6.3(a) this relationship is illustrated. As $\beta \rightarrow \beta_c^+$, $T_s/T \rightarrow \infty$, while for $\beta \rightarrow 100$, $T_s/T \rightarrow 7$ approximately.

In the following sections the synchronous and quasi-periodic periodic transitions are explored in more detail. In particular, transitions in three locations are examined in the two-dimensional subspace that are representative of the transitions between the three-dimensional regimes A↔D, A↔C and B↔E. A detailed three-dimensional treatment of these transitions follows in chapter 7. In the section following these the extent of the regimes S and QP is examined and the apparent conflict between the prediction

6.1. CURVE OF MARGINAL STABILITY

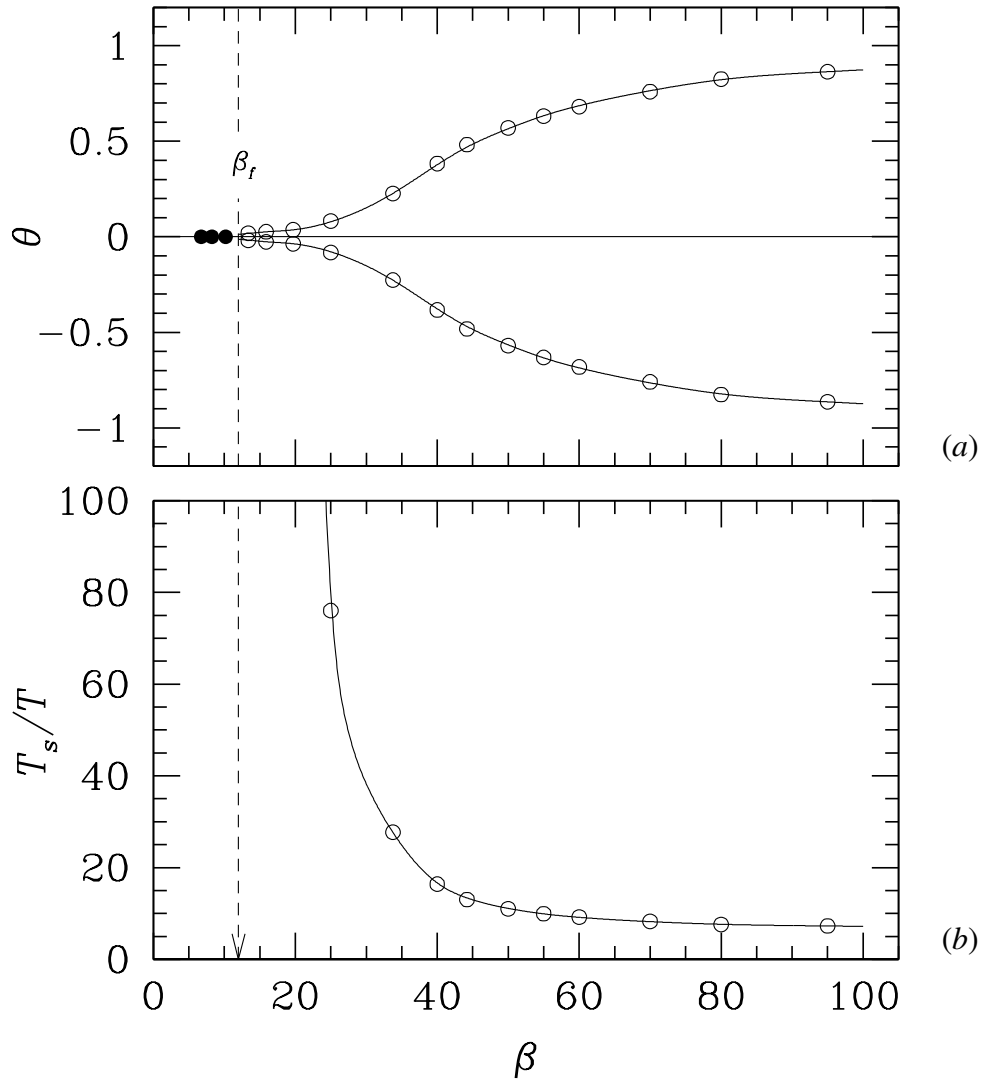


Figure 6.3: Complex multiplier phase angle and secondary period variation along the curve of marginal stability for the primary transition in a two-dimensional subspace. Figure (a) shows the phase angles of the critical multipliers and figure (b) shows the ratios of the corresponding secondary periods T_s to those of the base flows, T , both as functions of β . The dashed lines indicate the approximate position, β_f , at which the critical multiplier switches between real and complex-conjugate pair multipliers.

of an unstable quasi-periodic flow and the experimentally observed synchronous flow that occurs in regime D is addressed.

6.2 Synchronous Regime S

The transition from the symmetrical base state to the synchronous flows of regime S occurs for very low values of β and comparatively high values of KC , as shown in figure 6.1. At a fixed Keulegan–Carpenter number of $KC = 8.0$ the dependence of the critical Floquet multiplier on the Stokes number was determined, as presented in figure 6.4. Examination of this figure shows the dominant unstable multiplier branch to consist of real multipliers that intersects the neutral stability point at $\beta \approx 10.15$.

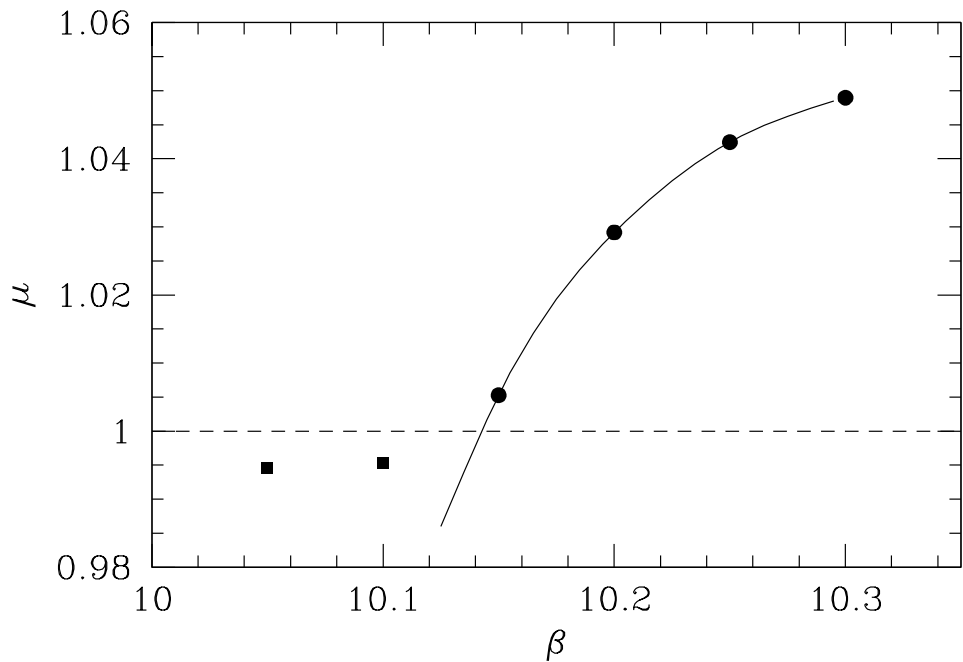


Figure 6.4: Dependence of the Floquet multiplier μ on the value of Stokes number β for a Keulegan–Carpenter number of 8. A critical Floquet multiplier denoting the onset of linear instability is found to lie at $\beta \approx 10.15$. Shown are the real Floquet multipliers, ●, and unity multipliers, ■.

The physical significance of an unstable linear mode with a real Floquet multiplier can be seen by examining the state of the flow after this transition has occurred. A two-dimensional nonlinear simulation, which was evolved from a quiescent fluid and not from the mode shape determined through Floquet analysis, was employed at a location in (KC, β) -space just beyond the predicted point of onset. This simulation was evolved until a final periodic state was achieved. In figure 6.5 a set of eight instantaneous vorticity contours from this simulation are shown over one period of cylinder motion. The distinctive feature that is seen here in comparison to the base flow is the broken symmetry about the oscillation axis. The induced flow now departs the near cylinder region at an angle to the oscillation axis. Consequently the vorticity contours, and by extension, the flow, now form a ‘boomerang’ like shape with the broad apex of this geometry being defined by the

6.2. SYNCHRONOUS REGIME S

amplitude of oscillation. In terms of the equations of symmetry, the spatial symmetry K_x (5.1) is clearly broken by the onset of this instability.

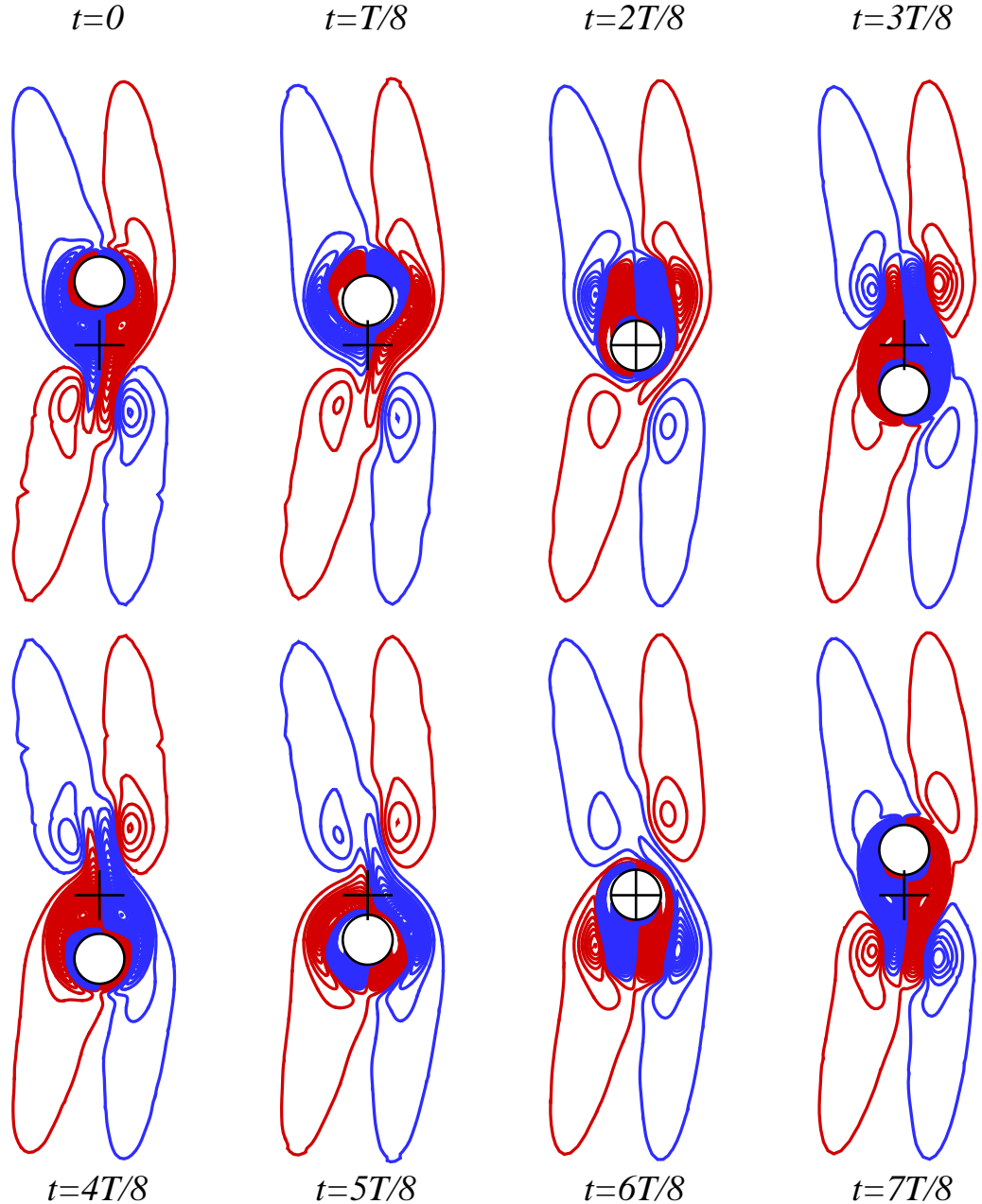


Figure 6.5: A set of instantaneous vorticity contours extracted over one motion period, T , at $KC=8$, $\beta=10.2$. Positive (anti-clockwise) and negative vorticity contours are denoted by red and blue colours respectively. The crosshairs denote the fixed point that the cylinder is oscillating about.

The temporal nature of this flow is established through examination of both the limit cycles and by the forces experienced by the cylinder. In the same manner as shown in chapter 5 for the base flows, the limit cycles for this flow form complete circuits over

6.2. SYNCHRONOUS REGIME S

one period of oscillation. An inspection of the force-time series for the cylinder shows a definite difference from those of the base flows. The force-time series for the coefficient of y -force is barely altered from its state before a transition to regime S occurred, however, the temporal variation of the coefficient of x -force is no longer constant and shows a bi-periodic variation for every cylinder oscillation. Additionally the mean of the coefficient of x -force is no longer zero over an entire period. This is entirely consistent with the broken symmetry in the vorticity contours seen in figure 6.5, which would result in a mean force exerted along the x -axis.

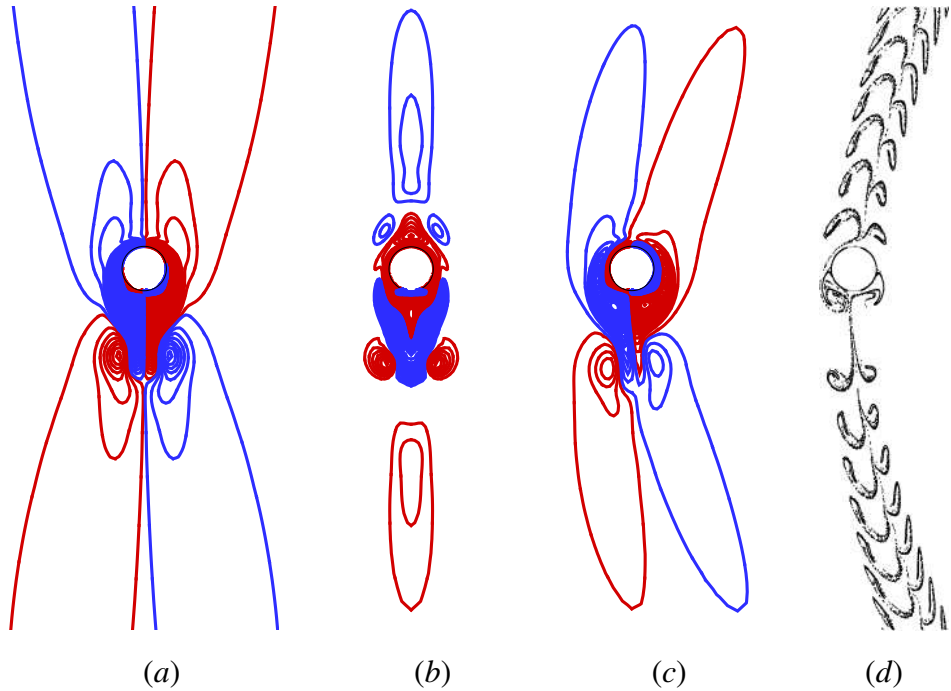


Figure 6.6: Flows of two-dimensional synchronous regime S, computed at ($\beta = 13.75$, $KC = 7$): (a), instantaneous vorticity contours for the basic state, with the cylinder at $y = y_{\max}$; (b), vorticity contours of the Floquet eigenfunction at the same phase of the motion cycle; (c), instantaneous vorticity contours obtained from two-dimensional DNS, again at $y = y_{\max}$; (d), computed positions of massless particles advected from close to the cylinder.

In terms of the symmetry properties it can be concluded that for the resultant flow of an unstable mode, due to a real Floquet multiplier, that both the spatial symmetry K_x (5.1) and the spatio-temporal symmetry H_2 (5.5) are broken, while the other spatio-temporal symmetry, H_1 (5.4), is preserved. In figure 6.6(a) the instantaneous vorticity contours for the base flow at ($KC=7$, $\beta=13.75$) are presented for the time at which the cylinder is at its maximum displacement in the y direction. Figures 6.6(b) and 6.6(c) show the vorticity contours at the same phase of the motion cycle for the Floquet eigenfunction and the resultant DNS flow. Although calculated at a different location in (KC, β)-space to those in figure 6.5 the vorticity contours of the DNS flow in figure 6.6(c) definitely

6.2. SYNCHRONOUS REGIME S

belong to regime S. However, a significant difference exists between these two images. In figure 6.5 the angle of deviation of the flow has occurred towards the $-x$ direction while in figure 6.6(c) it has occurred in the $+x$ direction. Throughout the simulations conducted in regime S the symmetry was found to break in either the $+x$ or $-x$ direction with no apparent preference for either direction. This is not an unexpected result because the base flow is symmetrical about the oscillation axis (K_x symmetry) and consequently a break in either direction is equally probable.

The vorticity eigenfunction of the unstable mode, figure 6.6(b), shows a positive symmetry of the vorticity contours about the y -axis, or equivalently a negated symmetry when considered in velocity variables. The combination of this even K_x symmetry with the odd K_x symmetry of the base flow results in the flows seen in figure 6.6(c) where the K_x symmetry is absent. A change in sign of the Floquet eigenfunction results in the flow breaking to the left, or $-x$ direction, as compared to the right, or $+x$ direction, version seen in 6.6(c). An additional consequence of a left or right handed break is that the sign of the net force in the x -direction changes accordingly.

In figure 6.6(d) an instantaneous image is shown of the computed positions of massless particles released into the flow from near the cylinder surface. Although this image of particles in the flow shows evidence of locally concentrated regions of particles that are possibly suggestive of vortex shedding, the corresponding vorticity contours show no corroborating far-field concentrations of vorticity. The far-field vorticity distribution is quite smooth and of very low magnitude in comparison to near the cylinder where the vorticity is formed. Instead these particle concentrations are formed near the cylinder and then advected away through the action of the induced flow.

An experimental visualisation of regime D in the x - y plane from Tatsuno and Bearman (1990) is shown alongside the computation obtained from two-dimensional DNS in figure 6.7. These match extremely well even though the DNS was conducted in a two-dimensional subspace. Experimental visualisations have detected distinct regular spanwise variations that are not accounted for in the two-dimensional simulations. However, despite the absence of spanwise variations the point of onset of this regime and the dynamics of the flow in the x - y plane match those obtained experimentally. The impact of the spanwise variations will be addressed in chapter 7.

The angle of deviation of the resultant flow in regime S from the axis of oscillation was found to increase with the distance in (KC, β) -space from the point of onset. In figure 6.8 a set of instantaneous vorticity contours of the flow are seen from the point of onset of the synchronous regime at $\beta = 10.10$ up until $\beta = 10.40$ for a fixed $KC = 8$. The angle of deviation is seen to increase with increasing β . The change in the angle of deviation is reflected in the measurement of the x component of force on the cylinder. In figure 6.9 the increase of the peak x -component of force on the cylinder can be seen as the distance in (KC, β) -space from the point of onset is increased. The peak force acts as

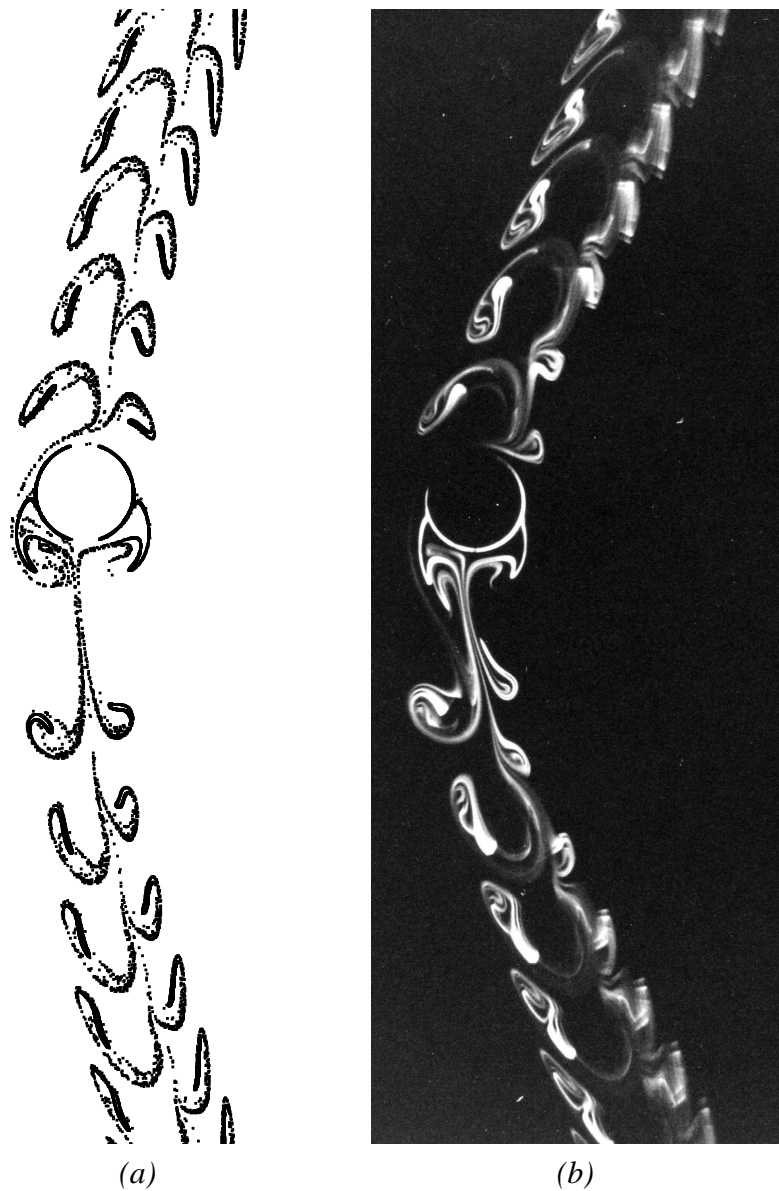


Figure 6.7: Visualisations of flows in regime D: (a) produced by two-dimensional DNS at $KC = 7$, $\beta = 13.75$ with massless particles released close to the cylinder; (b) experimental visualisation produced by electrostatic precipitation at $KC = 6.28$, $\beta = 18.0$. Image supplied by M. Tatsuno and P. Bearman.

a measure of energy in the solution and in this case it is seen to smoothly depart zero with no discontinuity when the onset of this mode occurs. Consequentially this bifurcation is considered to be supercritical. Note also that the value obtained through DNS for the onset of this instability, $\beta \approx 10.15$, matches the value found earlier through the use of Floquet analysis.

6.2. SYNCHRONOUS REGIME S

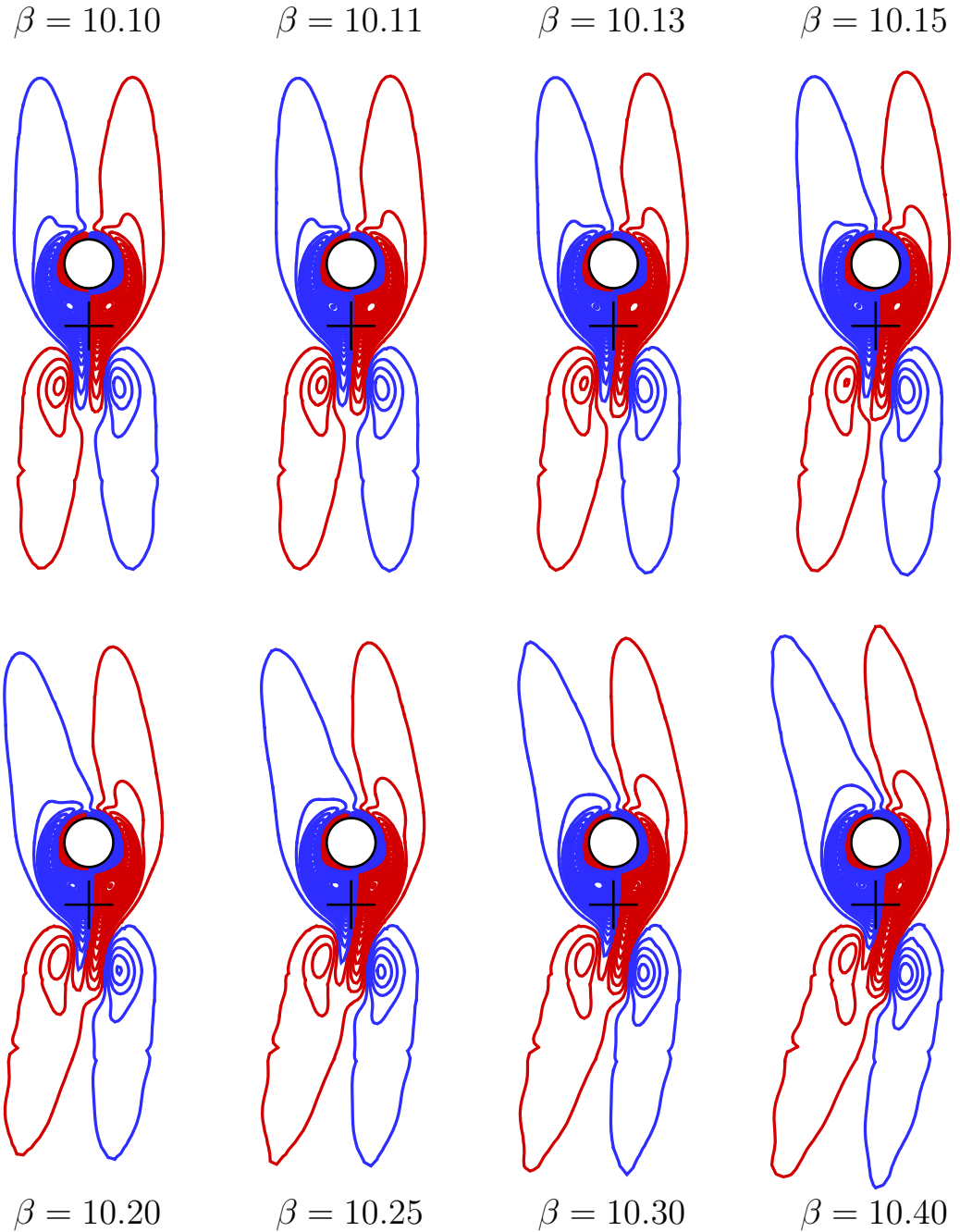


Figure 6.8: The influence of increasing Stokes number on the instantaneous vorticity contours extracted at the peak of the motion cycle for a fixed $KC=8$. With increasing distance in (KC, β) -space from the curve of marginal stability the angle of deviation of the induced flow increases. Positive (anti-clockwise) and negative vorticity contours are denoted by red and blue colours respectively. The crosshairs denote the fixed point that the cylinder is oscillating about.

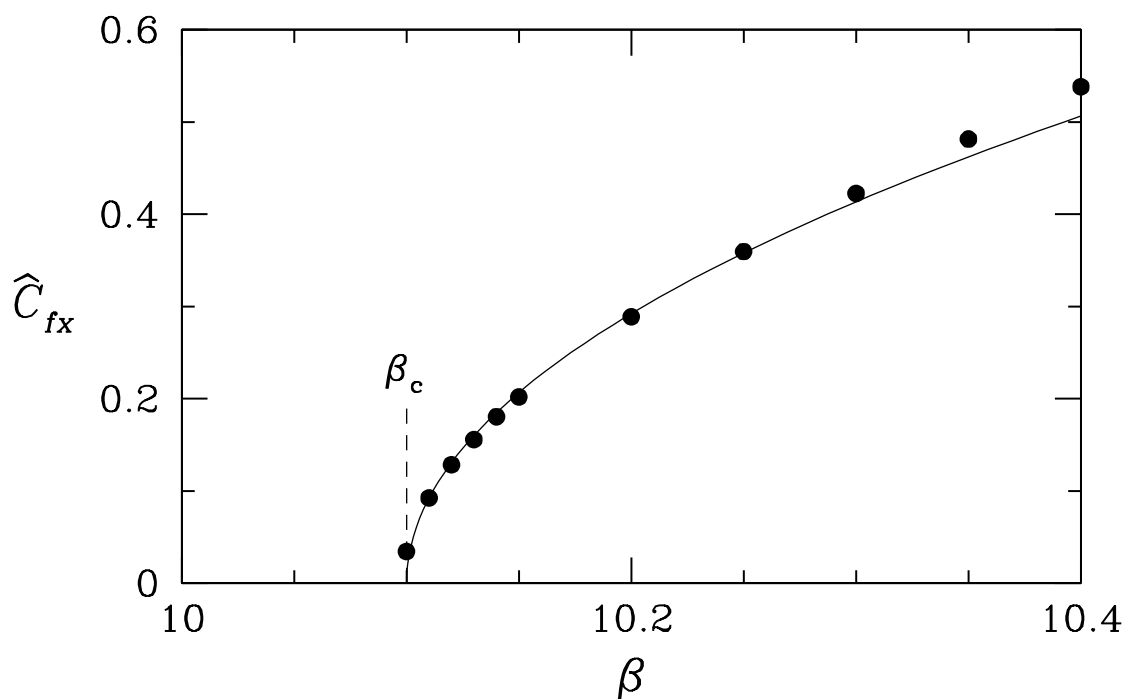


Figure 6.9: Bifurcation diagram for two-dimensional symmetry breaking to regime S at $KC = 8$, showing coefficients of the peak x -component of force as functions of the bifurcation parameter: β . At $\beta = 10.15$ the break in symmetry about the axis of oscillation results in a force component normal to the axis of oscillation.

6.3 Quasi-Periodic Regime QP

The transition from the symmetrical base state to the flows of regime QP are signalled in the Floquet analysis by an unstable mode with a complex-conjugate pair of multipliers. Within the (KC, β) -space considered, shown in figure 6.2, this transition coincides well with the three-dimensional transitions between regimes A to C and B to E. In the following investigation of the transition to the QP regime, two locations that are representative of the transitions $A \rightarrow C$ and $B \rightarrow E$ are focused on. The chosen values of β that are used for this purpose are $\beta = 44.2$ which represents the $A \rightarrow C$ transition and $\beta = 80.0$ which represents the $B \rightarrow E$ transition. For each location the nature of the transition and the resultant flow are examined in detail.

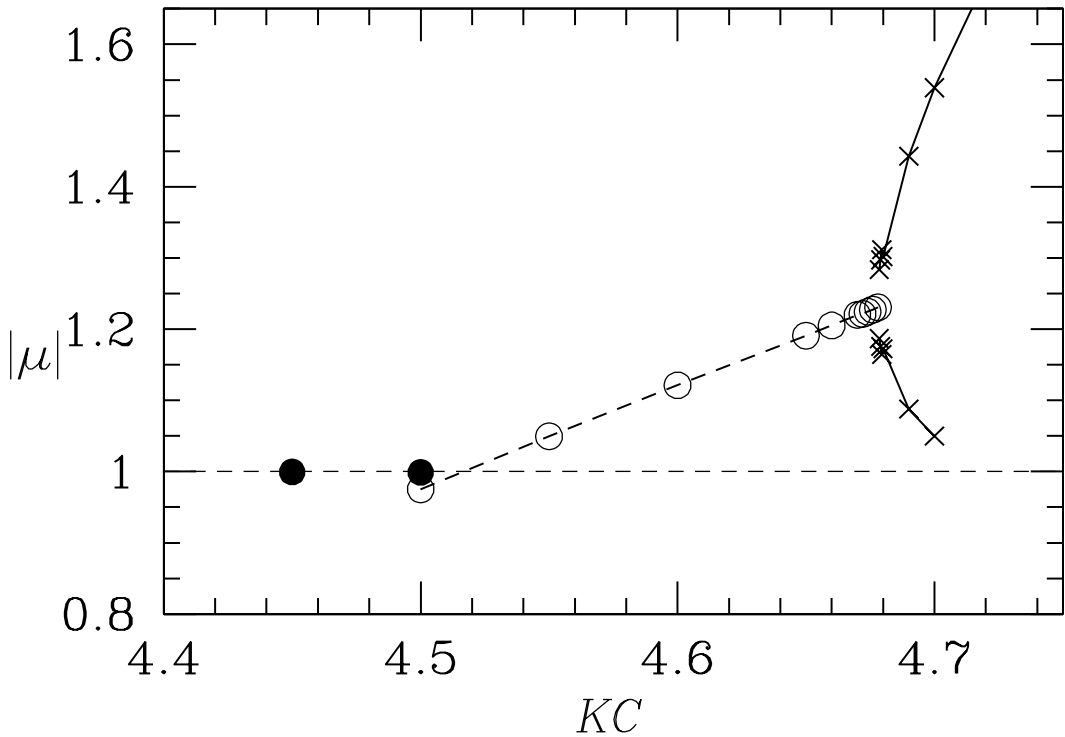


Figure 6.10: Dependence of the Floquet multipliers on KC at $\beta = 44.2$. Shown are the complex-conjugate pairs of multipliers (\circ), real multipliers (\times) and spurious multipliers due to the ‘unity’ multiplier issue, (\bullet), as discussed in §6.1. The critical value at which the complex-conjugate locus crosses the unit circle at $|\mu| = 1.0$ is $KC = 4.515$.

The dependence of the Floquet multiplier on KC at $\beta=44.2$ is shown in figure 6.10. At a critical value of $KC \approx 4.515$ a complex-conjugate pair of multipliers crosses the curve of neutral stability. At values of KC less than this critical value the ‘unity’ multiplier, as discussed in §6.1, is present which makes it difficult to determine values of the complex-conjugate branch of multipliers that have not crossed the unit circle, $|\mu| < 1$. After crossing through neutral stability the complex-conjugate pair of multipliers increases in

6.3. QUASI-PERIODIC REGIME QP

magnitude until a value of $KC = 4.78$ is reached. At which point the complex-conjugate pair of multipliers ceases to exist and two branches of real multipliers are detected. Further increasing KC beyond $KC = 4.78$ causes one of these branches to rapidly drop below the neutral stability curve while the other branch increases. The dependence of the phase angle of the complex-conjugate multipliers on KC is shown in figure 6.11. At the point of marginal stability ($KC \approx 4.515$) the phase angle is approximately 0.5. As KC is increased the phase angle decreases until it reaches zero at the same point that the complex-conjugate multipliers cease to exist and the pair of real multiplier branches form.

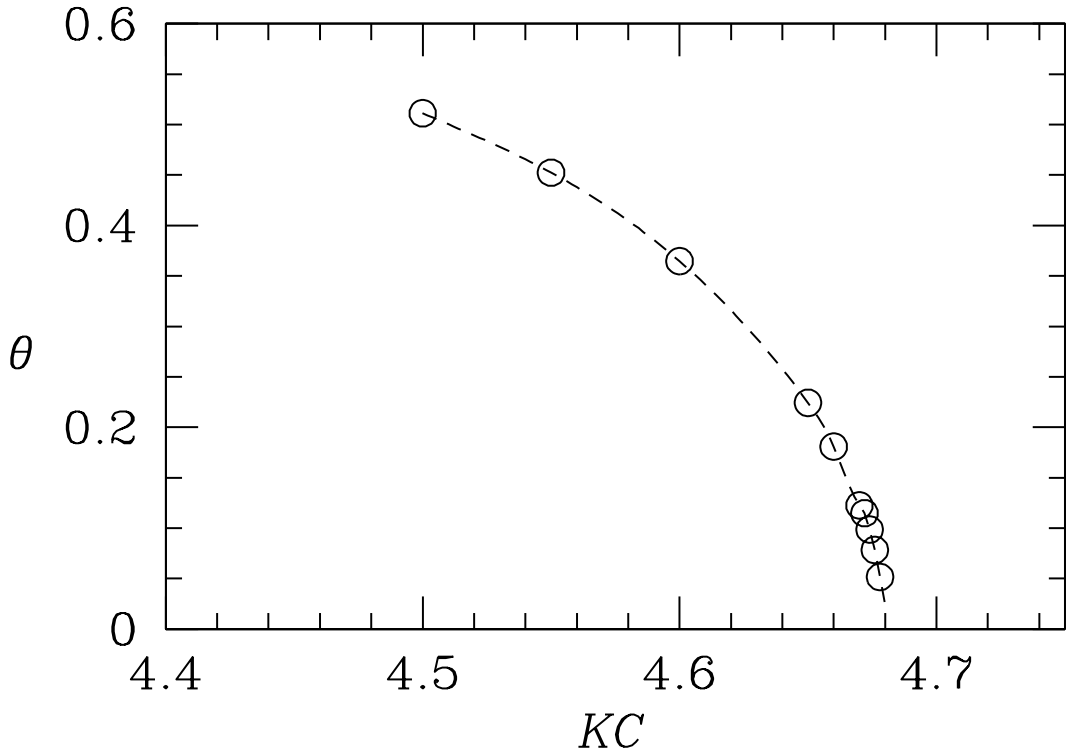


Figure 6.11: Dependence of the phase angle of the complex-conjugate pair of Floquet multipliers (\circ) on KC at $\beta = 44.2$. The critical value at which the complex-conjugate locus crosses the unit circle at $|\mu| = 1.0$ is $KC = 4.515$ with $\theta \approx 0.5$.

The dependence of the Floquet multiplier on KC at $\beta=80.0$ is shown in figure 6.12. An identical behaviour to that seen at $\beta=44.2$ is observed to occur, although for this case the critical value at which the complex-conjugate pair of multipliers branch crosses the curve of neutral stability is $KC = 3.815$. After crossing the curve of marginal stability subsequent increases in the value of KC correspond to a linear increase in the magnitude of the complex-conjugate pair multiplier branch. At the same time the phase angle of the complex-conjugate multipliers decreases, although not in a linear fashion, as shown in figure 6.13. In both cases the physical significance of the subsequent bifurcation of

6.3. QUASI-PERIODIC REGIME QP

the complex-conjugate multipliers to a set of real branches is unknown. Critically the use of Floquet analysis is predicated on determining the first critical linear instability to a known periodic base flow. In this case the onset of a mode with a complex-conjugate pair of multipliers and the associated secondary period means that the underlying flow may no longer be periodic and/or symmetric. Consequently the condition under which the bifurcation from the complex-conjugate branch to the pair of real branches occurs may no longer exist as the unstable mode will have perturbed the periodic base flow. This issue is further investigated in §6.4 when secondary transitions are examined.

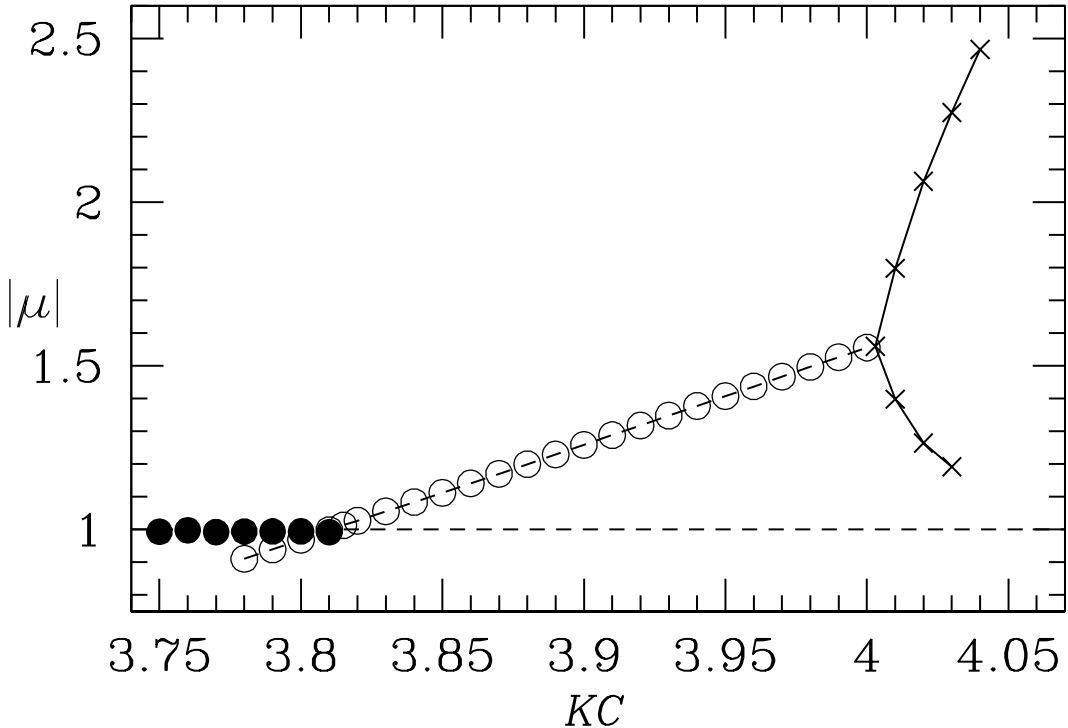


Figure 6.12: Dependence of the Floquet multipliers on KC at $\beta = 80.0$. Shown are the complex-conjugate pairs of multipliers (\circ), real multipliers (\times) and spurious multipliers due to the ‘unity’ multiplier issue, (\bullet). The critical value at which the complex-conjugate locus crosses the unit circle at $|\mu| = 1.0$ is $KC = 3.815$.

The temporal impact of a complex-conjugate pair of multipliers can be detected through an examination of the forces experienced by the cylinder. In figures 6.14 and 6.15 the x -component force-time series over two hundred and fifty periods of oscillation are presented for the $\beta = 44.2$ and $\beta = 80.0$ cases respectively. The impact of the secondary period introduced by the complex-conjugate pair of multipliers is clearly visible in the time series of coefficient of x -component force experienced by the cylinder. No longer is it constant over an entire period but it is now seen to vary with a period that is incommensurate with the oscillation period of the cylinder. The time series of the coefficient of y -component force shows no visible influence of the secondary period. However, there

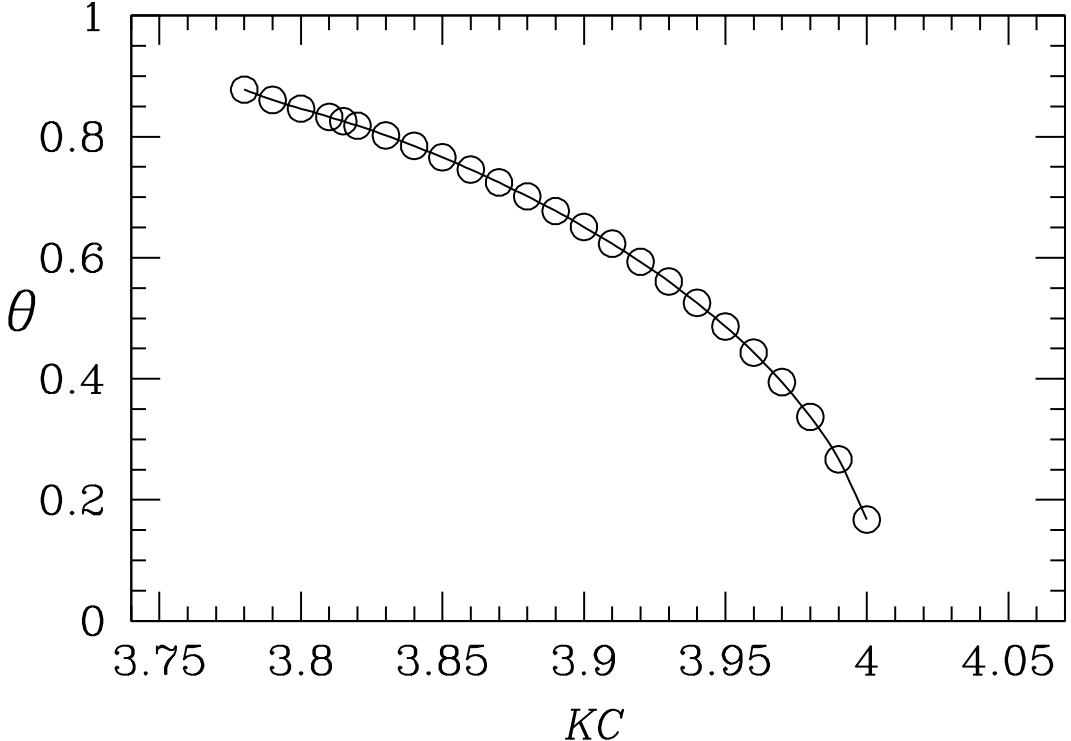


Figure 6.13: Dependence of the phase angle of the complex-conjugate pair of Floquet multipliers on KC at $\beta = 80.0$. The critical value at which the complex-conjugate locus crosses $|\mu| = 1.0$ is $KC = 3.815$ with $\theta \approx 0.82$.

is an order of magnitude difference between the peak x and y forces experienced by the cylinder. This would explain why the secondary period is not visible in the time series of the y force because the variation caused by the new mode is much less than the forces generated in the symmetric stable mode. The secondary period in both of the cases presented is $T_s \approx 13.8T$ and $T_s \approx 7.9T$ for the $\beta = 44.2$ and $\beta = 80.0$ cases respectively. As the critical curve is traversed from the ‘freezing point’ towards $\beta \rightarrow 100$ the secondary period is found to decrease which is a result of the increasing phase angle of the complex-conjugate pair of multipliers which increases as $\beta \rightarrow 100$ (see figure 6.3). Exact determination of the secondary period found in the DNS requires a spectral analysis and consequently long simulations in order to provide enough data to the FFT. This is computationally expensive and was only performed for one transition, the results of which are shown later.

In figures 6.16 and 6.17 a set of instantaneous vorticity contours are displayed at eight points in time over one motion cycle for $\beta = 44.2$ and $\beta = 80.0$ respectively. These are at different points in the (KC, β) -space and as a consequence they have different secondary periods present. However, it can be seen that they are very similar and belong to the same flow regime: QP. In both of these figures evidence of vortex shedding is clear with the presence of far field concentrations of vorticity clearly visible. It is therefore concluded

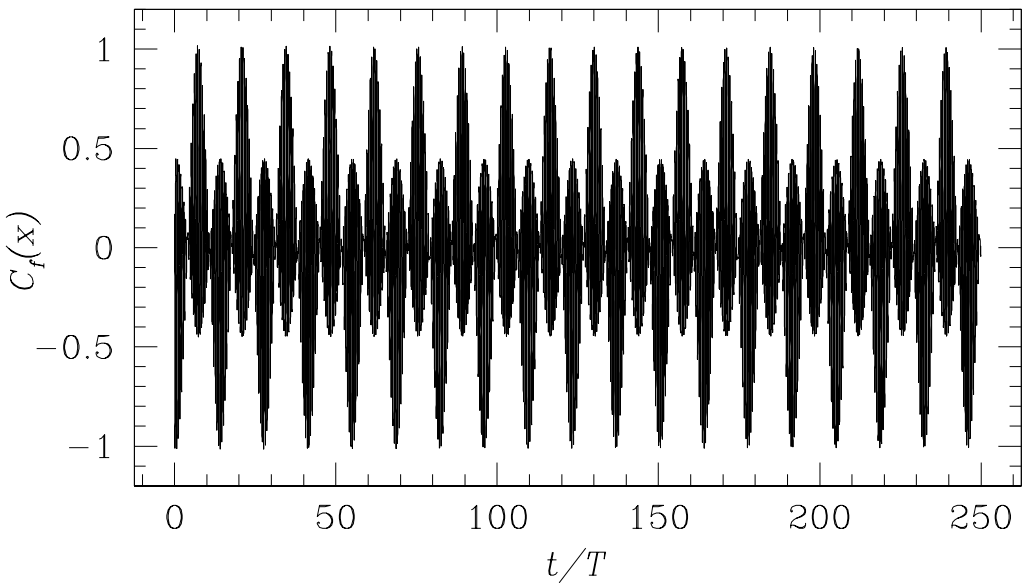


Figure 6.14: Plot of the coefficient of total x -force exerted on the cylinder over two hundred and fifty periods of motion. The simulation was carried out at $KC=4.55$, $\beta=44.2$. The force is non-dimensionalised with respect to the root mean square of the cylinders prescribed y -axis velocity and the cylinder diameter, D .

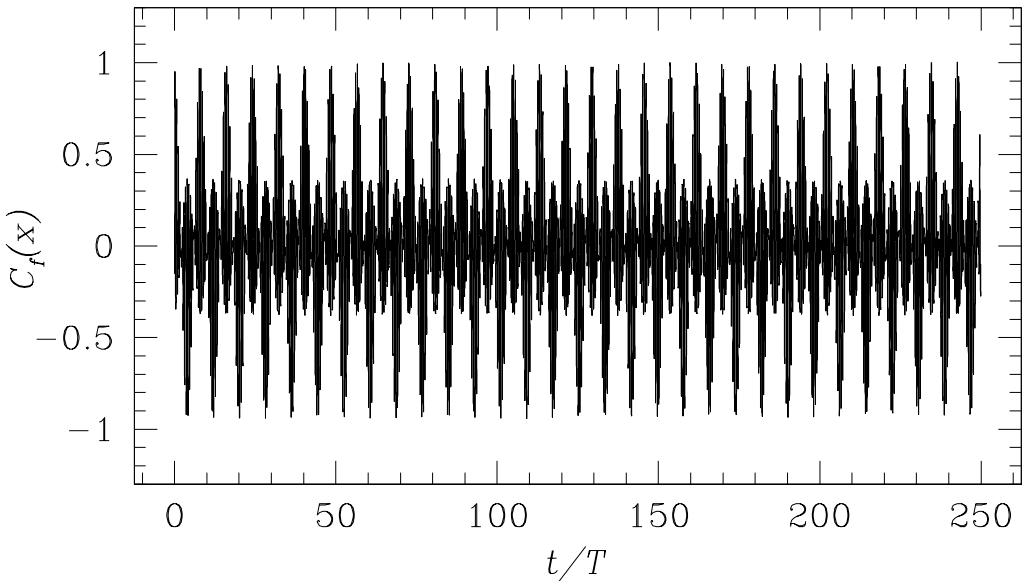


Figure 6.15: Plot of the coefficient of total x -force exerted on the cylinder over two hundred and fifty periods of motion. The simulation was carried out at $KC=3.85$, $\beta=80.0$. The force is non-dimensionalised with respect to the root mean square of the cylinders prescribed y -axis velocity and the cylinder diameter, D .

that at the onset of this regime there is no difference in the restricted two-dimensional subspace between the transitions $A \rightarrow C$ and $B \rightarrow E$ and in the flows that result near this

6.3. QUASI-PERIODIC REGIME QP

transition boundary. Both cases also indicate the presence of vortex shedding. The only aspect that differs is the secondary period introduced into this flow by the bifurcation, which varies along the critical curve. In terms of the symmetry properties present in the base symmetric state, that of K_x , H_1 and H_2 , all three symmetries are seen to be broken. A cursory inspection of these plots would suggest that perhaps the symmetry H_1 is present, however, this is not the case and this is explained in greater detail in subsequent paragraphs when the impact of the secondary period T_s is discussed.

The secondary period T_s has been mentioned previously in this text, however until now, only limited comments have been made in regard to its variation with the control parameters away from the marginal stability boundary. From the linear Floquet analysis the phase angle of the complex-conjugate pair of multipliers are obtained, which can then be related to the secondary period introduced into the flow, as described in (6.1). It must be emphasised that this is the linear prediction of what occurs. To determine the nonlinear response to the onset of an unstable quasi-periodic mode, two-dimensional DNS was employed to obtain a time series of the coefficient of x force over a very long period of time. A FFT was then applied to this force history to obtain the dominant frequencies. In figure 6.18 a comparison between these two sources of data is presented. Near the point of the instability onset, both the nonlinear and linear methods agree on the secondary period. Increasing KC beyond this point results in the value predicted by Floquet analysis increasing exponentially such that as the phase angle approaches zero, $T_s \rightarrow \infty$. However over the same range of KC , and even beyond the point at which the complex-conjugate pair of multipliers phase angle ceases to exist, the secondary period determined from DNS remains finite and shows only a mild increase in relation to its value at the onset of regime QP. It is concluded that the coalescence of the complex-conjugate pair of multipliers has no physical significance in the restricted two-dimensional subspace and that the prediction of the Floquet analysis is accurate at the onset of an instability mode.

Figure 6.19 shows instantaneous vorticity contours for two-dimensional saturated DNS at ($KC = 4.7$, $\beta = 40$), at eight phase points equi-spaced over the secondary period T_s . In contrast with a conventional planar Kármán wake, the signs of rotation associated with concentrations of vorticity are reversed, instead a pair of phase-locked Kármán-street planar jets are seen. A single vortex pair is shown to be shed from the attached jets, both above and below the cylinder, for each secondary period. These shed vortices are convected away from the cylinder by the induced flow. Additionally the angle of deviation from the oscillation axis of the upper and lower jets cycles from $+x$ to $-x$ and back again once for each secondary period. It is for this reason that this flow breaks the H_1 symmetry because the wake oscillates with the secondary period and the vortices are shed at the secondary period and not the oscillation period.

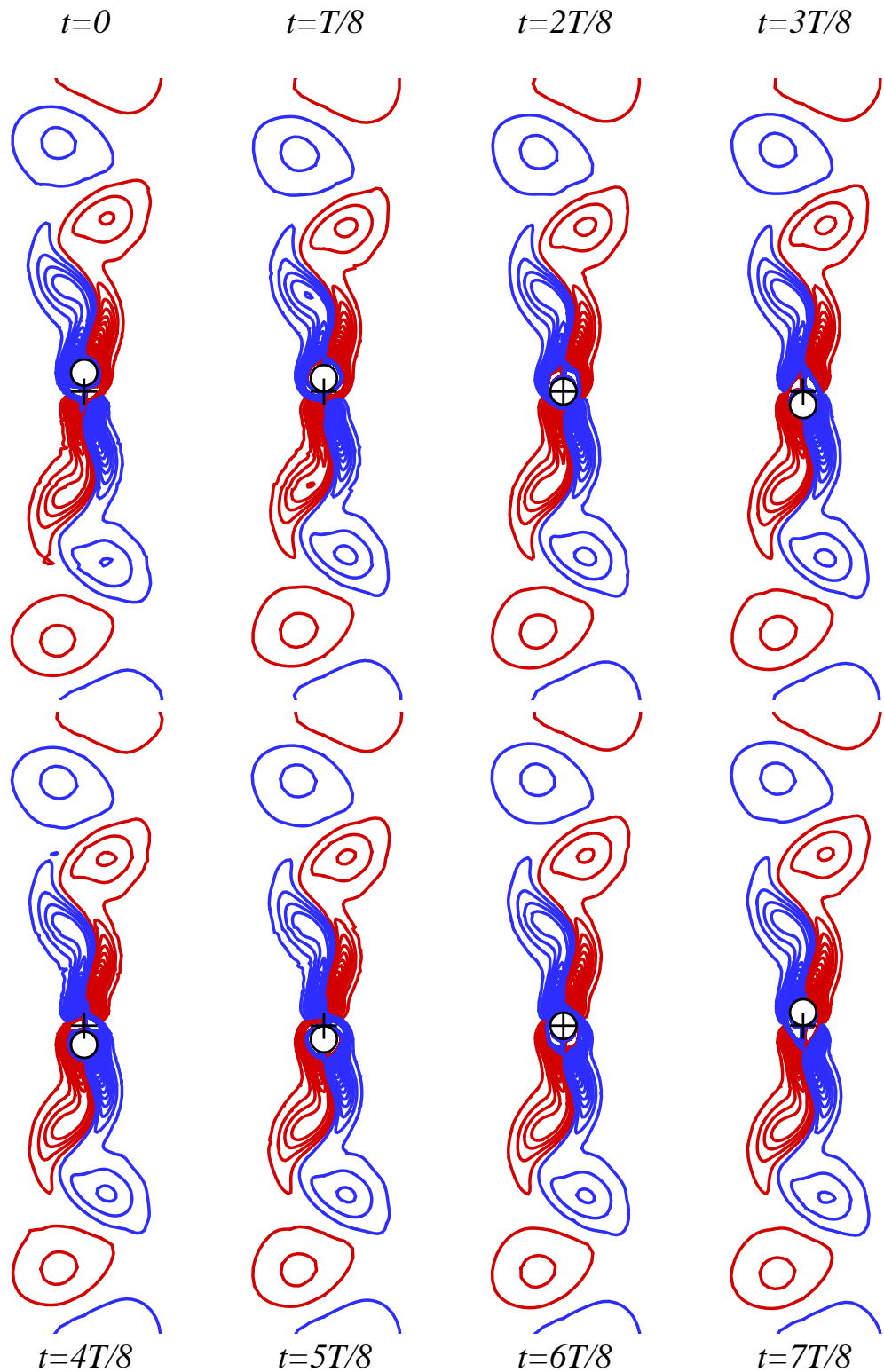


Figure 6.16: A set of instantaneous vorticity contours extracted over one motion period, T , at $(KC=4.55, \beta=44.2)$. Positive (anti-clockwise) and negative vorticity contours are denoted by red and blue colours respectively. The crosshairs denote the fixed point that the cylinder is oscillating about.

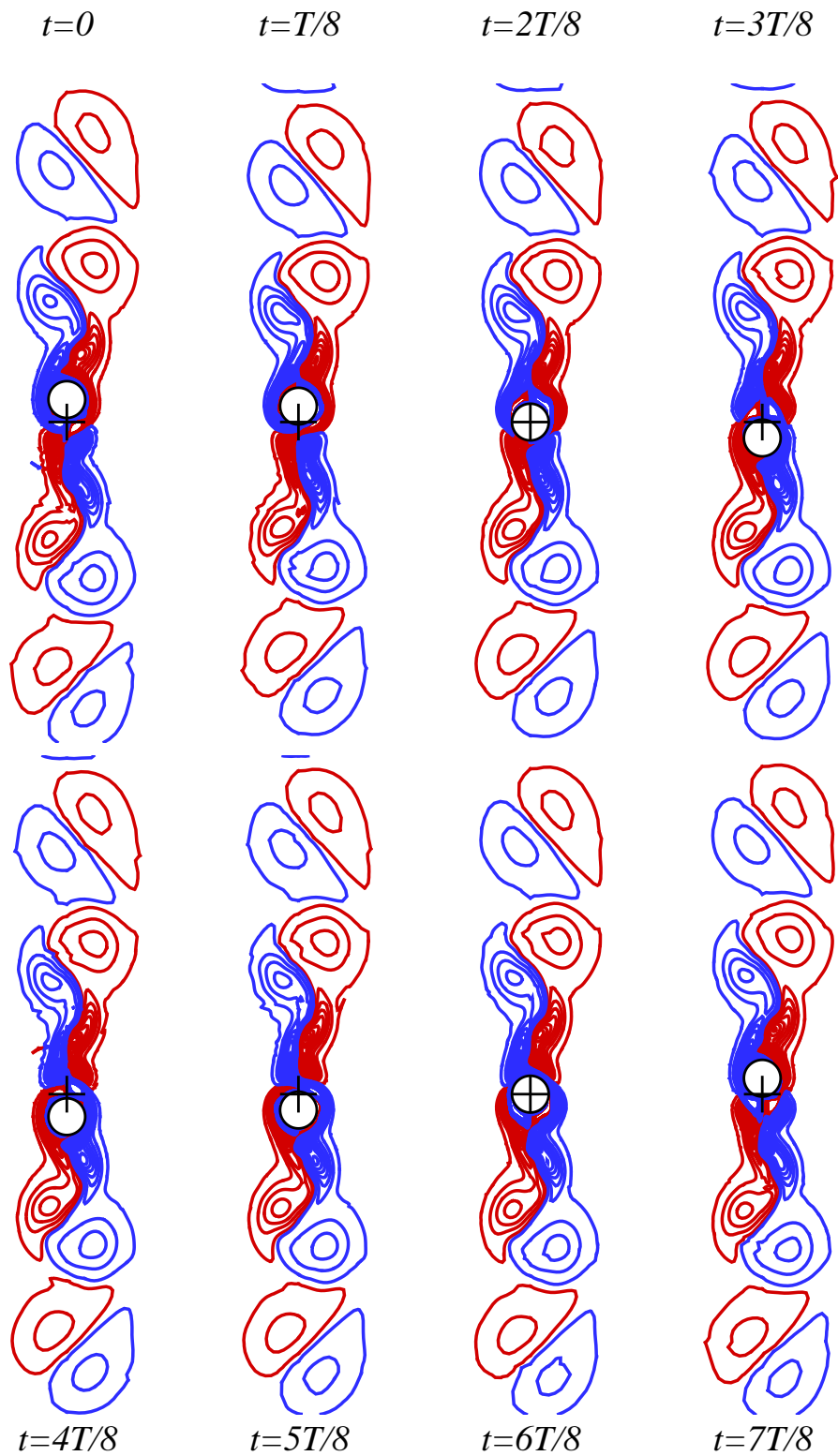


Figure 6.17: A set of instantaneous vorticity contours extracted over one motion period, T , at ($KC=3.85$, $\beta=80.0$). Positive (anti-clockwise) and negative vorticity contours are denoted by red and blue colours respectively. The crosshairs denote the fixed point that the cylinder is oscillating about.

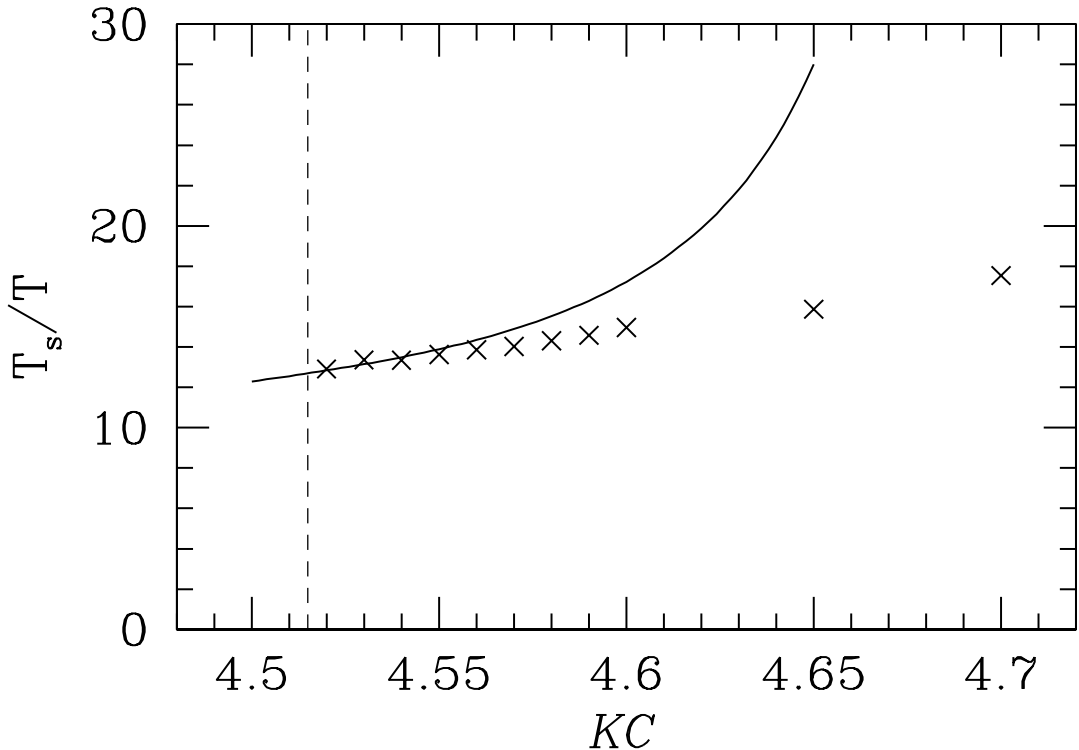


Figure 6.18: Comparison of the secondary period, T_s/T , obtained from the phase angle of a pair of complex-conjugate Floquet multipliers (—), with the secondary period obtained via two-dimensional DNS (×). Simulations were conducted for a fixed $\beta = 44.2$. The dashed line represents the critical KC number for stability.

In figure 6.20 instantaneous vorticity contours are shown for the base flow, the real and imaginary parts of the critical Floquet eigenfunction and for the saturated DNS. Also shown is particle tracking image at the same location. All are presented at the instant when the cylinder is at its maximum y displacement for ($KC = 4.7, \beta = 40$). The base flow and the eigenfunctions have the same symmetries as the case presented earlier with the real multiplier (see figure 6.6). As before the eigenfunctions have an even reflection symmetry about $x = 0$ in comparison to the base flow with its odd reflection symmetry about $x = 0$ (K_x). The eigenfunctions vorticity fields are normalised to the same energy level in both cases and the contouring levels are identical. The difference between the two eigenfunctions are subtle but are present, one such example can be seen just above the cylinder in the second eigenfunction where a region of negative vorticity has formed that is not present in the first eigenfunction. The real and imaginary components are related and one can be obtained from the other by evolution, at $|\mu| = 1$, with the linearised Navier–Stokes equations through a suitable fraction of the secondary period. e.g the imaginary eigenfunction can be obtained from the real component by evolution through $T_s/4$ as described in Blackburn and Lopez (2003). The presence of both real and imaginary eigenfunctions enables the construction of real Floquet modes that have an arbitrary starting phase with

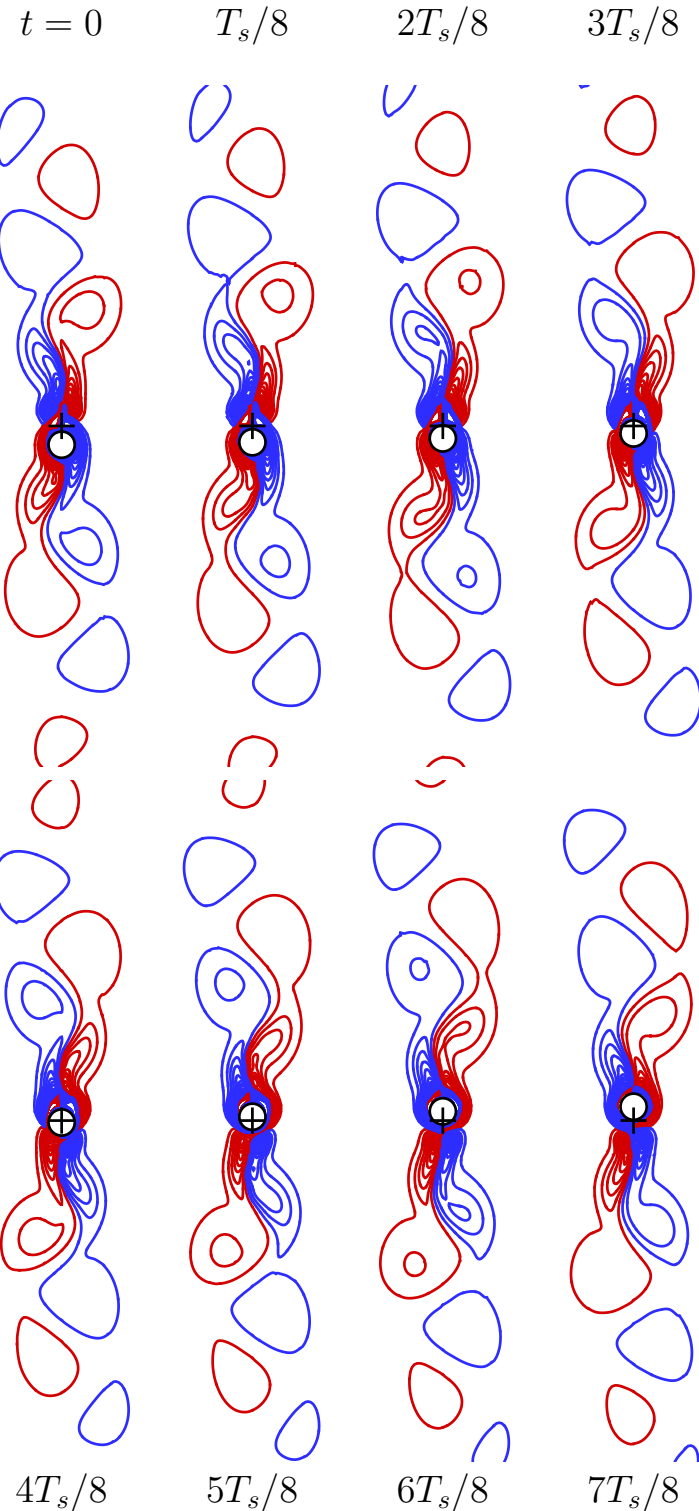


Figure 6.19: A set of instantaneous vorticity contours for the quasi-periodic two-dimensional flow of regime QP, computed at ($KC = 4.7$, $\beta = 40$), where $T_s/T = 15.6$, at eight phases of the secondary period T_s . Positive (anti-clockwise) and negative vorticity contours are denoted by red and blue colours respectively. The crosshairs denote the fixed point that the cylinder is oscillating about.

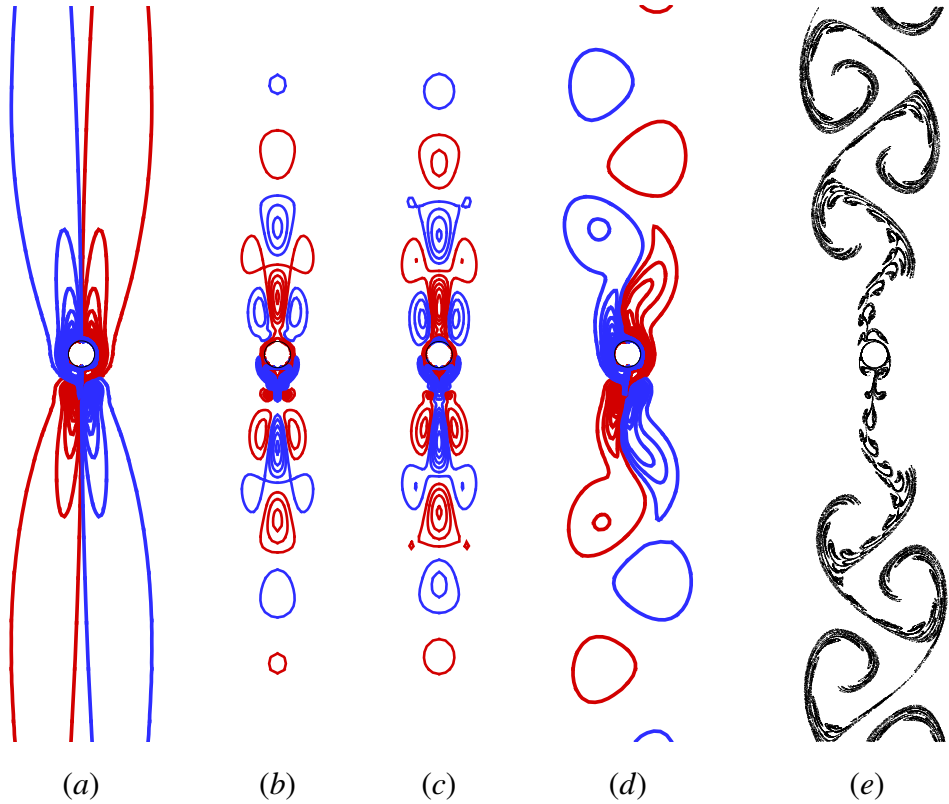


Figure 6.20: Flows of two-dimensional quasi-periodic regime QP, computed at ($KC = 4.7$, $\beta = 40$): (a), instantaneous vorticity contours for the basic state, with the cylinder at $y = y_{\max}$; (b, c), vorticity contours of the real and imaginary parts of the Floquet eigenfunction at the same phase of the motion cycle; (d), instantaneous vorticity contours obtained from two-dimensional DNS, again at $y = y_{\max}$; (e), computed positions of massless particles advected from close to the cylinder.

respect to the base flow, as required by the quasi-periodic nature of the flows.

In figure 6.20(d) the vorticity contours from the saturated DNS show the presence of far field concentrations of vorticity and indicate the presence of vorticity shedding. An image of structures formed by particle tracking is shown in figure 6.20(e). The relationship between the vorticity concentrations and the particle locations is clearly evident when these two figures are compared. At a number of diameters from the cylinder the small scale puffs of particles shed with the frequency of oscillation form into larger scale structures. The period of formation of these larger structures is that of the secondary period, T_s . In figure 6.21 the same image of particle tracking is again presented, although now it has been scaled and rotated 180° about the cylinder axis so that it has the same orientation as the experimental visualisation of Tatsuno and Bearman's image of regime C. Despite being produced at slightly different locations in (KC, β) -space the images are clearly very similar. This is remarkable given that the numerical image was produced in a restricted two-dimensional subspace and the experimental image is produced in a regime that shows quite clear and definite spanwise variations that do not appear to be regular along the span.

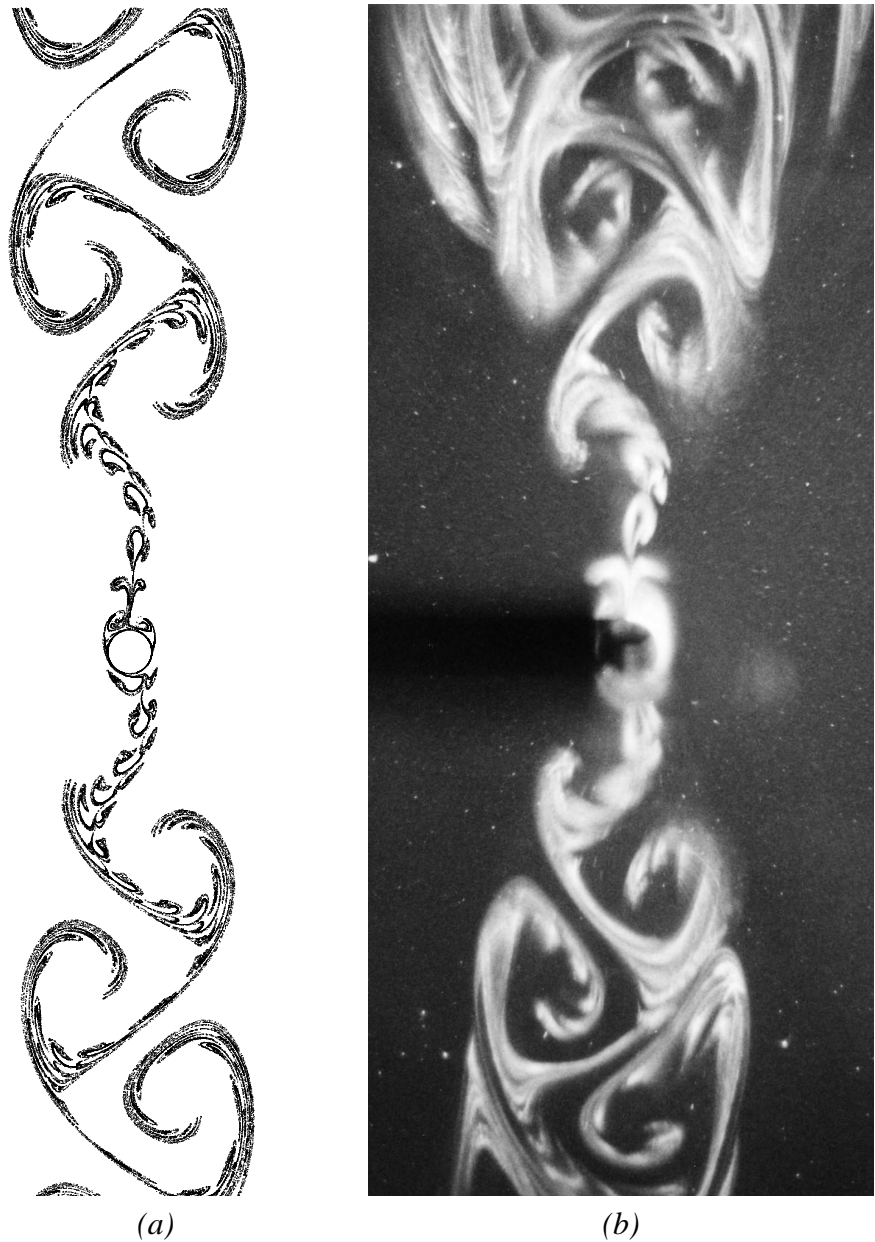


Figure 6.21: Visualisations of flow: (a) produced by two-dimensional DNS at ($KC = 4.7$, $\beta = 40.0$) in regime QP with massless particles released close to the cylinder; (b) experimental visualisation produced by electrostatic precipitation at ($KC = 4.4$, $\beta = 44.2$) in regime C. Image supplied by M. Tatsuno and P. Bearman.

The nonlinear property of this bifurcation can be determined from figure 6.22. In this figure the β control parameter has been held fixed at $\beta = 80$ while KC has been varied across a parameter range that includes the point of marginal stability. As for the synchronous regime S, the measure of energy, the peak coefficient of x -force, increases smoothly from zero with no discontinuity as the critical bifurcation parameter is passed. It is concluded that this transition is supercritical.

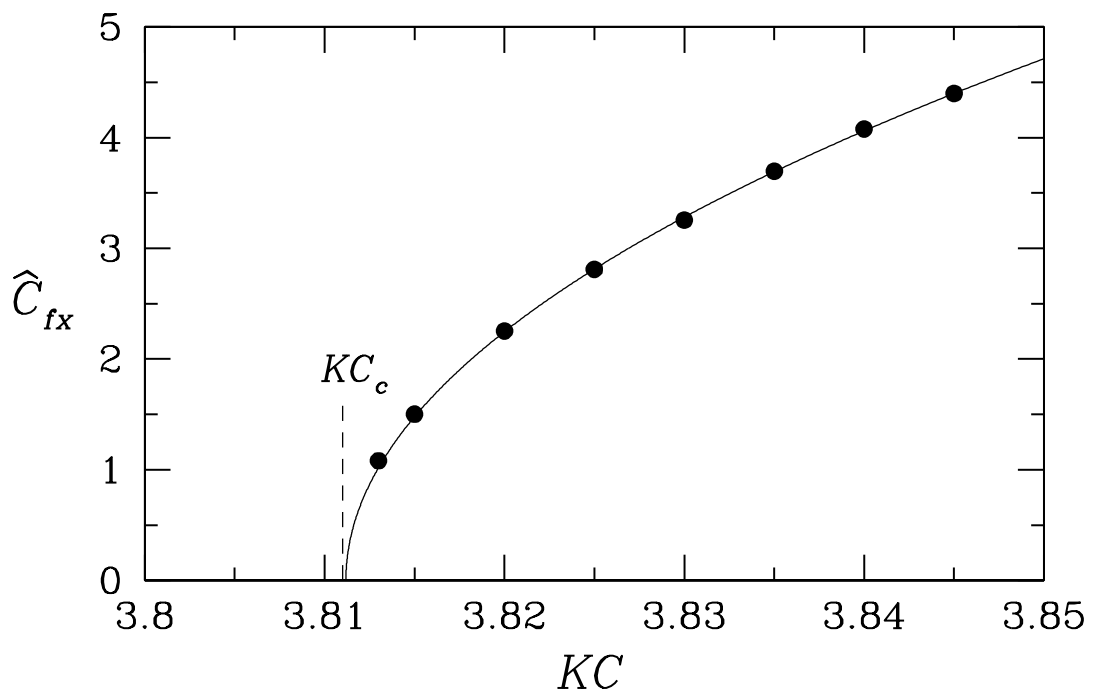


Figure 6.22: Bifurcation diagram for two-dimensional symmetry breaking to regime QP at a fixed $\beta = 80.0$, showing coefficients of peak x -component force as functions of the bifurcation parameter: β .

6.4 Secondary Transitions beyond Criticality

Transitions that occur above the curve of marginal stability in (KC, β) -space are not the primary focus of this investigation. Also it should be emphasised that the Floquet predictions of the S and QP regimes only holds on the marginal stability curve. However it is clear from the DNS results presented previously these regimes exist beyond the marginal stability curve and that the extent of the regimes S and QP are bounded e.g. the behaviour at $KC = 7$ where two-dimensional Floquet analysis predicts a quasi-periodic flow yet experimental visualisations show a synchronous flow. In addition the complex-conjugate multiplier has been shown to only exist over a short range of KC before it coalesces and forms two real branches of multipliers, one decreasing and the other increasing, yet, as noted in §6.3, two-dimensional DNS flows above this coalescence point belong to the quasi-periodic regime. At the other end of the parameter range considered, $KC \rightarrow 10$, Tatsuno and Bearman (1990) have shown a second form of synchronous flow, regime F, where possibly the symmetry H_1 is broken yet H_2 is not. In the examination of the extent of these regimes it would be convenient to use Floquet analysis to identify the locations in (KC, β) -space of secondary transitions. However, this is not possible for a number of reasons. Firstly a periodic base flow is required to use Floquet analysis and this is not achievable with the flows of regime QP. Secondly the ‘unity’ multiplier issue forces the search for a marginal stability curve to occur above the point of transition. In the case of regime S this means a synchronous flow with broken K_x symmetry must be enforced beyond any secondary transition, something that is not feasible at present as there is no reflection symmetry about $x = 0$. In the following section the extent of the regimes S and QP are considered and the boundary between these two regimes is examined using two-dimensional DNS.

In figure 6.23 a set of time series of coefficients of force in the x direction are shown for simulations started from rest. These results were produced at $KC = 7.0$, with Stokes numbers $\beta = 13.5 - 13.75$. In the plot of marginal two-dimensional stability, figure 6.1, the fixed value of $KC = 7.0$ intercepts the neutral stability curve below the freezing point, consequently quasi-periodic behaviour would be expected near this point of onset. However, according to the regime map of Tatsuno and Bearman (1990, see figure 2.16) these parameters all lie within the synchronous regime D, with reported extent from $\beta \approx 13$ to $\beta \approx 20$ at $KC = 7$. In contrast, the two-dimensional DNS result at $\beta = 13.5$ in figure 6.23(a) is clearly quasi-periodic with $T_s/T \approx 200$. A slight increase in the Stokes number to between $\beta = 13.75$ and $\beta = 15$ results in flows that belong to the synchronous regime S. Subsequent increases in β beyond $\beta = 13.75$ lead to flows that demonstrate irregular switching of the angle of deviation of the flow about the oscillation axis from $+x$ to $-x$. This behaviour has been reported to be a characteristic of regime E, for example, and is one that is clearly not a characteristic of regimes S or QP.

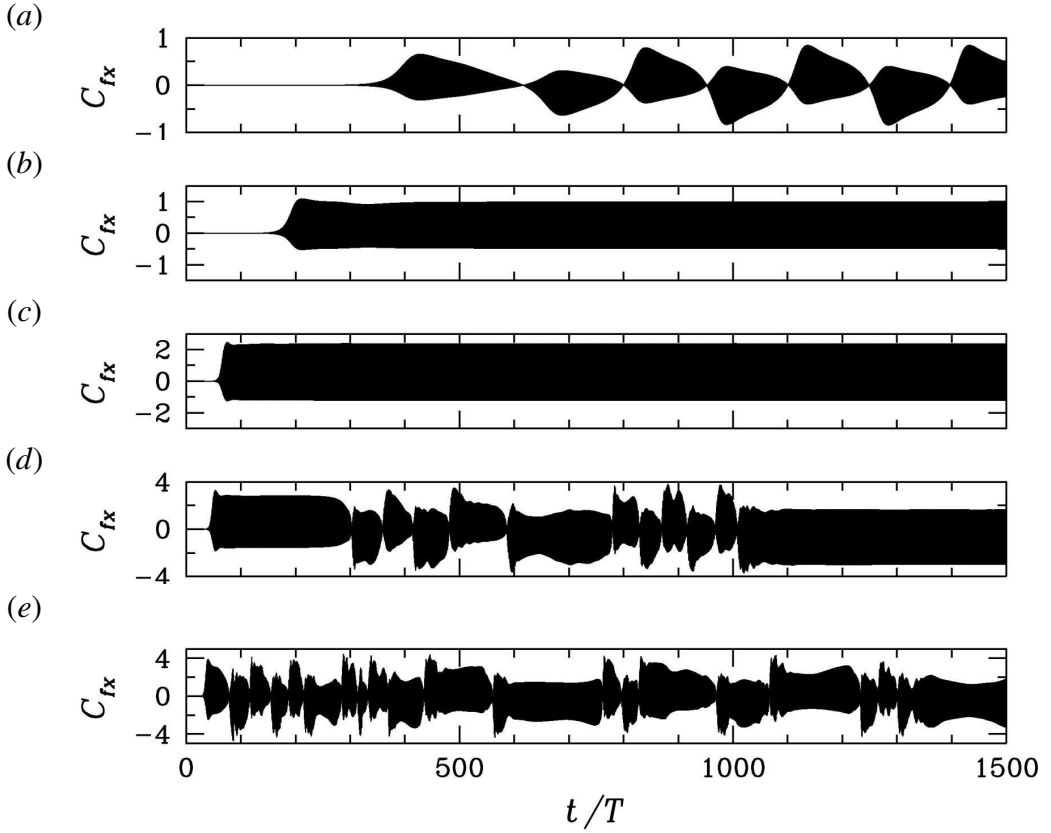


Figure 6.23: Time series of coefficients of force normal to oscillation axis for two-dimensional flows at $KC = 7$. (a), $\beta = 13.5$; (b), $\beta = 13.75$; (c), $\beta = 15$; (d), $\beta = 16$; (e), $\beta = 17.5$.

In the following paragraphs a number of locations in (KC, β) -space are examined as examples of what can occur at a distance in (KC, β) -space from the marginal stability curve. No attempt has been made to accurately determine a set of boundaries for the onset of flows of these types. The points considered are indicated in figure 6.24 by a \times symbol. The extent of regime S for increasing Stokes numbers is bounded by either the formation of a quasi-periodic type mode with intermittent switching (see figure 6.23) or, at higher Keulegan–Carpenter numbers by a flow state that breaks the H_1 symmetry. Figure 6.25 shows the instantaneous vorticity contours for two-dimensional DNS at $(KC = 8, \beta = 25.0)$ and $(KC = 10, \beta = 20.0)$ at the maximum displacement of the cylinder. In both cases two jets of vortices are formed above and below the cylinder. The axis of the convection of these jets is displaced horizontally from the axis of oscillation. The orientation of the jets above and below the cylinder is similar but not identical. In the two cases shown the far field orientation of these jets is different in each case. It is this aspect that would suggest that the symmetry property H_2 does not apply. The jets also appear to be composed of localised concentrations of vorticity which would suggest that vorticity shedding is occurring here, an aspect not present in regime S.

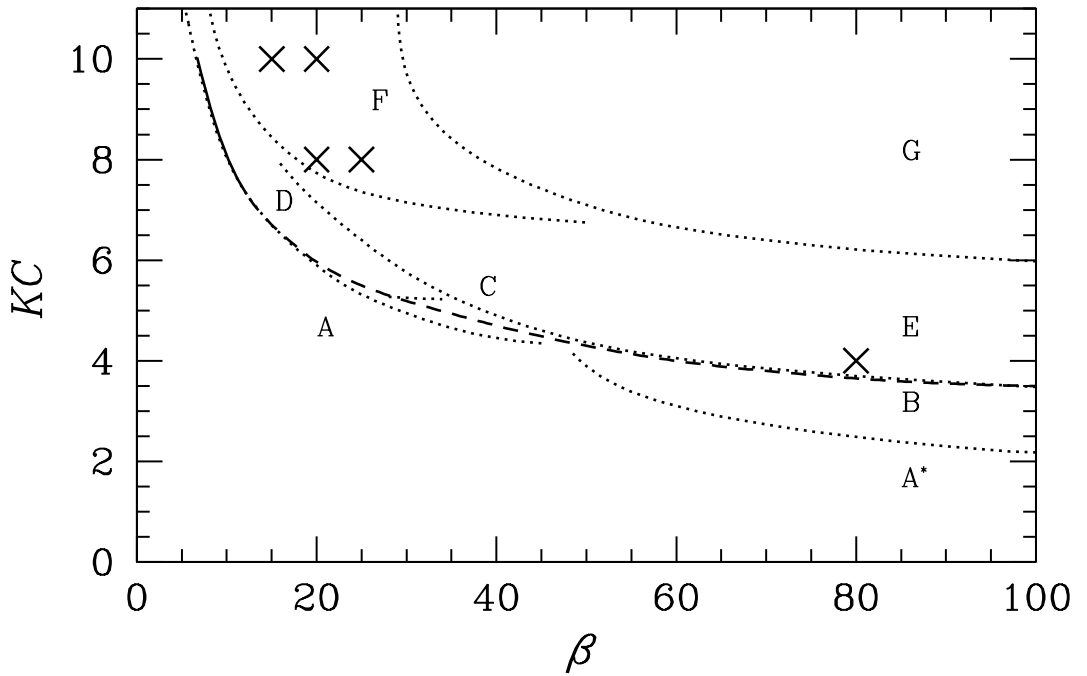


Figure 6.24: (KC, β) -space map showing the two-dimensional marginal stability curves for real (—) and complex-conjugate (- -) multipliers. Also shown are a selection of boundaries and regimes from Tatuno and Bearman (1990). Point marked with an \times indicate a location discussed in §6.4.

Figure 6.26 shows four time series of the x -component of force on the cylinder for high Keulegan–Carpenter numbers. At $(KC = 8.0, \beta = 20.0)$ it can be seen that the forcing characteristic of the synchronous regime is not present and that a more chaotic forcing is experienced by the cylinder. This type of forcing is typical of flows in regime E. A slight increase in β beyond this point to $\beta = 25$ alters the dynamics considerably. Instantaneous vorticity contours are obtained that resemble the flows of three-dimensional regime F (figure 6.25). The forces experienced by the cylinder reflect this with the mean force for this case approaching zero. Additionally, it does not appear that the flow is purely periodic with the force history exhibiting a minor, but clearly detectable, variation in the amplitude of force. The second image of instantaneous vorticity contours for $(KC = 10, \beta = 15)$ exhibits an identical behaviour which again indicates, in conjunction with its force trace in figure 6.26(c), that this location is in regime F.

The extent of regime QP for increasing Keulegan–Carpenter numbers is delineated by the onset of some intermittency in the quasi-periodic shedding period. In figure 6.27 a small subset of a time series for the x -component of force on the cylinder is presented at the location $(KC = 4, \beta = 80.0)$, as indicated in figure 6.24. Over the first twenty five periods of oscillation the force trace resembles a quasi-periodic mode with its secondary period, however beyond this the regular beating effect is seen to be no longer

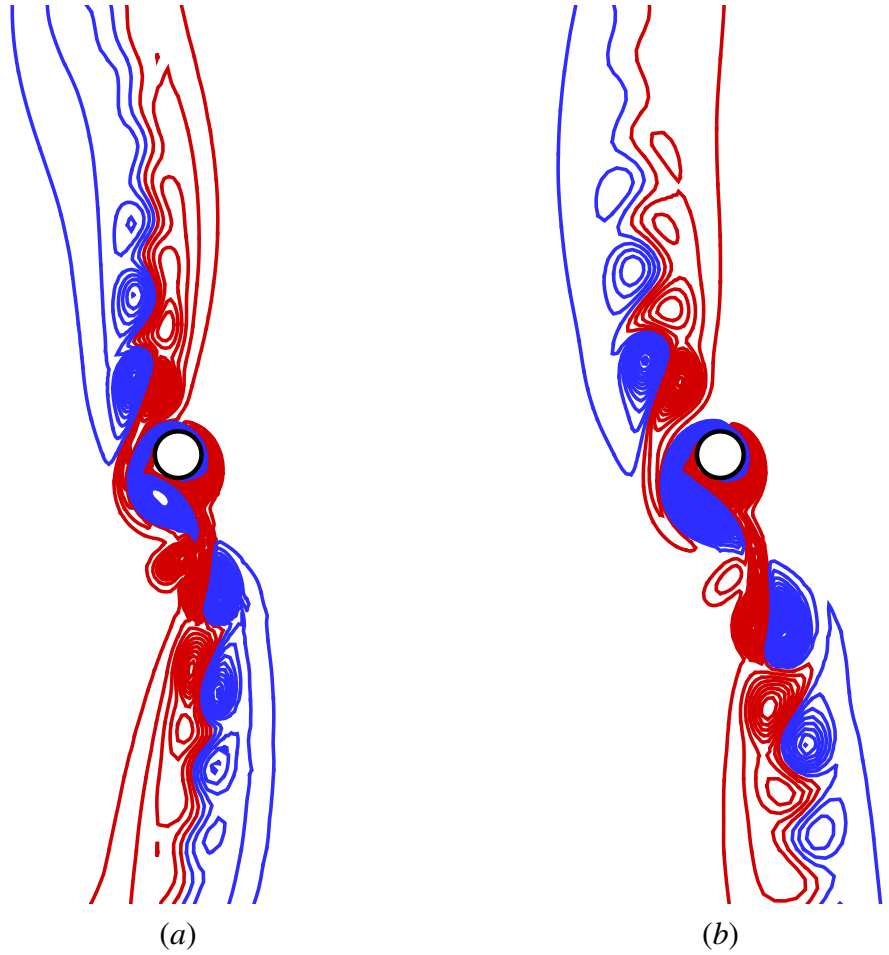


Figure 6.25: Instantaneous vorticity contours for two-dimensional flow in regime F shown at $y = y_{max}$. The flows were computed at: (a) ($KC = 8, \beta = 25.0$); and (b) ($KC = 10, \beta = 20.0$).

purely consisting of the oscillation period and the secondary period. Examination of the instantaneous vorticity contours, figure 6.28, at a set of times over the subset of oscillation periods presented in 6.27, shows a number of differences that occur between this flow and that of regime QP. At times $30T$, $40T$ and $50T$ asymmetries in the far field vorticity contours are clearly seen with pairs and triplets of vortices appearing. These were not observed earlier in the quasi-periodic regime where a staggered array of vortices was seen to occur in the jets. Additionally in all the contours presented, braids of vorticity can be seen connecting the structures near the cylinder with those being convected away by the induced flow. These braids were never visualised in the instantaneous contours of regime QP.

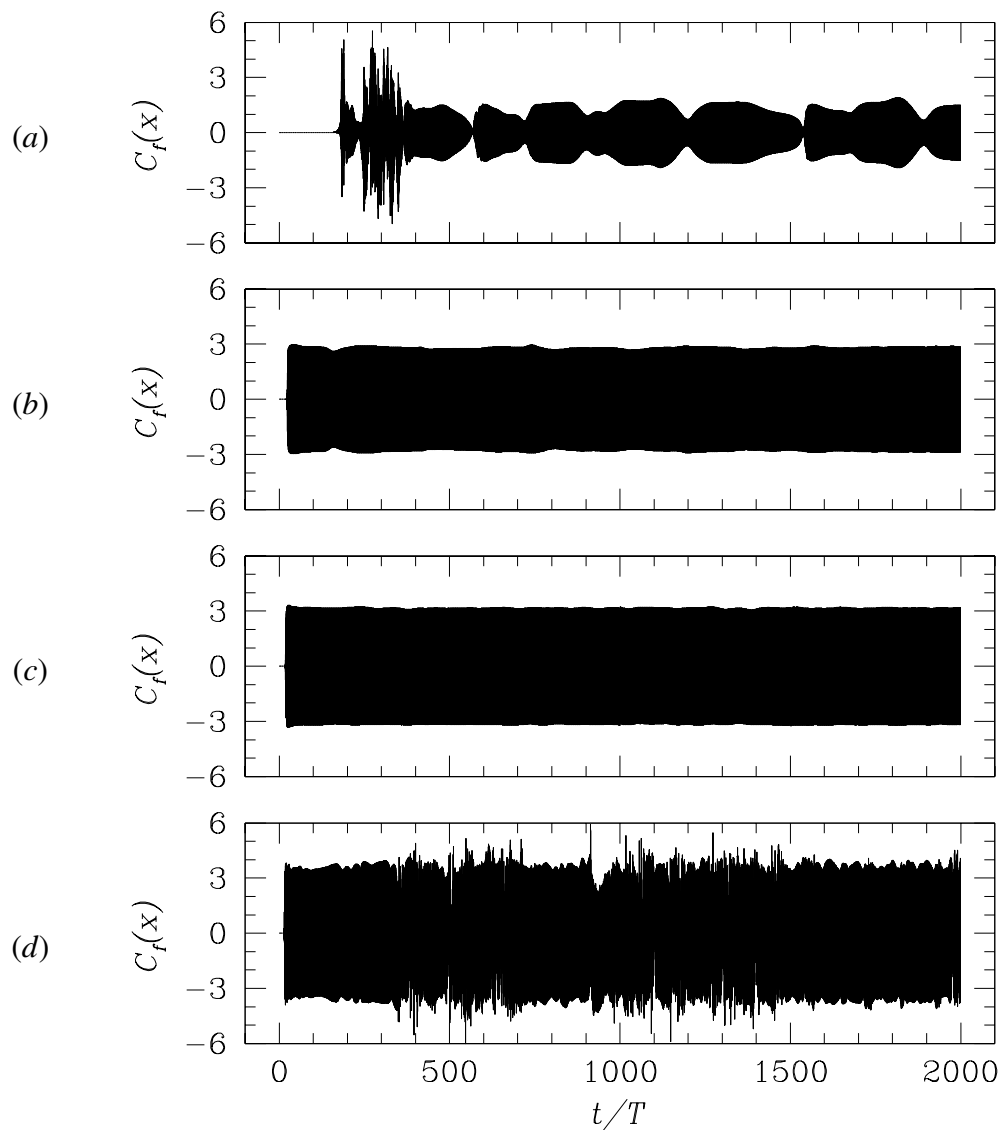


Figure 6.26: Time series of coefficients of force normal to the oscillation axis for two-dimensional flows at: (a), $KC = 8, \beta = 20.0$; (b), $KC = 8, \beta = 25.0$; (c), $KC = 10, \beta = 15.0$; (d), $KC = 10, \beta = 20.0$.

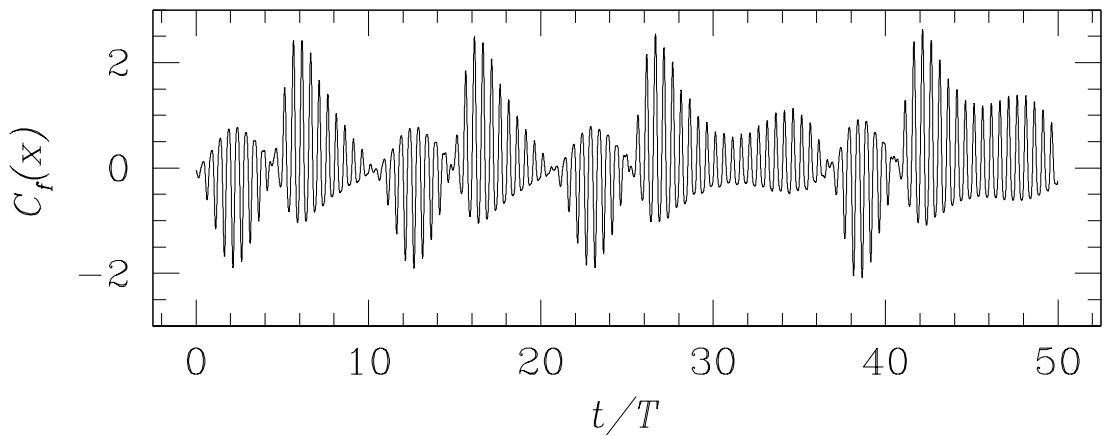


Figure 6.27: Time series of coefficients of force normal to oscillation axis for ($KC = 4, \beta = 80.0$).

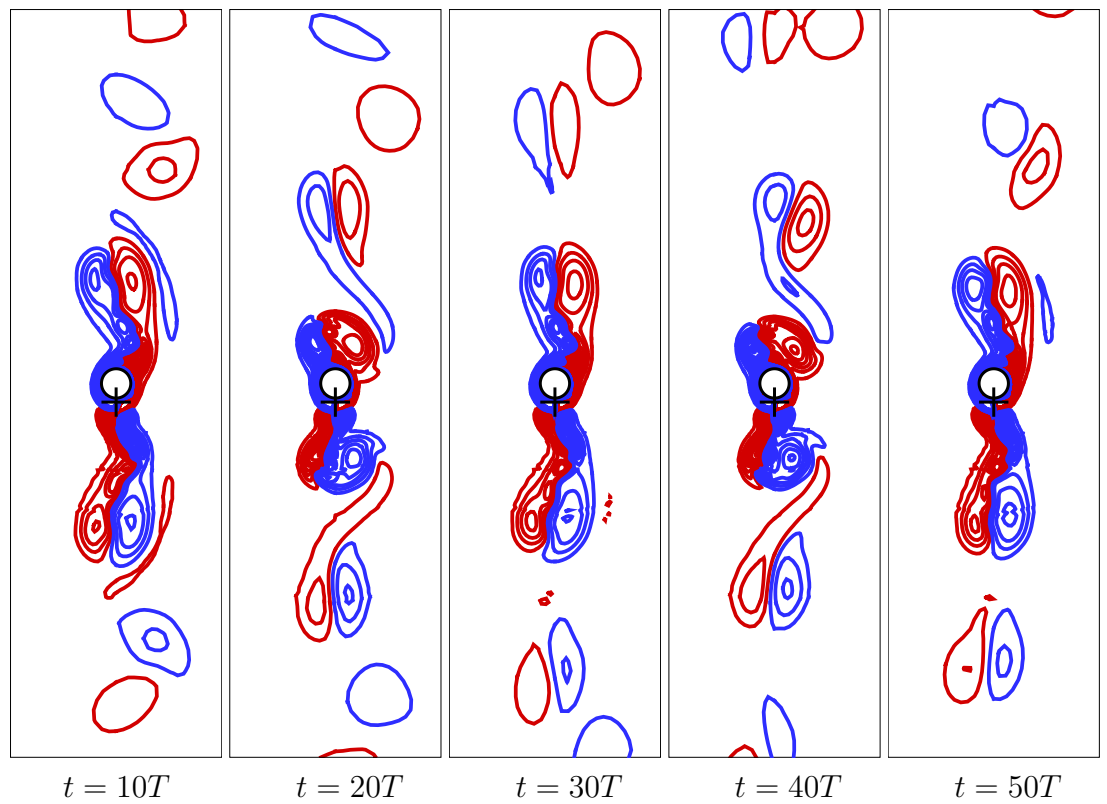


Figure 6.28: Instantaneous vorticity contours at ($KC = 4, \beta = 80.0$), with the cylinder at $y = y_{max}$. The vorticity contours are shown at the times corresponding to figure 6.27.

6.5 Discussion

The application of Floquet analysis to the two-dimensional subspace was very successful in detecting the location in (KC, β) -space of the onset of the primary instability of the base flow. This is despite the complication introduced by the presence of the numerical artifact of the ‘unity’ multiplier. The curve of neutral stability in (KC, β) -space, figure 6.2, matches the location of an amalgam of the experimentally derived boundaries of Tatsuno and Bearman (1990) extremely well in the high and low- β limits. This is quite remarkable given that the Floquet analysis in this chapter is restricted to a two-dimensional subspace perpendicular to the cylinder span, yet the experiments of Tatsuno and Bearman have shown that distinctive three-dimensional structures exist in the flows bordering the boundaries identified. In particular the transitions from regimes A to D and A to C have been shown to be transitions from a two-dimensional flow perpendicular to the span to flows that have both changes in the x - y plane and three-dimensional structure. Given that the two-dimensional analysis of this chapter predicts the location of these transitions so well it is likely that the onset of the spanwise variations in the flow are instabilities of the resultant flows after a two-dimensional transition, although it is possible that the onset of spanwise variations is coincident with the onset of a two-dimensional transition, an aspect that is explored in chapter 7.

At higher Stokes numbers the boundary between regime B to E is also predicted extremely well by the Floquet analysis. Unlike the previous two transitions where the ‘base flow’ was two-dimensional, the flow of regime B has distinctive regular spanwise variations present. By representing this flow in a two-dimensional subspace some information regarding the dynamics of the flow is omitted, yet despite this the two-dimensional Floquet analysis predicts the location of the B–E boundary at the upper limit of the Stokes numbers employed here to within the accuracy of the experimental regime boundaries. It is concluded from this that the transition from regime B to E is in large part due to an instability in the dynamics of the flow in the x - y plane. However, as with the previous two transitions, it is possible that a three-dimensional transition occurs after or coincidentally with this two-dimensional transition. The issue of whether three-dimensional transitions occur at the same time is explored in chapter 7.

A numerical prediction of the critical curve has been previously established by Iliadis and Anagnostopoulos (1998) using DNS, see figure 6.29. The prediction provides a reasonable qualitative match to the regime boundaries found through Floquet analysis and experimental visualisations. However values determined for the location of the transition in (KC, β) -space through that study appear to be shifted towards higher values than those established in this study or experimentally. This is probably due to a limitation in the details of the numerical treatment of Iliadis and Anagnostopoulos.

Along the marginal stability curve a change occurs from Floquet multipliers with

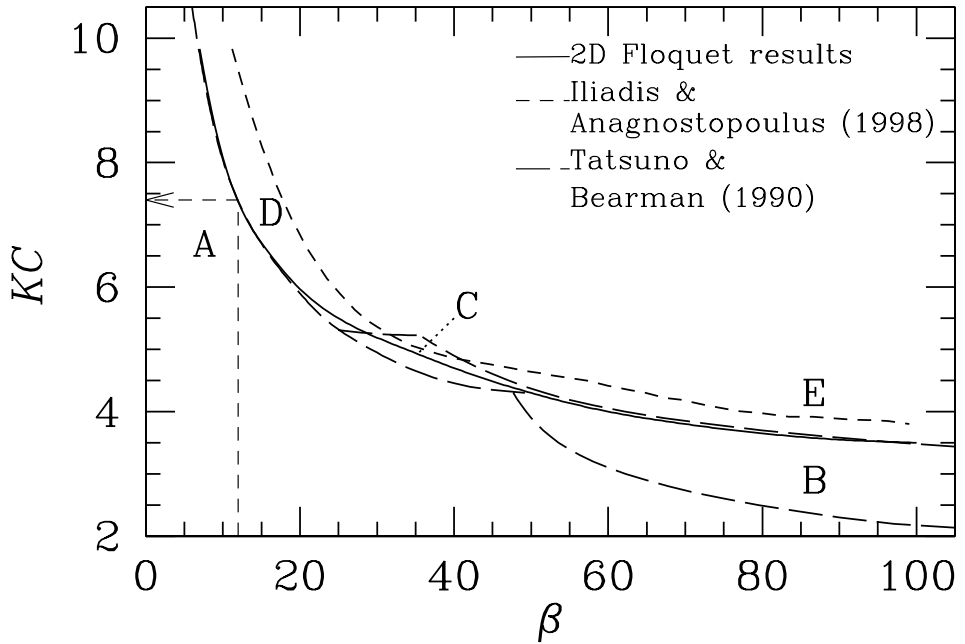


Figure 6.29: Curve of marginal stability for the primary transition in a two-dimensional subspace shown with the two-dimensional numerical results of Iliadis and Anagnostopoulos (1998) and a selection of the experimental regimes of Tatsuno and Bearman (1990). The dashed lines indicate the approximate position at which the critical multiplier switches between real and a complex-conjugate pair of multipliers.

real multipliers, $\mu = +1$, to a pair of complex-conjugate multipliers, $\mu = e^{\pm i\theta}$ at the codimension-2 ‘freezing point’. At this point the phase angle of the complex-conjugate pair of multipliers decreases to zero with reducing β and the complex-conjugate multipliers coalesce to form the single real-multiplier branch. Prior to coalescence, for high Stokes numbers, bifurcations crossing the marginal stability curve correspond to a pair of complex-conjugate Floquet multipliers crossing the unit circle. After coalescence, bifurcations across the marginal stability curve correspond to a single real Floquet multiplier crossing the unit circle. The bifurcations to the two-dimensional regimes S and QP (as distinct from the three-dimensional regimes of Tatsuno and Bearman (1990)) correspond to the single real and the complex-conjugate multiplier branches respectively.

The bifurcation to regime S appears to be analogous to the codimension-1 pitchfork bifurcation at $\mu = +1$, as discussed by Kuznetsov (1995, § 7.4.4). The bifurcation leads to two conjugate solutions that correspond to a break of the K_x symmetry towards either $-x$ or $+x$. The results of this bifurcation in either direction are seen in the vorticity contours of figures 6.5(a) and 6.6(c). The resultant flows in regime S correspond to the visualised flows in the x - y plane of regime D. The similarity between the flows of regimes S and D is further reinforced when a computed particle tracking image from regime S is

6.5. DISCUSSION

compared with the experimental visualisations from regime D (see figure 6.7). Owing to the presence of discrete concentrations of particles, both of the images shown suggest the presence of vortex shedding. However, examination of the vorticity contours at the same location, figure 6.6(c), contradicts this suggestion, as no concentrations of far-field vorticity are seen. Tatsuno and Bearman (1990) made a similar observation, in reference to both regimes A and D, that the dye patterns shown in their visualisations do not represent vortex shedding, except near the cylinder. It is concluded that the onset of the single real multiplier does not lead to the onset of vortex shedding.

The transition to regime QP arises through a complex-conjugate pair of Floquet multipliers crossing the unit circle, which is a bifurcation of a Neimark-Sacker type (Kuznetsov; 1995, see § 7.4.4). As a consequence of the introduction of a secondary period into the flow, the bifurcation produces a 2-torus about the periodic limit cycle of the base flow. It is inferred from inspection of the particle-track image of figure 6.21(a) that the 2-torus has H_1 symmetry. In this case it is found that the secondary period is directly related to the phase angle of the multipliers, such that $T_s = 2\pi T/\theta$. Both the Floquet multipliers and their eigenfunctions arise in complex-conjugate pairs, but it is sufficient to examine either the real or imaginary parts of the eigenfunctions, as, at $|\mu| = 1$, one can be obtained from the other by evolution in $T_s/4$, as stated in Blackburn and Lopez (2003). The portion of the marginal stability curve that signals the transition to the two-dimensional regime QP agrees well in (KC, β) -space with two experimental regime transitions from Tatsuno and Bearman (1990); that of regime A to C and B to E. However, no distinction could be drawn between these two transitions in the restricted two-dimensional subspace, except that the magnitude of the secondary period introduced varied along the curve of marginal stability. The secondary period is found to be linked to a slow flapping of the induced flow from $+x$ to $-x$ and the shedding of vortices, as illustrated in figure 6.19. It is clear from the vorticity contours in figure 6.20(d) that for this regime discrete far-field concentrations of vorticity are present. The relationship between the vorticity contours and the advected particle locations is seen by comparing figures 6.20(d)&(e). The comparison between this particle shedding image and an experimental image of the x - y -plane from regime B, shown in figure 6.21, shows a clear similarity. This is despite the experimentally visualised presence in the three-dimensional experiments of definite spanwise variations in the flow.

Beyond the curve of marginal stability the predictions of the linear Floquet analysis are not guaranteed to be relevant because by definition they cannot account for nonlinear effects. However, it is clear that some aspects, such as the value of the secondary period, that arise at marginal stability are retained at a distance from the curve of marginal stability e.g. see figure 6.18 where the flows at a distance from onset have been determined to have a secondary period similar to that at onset. This is despite the fact that in linear analysis the Floquet multiplier may have ceased to be complex at this point and has coalesced

6.5. DISCUSSION

into real branches (see figure 6.10). The conclusion from this is that while the nonlinear dynamics may retain signature characteristics of the linear instability modes, the extent of the nonlinear regime is not tied to the extent of the Floquet multiplier and its associated instability mode.

In figures 6.10 and 6.12 the complex-conjugate Floquet multipliers are seen to coalesce and then bifurcate into two real branches with increasing distance in (KC, β) -space from the curve of marginal stability. While the subsequent bifurcation of the unstable complex-multiplier branch into two real branches is based on a base flow that is symmetric and T -periodic it may still have an impact on the flow dynamics, particularly if the region in the x - y plane in which the eigenfunction grows is minimally affected by the already unstable quasi-periodic mode. The increment in the Keulegan–Carpenter number, ΔKC , between the onset of the quasi-periodic mode and the subsequent point of coalescence was found to increase with Stokes number from zero at the freezing point. The narrowing of this envelope for the existence of the quasi-periodic mode as $\beta \rightarrow \beta_f^+$ may in part explain the discrepancy between the location of the freezing point ($KC_f \approx 7.4$, $\beta_f \approx 12$) and the regime boundary C to D found by Tatsuno and Bearman (1990) which occurs at ($KC \approx 5.3$, $\beta \approx 25$). Experimentally an increasingly small regime of existence for the quasi-periodic mode might not be detected.

The β -dependence of the flow for a fixed $KC = 7$ (see figure 6.23) illustrates the codimension-2 nature of the flow. On the curve of marginal stability a complex-conjugate pair of multipliers are the first multipliers to cross the unit circle at $\beta = 13.5$. A synchronous flow regime is detected at $\beta = 13.75$. As the $\Delta\beta$ increment is so small at this fixed KC between the onset of the complex-conjugate multiplier branch and the subsequent coalescence to a real multiplier branch it is unlikely to be experimentally detected. This progression from synchronous (unbifurcated) to quasi-periodic and back to synchronous (bifurcated) behaviour is possible because the control space is two-dimensional. Locations in (KC, β) -space beyond the curve of marginal stability need not retain the characteristics of the nearest point on the marginal curve, as would be expected for a codimension-1 control parameter, but instead, due to the codimension-2 nature of the (KC, β) -space, can have the characteristics of different transitions. Subsequent increases in KC at the fixed $KC = 7$ result in a flow that appears to intermittently transition between the flows of regime S and QP. This characteristic matches the description of regime E provided by Tatsuno and Bearman: the “*flow pattern in this regime temporarily resembles that in regime D. The flow which convects to one side of the axis of oscillation, however intermittently changes its direction to the other side*”.

In their three-dimensional simulation at ($KC = 6.5$, $\beta = 20$) Nehari et al. (2004), nominally investigating regime D, reported that the flow, instead of maintaining a constant sign of broken two-dimensional symmetry as they expected from the work of Tatsuno and Bearman (1990), switched orientation intermittently from one side of the oscillation axis

6.5. DISCUSSION

to the other. However, in two-dimensional simulations at the same location in (KC, β) -space, intermittent switching behaviour like that of figure 6.23(d, e) was found. Thus their simulation might be better categorised as being of regime E flow, rather than D.

In the experimental visualisations of Tatsuno and Bearman (1990) the extent of regime D at high Keulegan–Carpenter numbers is bounded by the onset of regime F for increasing Stokes numbers. From these visualisations it would appear that the flow is periodic and possessed of a H_2 symmetry characteristic in comparison to that of regime D or the two-dimensional regime S which have a H_1 symmetry property. From the limited two-dimensional investigation at a number of points in regime F, see figures 6.26(b)&(c), it appears that the resultant flow is only superficially synchronous. It is not completely synchronous as variations of small magnitude in the envelope of force are detected, see figures 6.26(b)&(c). These variations are most probably due to the absence of symmetry in the angle that the vortex jets depart the cylinder at. In figure 6.25 the instantaneous vorticity contours of two cases exhibiting regime F characteristics are shown. In these two cases the vortex jets above and below the cylinder are not symmetrical displaced about the axis of oscillation and also their orientation varies slightly with time which would lead to a slight imbalance in the force experienced by the cylinder.

While three-dimensional bifurcations will be discussed more fully in the following chapter, it should be noted that for $\beta > 15$ increasing the Keulegan–Carpenter number has been observed by Tatsuno and Bearman (1990) to result in a transition to the three-dimensional regime E. As noted previously at $(KC = 7, \beta = 16)$, figure 6.23(d), the force experienced by the cylinder in the two-dimensional representation of this regime resembles an intermittent mix of the forcing experienced in the quasi-periodic and synchronous regimes. This is further illustrated through consideration of the forcing experienced by the cylinder at the other end of the (KC, β) -space considered, for high Stokes numbers. In figure 6.27 the time series of the x -component of force at $(KC = 4, \beta = 80)$ demonstrates behaviour that for the first ≈ 20 periods is indicative of the QP regime. After 20 periods some intermittency is seen to appear in the force trace, although it does not lead to a complete breakdown in the quasi-periodic oscillation of the force. It should be noted that the Floquet multiplier at this location, $(KC = 4, \beta = 80)$, is just on the point of coalescence (figure 6.12). A set of instantaneous vorticity contours taken every $10T$ over the same force history is shown in figure 6.28. The contours of figure 6.28(a) are similar to those shown of regime QP with the formation of a reverse Kármán street in the induced flow. At successive times later the nature of the vortices in the induced flow has changed from a staggered arrangement of oppositely signed vorticity to that of vortex pairs and triplets being convected away by the induced flow. It is speculated that onset of regime E may be caused by the onset of an instability of the quasi-periodic mode which leads to intermittency in the vorticity shed from the cylinder.

Along the curve of marginal stability it was found that for the onset of both regimes

6.5. DISCUSSION

S and QP the type of nonlinear bifurcation was supercritical. This implies a smooth departure of bifurcated solutions symmetry as control parameters are increased. In the synchronous regime the impact of this is readily seen as an increasing deviation of the induced flow from the axis of oscillation, see figure 6.8. In the quasi-periodic regime it is thought that the supercriticality has the effect of increasing the peak angle of deviation of the induced flow near the cylinder. However, this is less clear than for the synchronous regime as the oscillatory nature of the flow and the lack of synchronisation make observations of the angle of deviation very phase dependent. Eventually the increase in deviation cannot be sustained leading to breakdown of either synchronicity or the quasi-periodicity. In the quasi-periodic regime this effect is observed where the increasing angle of deviation may lead to breakdown of the shedding mode of single vortices per $1/2T_s$ into one that sheds vortex pairs and triplets for each T_s , as seen in figure 6.28.

6.6 Summary

In this chapter results of a combined two-dimensional Floquet stability analysis and DNS investigation into the primary bifurcation from the symmetric and periodic flow state detailed in chapter 5 were presented. It was found that two different types of bifurcation were present along the curve of marginal stability that resulted in two-dimensional symmetry breaking. Particularly in the low- β , high- KC limit and in the high- β , low- KC limit, the location of the marginal stability curve coincided well with existing experimentally derived boundaries. This was remarkable given that the experimentally observed behaviours of these flows following bifurcation have all been three-dimensional. The two forms of Floquet multiplier found were (*a*) a single real and (*b*) a complex-conjugate pair which gave rise to a synchronous regime, S, and a quasi-periodic regime, QP, respectively. In transitioning to the synchronous regime the flow broke the spatial K_x symmetry about the axis of oscillation but still retained a spatio-temporal symmetry of the H_1 type. The transition to regime QP also broke the K_x symmetry. Additionally in the QP regime a secondary period, T_s was introduced as a consequence of the complex-conjugate multipliers which crossed the unit circle. A 2-torus is formed as a result of this bifurcation which has H_1 symmetry. The shedding of vortices and a flapping of the induced flow from the $-x$ to $+x$ direction were found to be synchronised with the secondary period T_s . Regime QP was also the first regime in which vortex shedding was observed.

The nonlinear behaviour beyond the onset of these regimes was also examined. It was found that both bifurcations were supercritical. In the synchronous regime this supercriticality was manifested as an increase in the angle of deviation of the induced flow from the axis of oscillation. In the QP regime this influence was difficult to determine due to the flapping effect observed. It is speculated that the supercriticality manifests as an increased angle of deviation of the flapping flow. Subsequent transitions to the experimentally observed regimes E and F were also briefly examined.

Chapter 7

Rectilinear Oscillation: Symmetry Breaking in Three–Dimensional Space

In chapter 6 the domain of investigation was restricted to a two-dimensional subspace perpendicular to the span of the cylinder. Within this restricted domain a curve of marginal stability was located as a function of the controlling parameters, (KC, β) , above which several of the symmetry characteristics of the base flow identified in chapter 5 were found to be broken. Along the curve of marginal stability two forms of bifurcation were observed: a real Floquet multiplier resulting in a pitchfork bifurcation to a conjugate set of spatially symmetric, periodic states; and a complex conjugate set of Floquet multipliers resulting in a Neimark-Sacker bifurcation to a quasi-periodic flow.

In this chapter the domain of investigation is expanded to include the spanwise dimension and consequently an additional parameter, the spanwise wavelength λ or equivalently wavenumber $k = 2\pi D/\lambda$, must be introduced to characterise the instability modes. It is known from the results of the previous chapter in combination with the visualisations of Tatsuno and Bearman (1990) that two-dimensional symmetry breaking occurs at nearly the same location in (KC, β) -space as three-dimensional symmetry breaking for the transition from regime A to D. However it is not established if the two-dimensional and three-dimensional symmetry breaking are coincidental or if one occurs before the other. Additionally it is not known if the three-dimensional symmetry breaking is dependent on the two-dimensional symmetry breaking. In the case of the transition A* to B the previous chapter established that it is a purely three-dimensional transition as it occurs below the onset of two-dimensional symmetry breaking. For both of these transitions a combination of Floquet analysis and DNS is employed to investigate the transition and the nature of the resultant flow. The technique of enforcing the symmetry about the axis of oscillation of the base flow is also used to determine the impact of two-dimensional symmetry breaking on the three-dimensional symmetry breaking.

In contrast to the aforementioned cases where the resultant three-dimensional flow has

been experimentally observed to be synchronous with the oscillation, the flow of regime C has been observed to be unsynchronised with the cylinder oscillation. This lack of synchronisation was identified as being caused by the onset of a two-dimensional quasi-periodic instability in the previous chapter. However, this was in a restricted two-dimensional subspace and it remains to be determined whether this still holds when this restriction is removed. As Floquet analysis requires a periodic base flow it cannot be used to study this regime. Consequently only three-dimensional DNS is used to study this regime and this transition.

In the following sections the curve of neutral stability and the associated critical wavenumbers determined using Floquet analysis are presented in §7.1. Three transitions are identified using Floquet analysis that each have different underlying two-dimensional base flows. These three transitions to regimes B, D and a modified regime D with forced K_x symmetry are examined with Floquet analysis and DNS in §§7.2 and 7.3. In §7.4 the transition to regime C and the nature of the flow in this regime are examined using DNS only. In §§7.5 and 7.6 the results of these five sections are discussed and summarised.

7.1 Marginal Stability Curves

The locations in (KC, β) -space of the primary three-dimensional instability identified using Floquet analysis are presented in figure 7.1. The procedure used to determine this curve was more complicated than that used to determine the two-dimensional curve of marginal stability due to the presence of an additional parameter: the spanwise wavenumber, k . In the initial stages the procedures are nearly identical in that a two-dimensional base flow was produced and stored using 64 equi-spaced in time snapshots of the velocity fields over one period of oscillation. Although in this section, unlike the previous chapter, the base flow was permitted to break K_x symmetry about $x = 0$, depending on the location in (KC, β) -space and the aspect being tested, and was computed on the full domain. Typically this increased the computational time required owing to the number of extra calculations needed per time-step and the additional time required for the base flow to converge to a final periodic solution. It is at the Floquet analysis stage that the investigation of the three-dimensional flow becomes much more computationally expensive. Whereas for the two-dimensional analysis a single Floquet analysis would be employed on each base flow, in this case a Floquet analysis was used for each wavenumber that was tested. Typically a minimum of ten wavenumbers were tested for each location in (KC, β) -space. This procedure was repeated at numerous locations in (KC, β) -space in order to determine the location of the marginal stability curves and the critical wavenumbers on these curves. The entire process is approximately ten times more computationally expensive than the two-dimensional Floquet analysis. The difficulty mentioned in §6.1 due to the presence of a ‘unity’ multiplier did not arise for the majority of the cases tested, as only three-dimensional modes close to the two-dimensional subspace are afflicted.

In contrast to the curve of two-dimensional symmetry breaking where both complex and real Floquet multipliers were found, in this case only unstable modes with real multipliers are found. A consequence of this is that the three-dimensional instability modes that are identified are synchronous with the cylinder oscillation. In the low Stokes number, high Keulegan–Carpenter number region the transition to three-dimensionality is observed to occur at approximately the same location as the two-dimensional transition to regime S, as shown by multiplier branch I in figure 7.1(a). The base flows used for determination of this boundary were calculated on a full domain and therefore were permitted to break K_x symmetry. The exact nature of this transition and the resultant flows are discussed in detail later in §7.3.

The two curves in figure 7.1(a) having circular data points, multiplier branches II and III, were achieved using base flows that were constrained to be K_x -symmetric. This was done for two reasons: firstly to continue the lower curve, branch II, above the two-dimensional symmetry breaking curve; and secondly to isolate the impact that the break in K_x symmetry has on the onset of three-dimensional symmetry breaking. The mode whose

7.1. MARGINAL STABILITY CURVES

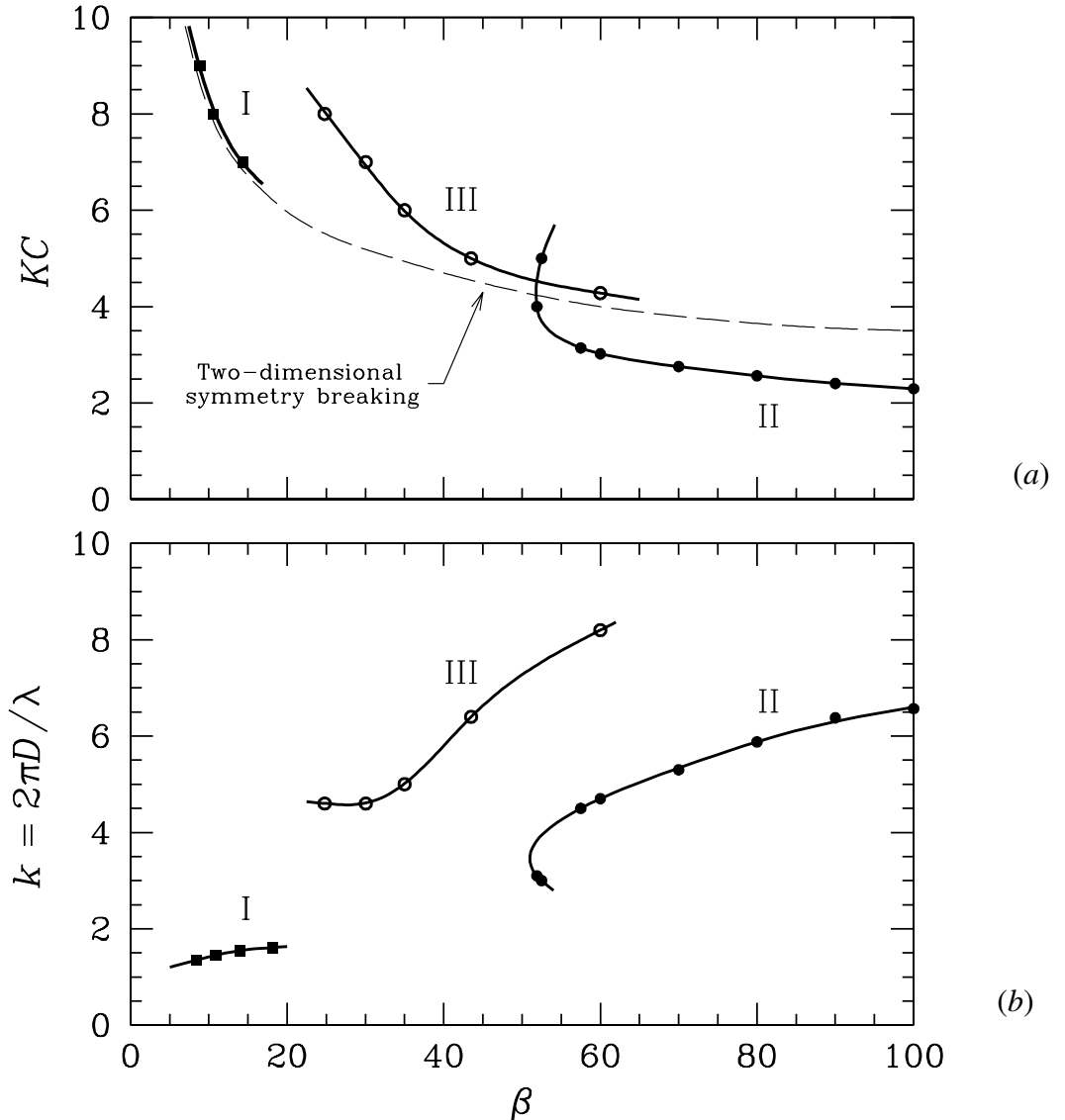


Figure 7.1: Marginal stability curves for three-dimensional modes. For data labelled \bullet , \circ , the base flow had two-dimensional reflection symmetry, and respectively the three-dimensional modes have H_1 and H_2 spatio-temporal symmetry at any z . For data labelled \blacksquare , the base flow had broken two-dimensional symmetry. In (a), the curve of two-dimensional symmetry breaking from figure 6.1 (a) is shown.

curve crosses the two-dimensional transition from below, for the most part, did not require the use of a base flow that was constrained to be K_x -symmetric and the same result was achieved for base flows that were not constrained and were naturally K_x -symmetric. The only point where this was required was the point above the curve of marginal two-dimensional stability. The curve lying entirely above the two-dimensional symmetry breaking curve, branch III, is a fictional result. It is fictional in the sense that the base flow from which it was produced, a K_x symmetric base flow, no longer exists as the two-dimensional symmetry breaking curve above which it lies breaks the K_x symmetry. However, it does

7.1. MARGINAL STABILITY CURVES

establish an important characteristic of the three-dimensional symmetry breaking: the three-dimensional symmetry breaking curve (branch I) found for $5 \leq \beta \leq 20$ requires the K_x symmetry to be broken in order to occur. In the absence of the broken K_x symmetry no three-dimensional transition was observed for $5 \leq \beta \leq 20$.

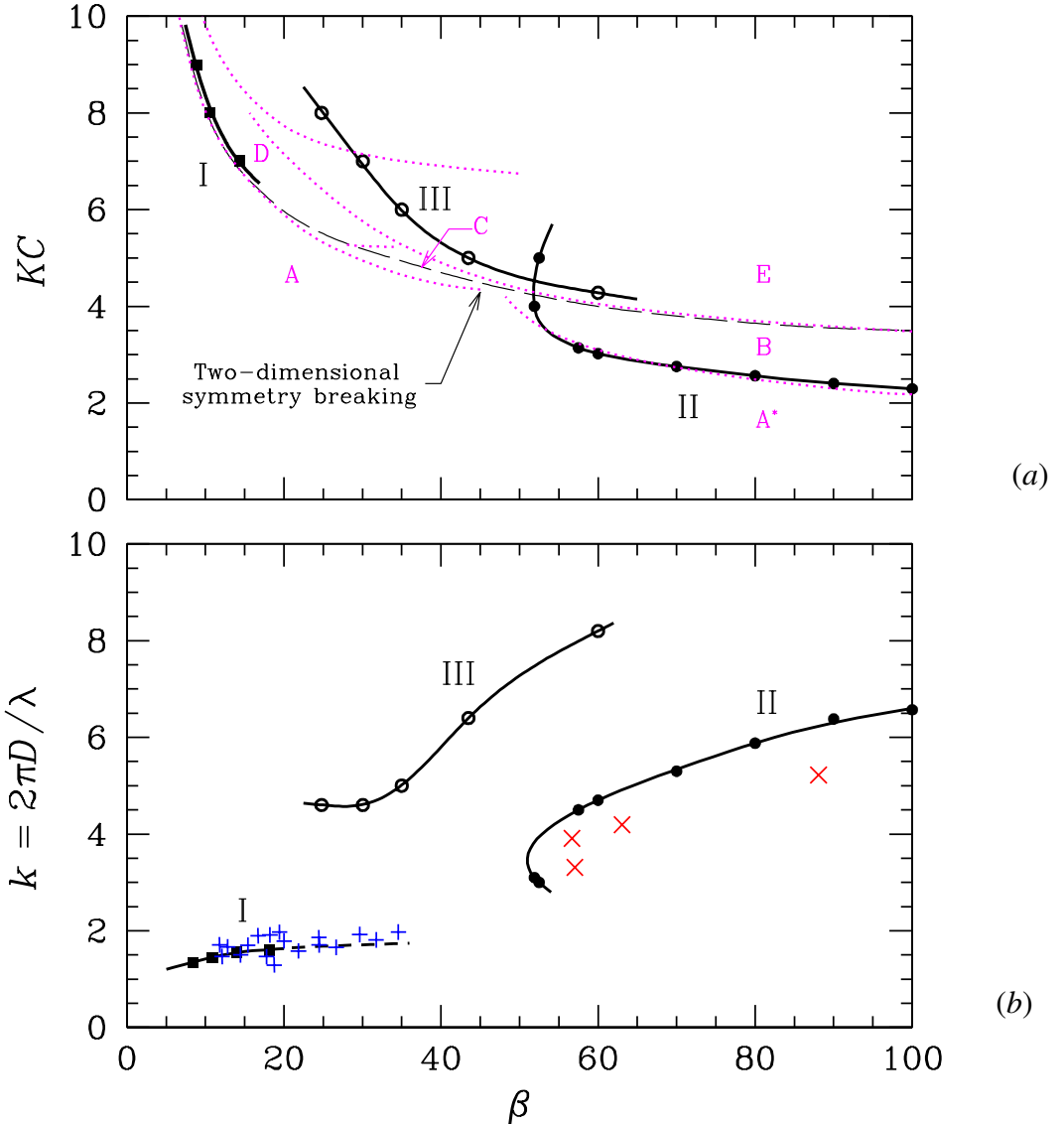


Figure 7.2: Marginal stability curves for three-dimensional modes. For data labelled ●, ○, the base flow had two-dimensional reflection symmetry, and respectively the three-dimensional modes have H_1 and H_2 spatio-temporal symmetry at any z . For data labelled ■, the base flow had broken two-dimensional symmetry. In (a), the curve of two-dimensional symmetry breaking from figure 6.1 (a) is shown. In (b), wavenumber data from Tatsuno and Bearman (1990) are represented by × (regime B) and + (regime D).

On the curve of marginal two-dimensional symmetry breaking there is a large gap between the end of branch I and the onset of branch II. In this region the underlying

7.1. MARGINAL STABILITY CURVES

two-dimensional flow has been shown to be quasi-periodic. This quasi-periodicity breaks a fundamental requirement for the application of Floquet analysis, that of a periodic base flow, and hence, as stated earlier, no Floquet results could be obtained here for the primary onset of a three-dimensional instability.

The locations of the three-dimensional transitions found using Floquet analysis compare favourably with the regime boundaries of Tatsuno and Bearman (1990), as shown in figure 7.2(a). The lower curve, branch II, agrees well with the experimental observations of a transition between regimes A* and B. Additionally from the experimental observations of regime B it would appear that these flows have H_1 symmetry at any z -location. A more detailed treatment of this regime and this three-dimensional transition is provided in §7.2.

In contrast to branch II the onset of three-dimensionality occurs after the onset of two-dimensional symmetry breaking for branch I. The underlying break in two-dimensional symmetry is the transition to regime S and the base flow breaks the spatial K_x symmetry and the spatio-temporal H_2 symmetry but preserves H_1 . The subsequent onset of three-dimensionality occurs almost immediately after the two-dimensional transition. From the location of the three-dimensional transition branch III, which was created using base flows forced to be K_x -symmetric, it can be concluded that the flow of regime S is unstable to three-dimensional perturbations. The location of branch III of the Floquet multipliers does not agree with any experimental regime boundaries, a fact that is not surprising given that it was artificially created by enforcing K_x symmetry of the base flow. A detailed treatment of the nature of branches I and III is provided in §7.3. Regime C has been observed to have three-dimensional characteristics, however, Floquet analysis cannot be applied in this regime. Consequently DNS studies are used to investigate the nature of this transition to three-dimensionality and the subsequent flows that result. These investigations are detailed in §7.4.

In figures 7.1(b) and 7.2(b) wavenumbers for the most unstable three-dimensional modes are presented. The wavenumbers for the fictitious branch III are seen to be substantially higher than the neighbouring branches. Tatsuno and Bearman (1990) did not record any wavelengths for this region of (KC, k) -space as the experimental flows of regime C and E were observed to have no regular spanwise variations. The wavenumber values predicted for the onset of regime D are in excellent agreement with that experimentally recorded. In figure 7.2(b) the line of best fit through the Floquet results has been extrapolated to encompass the range of β values recorded by Tatsuno and Bearman (1990) and in all cases the predictions are well within experimental error margins. The predictions for the wavenumbers at the onset of regime B are reasonable. While not as good a match as for the onset of regime D, the predicted values are close and follow the same pattern as the experimental results. Potential reasons for the discrepancies are discussed later in §7.5.

7.2 Regime A^{*} – B

In this section both the three-dimensional transition of branch II in figure 7.1(a) and the resultant flow are investigated in detail. In this case the underlying base flow on either side of this transition has not broken two-dimensional symmetry. In simulations with either the full or half domain (to enforce K_x symmetry) the Floquet results obtained were identical. Due to this expected result the half-domain was used to produce the base flows as it was computationally cheaper and it permitted the tracking of this transition above the onset of two-dimensional symmetry breaking.

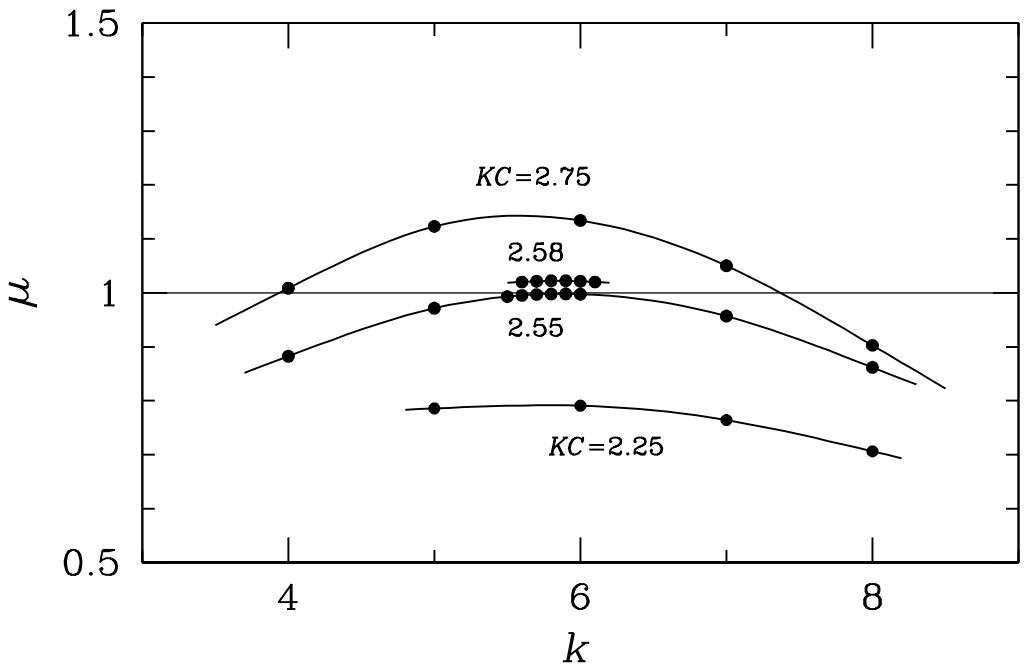


Figure 7.3: Floquet multipliers as function of wavenumber and Keulegan–Carpenter number for the three-dimensional instability of regime B at $\beta = 80$.

In figure 7.3 the variation of the Floquet multiplier is presented as a function of the spanwise wavenumber for a number of fixed Keulegan–Carpenter numbers. The results are shown for a fixed $\beta = 80$, however a wider range of Stokes numbers was examined in order to produce the critical point data, as can be seen in figure 7.1. This particular Stokes number was arbitrarily chosen as being representative of this bifurcation. Although only a portion of the spanwise numbers examined are shown $4 \leq k \leq 8$, beyond this range no unstable wavenumbers were found near the point of onset. Obviously as the point in (KC, β) -space is increased beyond the point of marginal stability an increasing range of wavenumbers became unstable and it is possible that wavenumbers beyond that shown in figure 7.3 will be unstable. However, as the application of Floquet analysis is applicable at the onset of an instability it is deemed unnecessary to quantify this change

7.2. REGIME A* – B

in the unstable wavenumber ranges. The critical multiplier branches shown in figure 7.3 consist entirely of real Floquet multipliers. Consequently Floquet analysis predicts that the resultant flow will be synchronous with the cylinder oscillation and that the bifurcation will introduce no new frequencies into this flow. By interpolation the critical point at a fixed $\beta = 80$ is ($KC_c = 2.564$, $k_c = 5.88$). In figure 7.4 the force time-series for the saturated DNS computations are presented. Inspection of these series shows that the flow remains synchronous with the cylinder oscillation and that x -force component remains zero and constant. With reference to the temporal characteristics of the flow, the prediction of the linear stability analysis matches the DNS computations.

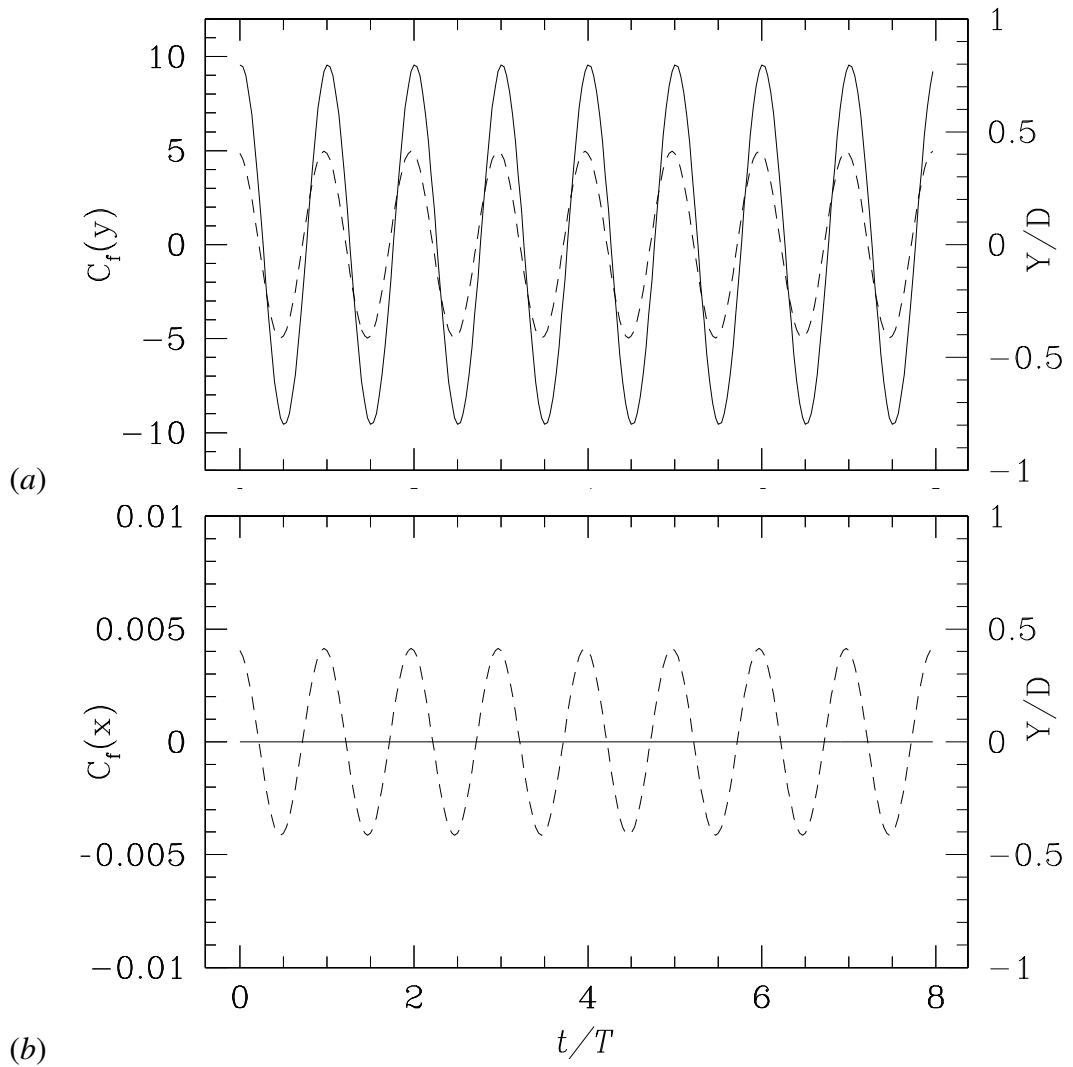


Figure 7.4: Plot of the coefficients of total y - & x -force per unit spanwise length exerted on the cylinder over eight periods of cylinder motion. The simulation was carried out at ($KC=2.6, \beta=80.0$). The force is non-dimensionalised with respect to the root mean square of the cylinders prescribed y -axis velocity and the cylinder diameter D . Also shown is the cylinders displacement (dashed line) over one period of motion.

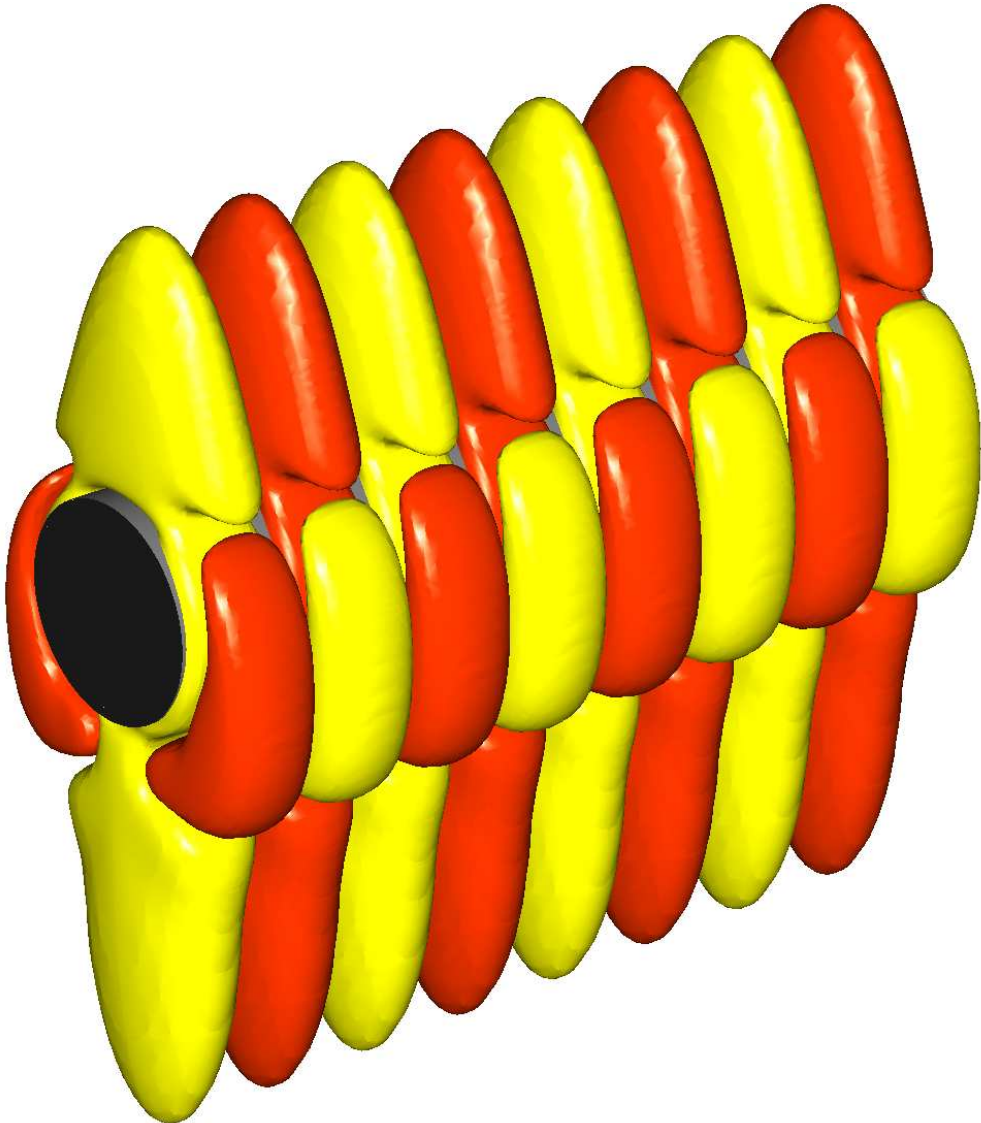


Figure 7.5: Instantaneous vorticity isosurfaces for the regime B instability at ($KC = 2.58$, $\beta = 80$, $k = 5.88$), showing the Floquet mode. Four spanwise repetitions are represented, at the instant when the cylinder is at y_{\max} . The solid isosurfaces show y -component vorticity of equal magnitude but opposite signs.

In figures 7.5 and 7.6 isosurface visualisations of the most unstable Floquet mode and those obtained from saturated DNS computed at ($KC = 2.58$, $\beta = 80$, $k = 5.88$) are presented. The location these computations were performed at in (KC, β) -space lies just above the point of marginal stability. In both cases four spanwise repetitions of a single simulated wavelength are shown. For the DNS, eight spanwise Fourier modes (16 real data planes) were employed to discretise a single spanwise wavelength. In both figures an alternating array of y -component vorticity can be seen above and below the cylinder. Given the shape and alignment of this array of vortices, it might be expected to give rise to a spanwise waviness of the induced flow past the cylinder. This matches the experi-

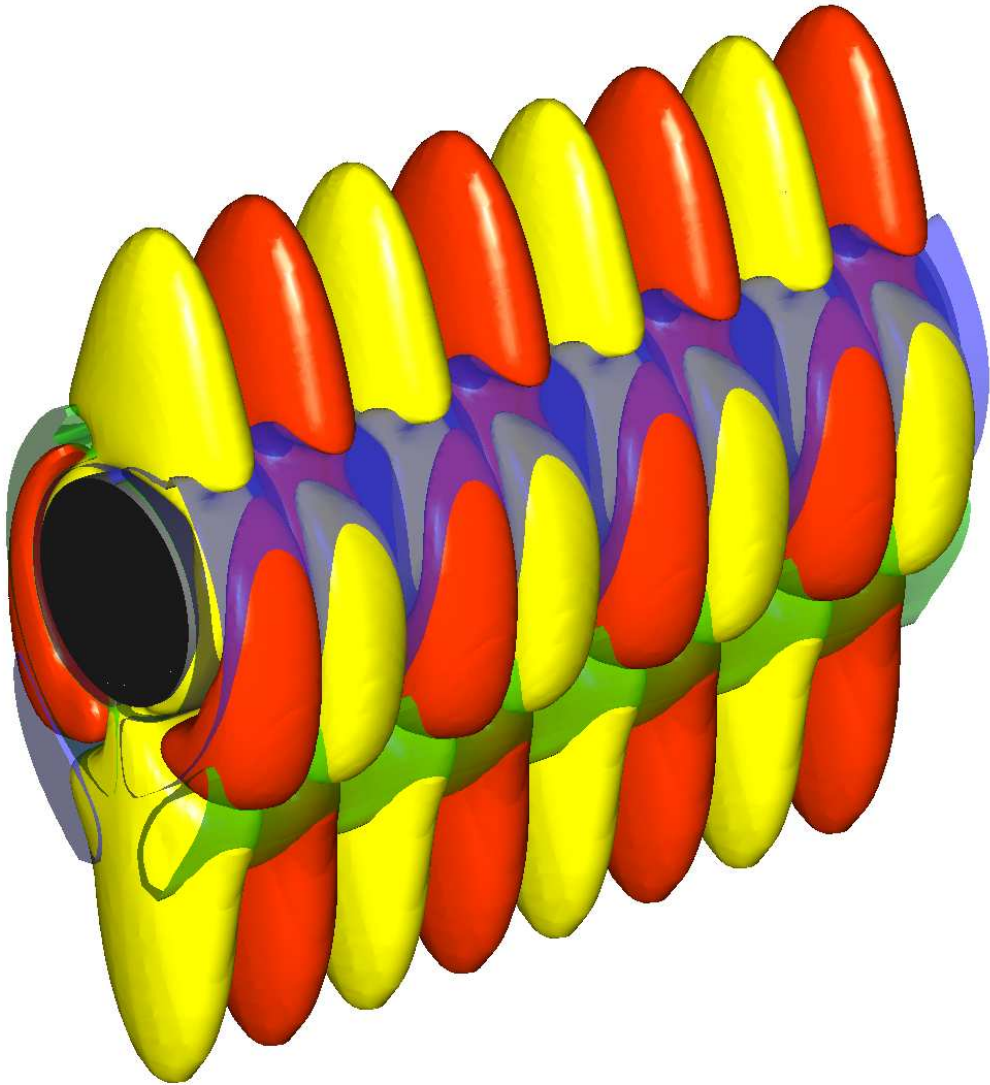


Figure 7.6: Instantaneous vorticity isosurfaces for the regime B instability at ($KC = 2.58$, $\beta = 80$, $k = 5.88$), showing the DNS result. Four spanwise repetitions are represented, at the instant when the cylinder is at y_{\max} . The solid isosurfaces show y -component vorticity of equal magnitude but opposite signs, while additionally translucent isosurfaces show z -component vorticity.

mental observations of Honji (1981), who observed that regime B was characterised by regular spanwise streaks in the flow, and those of Tatsuno and Bearman (1990), e.g. figure 2.18(a). Evidently flow obtained through DNS, and correspondingly experimentally visualised, is closely related to the Floquet instability mode.

In figures 7.7(a) & (b) isosurface visualisations of the Floquet mode and those obtained from saturated DNS computed at ($KC = 2.58$, $\beta = 80$, $k = 5.88$) are presented from a different perspective than those shown previously. In these figures the main influence of the nonlinear interaction on the three-dimensional instability can be seen in three

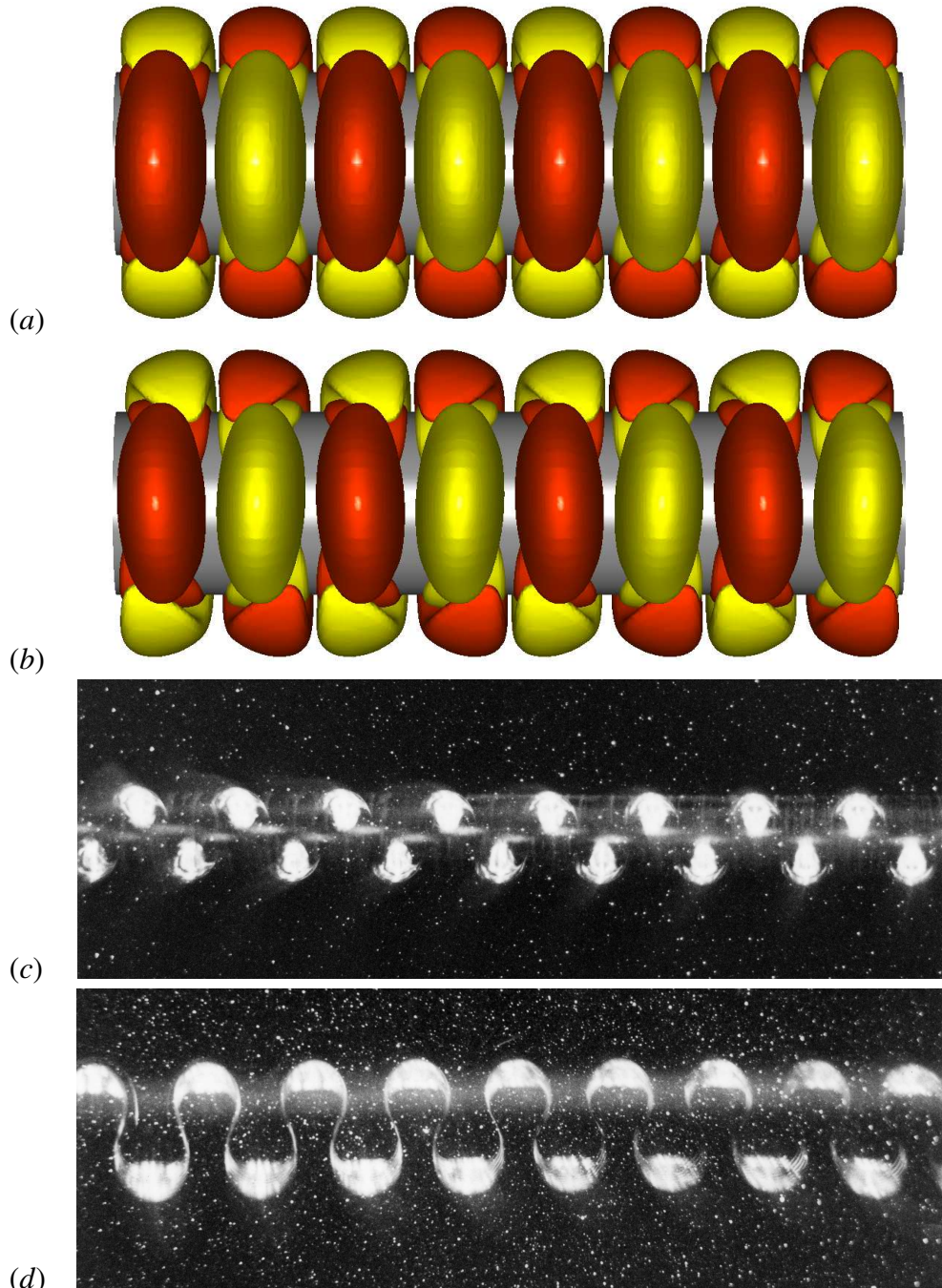


Figure 7.7: Instantaneous vorticity isosurfaces and experimental visualisations for the regime B instability. Shown are the (a) Floquet mode and (b) DNS result at ($KC = 2.58$, $\beta = 80$, $k = 5.88$). Four spanwise repetitions are represented, at the instant when the cylinder is at y_{\max} . The solid isosurfaces show y -component vorticity of equal magnitude but opposite signs. Figures (c) and (d) are from Tat-suno and Bearman (1990) and show visualisations of the flow structure at (c) $2.5D$ above the x - z plane for ($KC = 2.93$, $\beta = 77.7$) and (d) $5D$ above the x - z plane for ($KC = 3.14$, $\beta = 72.6$)

7.2. REGIME A* – B

aspects: firstly, in the way that the vortex pairs on the shoulders of the cylinder are drawn more closely together and are clearly paired; secondly, in the way this pairing alternates on either side of the cylinder; and thirdly, the orientation of the array of vortices above and below the cylinder is no longer parallel to the x - y plane. In figures 7.7(c) & (d) experimental visualisation from Tatsuno and Bearman (1990) are shown. These figures match the vorticity contours shown. In particular, in figure 7.7(c), the small streaks crossing over the cylinder exhibit an alternating orientation to the x - y -plane in the same manner as the vortex array in figure 7.7(b) does.



Figure 7.8: Contours of instantaneous kinetic energy in the fundamental spanwise harmonic for three-dimensional synchronous flow in regime B, obtained over one temporal period via saturated DNS at ($\beta = 80$, $KC = 2.6$, $k = 5.88$).

At any spanwise location, the sign of y -vorticity above and below the cylinder (and also at $\pm x$, for any y -location), is the same, but near the shoulder of the cylinder there is a change of sign of y -vorticity on a radial traverse. Although as noted previously, nonlinear effects may result in a change of magnitude of the vorticity at $\pm x$, for any y -location. It

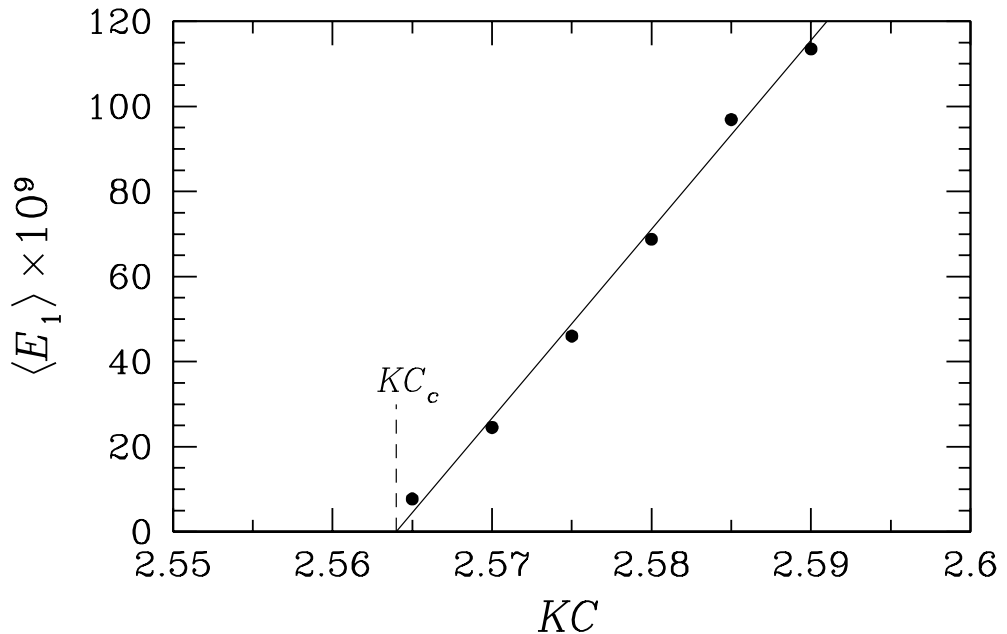


Figure 7.9: Bifurcation diagram for three-dimensional symmetry breaking in regime B, showing normalised time-average kinetic energy in the first spanwise harmonic, $\langle E_1 \rangle$ as a function of KC at $\beta = 80$, and $k = 5.88$. Values of E_1 are small because the normalisation has the computational domain area in the denominator, while most of the three-dimensional energy is concentrated near the cylinder.

appears that the y -vorticity at locations above and below the cylinder is generated on the cylinder surface, and is advected away from the cylinder by the oscillatory flow. The outer vorticity structures near the shoulders of the cylinder apparently remain in a broadly similar location relative to the cylinder over a motion cycle, and preserve their sense of spin. In figure 7.8 contours of kinetic energy in the first spanwise harmonic from the saturated DNS are presented, plotted at $T/8$ increments. This measure highlights the spatial regions in the x - y plane that have the highest spanwise velocities and are therefore indicative of where this mode is formed. The energy is closely confined to the near-cylinder region and coincides with the innermost y -vorticity structures of both signs shown in figures 7.5 and 7.6. Also evident in figure 7.8 is the spatio-temporal symmetry that occurs every $T/2$. It appears that, in agreement with the high- β -asymptotic stability analysis of Hall (1984), the likely underlying mechanism for this mode is a centrifugal instability arising in the boundary layer flows as they sweep past the shoulders of the cylinder.

To examine the nonlinear properties of the bifurcation and the agreement between the Floquet prediction and the DNS computations for the onset of this bifurcation, the variation of the normalised time-average kinetic energy in the fundamental spanwise harmonic, $\langle E_1 \rangle$ from saturated DNS is explored. In figure 7.9 the outcome of this investigation is plotted for various Keulegan–Carpenter numbers at a fixed $\beta = 80$. Also displayed in this figure is the critical KC_c number arising from the Floquet analysis. The onset of

7.2. REGIME A* – B

the bifurcation in DNS agrees well with the linear stability analysis. The nature of this bifurcation is clearly supercritical, as shown by the continuous increase in energy after the point of onset. This finding of supercriticality disagrees with Hall (1984)'s suggestion that the bifurcation is subcritical in the high- β limit, although it should be noted that there is no requirement for the nonlinear nature of a bifurcation (sub- or supercritical) to be invariant along the curve of marginal stability, and also that Hall was rather equivocal about his prediction.

7.3 Regime A – D

In this section the three-dimensional bifurcation corresponding to the Floquet multiplier branch I of figure 7.1 and the resultant flow are investigated. It has been established in chapter 6 that a two-dimensional bifurcation occurs at approximately the same location in (KC, β) -space as the three-dimensional transition A–D visualised by Tatsuno and Bearman (1990). In §7.1 it was reported that the critical Floquet multiplier branch was detected after the onset of the two-dimensional symmetry breakage had occurred.

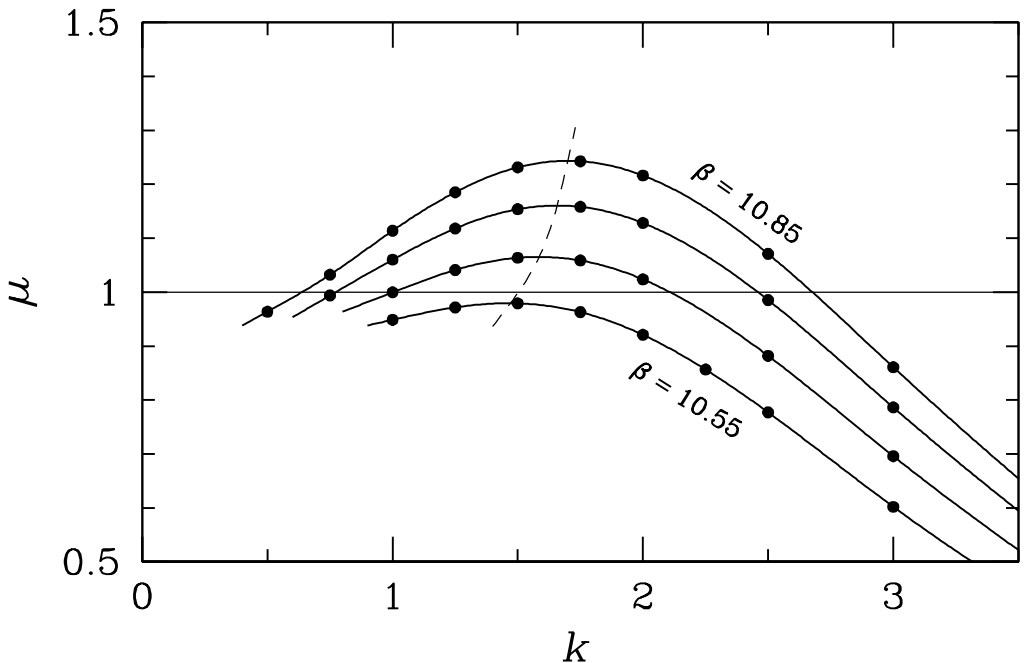


Figure 7.10: Floquet multipliers as function of wavenumber and Stokes number for the three-dimensional instability of regime D at $\beta = 8$.

In figure 7.10 the variation of the Floquet multiplier is presented as a function of the spanwise wavenumber for a number of fixed Stokes numbers. The results are shown for a fixed $KC = 8$, however a wider range of Keulegan–Carpenter numbers was examined in order to produce the critical point data, as can be seen in figure 7.1. This particular Keulegan–Carpenter number was chosen as being representative of this bifurcation. Although only a portion of the spanwise numbers examined are shown, $0.5 \leq k \leq 3.0$, beyond this range no unstable wavenumbers were found near the point of onset. As with the bifurcation to regime B, subsequent increases of the control parameters beyond the critical value cause the band of unstable wavenumbers to increase. With each increase the apex of this band of wavenumbers is seen to also increase, both in Floquet multiplier magnitude and in the value of the spanwise wavenumber it occurs at, as shown by the dashed line in figure 7.10. The critical multiplier branches shown in figure 7.10 consist entirely

7.3. REGIME A – D

of real Floquet multipliers. Consequently Floquet analysis predicts that the resultant flow will be synchronous with the cylinder oscillation and that the bifurcation will introduce no new frequencies into this flow. By interpolation the critical point at a fixed $KC = 8$ is ($\beta_c = 10.58$, $k_c = 1.51$).

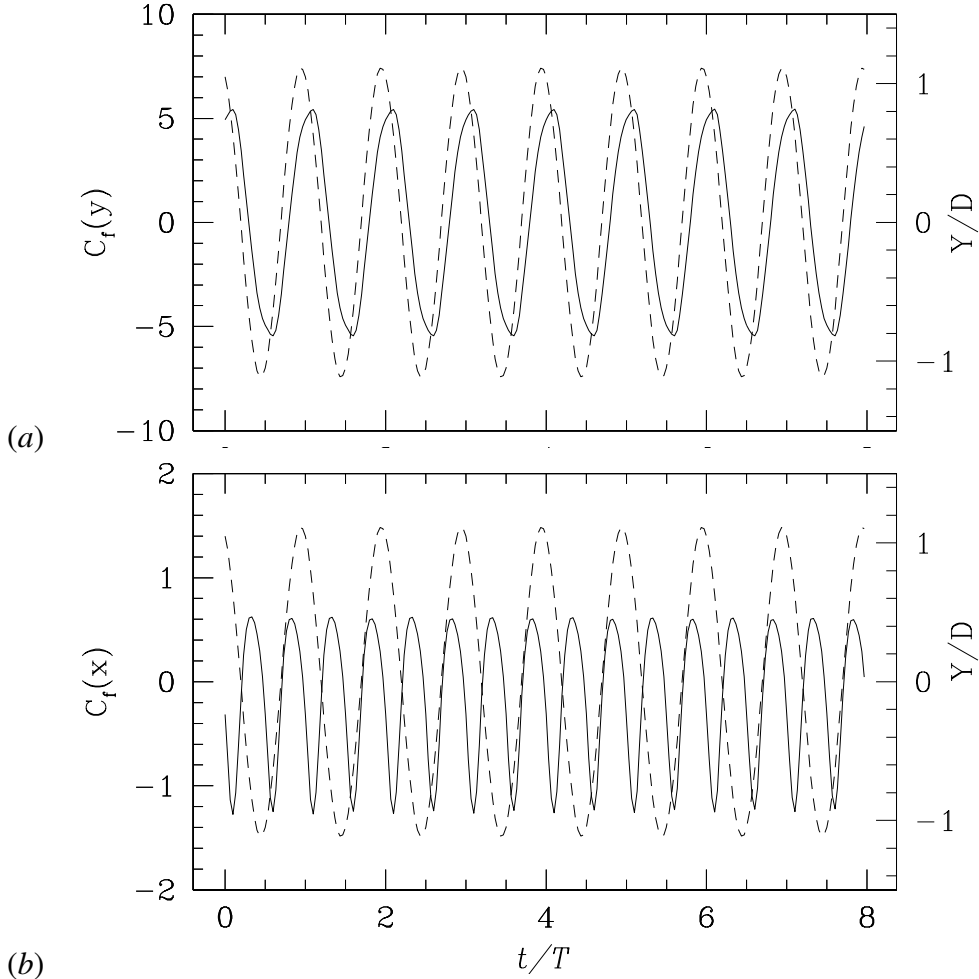


Figure 7.11: Plot of the coefficients of total y - & x -force per unit spanwise length exerted on the cylinder over eight periods of cylinder motion. The simulation was carried out at ($KC=7$, $\beta=14.25$). The force is non-dimensionalised with respect to the root mean square of the cylinders prescribed y -axis velocity and the cylinder diameter D . Also shown is the cylinders displacement (dashed line) over one period of motion.

In figure 7.11 the force time-series for the saturated DNS computations are presented. Inspection of these series shows that the flow remains synchronous with the cylinder oscillation and that the x -force component retains the bi-periodic, non-zero characteristic of the two-dimensional regime S. With reference to the temporal characteristics of the flow, the prediction of the linear stability analysis matches the DNS computations.

Instantaneous vorticity isosurfaces for the leading Floquet mode and for saturated DNS computed at ($KC = 7$, $\beta = 14.15$, $k = 1.75$) are shown in figures 7.12 and

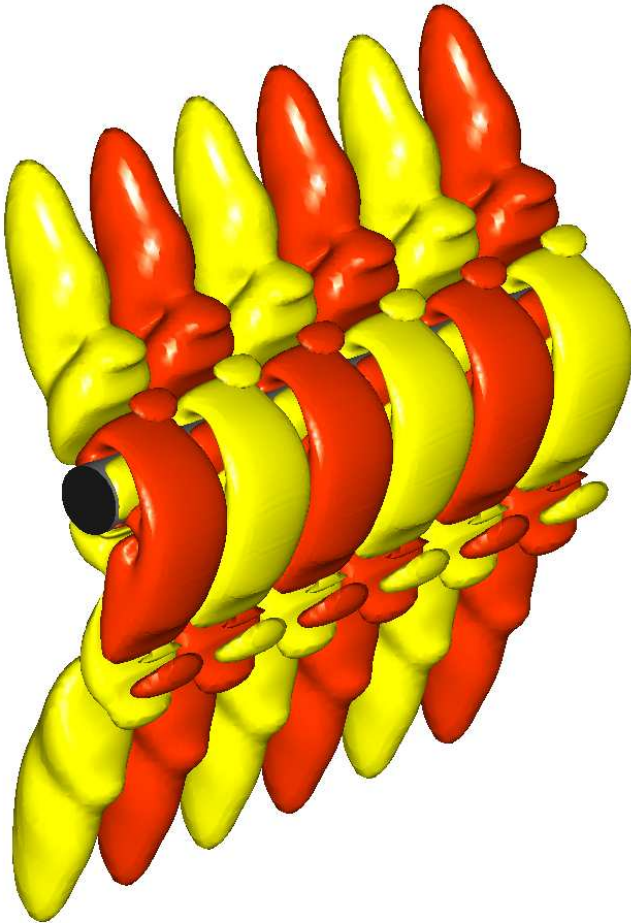


Figure 7.12: Instantaneous vorticity isosurfaces for the regime D instability at ($KC = 7$, $k = 1.75$, $\beta = 14.15$), showing the Floquet mode. Three spanwise repetitions are represented, at the instant when the cylinder is at y_{\max} . The solid isosurfaces show y -component vorticity of equal magnitude but opposite signs.

7.13. The location these computations were performed at in (KC, β) -space lies just past the point of marginal stability. In both cases three spanwise repetitions of a single simulated wavelength are shown. For the DNS, eight spanwise Fourier modes (16 real data planes) were employed to discretise a single spanwise wavelength. The feature dominating the macro structure of both figures is immediately recognisable as the broken K_x two-dimensional symmetry. In the cases shown it breaks to the left of the page, although the alternative break to the right is equally probable. With the knowledge that the Floquet multiplier is real, and consequently introduces no new frequencies into the flow, and from figure 7.12, it is clear that the Floquet mode preserves the H_1 symmetry of the regime S basic state. Likewise, the resultant saturated DNS flow has been shown to experience a force that is synchronised with the cylinder oscillation and from the contours of figure 7.13 it can also be seen that this flow preserves the H_1 symmetry of the regime S basic state.

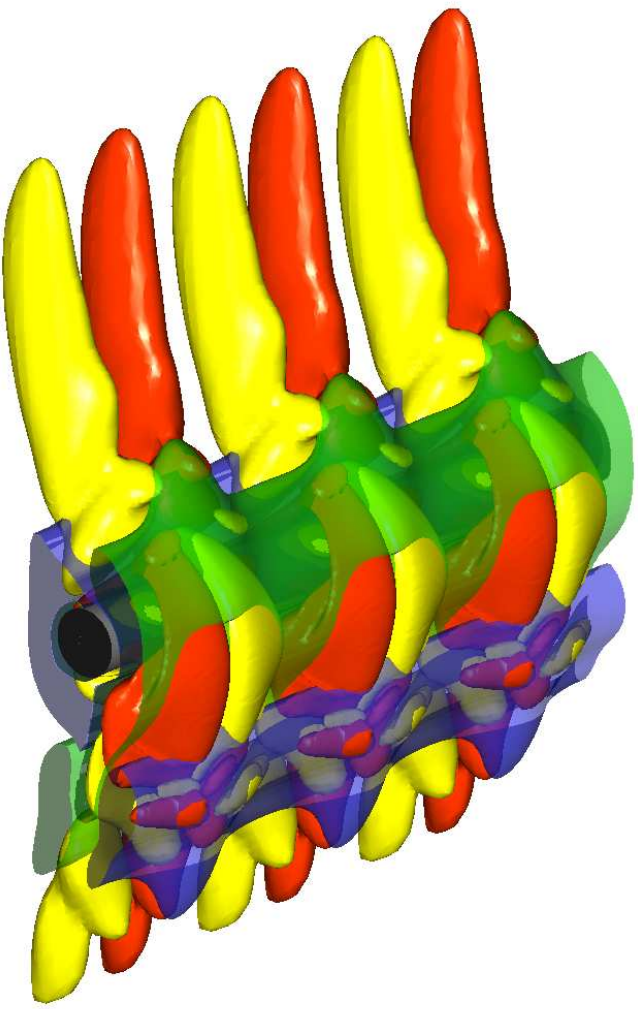


Figure 7.13: Instantaneous vorticity isosurfaces for the regime D instability at ($KC = 7$, $\beta = 14.15$, $k = 1.75$), showing the DNS result. Three spanwise repetitions are represented, at the instant when the cylinder is at y_{\max} . The solid isosurfaces show y -component vorticity of equal magnitude but opposite signs, while additionally translucent isosurfaces show z -component vorticity.

Figures 7.14 and 7.15 present the same instantaneous vorticity isosurfaces from a different viewpoint. In these figures the changes resulting from nonlinear interactions are more readily visualised and related back to the experimental observations of Tatsuno and Bearman (1990). In both figures the coupling of alternately signed vorticity into pairs can be seen. In the vorticity contours on the shoulders of the cylinder pairs of vorticity are seen to roll up towards each other in the same manner as was observed for flows of regime B. As with regime B, an array of alternating vorticity is seen to emanate from above and below the cylinder. However, in contrast to the DNS flow of regime B, where the primary influence of the nonlinear interactions was seen to result in an alternating twisting of the orientation of the vorticity, here it is seen to result in the pairing of adjacent vorticity. Con-

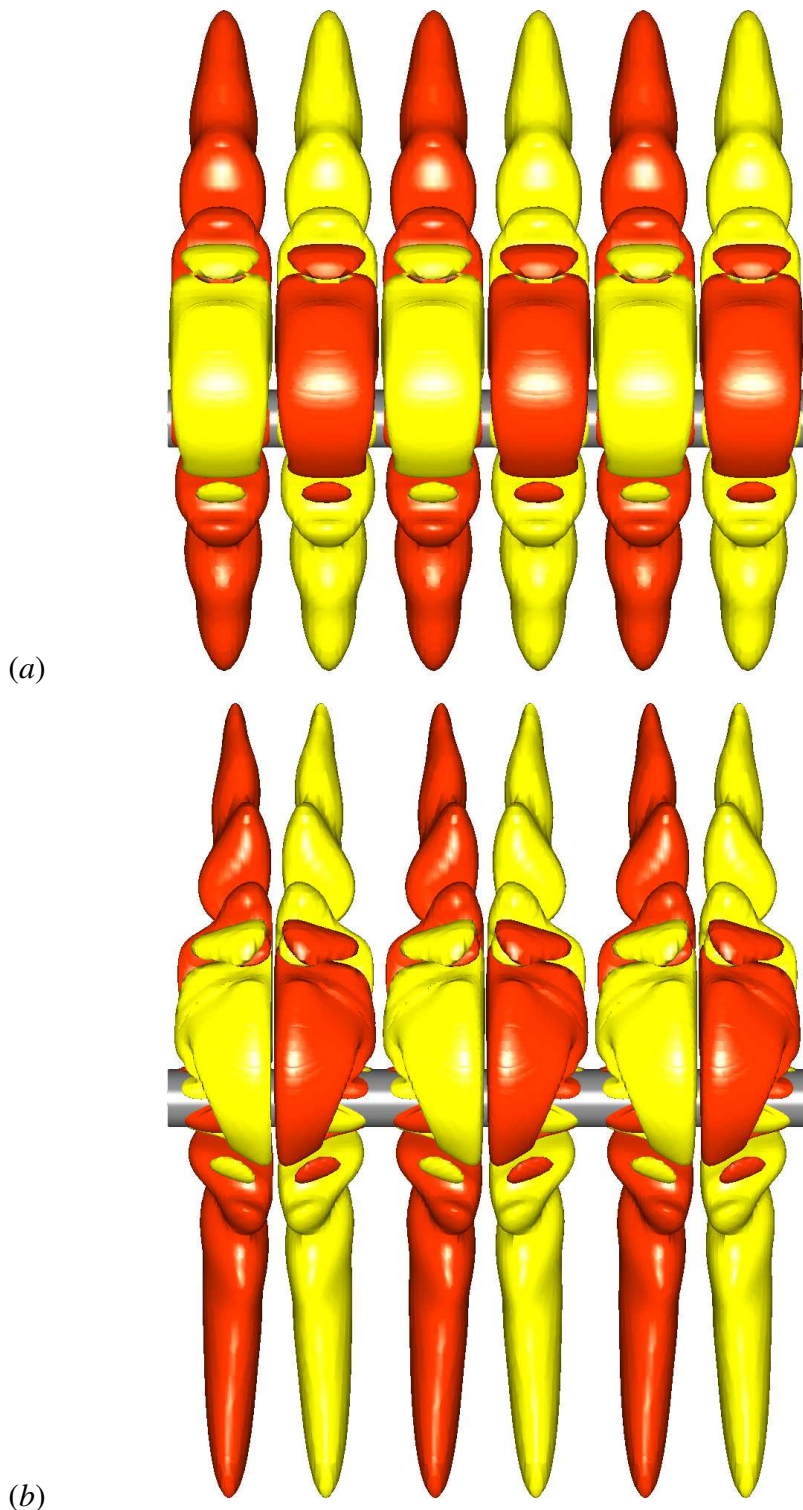


Figure 7.14: Instantaneous vorticity isosurfaces for the regime D instability. Shown are the (a) Floquet mode and (b) DNS result at ($KC = 7$, $\beta = 14.15$, $k = 1.75$). Three spanwise repetitions are represented, at the instant when the cylinder is at y_{\max} . The solid isosurfaces show y -component vorticity of equal magnitude but opposite signs.

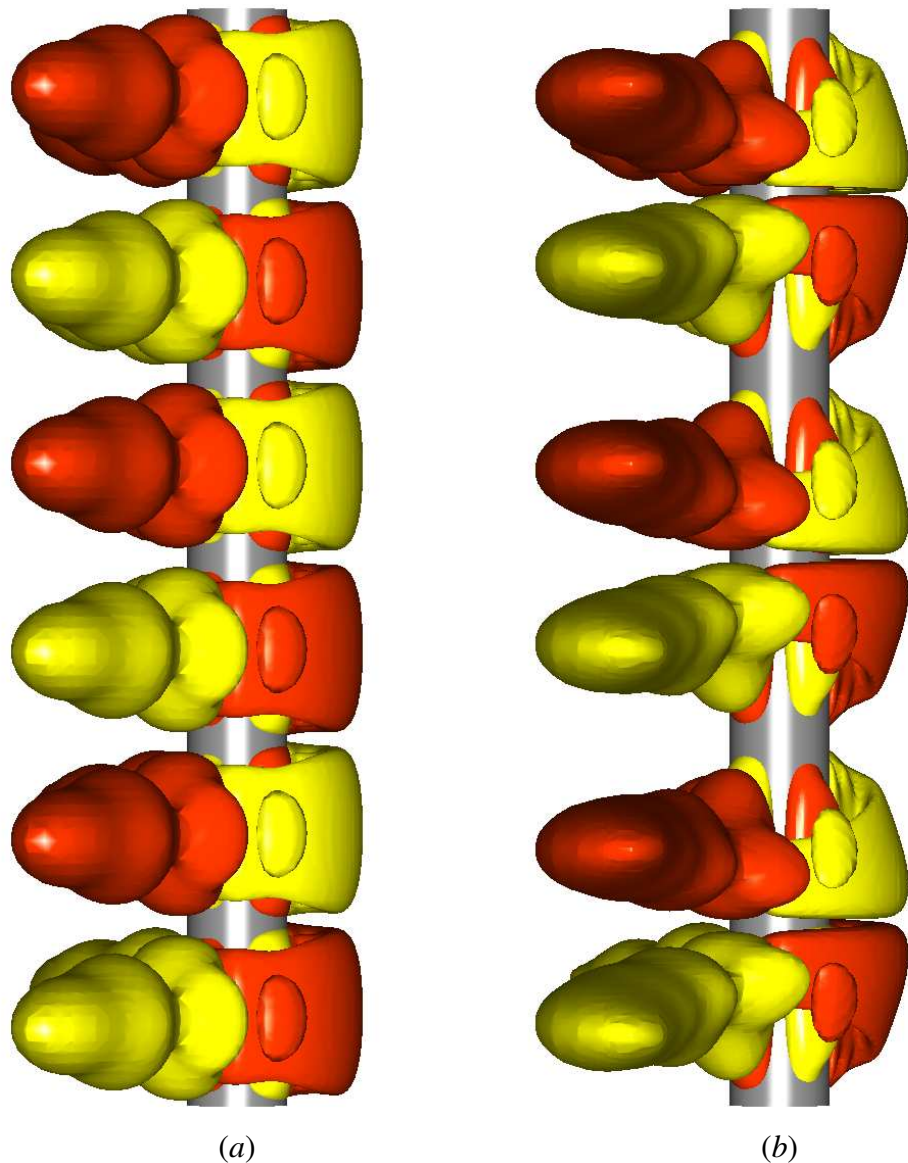


Figure 7.15: Instantaneous vorticity isosurfaces for the regime D instability. Shown are the (a) Floquet mode and (b) DNS result at ($KC = 7$, $\beta = 14.15$, $k = 1.75$). Three spanwise repetitions are represented, at the instant when the cylinder is at y_{\max} . The solid isosurfaces show y -component vorticity of equal magnitude but opposite signs.

sequently the spacing between sequential vorticity ‘spikes’ varies depending on whether it is coupled with the previous spike. Tatsuno and Bearman (1990) noted that “...tubes seemed to be formed perpendicular to the cylinder at certain intervals along the axis of the cylinder, in which fluid is travelling faster than the surrounding fluid.” It is likely that these tubes are a consequence of the stronger pairing of the vorticity ‘spikes’ above and below the cylinder.

The stronger nonlinear effects present and the breaking of the K_x symmetry mean that the mechanism of vorticity production and transport for regime D is more compli-

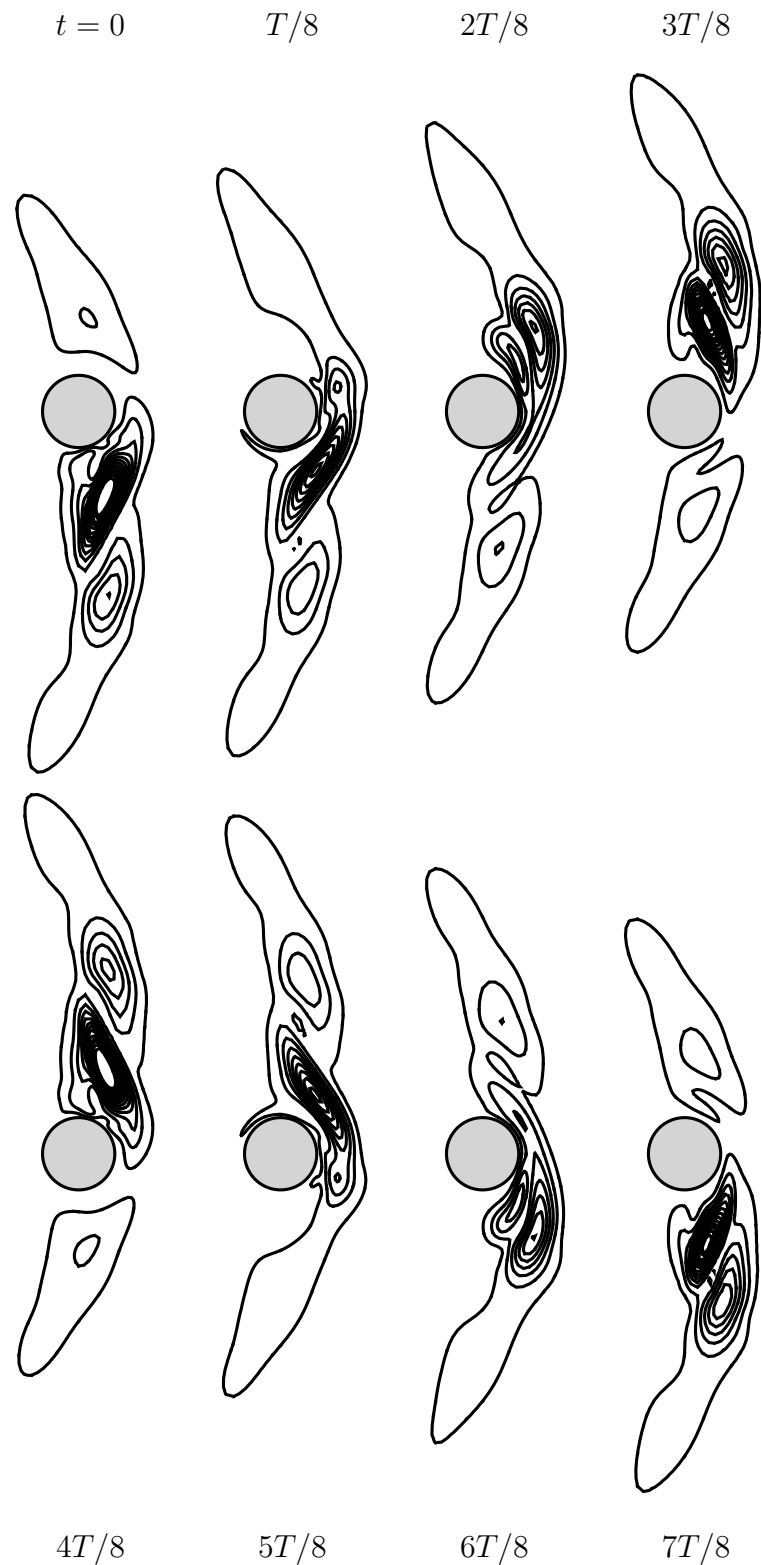


Figure 7.16: Contours of instantaneous kinetic energy in the fundamental spanwise harmonic for three-dimensional synchronous flow in regime D, obtained over one temporal period via saturated DNS at ($\beta = 14.15$, $KC = 7$, $k = 1.75$).

7.3. REGIME A – D

cated than that of regime B. As with regime B, it retains the feature that at any spanwise location the sign of y -vorticity that advects far away from the cylinder agrees with that generated at the cylinder surface, and is opposite that which appears most prominent near the shoulder of the cylinder in figures 7.12 and 7.13. In figure 7.16 a sequence of contours of kinetic energy in the first spanwise harmonic from the saturated DNS are presented, plotted at $T/8$ increments. Unlike their equivalents for regime B, the energy distribution is not symmetric and it appears most of the energy in the spanwise mode arises with each oscillation from a sweep past a single shoulder of the cylinder. The shoulder for which this occurs is on the opposite side of the cylinder from the direction the resulting flow breaks toward. This is consistent with Tatsuno and Bearman's description of a stronger vortex being formed only on one side of the cylinder per half-cycle. Again it appears likely that the three-dimensional structure of regime D results from a centrifugal instability, re-energised in each sweep past a (in this case, principally a single) shoulder of the cylinder.

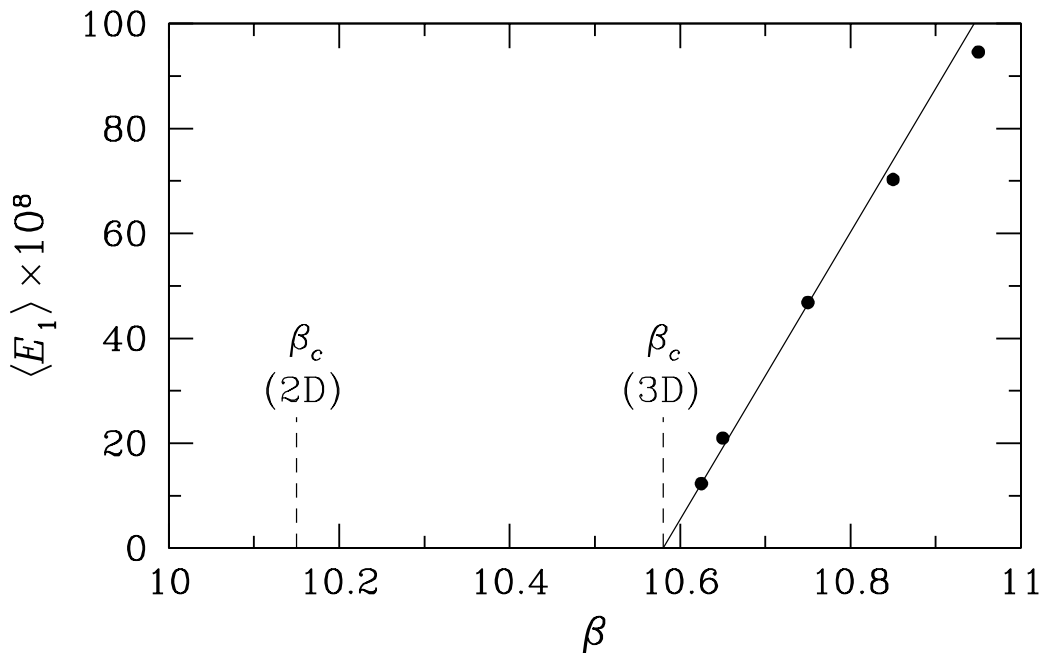


Figure 7.17: Bifurcation diagram for three-dimensional symmetry breaking in regime D, showing normalised time-average kinetic energy in the first spanwise harmonic, $\langle E_1 \rangle$ as a function of β at $KC = 8$, $k = 1.55$. Also indicated is the Stokes number for two-dimensional symmetry breaking at the same oscillation amplitude.

To examine the nonlinear properties of the bifurcation and the agreement between the Floquet prediction and the DNS computations for the onset of this bifurcation, the variation of the normalised time-average kinetic energy in the fundamental spanwise harmonic, $\langle E_1 \rangle$ from saturated DNS is explored. In figure 7.17 the outcome of this investigation is

7.3. REGIME A – D

plotted for various Stokes numbers at a fixed $KC = 8$. The onset of the bifurcation in DNS agrees well with the three-dimensional linear stability analysis value, β_c (3D). The nature of this bifurcation is clearly supercritical, as shown by the continuous increase in energy after the point of onset. Also shown is the location of the two-dimensional linear stability analysis value, β_c (2D). The margin between the two-dimensional and three-dimensional bifurcation onsets is most likely due to the two-dimensional bifurcation being supercritical. It was established through use of forced K_x -symmetric base flows, as seen by branch III of figure 7.1(a), that this three-dimensional bifurcation requires the two-dimensional bifurcation to have occurred prior to its onset. As the two-dimensional bifurcation is supercritical it will develop with distance in (KC, β) -space space from the point of onset and it is likely that the three-dimensional bifurcation requires a certain saturation of regime S type flow before it can occur.

7.4 Regime C

The section of the two-dimensional symmetry breaking curve, see figure 7.1(a), between the onset of the three-dimensional modes I and II denotes the onset of a quasi-periodic mode. This two-dimensional bifurcation introduces a new period into the flow and consequently breaks a core requirement for the use of Floquet analysis: a periodic flow. The onset of the quasi-periodic mode results in a flow that resembles the experimental images of regime C in the x - y -plane. In order to study the bifurcation to three-dimensionality along this curve three-dimensional DNS has been employed. This has a much greater computational expense than Floquet analysis and introduces more parameters into the computations such as the appropriate choice of spanwise wavenumber and the number of spanwise planes required to accurately model the flow. In order to reduce the computational overhead a number of restrictions were made to the scope of investigation. Instead of determining the marginal stability curve in (KC, β) -space for this bifurcation, attention was restricted to a single Stokes number: $\beta = 40$. Additionally, the stability characteristics of a particular wavenumber were determined by monitoring the time-averaged kinetic energy in the spanwise harmonic associated with this wavenumber. This meant that DNS could be employed with a single spanwise mode to model the flow. Although this does not result in a completely accurate modelling of the flow, it is sufficient to determine if a particular wavenumber has energy associated with it. DNS with multiple spanwise modes is employed later to visualise the results.

Figure 7.18(a) presents the results of a large number of three-dimensional DNS computations in (KC, k) -space with a single spanwise mode. The simulations required longer computational times to achieve a result in comparison to the Floquet analysis simulations. Locations in (KC, k) -space were classified as stable or unstable depending on the time-averaged kinetic energy in the spanwise mode. The boundaries of the unstable regions were detected by the sudden jump in the time-averaged kinetic energy.

Three bands of wavenumbers, C_I , C_{II} , and C_{III} , were identified which represent regions in (KC, k) -space that contain unstable wavenumbers. The boundaries of these bands are not explicitly defined, although some refinement at the tips of these regions was achieved, due to the computational expense involved in mapping them out. The first band of wavenumbers, band C_I , found to have energy in the spanwise mode was centered about $(KC \approx 4.6, k = 0.5)$. It is possible that this band of wavenumbers emanates from $k = 0$, i.e. as perturbations of two-dimensional flow, however it was not possible to accurately determine the stability of spanwise modes with $k < 0.5$. Additionally this band of wavenumbers occurs prior to the onset of the two-dimensional QP mode and it is speculated that the nature of the bifurcation to this mode is sub-critical. The second band of wavenumbers to become unstable was centered about $k \approx 1.75$. When plotted against predicted wavelengths from Floquet analysis, figure 7.1(b), this wavelength

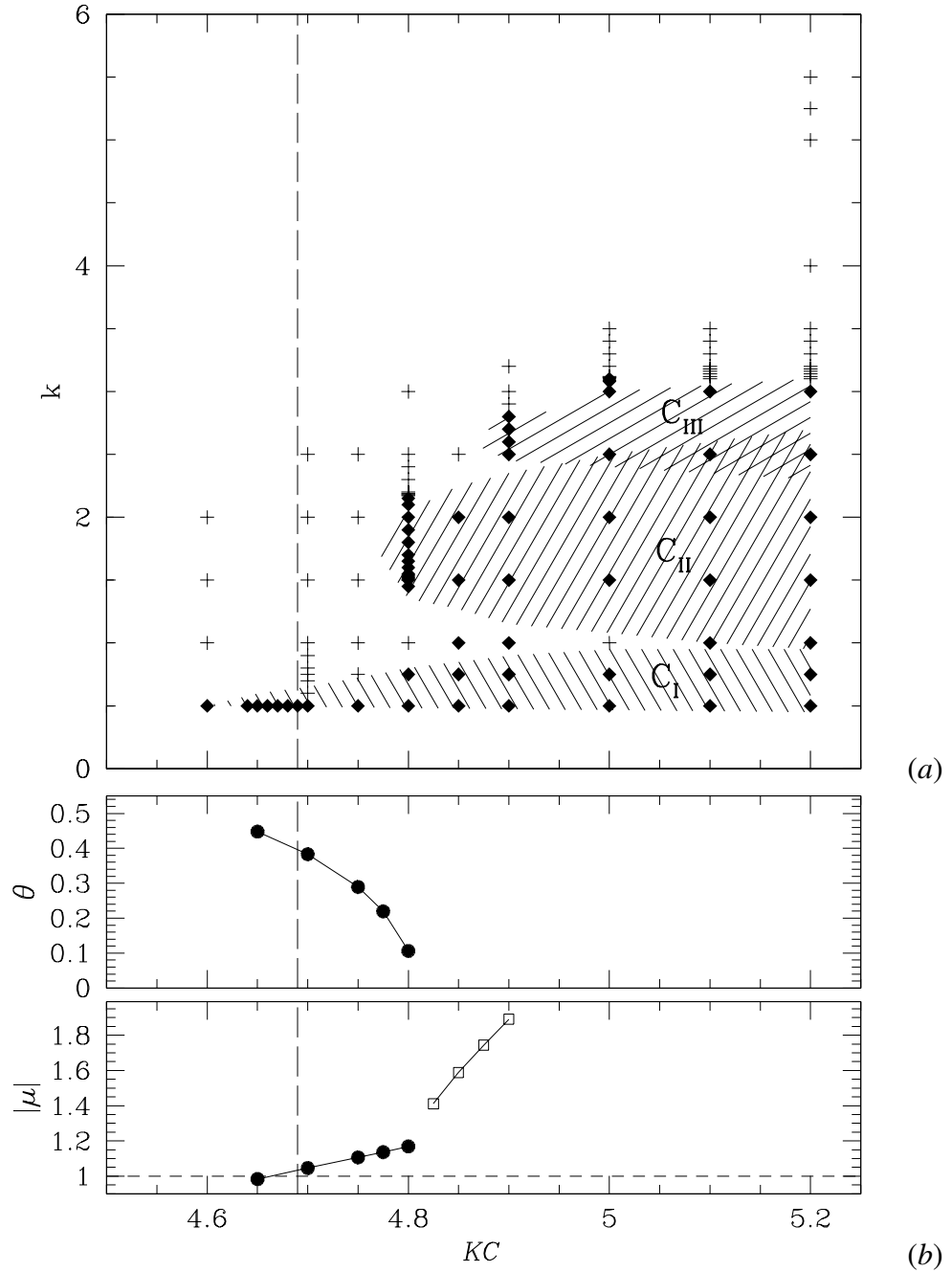


Figure 7.18: Results of a stability analysis using DNS with a single spanwise mode at a fixed $\beta = 40$. Figure (a) shows the variation of the stability of points in this control space as a function of KC and the spanwise wavenumber, k . Points are classified as: \blacklozenge unstable or $+$ stable. The three shaded regions, C_I , C_{II} , and C_{III} , indicate possible bands of unstable wavenumbers. In (b) are shown the variation of the Floquet multiplier magnitude and phase angle at $\beta = 40$.

lies on a curve extrapolated through the points denoting the transition to regime D. It is therefore considered likely that this band of wavenumbers is arising from regime D like structures in the flow which would form quasi-periodically as a consequence of the two-

7.4. REGIME C

dimensional regime QP. The third band of wavenumbers, which again occurs for a slight increase in KC is centered around $k = 2.5$. This band could conceivably be part of the second band of unstable wavenumbers, however doing so would encompass a stable point at $(KC = 4.85, k = 2.5)$. This point was found to be stable and thus bands C_{II} , and C_{III} are drawn as two separate regions.

An attempt was made to isolate a fourth band of wavenumbers for $KC = 5.2$, $5.0 \leq k \leq 5.5$. As noted previously in this chapter, K_x symmetry was enforced in the Floquet analysis and the location of the unstable wavenumbers that would occur for flows with enforced symmetry was computed, see branch III on figure 7.1(a). At the locations predicted by three-dimensional Floquet analysis, see figure 7.1(b) for values, no unstable wavenumbers were detected using DNS.

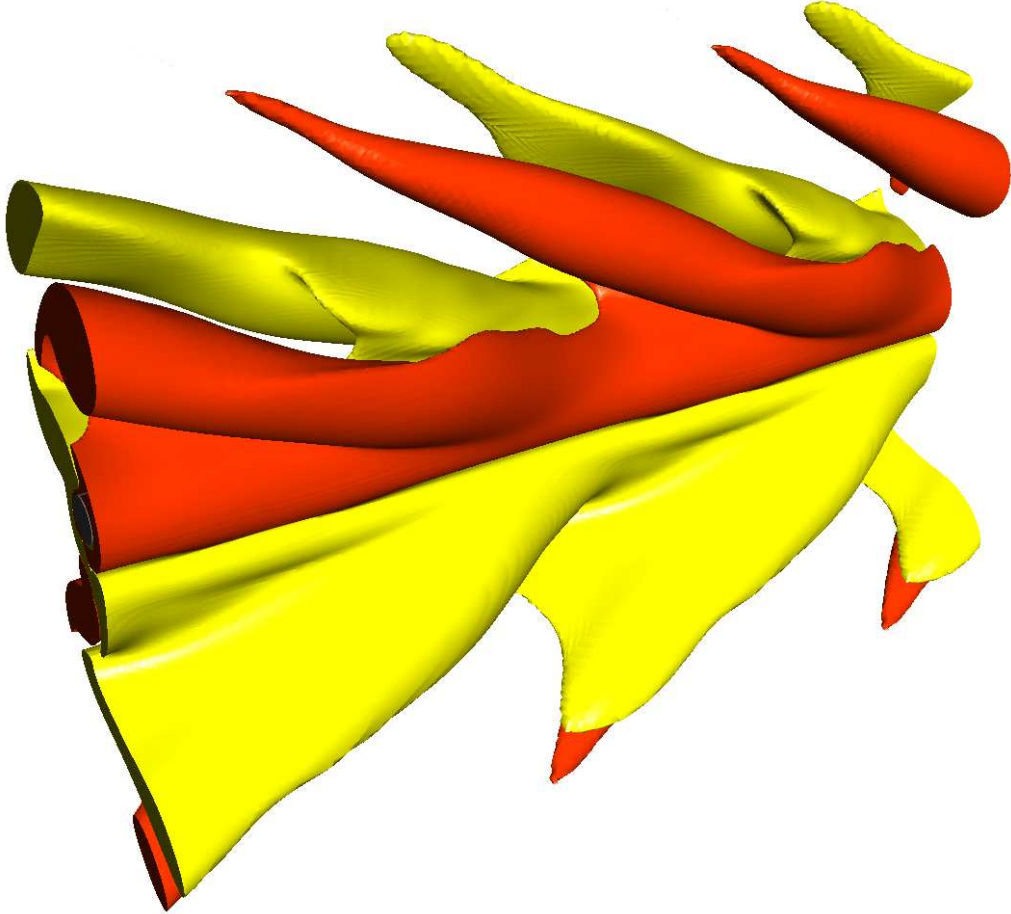


Figure 7.19: Instantaneous vorticity isosurfaces for the regime C instability, obtained from DNS at $(\beta = 40, KC = 4.8, k = 0.5)$. Two spanwise repetitions of equal-magnitude positive and negative isosurfaces of spanwise vorticity component are shown in a perspective view.

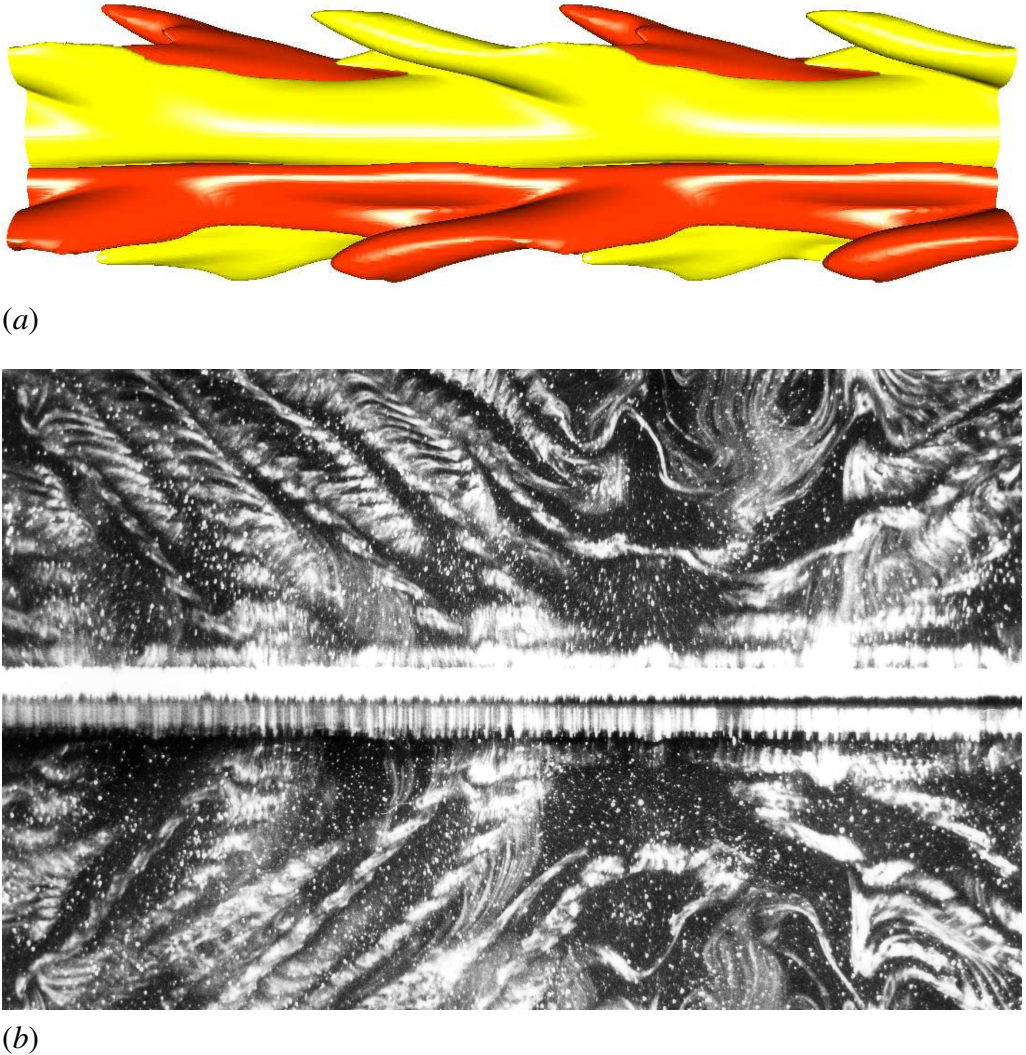


Figure 7.20: Views of structures for the regime C instability in the y - z plane. In (a) are shown instantaneous vorticity isosurfaces, obtained from DNS at ($\beta = 40$, $KC = 4.8$, $k = 0.5$). Two spanwise repetitions of equal-magnitude positive and negative isosurfaces of spanwise vorticity component are shown. The isosurface magnitudes are higher than those shown in figure 7.19. In (b) an experimental image, provided by Tatsuno and Bearman, at ($\beta = 50.1$, $KC = 4.4$) is shown. The plane of visualisation is through the centre of the cylinder. Images are not shown to the same scale.

Three-dimensional DNS was conducted at ($\beta = 40$, $KC = 4.8$, $k = 0.5$), which lies within the first instability region, C_I , with 32 spanwise Fourier modes. In figures 7.19, 7.20 and 7.21 isosurfaces of the spanwise vorticity component are presented. Additionally in figures 7.20 and 7.21 experimental visualisations from Tatsuno and Bearman (1990) obtained from the same spatial viewpoint are presented. The isosurfaces in figure 7.19 are suggestive of a travelling wave which in combination with the progression of the contours of vorticity in the x - y -plane figure 6.19 would indicate that the slantwise vortices are travelling to the right in the figure 7.19. In figure 7.20 a side view of these vorticity

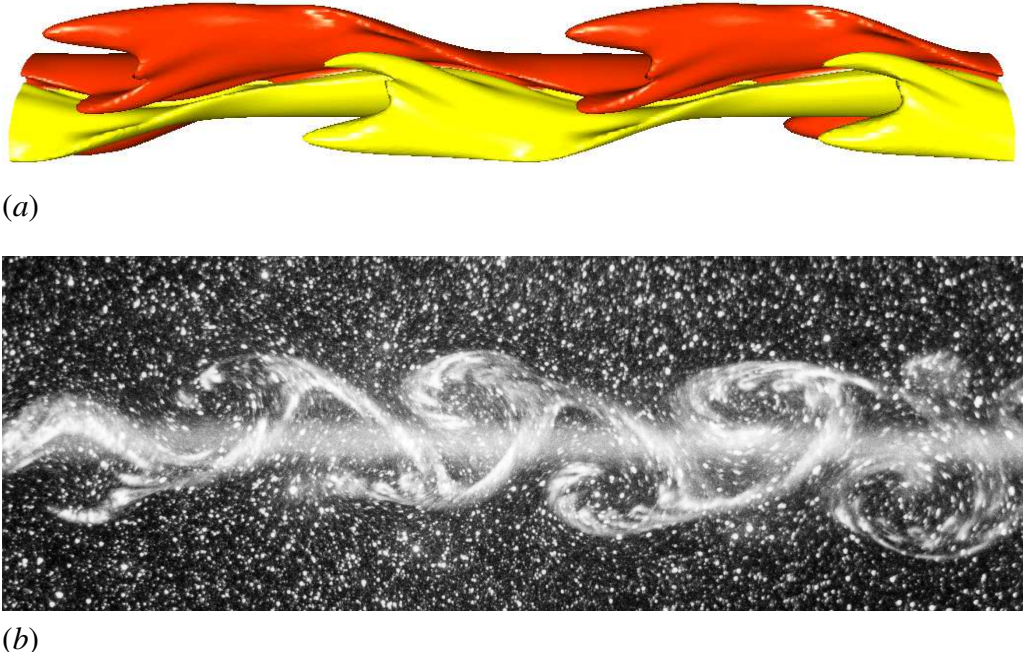


Figure 7.21: Views of structures for the regime C instability in the x - z plane. In (a) are shown instantaneous vorticity isosurfaces, obtained from DNS at ($\beta = 40$, $KC = 4.8$, $k = 0.5$). Two spanwise repetitions of equal-magnitude positive and negative isosurfaces of spanwise vorticity component are shown. The isosurface magnitudes are higher than those shown in figure 7.19. In (b) an experimental image, provided by Tatsuno and Bearman, at ($\beta = 46.9$, $KC = 4.4$) is shown. The plane of visualisation is $4.5D$ above the centre of the cylinder. Images are not shown to the same scale.

isosurfaces are shown alongside a dye visualisation of Tatsuno and Bearman. While the angle between the cylinder and the array of chevron-like shapes is different, there is a definite similarity between the two. The difference in this angle could be caused by the different location in (KC, β) -space that the two image were produced at. The top views, figure 7.21, also have a remarkable similarity between them.

In figure 7.22 a sequence of contours of kinetic energy in the first spanwise harmonic from saturated DNS is presented, plotted at $T/8$ increments. Near the cylinder the contours more closely resemble those of regime B, see figure 7.8, with the energy contours seeming to be split equally about the cylinder as it oscillates. Although, unlike regime B, it is not perfectly symmetrical about the y -axis and with increasing distance from the cylinder this becomes more evident. However, further from the cylinder the contours have a passing resemblance to those of regime D, see figure 7.16, with its distinctive boomerang like shape.

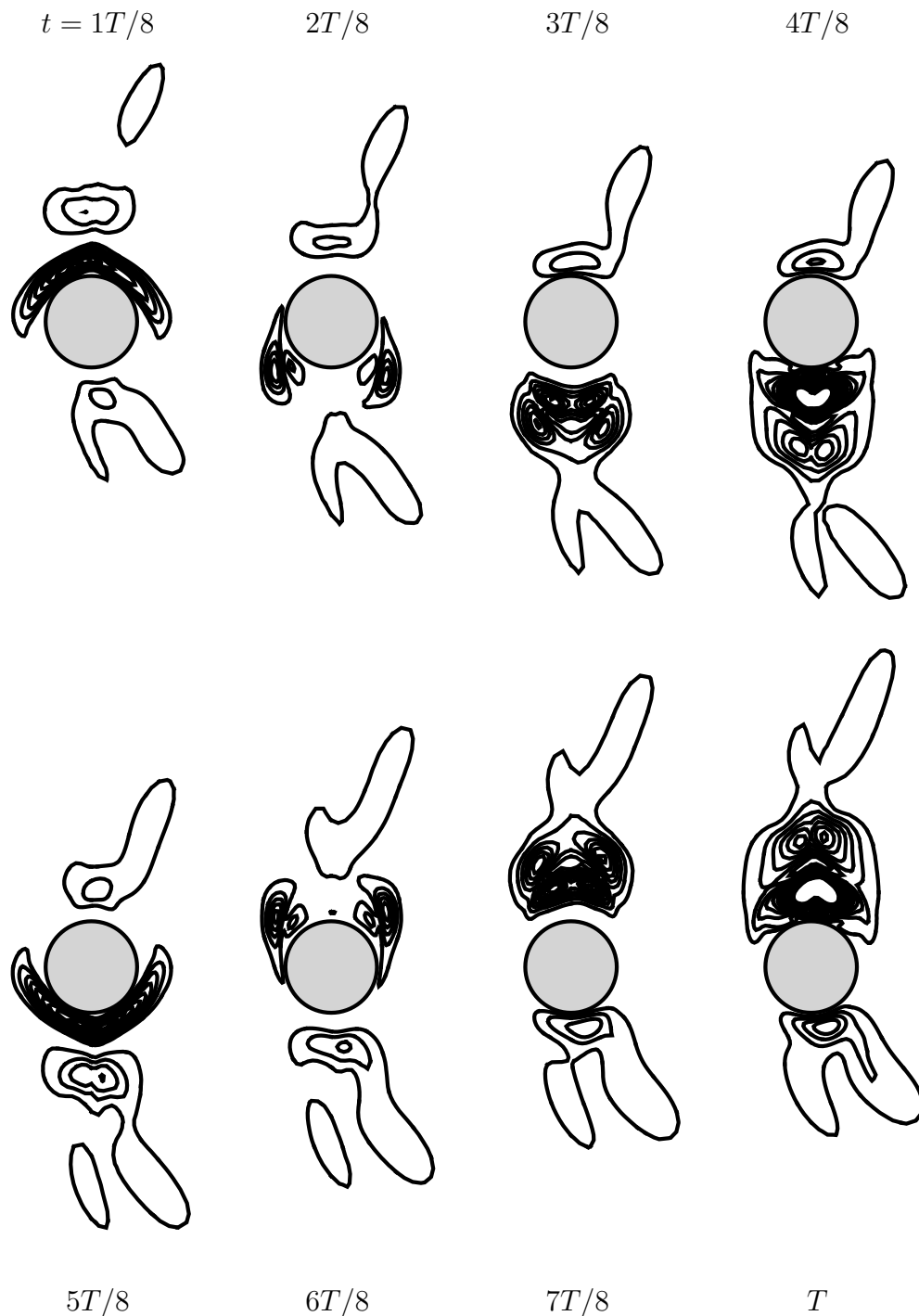


Figure 7.22: Contours of instantaneous kinetic energy in the fundamental spanwise harmonic for three-dimensional synchronous flow in regime C, obtained over one temporal period via saturated DNS at ($KC = 4.8$, $\beta = 40$, $k = 0.5$).

7.5 Discussion

The marginal stability curves identified by three-dimensional Floquet analysis were found to be in excellent agreement with an amalgam of the regime boundaries identified by Tatsuno and Bearman (1990) (see figure 7.2). The multiplier branches I and II matched the locations of the three-dimensional transitions A→D and A^{*}→B, respectively. It is however the result of branch III that is particularly notable. It was stated previously that this branch is a spurious result and it has been detected neither by experiments or three-dimensional DNS. The interest in this result lies in its relationship to the bifurcation that actually occurs along branch I: enforcing K_x symmetry shifts the onset of a three-dimensional instability in (KC, β) -space from its location of branch I to the right. It was established in §7.3 that a transition to the two-dimensional flow of regime S, with its broken K_x symmetry, must occur before any three-dimensional transition occurs. In addition, as the onset of regime S is supercritical, there is a very small regime beyond the onset of regime S, see figure 7.17, and before the onset of the three-dimensional mode where the flow remains two-dimensional. Only a very small change in either KC or β is required before the transition to regime D occurs and it might be difficult to determine this experimentally. The wavenumbers predicted by Floquet analysis for branch I (the A–D transition) were in excellent agreement with the wavenumbers identified by Tatsuno and Bearman (1990).

In figure 7.23(a) the two- and three-dimensional outcomes of the Floquet analysis for the regimes A^{*}, B and E are compared with a wider selection of previous experimental and analytical results. Branch II agrees well with the location of Tatsuno and Bearman's boundary between regimes A^{*} and B, with the experimental results of Honji (1981), and, towards the upper limit of the Stokes numbers we have used, with the stability analysis of Hall (1984, here, equation 2.3), as well as the correlation of Sarpkaya (2002, here, 2.4). As noted in §7.2 and shown again here in figure 7.23(b), the predictions of the spanwise wavelengths are in reasonable agreement with the measurements of Tatsuno and Bearman (1990). While these values are not as close as the agreement reached for wavelengths on the A–D boundary (branch I), the values are quite close. Both the linear predictions of this investigation and the experimental values of Tatsuno and Bearman (1990) for the wavelengths along this transition lie between the correlation supplied by Sarpkaya (2002, here, 2.4) and the high- β -asymptotic result of Hall (1984, here, 2.5). Also shown in 7.23(a) is the transition between regimes B and E which coincides well with the two-dimensional transition to regime QP and the ‘upper curve’ of Honji (1981). The flows of regime E have been characterised by Tatsuno and Bearman (1990) as switching the direction of the induced flow direction from side to side intermittently. The flow of two-dimensional regime QP switches the induced flow direction side to side on a quasi-periodic basis. It is concluded that the B–E transition is fundamentally a two-dimensional one

7.5. DISCUSSION

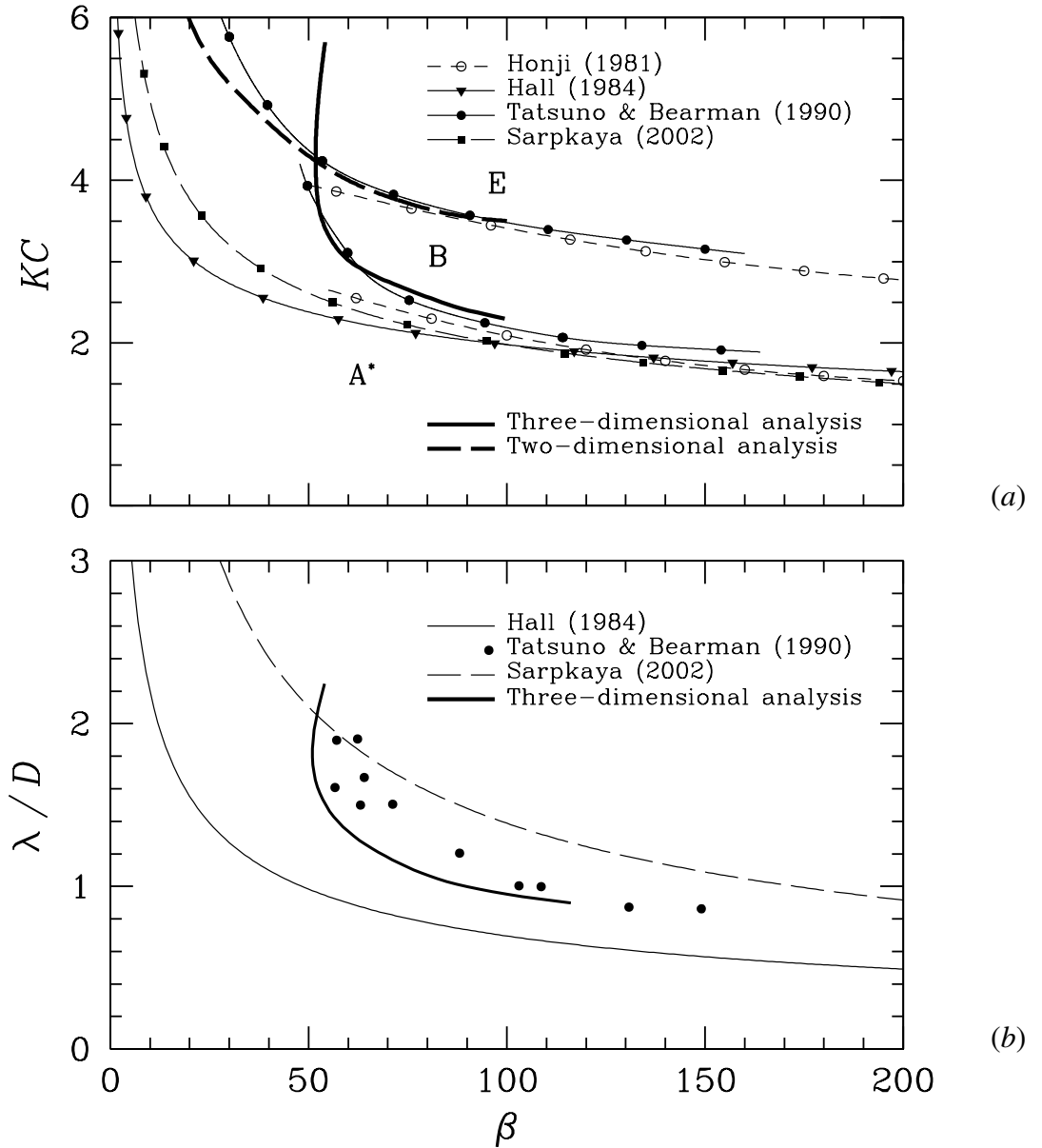


Figure 7.23: Comparison of previous results with those established via Floquet analysis. In (a), thin lines with symbols show (KC, β) marginal stability boundaries presented in previous experimental and theoretical studies (see legend), and thick lines those established in the present Floquet analysis. Text labels A*, B, and E are the regime names given by Tatsuno and Bearman (1990). In (b), lines and symbols show wavelengths of the corresponding three-dimensional instabilities.

with the intermittency in the regime E flows arising through a subsequent instability of the two-dimensional quasi-periodic flow.

Determination of the A-C boundary was not attempted due to the inability to use Floquet analysis. However, through the use of DNS, at greater computational expense, an approximate map of unstable wavenumbers as a function of KC for a fixed $\beta = 40$ was constructed and is shown in figure 7.18. Three bands of unstable wavenumbers are

7.5. DISCUSSION

shown with leading band C_1 , centered around $k = 0.5$. The interesting feature of this band is that it can be detected at values of control parameters below the two-dimensional linear stability boundary for the onset of the two-dimensional regime QP. Visualisations of the three-dimensional DNS flow at this wavenumber (but above the linear stability boundary), see figure 7.19, shows it to have a structure in the x - y plane similar to that of the two-dimensional regime QP. Superimposed on top of this structure are spanwise-travelling waves which give the flow the distinctive chevron-like structure seen in the vorticity contours. Since these travelling waves break the spanwise reflection symmetry (5.3) they will come in K_z -conjugate pairs. In figure 7.24 a close up of the boundaries of regime C is shown along with the curve denoting the onset of the two-dimensional regime QP. This particular region was the only region where the two-dimensional boundaries predicted by the stability analysis did not match the regime boundaries of Tatsuno and Bearman (1990) very well. This aspect, in combination with the detection of a three-dimensional mode before the onset of the two-dimensional regime QP, leads to the tentative conclusion that a three-dimensional subcritical instability of the two-dimensional regime QP may exist.

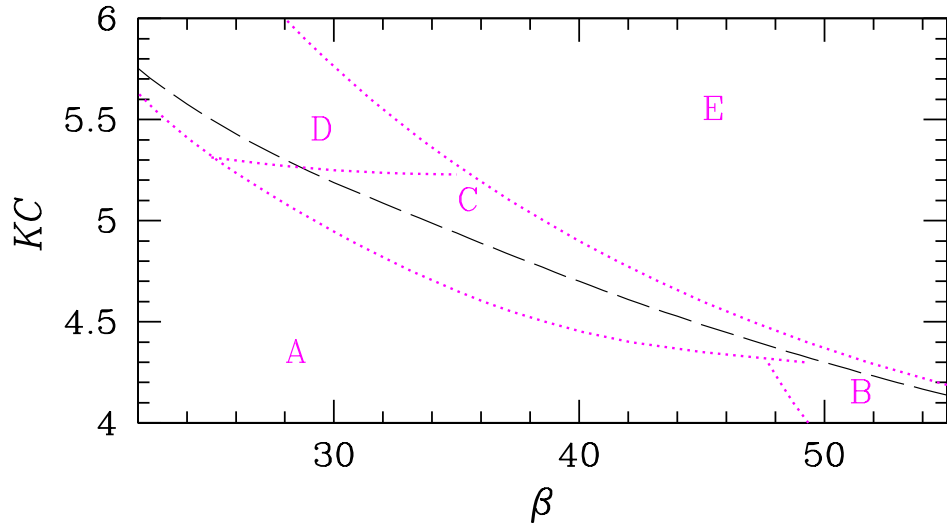


Figure 7.24: Close up in (KC, β) -space of regime C. Shown are regime boundaries and labels of Tatsuno and Bearman (1990) and the two-dimensional quasi-periodic marginal stability curve (dashed line).

7.6 Summary

In this chapter results of a three-dimensional Floquet analysis were presented. Three marginal stability curves in the (KC, β) -space were identified of which two corresponded extremely well to experimental regime transition boundaries. The third marginal stability curve did not have an equivalent in experimental results, which was due to the artificial enforcement of a two-dimensional spatial symmetry. However, it did highlight that a necessary condition for a three-dimensional transition to occur was for the underlying two-dimensional symmetry to be broken. The predicted wavelengths from Floquet analysis agreed with experimental results. In regime C, DNS was used to identify a spanwise-travelling wave. It was hypothesised that the onset of three-dimensionality for the transition A–C may be subcritical in nature. The other transitions, A–D and A^{*}–B, were both found to be supercritical.

Chapter 8

The ‘Swimming’ Cylinder

The study of flows created by the combined rotational and rectilinear oscillation of a circular cylinder has received little attention to date. It has been shown in a series of two-dimensional studies by Elston (1997); Blackburn et al. (1998, 1999) that varying the phase angle between the rotational and rectilinear motions can produce a variety of flow structures in the surrounding fluid. In particular when the rotational and rectilinear motions are synchronised and in-phase then a net thrust has been shown to result. No three-dimensional studies or experimental validation of this result has been published. It has been speculated that the thrust on the cylinder is due to the particular combination of the oscillations causing a net pressure difference across the cylinder which leads to a force being experienced by the cylinder. In this chapter the thrust experienced by the cylinder and the influence of the relative velocity between the rectilinear and rotational oscillations will be investigated in a two-dimensional subspace.

In §8.1 the parameters associated with the combined motions are reviewed and a new computational domain is introduced. In §§8.2 and 8.3 the forces experienced by the cylinder leading to a net thrust are explored in a restricted two-dimensional subspace. In these cases approximately the same control parameters used for the previous studies of Elston (1997) and Blackburn et al. (1999) are employed. An examination of the influence of the velocity ratio between the translational and rotational motions on the net thrust generated is presented in §8.4. In the §§8.5 and 8.6 the results are discussed and summarised.

8.1 Problem Definition & Numerical Validation

As outlined earlier in §1.1 the circular cylinder to be studied is subjected to two forms of simple harmonic motion: one rectilinear and one rotational, as shown in figure 1.1. This results in five dimensionless variables that combine to determine the state of the cylinder at any time. These five variables are restated below:

- The Keulegan–Carpenter number

$$KC = \frac{2\pi A_t}{D} \quad (8.1)$$

- The Stokes number

$$\beta = \frac{f_t D^2}{\nu} \quad (8.2)$$

- A rotational amplitude (in radians)

$$A_\theta \quad (8.3)$$

- A rotational Stokes number

$$\beta_\theta = \frac{f_\theta D^2}{\nu} \quad (8.4)$$

- The phase angle between translation & rotation

$$\phi \quad (8.5)$$

where A_t and f_t are the amplitude and frequency of rectilinear oscillation respectively, A_θ and f_θ are the amplitude (in radians) and frequency of rotational oscillation respectively and D is the diameter of the cylinder. The velocity ratio, taken at the surface of the cylinder, between the translational and rotational motions is expressed as:

$$V_r = \frac{v_t}{v_\theta} = \frac{\beta}{\beta_\theta} \frac{KC}{A_\theta \pi} \quad (8.6)$$

In the previous studies of Elston (1997); Blackburn et al. (1998, 1999) the Keulegan–Carpenter number was specified as $KC = \pi$ and the Stokes number as $\beta = 90$. On a purely rectilinear oscillation basis, this places the flow generated from the cylinder in three-dimensional regime B on a (KC, β) -space map (see figure 2.16) or, on a two-dimensional basis, below the curve of marginal stability denoting the transition to regime QP. In the following investigation these parameters do not vary. The rotational Stokes number is also fixed to a single value, that of the Stokes number, such that $\beta_\theta = \beta = 90$. This avoids a time-varying phase angle between the oscillations. Some preliminary investigations have been conducted into the effect of varying this parameter however they are not reported here. The phase angle between the motions is fixed at $\phi = \pi$ which

8.1. PROBLEM DEFINITION & NUMERICAL VALIDATION

has been shown in Blackburn et al. (1999) to result in net thrust being experienced by the cylinder along the x -axis. The final parameter required to determine the motion of the cylinder is the rotational amplitude, A_θ . In Elston (1997) and Blackburn et al. (1999) this was set to the value $A_\theta = 1.0$. This value will be used in the initial stages of this investigation when the mechanism causing a net thrust is examined, although in later stages it is varied. As a result of fixing the above parameters the equation for the velocity ratio now becomes: $V_r = 1/A_\theta$. This effect of varying this ratio between 0.2 and 2.0 is investigated in §8.4.

The final aspect that is required to completely define this problem concerns the way in which the cylinder is permitted to respond to the forces in a direction perpendicular to the rectilinear oscillation (along the x -axis). The two scenarios that were explored in Blackburn et al. (1999) were to: *a*) fix the cylinder at $x = 0$; and *b*) to permit the cylinder to move along the x -axis in response to the forces on the cylinder surface. Using the latter approach with two-dimensional DNS the cylinder was seen to ‘swim’ along the x -axis and achieve a terminal velocity. In order to permit the cylinder motion the following equation of motion along the x -axis was evaluated at each time step:

$$\ddot{x} + b\dot{x} + cx = \frac{F_x}{m} \quad (8.7)$$

where b and c are the damping and stiffness constants respectively, F_x is the net force per unit length along the x -axis and m is the mass per unit length. The cylinder is assumed to be freely mounted and therefore: $b = c = 0$. In Blackburn et al. (1999) a value of 20 was used for the mass per unit length and this value will again be used here.

8.1.1 Mesh and Boundary Conditions

The spectral element mesh used for this study is shown in figure 8.1. The size of the domain, Ω_s , is $33D \times 25D$ in the x and y directions respectively, with the cylinder placed $8D$ in from the left edge of the domain. On the surface of the cylinder the flow satisfies no-slip boundary conditions, $\mathbf{u} = \mathbf{u}_\theta$ where \mathbf{u}_θ is the rotational velocity of the cylinder surface. In both cases, where the cylinder was either fixed at $x = 0$ or free to ‘swim’, the upper and lower boundaries of the domain are set to prescribed velocity conditions. As described in chapter 3, the Navier–Stokes equations are solved in an accelerating reference frame attached to the cylinder. Consequently the velocity and pressure conditions on these boundaries are adjusted accordingly with the prescribed velocity set as $\mathbf{U}_p = 0$.

The form of the boundary conditions imposed on the left and right edges of the domain depended on whether the cylinder was ‘fixed’ or ‘swimming’ along the x -axis. When the cylinder was fixed, periodic boundary conditions were enforced on these boundaries so that flow leaving one side would reappear on the other side. In the majority of cases flow

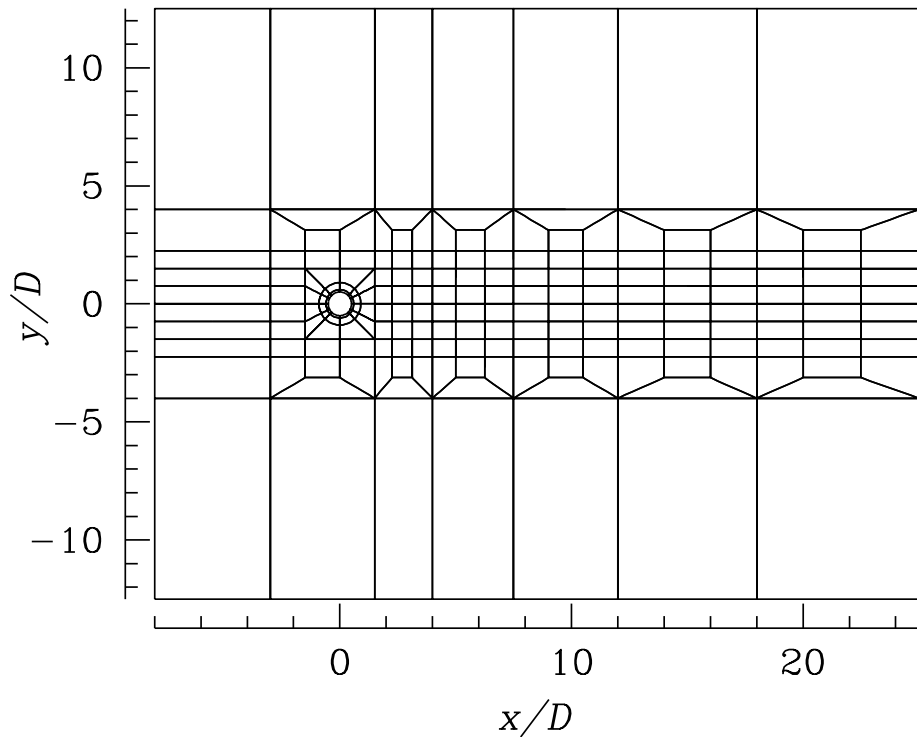


Figure 8.1: Outline of the 206-element $33D \times 25D$ domain, Ω_s , used for the swimming cylinder simulations.

would leave through the right edge and appear at the left edge with the same velocity that it had when it left the domain. In contrast, the boundary conditions when the cylinder was in the ‘swimming’ configuration were slightly time-dependent. In the initial stages of the ‘swimming’ case it was possible that the cylinder could move in the $+x$ direction resulting in the requirement that flow be permitted to enter the domain from the right boundary. To permit this, at this stage of the computations the boundary conditions on the left and right edges of the domain were the same as for the fixed case, periodic. Once the initial stage was past and the velocity of cylinder was always $-ve$, the simulation was stopped and the boundary conditions were altered. Along the left (inlet) boundary a prescribed velocity condition was now enforced, where the velocity was set to the negative of the reference frame velocity, while on the right (outlet) boundary an outflow boundary condition of the following form was enforced:

$$p = 0, \quad \frac{\partial u}{\partial x} = 0, \quad \frac{\partial v}{\partial x} = 0. \quad (8.8)$$

8.1.2 Convergence Studies

The polynomial order for the GLL tensor-product interpolants used with the domain Ω_s was determined through an initial two-dimensional study of a stationary cylinder in a

8.1. PROBLEM DEFINITION & NUMERICAL VALIDATION

p	4	6	8	10
St	0.1988	0.2009	0.2011	0.2011
\overline{C}_x	1.373	1.388	1.389	1.389

Table 8.1: Results of validation tests for two-dimensional flow past a stationary cylinder at $Re = 200$ showing variation in St (Strouhal number) and drag coefficient \overline{C}_x with polynomial order p used for the tensor-product shape functions employed in each spectral element of the domain Ω_s .

cross-flow at $Re = U_\infty D/\nu = 200$. The choice of this test was motivated by the availability of an independent result and that the root mean square value of the Reynolds number for a cylinder in rectilinear motion is $Re = KC\beta/\sqrt{2} = 200$. Curve fits published by Henderson (1995), computed using values obtained in a separate set of two-dimensional spectral element computations, give a Strouhal number $St = 0.1971$, mean drag coefficient $\overline{C}_x = 1.341$ at $Re = 200$ for a domain size of $41 D \times 56 D$ in the stream and cross flow directions respectively.

Computed values of St and \overline{C}_x are shown in table 8.1 against a range of polynomial orders, p , employed for the interpolants used in each spectral element. The results exhibit convergence to four significant figures at $p = 8$. The numerical values of both St and \overline{C}_x are slightly higher than those reported by Henderson although this is expected due to the increased blockage associated with the smaller domain used here. For the results in table 8.1, a timestep with dimensionless value $\Delta t U_\infty / D = 0.005$ was employed; coefficients obtained with $\Delta t U_\infty / D = 0.0025$ were the same to four figure accuracy.

8.2 ‘Fixed’ Cylinder at $V_r = 1.0$

In this section the results are presented for the case the velocity ratio was set to one and the cylinder was constrained in the x -axis to remain at $x = 0$. In figure 8.2 two sets of instantaneous vorticity contours for half a period of oscillation are shown. The white ‘cores’ of vorticity close to the cylinder represent the highest magnitudes of vorticity but are not shown due to the desire to achieve a reasonable resolution of the vorticity contours of lesser magnitude. Only half a period of this flow is shown owing to the spatial and temporal symmetry of the motion which, in this case, results in the flow having a H_1 symmetry. On the right is a set of vorticity contours, at $t \gtrsim 3480T$, produced using the domain Ω_s with periodic boundary conditions on the left and right edges. Also shown on the left side in figure 8.2 is a set of vorticity contours from Blackburn et al. (1998) conducted for the same set of motion parameters but in a closed domain and at a time much less than the set on the right: $t \approx 350T$. The previously published results show the outer layers of vorticity forming a continuous sheet, albeit of very low magnitude. In contrast the vorticity contours on the right show that this outer sheet of vorticity has evolved into a row of discrete vortices that are strongly interlocked with the inner vortex sheets. Two reasons exist for this discrepancy: firstly, the closed domain employed in Blackburn et al. (1998) will result in a different incident velocity profile than the more recent case where the periodic boundary conditions employed result in a more laminar velocity profile, secondly, the case on the right has been evolved approximately 10 times longer than the published case. Correspondingly the fluid circulating through the domain is closer to reaching its terminal velocity.

This particular combination of motion results in a jet of fluid perpendicular to the axis of translational oscillation in the $+x$ direction, as represented by the vorticity contours in figure 8.2. In these figures it can clearly be seen that the regions of highest vorticity formation are concentrated on the left-hand side of the cylinder. The equation for the formation of vorticity in a two-dimensional incompressible flow at a no-slip boundary is (Morton; 1984, see §3.2)

$$-\nu \mathbf{n} \cdot \nabla \omega = -\mathbf{n} \times (\nabla P + \mathbf{a}). \quad (8.9)$$

The combined oscillation results in the left-hand face always having a larger tangential acceleration and thus the vorticity production term, $\mathbf{n} \times \mathbf{a}$ is always larger on the left-hand side. The vortex sheets formed as a result of the oscillations rapidly cross-annihilate and diffuse in the wake, as can be seen in the vorticity contours on the right in figure 8.2, so that with increasing distance from the cylinder the vortex sheets are rapidly weakening. At a distance of approximately five diameters downstream the vorticity has dissipated to a level below the magnitude of the smallest contour.

8.2. ‘FIXED’ CYLINDER AT $V_R = 1.0$

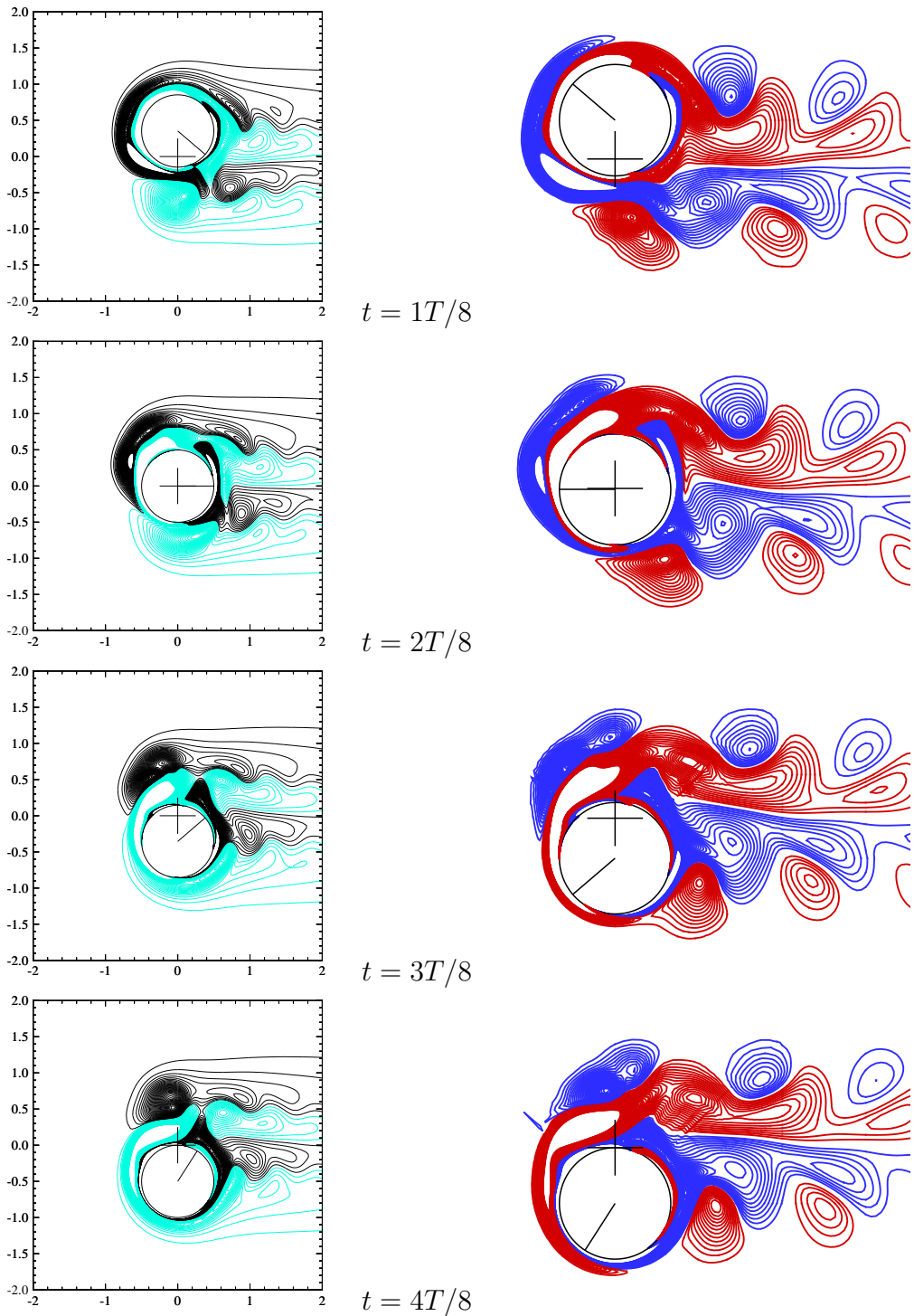


Figure 8.2: Instantaneous vorticity contours over half of one oscillation period, T for a cylinder fixed at $x = 0$. Images are shown at intervals of $T/8$. Two sets of vorticity contours are shown: on the left, in black and cyan coloring, are images first presented in Blackburn et al. (1998) at $t \approx 350T$ in a closed domain, while on the right, in red and blue coloring, are flows produced in the domain Ω_s with inflow and outflow boundary conditions at $t \gtrsim 3480T$. The cylinder’s rotation is indicated by the radial line and its vertical rest position by the crosshairs.

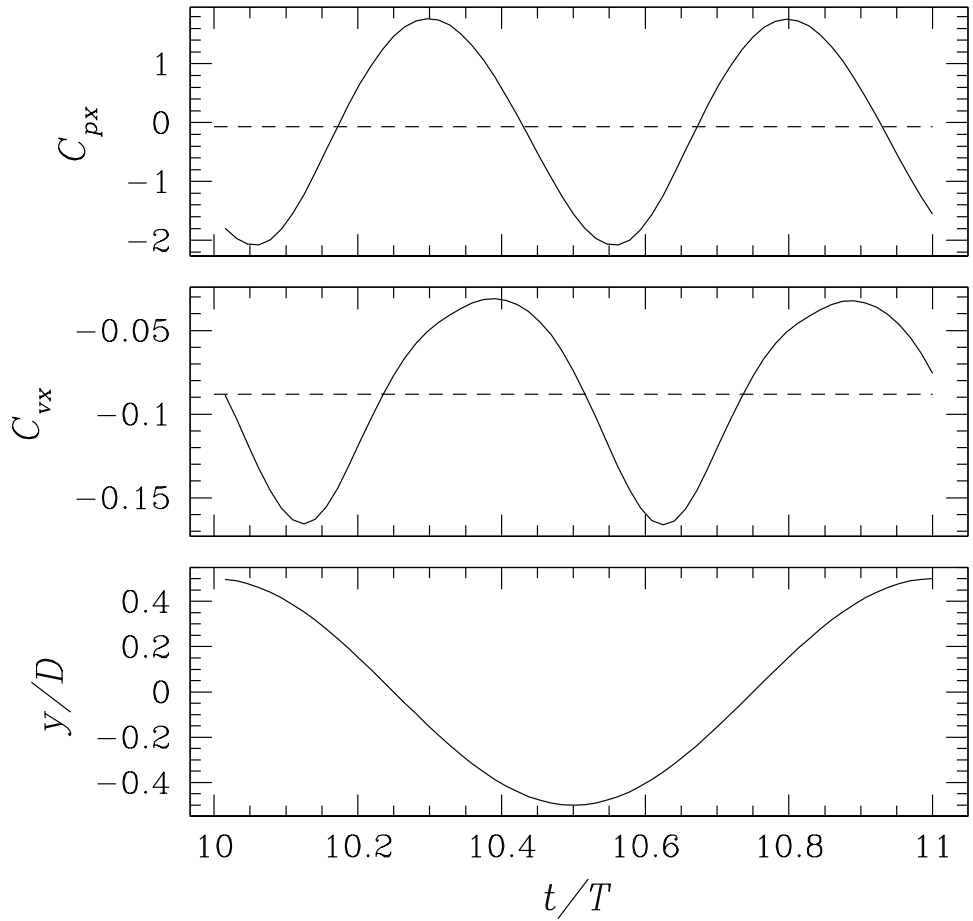


Figure 8.3: Variation of x -axis force components over a single period of oscillation starting at $t = 10T$. Shown are the coefficient of force due to pressure, C_{px} , due to viscosity, C_{vx} along with the cylinders displacement y/D . The coefficients of force are normalised using the cylinder diameter and a dynamic pressure based on the RMS mean of the rectilinear velocity. The dashed lines represent the mean values: $\bar{C}_{px} = -0.068$ and $\bar{C}_{vx} = -0.087$

In figure 8.3 the coefficients of force exerted on the cylinder and the displacement of the cylinder over one period of oscillation are presented. These coefficients are shown after 10 periods of oscillation have elapsed (the simulation was started in a quiescent fluid) and the cylinder is now experiencing a periodic forcing with a non-zero mean. The coefficient of force along the x -axis has been broken up into its two components: pressure and viscosity. Examination of the mean of both components of force shows them to have negative values: $\bar{C}_{px} = -0.068$ & $\bar{C}_{vx} = -0.087$. The significance of this is that both components of the force are of the same magnitude and that both are acting in the same direction and as a consequence a net force is exerted on the cylinder in the $-x$ direction. As the cylinder is fixed at $x = 0$ a propulsive jet in the $+x$ direction arises.

Due to the nature of the periodic boundary conditions, the volume of fluid in the domain will be accelerated by this force and therefore with time the force experienced by

8.2. ‘FIXED’ CYLINDER AT $V_R = 1.0$

the cylinder should reach equilibrium when the drag induced by the resultant cross-flow is equal to the force resulting from the combined oscillations. An examination of the same force components at a much later time of evolution, $t \gtrsim 3480T$, finds that these coefficients are: $\bar{C}_{px} = 0.047$ & $\bar{C}_{vx} = -0.075$. The net coefficient of force is non-zero, $\bar{C}_x = -0.028$ and still acting in the $-x$ direction, however, it is now only 18% of its previous value at $t = 10T$. Given a much greater period of evolution it is likely that the net force will attain the value of 0. The significant aspect here is that the pressure force has changed sign and now acts to accelerate the fluid in the $-x$ direction while the viscous force still acts to accelerate it in the $+x$ direction. It would appear that it is the viscous component that is always acting as a thrust on the cylinder. Initially, in the absence of a cross-flow, the pressure fields resulting from the combined motion also act as a thrust on the cylinder, however, as a crossflow develops the pressure force changes sign and acts to retard the cross-flow.

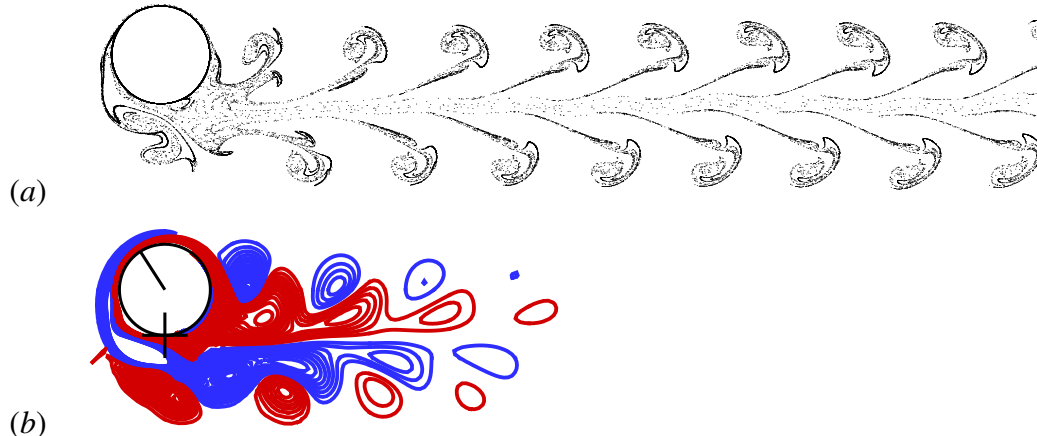


Figure 8.4: Flow produced by a cylinder fixed in the horizontal axis at $x = 0$ with a velocity ratio $V_r = 1.0$ between the translational and rotational oscillatory motions. Shown are: (a) fluid particle transport from ten massless particle sources placed near the cylinder surface, and (b) instantaneous vorticity contours. The cylinder’s rotation is indicated by the radial line and its vertical rest position by the crosshairs.

The resultant jet flow caused by this motion is illustrated in figure 8.4 by an image of particles shed into the fluid and the instantaneous vorticity contours at the same time, $t \gtrsim 3480T$. It illustrates how the vorticity cross-annihilates and diffuses so that it has virtually gone when a distance of $5D$ downstream is reached. The ‘puffs’ of particles are formed near the cylinder and then, as the vorticity diffuses, are convected downstream by the jet of fluid. The particle image also shows clearly the H_1 symmetry about the wake centreline.

8.3 ‘Swimming’ Cylinder at $V_r = 1.0$

In this section the oscillating cylinder is allowed to move in the x -direction in response to any forces acting on it. As mentioned in §8.1 this permits a change in the boundary conditions after an initial flow direction is established. With an inlet condition on the left edge and an outflow boundary condition on the right edge of the moving domain, a laminar cross-flow is achieved. The advantage of this configuration is that it is not subject to any persistent vorticity crossing through the periodic boundary conditions that were employed for the ‘fixed’ case. A set of instantaneous vorticity contours are shown in figure 8.5 for an entire period of oscillation, at $T/8$ intervals. The absolute frame of reference for these images is fixed and the cylinder is seen to be moving towards the

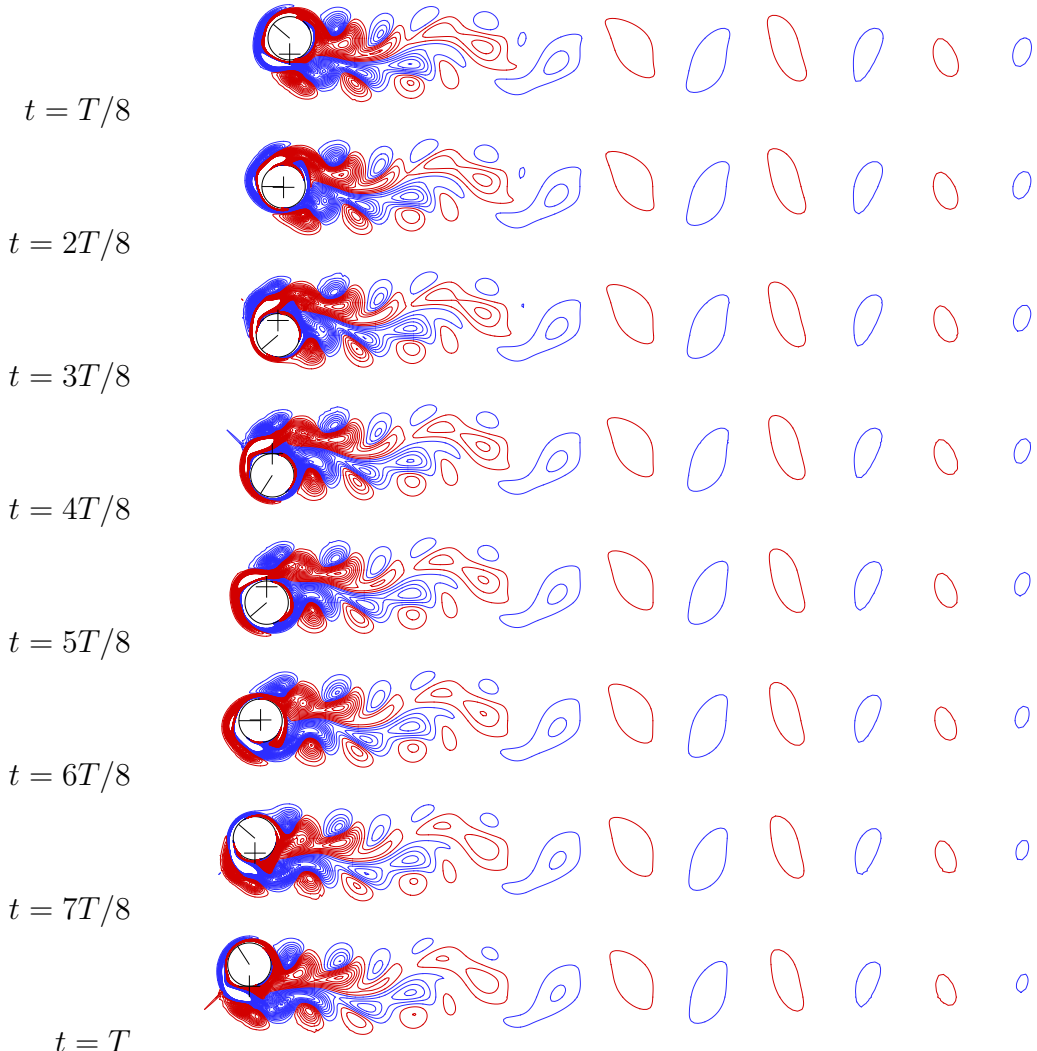


Figure 8.5: Instantaneous vorticity contours over one period of oscillation for the ‘Swimming Cylinder’ cylinder at $V_r = 1$, shown at intervals of $T/8$. The cylinder’s rotation is indicated by the radial line and its vertical rest position by the crosshairs.

8.3. ‘SWIMMING’ CYLINDER AT $V_R = 1.0$

left of the page. While the contours in the immediate vicinity of the cylinder resemble those for the fixed case, the far-field contours do not. In this case the vorticity does not completely cross-annihilate and diffuse, instead, almost immediately behind the cylinder a distinct oscillation in the vortex sheets becomes visible. With increasing distance from the cylinder the vortex sheets coalesce into discrete vortices to form an alternating row of vortices in the far-field, as shown. The vortex sheet oscillation and the formation of the far-field vortex row breaks the H_1 symmetry present in the ‘fixed’ case. Additionally, as it forms with a period of $2T$ it represents a period doubling bifurcation. This is also visible in the particle transport diagram of figure 8.6 where, with increasing distance from the cylinder, an oscillation in the particle structures becomes more pronounced.

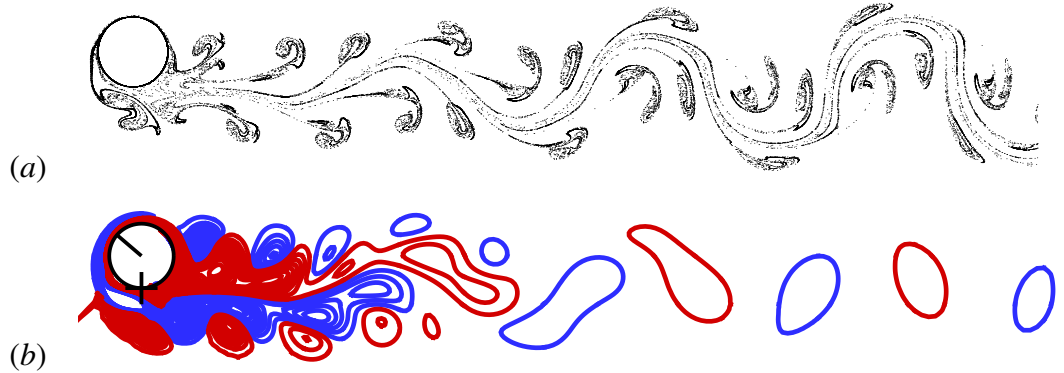


Figure 8.6: Flow produced by a cylinder free in the horizontal axis with a velocity ratio $V_r = 1.0$ between the translational and rotational oscillatory motions. Shown are: (a) fluid particle transport from ten massless particle sources placed near the cylinder surface, and (b) instantaneous vorticity contours. The cylinder is shown at its maximum vertical position and with its maximum anti-clockwise rotation.

The time-average of the coefficients of pressure and viscous force on the cylinder are at equilibrium at the instant shown. The values are (obtained over 50 periods): $\bar{C}_{vx} = -0.037$ & $\bar{C}_{px} = 0.037$. As with the fixed cylinder case the viscous force is acting as a thrust in the $-x$ direction, while the pressure is acting in opposition. The cylinder has reached an time-averaged terminal velocity, normalised by the RMS velocity of the rectilinear motion, of 0.48.

8.4 ‘Swimming’ Cylinder Simulations with Varying V_r

The impact of altering the velocity ratio between the rectilinear and rotational motions is examined by visualising the matching vorticity contours and particle transport images, and by determining the terminal velocity in each case. The ‘swimming’ case was used in preference to the ‘fixed’ case because the periodic boundary conditions used with the ‘fixed’ case would permit vorticity to re-enter the domain from the left edge and perturb the incident flow. The eight separate V_r cases that are examined are: $V_r = \{0.2, 0.35, 0.5, 0.75, 1.0, 1.25, 1.5, 2.0\}$, of which one has already been studied in §8.3. Presented in figure 8.7 is the terminal velocity attained by the ‘swimming’ cylinders as a function of the velocity ratio. The velocity ratio was found to have a considerable impact on both the terminal velocity and on the structure of the wake. It was found that as the velocity ratio was decreased, and correspondingly the amplitude of rotation increased, the terminal velocity increased. At $V_r = 0.35$ a peak increase in the terminal velocity of approximately 230% over the value at $V_r = 1.0$ was measured. A subsequent decrease in V_r caused the terminal velocity to decrease. Values of $V_r > 1.0$ resulted in a decrease in the terminal velocity.

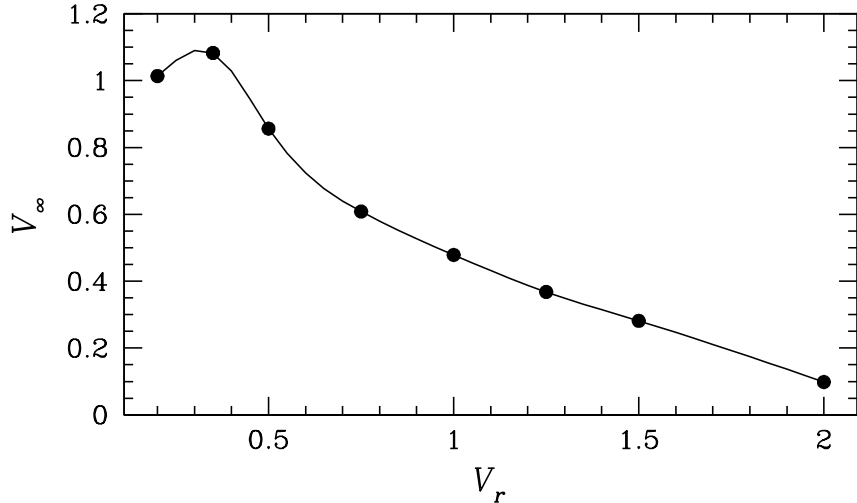


Figure 8.7: Variation of the two-dimensional terminal velocity, V_∞ as a function of the velocity ratio between translational and rotational motion. The terminal velocity is normalised by the RMS velocity of the rectilinear motion.

The variation in the terminal velocity is inherently related to changes in the formation of vorticity on the cylinder and the resulting structure of the wake. In figures 8.6, 8.8–8.14 the particle transport images and instantaneous vorticity contours are presented for the eight values of V_r considered. It should be noted that the contouring levels in figures 8.8–8.14 of the instantaneous vorticity plots are presented at the same levels so that a comparison might be made in terms of the cross-annihilation and diffusion of vorticity

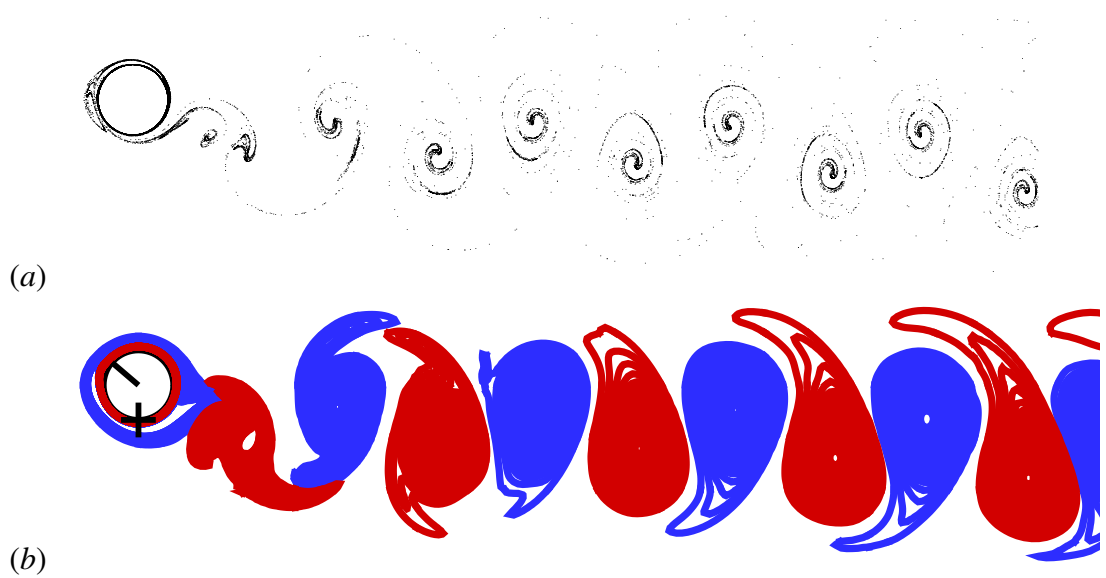


Figure 8.8: Flow produced by a cylinder free in the horizontal axis with a velocity ratio $V_r = 0.2$ between the translational and rotational oscillatory motions. Shown are: (a) fluid particle transport from ten massless particle sources placed near the cylinder surface, and (b) instantaneous vorticity contours. The cylinder is shown at its maximum vertical position and with its maximum anti-clockwise rotation.

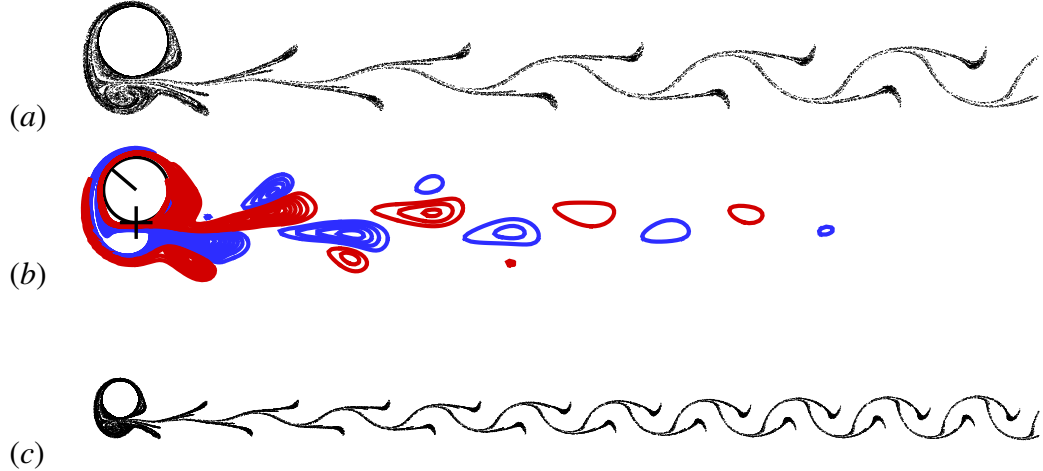


Figure 8.9: Flow produced by a cylinder free in the horizontal axis with a velocity ratio $V_r = 0.35$ between the translational and rotational oscillatory motions. Shown are: (a) fluid particle transport from ten massless particle sources placed near the cylinder surface, (b) instantaneous vorticity contours, and (c) fluid particle transport with particles leaving the domain boundary. The cylinder is shown at its maximum vertical position and with its maximum anti-clockwise rotation.

occurring. The $V_r = 1.0$ case shown in figure 8.6 has an additional level included to highlight the correspondence between the vorticity and the structures formed by the particles in the wake.

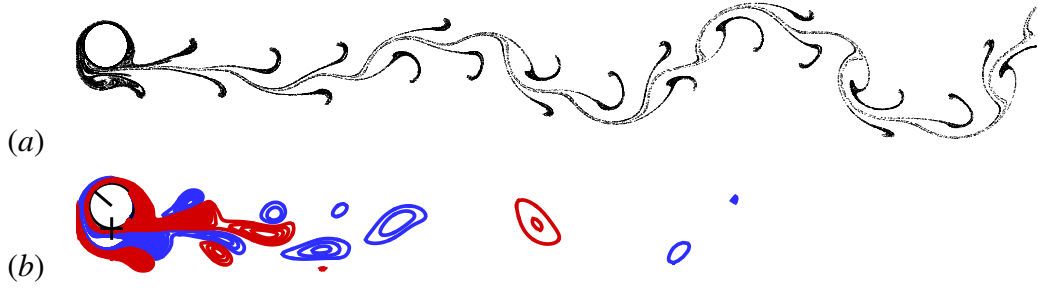


Figure 8.10: Flow produced by a cylinder free in the horizontal axis with a velocity ratio $V_r = 0.5$ between the translational and rotational oscillatory motions. Shown are: (a) fluid particle transport from ten massless particle sources placed near the cylinder surface, and (b) instantaneous vorticity contours. The cylinder is shown at its maximum vertical position and with its maximum anti-clockwise rotation.

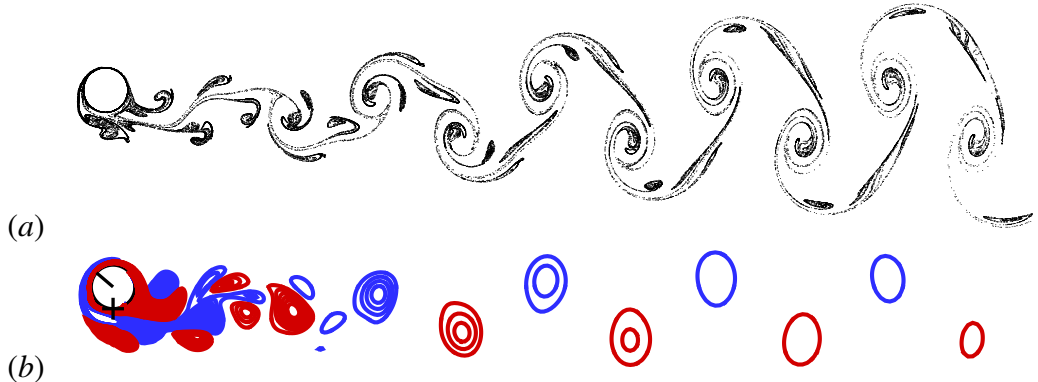


Figure 8.11: Flow produced by a cylinder free in the horizontal axis with a velocity ratio $V_r = 0.75$ between the translational and rotational oscillatory motions. Shown are: (a) fluid particle transport from ten massless particle sources placed near the cylinder surface, and (b) instantaneous vorticity contours. The cylinder is shown at its maximum vertical position and with its maximum anti-clockwise rotation.

The vorticity contours produced at $V_r = 0.2$, figure 8.8, did not show the same degree of diffusion and cross-annihilation found in the other cases. The vorticity present in the wake shows little sign of decreasing in the far-field and is of much greater magnitude than all the other cases at the same distance from the cylinder. The form of shedding of vorticity from the cylinder into the wake is also unique as it produces only a single vortex per half-cycle with the resultant wake immediately consisting of an alternating row of oppositely signed vorticity. The particle transport image reflects the locations of the shed vortices with discrete spirals of particles located at their cores, that are convected downstream with the wake.

The largest terminal velocity was achieved for $V_r = 0.35$, figure 8.9. In this case the width of the wake was at its narrowest with the majority of the cross-annihilation of the vorticity occurring near the cylinder. With each half-cycle of motion a pair of vortices are



Figure 8.12: Flow produced by a cylinder free in the horizontal axis with a velocity ratio $V_r = 1.25$ between the translational and rotational oscillatory motions. Shown are: (a) fluid particle transport from ten massless particle sources placed near the cylinder surface, and (b) instantaneous vorticity contours. The cylinder is shown at its maximum vertical position and with its maximum anti-clockwise rotation.

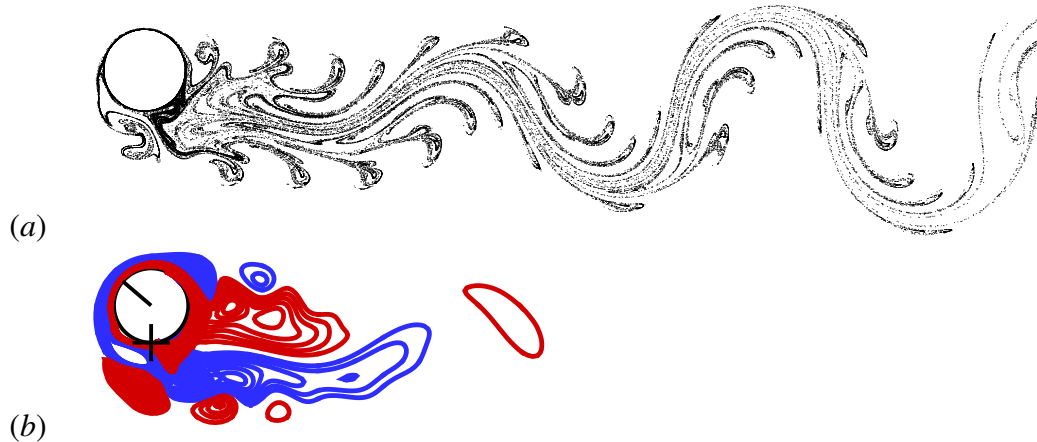


Figure 8.13: Flow produced by a cylinder free in the horizontal axis with a velocity ratio $V_r = 1.5$ between the translational and rotational oscillatory motions. Shown are: (a) fluid particle transport from ten massless particle sources placed near the cylinder surface, and (b) instantaneous vorticity contours. The cylinder is shown at its maximum vertical position and with its maximum anti-clockwise rotation.

formed. Although vorticity is detected further downstream than the other cases, where vortex pairs are formed each half-cycle, e.g. $V_r = 1.0$ in figure 8.6, this is largely due to the higher terminal velocity resulting in a lengthening of the region over which the vorticity dissipates. The particles shed from the cylinder form a very narrow, periodic wake, as shown in figure 8.9(c).

In figure 8.10 the increase of V_r to 0.5 has resulted in a loss of the H_1 spatio-temporal symmetry of the wake present at $V_r = 0.35$. The loss of symmetry is manifested in the particle transport image as large scale oscillations of the particle structures about the centreline of the wake. In the vorticity contours it is manifested as the beginning of the formation of an alternating vortex row, as was seen for $V_r = 1.0$ in figure 8.6. However, the vorticity has mostly cross-annihilated and diffused near the cylinder in comparison to

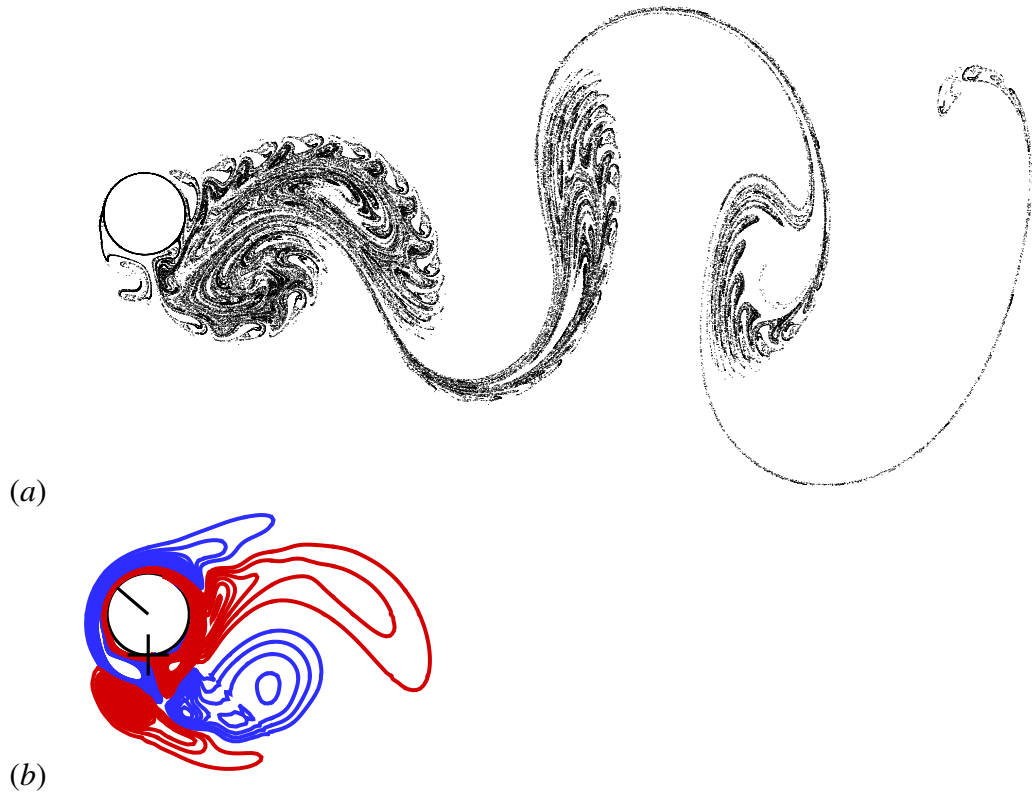


Figure 8.14: Flow produced by a cylinder free in the horizontal axis with a velocity ratio $V_r = 2.0$ between the translational and rotational oscillatory motions. Shown are: (a) fluid particle transport from ten massless particle sources placed near the cylinder surface, and (b) instantaneous vorticity contours. 32 periods of particle shedding have elapsed. The cylinder is shown at its maximum vertical position and with its maximum anti-clockwise rotation.

the $V_r = 1.0$ case, with the result that only a smaller scale oscillation forms in the wake. A slight increase in V_r to 0.75, figure 8.11, sees the wake structure completely change. In this case the vorticity forms an alternating double row (array) of oppositely signed vorticity leading to the distinctive patterns seen in the particle shedding image. These patterns clearly show that this flow is a jet as the sense of rotation associated with the concentrations of vorticity is reversed. This reversal of rotation direction is reflected in the particle image, where the spirals are rotating in the opposite direction from a conventional planar Kármán wake, i.e. the wake of figure 2.3. Near the cylinder the streaks of particles are rolling up to form small ‘puffs’ of particles. This was first distinctly observable for $V_r = 0.5$, but in the $V_r = 1.0$ case, figure 8.6, this effect has increased and the ‘puffs’ of particles are now a dominant feature of the wake.

The vorticity contours near the cylinder for $V_r = 1.25$, figure 8.12, form a distinctive pattern of two inner sheets of oppositely signed vorticity with two outer rows of discrete vortices. This feature is present for the cases $V_r = 1.0, 1.25 \& 1.5$. Although the far-field image of particle transport shows an oscillation at $V_r = 1.25$ the vorticity has largely

8.4. ‘SWIMMING’ CYLINDER SIMULATIONS WITH VARYING V_R

dissipated near the cylinder. At $V_r = 1.5$ the far-field oscillation of the wake seen for the previous case has grown considerably. Largely this is due to the tail of the vortex sheets coalescing into a row of vorticity of alternating signs of very low magnitude. Only one vortex can be seen here as the vorticity diffuses rapidly.

The flow for $V_r = 2.0$, figure 8.14, is considerably different from the previous cases for a number of reasons. No longer are discrete ‘puffs’ of particles being formed near the cylinder and convected downstream, instead two large vortices are formed behind the cylinder that oscillate up and down with a period much greater than the oscillation of the cylinder. The particle transport image in figure 8.14(a) shows all the particles shed over 32 periods of oscillation. The vorticity near the cylinder have a passing resemblance to the vorticity contours of regime S (chapter 6) with the distinctive boomerang like shape.

8.5 Discussion

It must be noted at the outset that this investigation is somewhat limited in scope owing to time constraints. Consequently the investigation has been restricted to a two-dimensional study of the forces experienced by the ‘swimming’ cylinder, as previously reported in Blackburn et al. (1999), and a qualitative examination of the influence of the velocity ratio on the wake structures produced by the ‘swimming’ cylinder.

The two components of force acting on a circular cylinder in a combined rotational and rectilinear oscillation are due to the pressure and viscous forces acting on the cylinder surface. In the initial phase of motion, when started in a quiescent fluid, it was shown for the fixed case in §8.2 that both components are exerting a force on the cylinder in the $-x$ direction. This combination of oscillations has led to a mean pressure distribution around the cylinder that acts in the $-x$ direction. This is consistent with the simplified explanation referred to in §2.5, where the higher velocity of the cylinder surface relative to the fluid on the left side of the cylinder generates a lower mean pressure relative than on the right side and thus a thrust is experienced by the cylinder to the left. However, it is also interesting that the velocity field surrounding the cylinder has resulted in the viscous force also acting on the cylinder in the $-x$ direction. In the specific example provided of a ‘fixed’ cylinder, §8.2, at $t = 10T$ the coefficients of viscous and pressure force acting on the cylinder were $\bar{C}_{px} = -0.068$ & $\bar{C}_{vx} = -0.087$. Both components are of the same order of magnitude and of the same sign.

After sufficient time has elapsed a cross-flow develops relative to the cylinder. This is either due to the jet of fluid produced when the cylinder is ‘fixed’ and the domain has periodic boundary conditions, or it is due to the motion of the reference frame attached to the cylinder in the $-x$ direction for the ‘swimming’ cylinder case. At equilibrium the time-averaged pressure and viscous forces are equal and opposite. As a consequence of the cross-flow, the net positive pressure distribution moves from the right of the cylinder to the left (front) of the cylinder resulting in a change in sign of the coefficient of time-average force due to pressure. This force component now acts against the motion of the cylinder in the $-x$ direction. Although the magnitude has decreased slightly, the mean force acting to keep the cylinder at a terminal velocity is the viscous force which is acting as the thrust. Therefore it is the viscous force which consistently acts to propel the cylinder through the fluid. It is likely that the pressure force is the sum of two components acting in opposition: that due to the combined oscillations of the cylinder and that due to bluff body drag which increases with the velocity of the cross-flow. It is concluded that both the pressure differential caused by the oscillatory motion and the viscous force act to propel the ‘swimming’ cylinder.

In the wake of the ‘swimming’ cylinder case, see figures 8.5 & 8.6, when compared with the ‘fixed’ case, see figure 8.4, the formation of a row of alternating single vortices

8.5. DISCUSSION

has clearly occurred. The formation of this feature represents a breaking of the H_1 symmetry present in the wake of the ‘fixed’ case. A careful examination of figure 8.5 shows that the two-dimensional bifurcation breaking this symmetry has resulted in a period doubling in the far-field wake. It is speculated that the instability leading to this symmetry breaking is not present in the ‘fixed’ case as the fluid circulating through the domain has not yet attained a terminal velocity. In other cases, e.g. $V_r = 0.5 - 1.5$, a similar form of symmetry breaking is observed with the wake forming structures in the flow that vary with $2T$.

Varying the velocity ratio, V_r , caused significant changes in the wake structure behind the ‘swimming’ cylinder. Decreasing the velocity ratio, which corresponds to increasing the amplitude and velocity of rotation, resulted in a critical value being obtained for $V_r = 0.35$ at which point a very narrow wake was formed. This corresponded with the highest terminal velocity achieved. The near wake structure of the cylinder for this case was formed by a pair of vortices being introduced by the cylinder every half-cycle. This aspect was observed for all cases with $V_r \geq 0.35$. The wake structure at $V_r = 0.2$ was substantially different from all the other cases primarily because only a single vortex is being shed per half-cycle. This has two effects: firstly, a single row of alternating signed vortices is formed immediately in the wake, and secondly, the vorticity does not dissipate due to cross-annihilation and diffusion to the same degree as the other cases.

8.6 Summary

In this chapter the results of an initial exploratory investigation into the forces providing a thrust to a cylinder in combined rotational and rectilinear oscillation are presented. The thrust was found to be due to both a viscous thrust induced by the particular combination of oscillations employed and due to a thrust created by the pressure differential across the cylinder that was induced by the combined motions. An examination of the impact of varying the velocity ratio between the translational and rotational oscillations found a critical value at which the highest terminal velocity was found and a very narrow wake structure was produced. A velocity ratio less than this critical value resulted in a different mode of vorticity shedding into the wake.

Chapter 9

Conclusions

There have been two related themes of study presented in the preceding chapters. The vast majority of the investigation has focused on an examination of the transitions between different regime states for the flow produced by the rectilinear oscillation of a circular cylinder. To a much smaller degree the flows produced by a circular cylinder in rectilinear oscillation with an additional rotational oscillation imposed have also been investigated. In the following sections the major conclusions arrived at for each theme are stated.

9.1 Rectilinear Oscillations of a Circular Cylinder

The objective of this study was to investigate the primary two- and three-dimensional transitions for a circular cylinder performing rectilinear oscillations in a quiescent fluid within the range of control parameters $KC \in [0, 10]$, $\beta \in [0, 100]$. The results, obtained using a combination of Floquet stability analysis and DNS, are summarised in figure 9.1. Within the two-dimensional subspace perpendicular to the cylinder span two forms of primary symmetry breaking bifurcations were located. The two forms of two-dimensional symmetry breaking are: a synchronous instability (regime S) leading to a change in the spatial characteristics of the flow but preserving synchronisation with the cylinder oscillation, and a quasi-periodic instability (regime QP) which introduced a second incommensurate frequency into the flow dynamics and consequently broke both the spatial and temporal characteristics of the flow. The point of transition between these two forms of instability is denoted as the ‘freezing point’ in figure 9.1.

Both forms of two-dimensional symmetry breaking were determined to be supercritical in their nature. In the synchronous instability the supercriticality was manifested as increased deviation of the induced flow from the axis of oscillation with distance in (KC, β) -space from the curve of marginal stability. The supercriticality of the quasi-periodic instability was also manifested as an increased deviation of the flow from the axis of oscillation, although due to the quasi-periodic oscillation of the flow this was harder

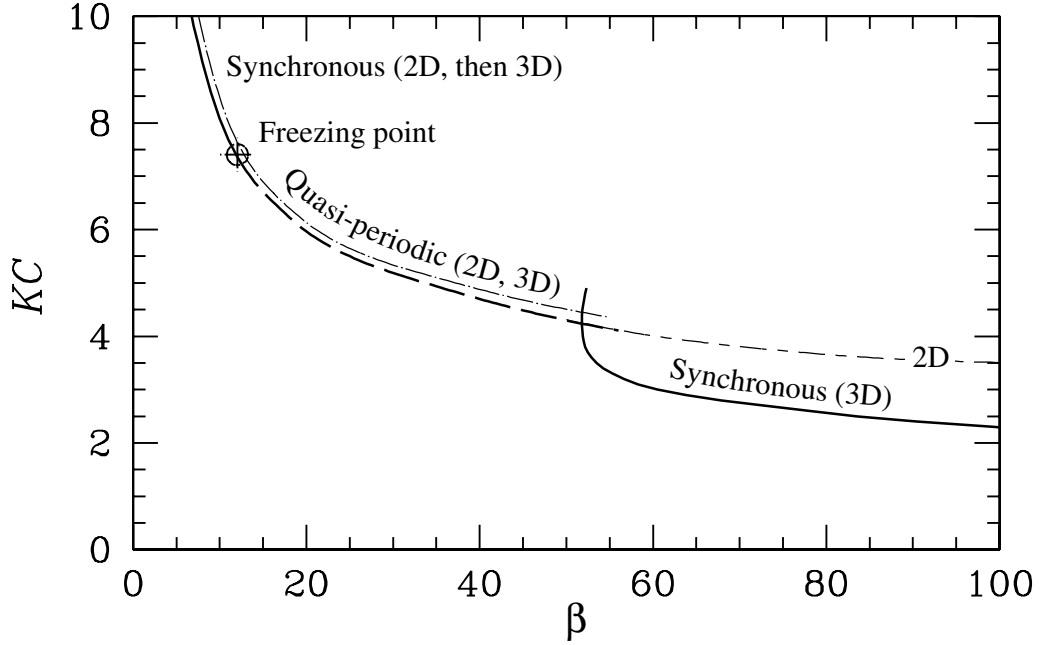


Figure 9.1: Locations and characteristics of the primary and secondary symmetry breaking bifurcations.

to directly determine. However, the measure used to determine that this is a supercritical bifurcation was the peak force in the direction perpendicular to the axis of oscillation, which is related to the angle of deviation of the induced flow near the cylinder.

In three-dimensional space a symmetry breaking transition occurs slightly after the two-dimensional synchronous transition in (KC, β) -space, as shown in figure 9.1. The distance in (KC, β) -space between the two-dimensional onset of regime S and the subsequent three-dimensional bifurcation is not large and is related to the supercriticality of the two-dimensional symmetry breaking mode. No experimental observations of a pure regime S have been recorded and this is most likely owing to the narrowness of this regime in (KC, β) -space. The experimentally derived boundary between regimes A and D of Tatsuno and Bearman (1990) agrees extremely well with the predicted boundary for the onset of the three-dimensional regime. Through an examination of the energy in the spanwise mode the three-dimensional bifurcation associated with this transition was determined to be supercritical. As shown in figure 9.1 the primary breakage for the synchronous transition is the two-dimensional supercritical transition to regime S, which is almost immediately followed by a secondary three-dimensional supercritical bifurcation to regime D.

Within the range of consideration, for higher Stokes numbers, $\beta \gtrsim 50$, and lower Keulegan–Carpenter numbers, $KC \lesssim 4$, a primary three-dimensional bifurcation was detected before any two-dimensional bifurcation occurred, see figure 9.1. This bifurcation

9.1. RECTILINEAR OSCILLATIONS OF A CIRCULAR CYLINDER

is synchronous with the cylinder oscillation and introduces a spanwise variation into the symmetric flow of the x - y plane. The location of this transition corresponds with the lower boundary leading to regime B flow, which has experimentally been visualised as a regular spanwise formation of streaks of dye. The resultant flow, regime B, is also synchronous with the cylinder oscillation and was first reported by Honji (1981), analysed by Hall (1984), noted by Tatsuno and Bearman (1990) and most recently investigated experimentally by Sarpkaya (2002). The upper limit of regime B for increasing KC coincides with the location reported for the two-dimensional transition to regime QP. The secondary instability from regime B to E is driven by a two-dimensional transition to regime QP.

While the transition to regime E is preceded by a primary transition to regime B, the situation for the transition to regime C is not as clear. Underlying the three-dimensional transition to regime C is the supercritical transition to regime QP, and this is evidenced by regime C flows being quasi-periodic. As shown in figure 9.1, the onset of regime C appears to nearly coincide with the onset of the two-dimensional regime QP, however, due to the techniques employed, this has not been absolutely established. In figure 9.1 the transition to three-dimensional flow is shown to occur slightly after the two-dimensional onset to regime QP. The evidence regarding the type of bifurcation that occurs for the transition to three-dimensional flow is inconclusive. On one hand it is known that the neighbouring transition to the three-dimensional flows of regime D is supercritical. Yet, on the other hand the greatest difference between the numerical predictions and the results of Tatsuno and Bearman (1990) occurs for the onset of regime C, with Tatsuno and Bearman's boundaries occurring below the numerical prediction in (KC, β) -space. This is the only region that the match between numerical and experimental results was not excellent, although by no means is the current match poor. It is however consistent with a weakly sub-critical three-dimensional bifurcation occurring to the two-dimensional flows of regime QP. It is speculated that the onset of regime C, in contrast to all the other transitions, could be weakly sub-critical.

The ‘freezing point’, shown in figure 9.1, represents the location in (KC, β) -space where the two-dimensional marginal stability curve transitions between regimes S and QP and this is where the complex-conjugate Floquet multipliers approach the real axis and coalesce into a single real mode. However, the experimental map of Tatsuno and Bearman (1990) does not reflect this, with the transition between regimes D and C on the marginal stability curve occurring at a higher value of β . This is due to the codimension-2 nature of the flow which means that beyond the curve of marginal stability the flow need not be what was predicted on the nearest marginal stability curve. In this case, an extremely narrow extension of regime C up to the ‘freezing point’ was predicted. As it is so narrow in (KC, β) -space it is again unlikely, although not impossible, to be observed in experiments. This aspect represents an advantage that computational methods have over experimental methods in that such fine-grained features can be examined. Above the

9.2. THE ‘SWIMMING’ CYLINDER

curves of marginal stability identified by Floquet analysis in (KC, β) -space the predictions of the linear analysis are not guaranteed to apply due to nonlinear effects. However, Floquet stability analysis at the onset of the two-dimensional quasi-periodic mode predicted the value of the secondary period introduced into the flow to make it quasi-periodic. Subsequent two-dimensional DNS simulations have shown that the secondary period at onset is retained in the flow, often at considerable distance from the onset in (KC, β) -space.

The research presented in this thesis has resolved a number of issues and introduced new findings into the existing body of knowledge regarding bluff body flows. The primary and secondary instabilities of the flow produced by a circular cylinder in quiescent fluid have been located and identified, as summarised in figure 9.1. Fundamentally it has been shown that the symmetry breaking instabilities that occur can be grouped into two-dimensional and three-dimensional transitions. The three-dimensional flows that occur above the line of marginal two-dimensional stability have been observed to have the characteristics of the two-dimensional instabilities. Specifically the flows of regimes C and D have been observed to have quasi-periodic and synchronous flows respectively, as predicted by two-dimensional Floquet analysis. In both cases where the primary instability is two-dimensional a three-dimensional instability has been found to occur almost immediately, one to a supercritical three-dimensional instability, regime D, and the other to a, possibly, subcritical three-dimensional instability. Within the range of control parameters considered as $\beta \rightarrow 100$ the flow has been shown to be primarily unstable to a three-dimensional supercritical transition that results in the formation of spanwise regular structures in the flow (regime B). It is particularly notable that the upper limit of this regime, that has been observed experimentally, is predicted by two-dimensional analysis. Beyond transition the flow has been illustrated to be codimension-2, that is, the state of the flow is determined by two parameters and not necessarily the nearest marginal stability location. Additionally the three-dimensional nonlinear flows have been shown to retain signature characteristics predicted by two-dimensional linear analysis at considerable distances in (KC, β) -space from the marginal stability curve, i.e. the introduction of a secondary period.

9.2 The ‘Swimming’ Cylinder

This theme of the research focused on examining the thrust generated by a circular cylinder in rectilinear motion with an additional rotational oscillation imposed. The force experienced by the cylinder was due to three components: the viscous force at the cylinder surface; the pressure differential caused by the relative velocity of the cylinder surface to the surrounding of the fluid and; the pressure differential caused by a cross-flow. Initially the viscous and pressure forces act in concert to exert a thrust on the cylinder. At equilibrium the pressure forces are opposed to the cylinder motion and are balanced by

9.2. THE ‘SWIMMING’ CYLINDER

the viscous force, which is still acting as a thrust.

The velocity ratio between the rectilinear and rotational oscillations was found to substantially effect the terminal velocity of a cylinder permitted to move in response to the forces on its surface. A critical value of $V_r \approx 0.35$ was identified where the terminal velocity was highest and the resultant wake was very narrow. The relative velocity between the rotation and translation was also found to influence the number of vortices shed per half-cycle, for $V_r < 0.35$ only one vortex was observed to be shed per half-cycle with the consequence that the vorticity in the wake formed an alternating row of oppositely signed vorticity that persisted far further downstream than all the other cases considered. At values of $V_r > 0.35$ two vortices were observed to be formed and shed into the wake each half-cycle. Consequently the wake formed immediately behind the cylinder consisted of two inner sheets of oppositely signed vorticity surrounded by rows of discrete concentrations of vorticity. Dependent upon the different values of V_r the vorticity in this wake rapidly cross-annihilated and diffused into the flow. At $V_r = 0.35$ the wake was observed to be have H_1 symmetry about $y = 0$. With increasing V_r instabilities formed resulting in the breakdown of the wake into a single row of vorticity of alternating signs which caused large scale oscillations in the particle traces presented. In one case, $V_r = 0.75$, a double row of alternating vorticity was formed that resembled a reverse Kármán street.

9.3 Directions for Future Work

It is hoped that the present investigation has provided some additional understanding of the dynamics of flows created by oscillating bluff bodies. However it has also raised a number of issues that warrant further investigation. In relation to a cylinder performing rectilinear oscillations some of these include:

- A detailed determination of the nature of the bifurcation to regime C.
- A more substantial investigation of further transitions beyond the primary and secondary transitions detailed here.

The ‘Swimming’ cylinder problem also raises a number of questions that have not been addressed in this initial study:

- The different wake states have only been discretely examined, A finer-grained study may reveal other states of shedding of fundamental interest.
- The three-dimensional nature of the ‘swimming’ cylinder problem was not addressed here. Some initial computational research (not presented) using Floquet analysis and DNS has been conducted in this area which does show that the thrust exists. However, more research is required.
- In particular, experimental studies of a ‘swimming’ cylinder would be a useful validation of this work.

Appendix A

Bibliography

- Anderson, J. M., Streitlien, K., Barrett, D. S. and Triantafyllou, M. S. (1998). Oscillating foils of high propulsive efficiency, *J. Fluid Mech.* **360**: 41–72.
- Barkley, D. and Henderson, R. D. (1996). Three-dimensional Floquet stability analysis of the wake of a circular cylinder, *J. Fluid Mech.* **322**: 215–241.
- Barkley, D., Tuckerman, L. S. and Golubitsky, M. (2000). Bifurcation theory for three-dimensional flow in the wake of a circular cylinder, *Phys. Rev. E* **61**(5): 5247–5252.
- Bearman, P. W. (1984). Vortex shedding from oscillating bluff bodies, *Ann. Rev. Fluid Mech.* **16**: 195–222.
- Becker, E. B., Carey, G. F. and Oden, J. T. (1981). *Finite Elements: An Introduction*, Vol. 1, Prentice-Hall.
- Blackburn, H. and Henderson, R. (1996). Lock-in behavior in simulated vortex-induced vibration, *Exptl Thermal & Fluid Sci.* **12**: 184–189.
- Blackburn, H. M., Elston, J. R. and Sheridan, J. (1998). Flows created by a cylinder with oscillatory translation and spin, *ASME Fluids Engineering Division Summer Meeting*, number FEDSM98-5157, Washington, DC.
- Blackburn, H. M., Elston, J. R. and Sheridan, J. (1999). Bluff-body propulsion produced by combined rotary and translational oscillation, *Phys. Fluids* **11**(1): 4–6.
- Blackburn, H. M. and Henderson, R. D. (1999). A study of two-dimensional flow past an oscillating cylinder., *J. Fluid Mech.* **385**: 255–286.
- Blackburn, H. M. and Karniadakis, G. E. (1993). Two and three dimensional simulations of vortex-induced vibration of a circular cylinder, *3rd INT. Offshore & Polar Engng Conf.*, Vol. 3, Singapore, pp. 715–720.
- Blackburn, H. M. and Lopez, J. M. (2002). Modulating rotating waves in an enclosed swirling flow, *J. Fluid Mech.* **465**: 33–58.
- Blackburn, H. M. and Lopez, J. M. (2003). The onset of three-dimensional standing and modulated travelling waves in a periodically driven cavity flow, *J. Fluid Mech.* **497**: 289–317.

- Blevins, R. D. (1977). *Flow-Induced Vibration*, Van Nostrand Reinhold Company, New York.
- Canuto, C., Hussaini, M. Y., Quarteroni, A. and Zang, T. A. (1988). *Spectral Methods in Fluid Dynamics*, Springer series in computational physics, Springer-Verlag.
- Carberry, J., Sheridan, J. and Rockwell, D. (2001). Force and wake modes of an oscillating cylinder, *J. Fluids & Struct.* **15**: 523–532.
- Cheng, M. and Moretti, P. M. (1991). Lock-in phenomena on a single cylinder with forced transverse oscillation, in M. K. Au-Yang and F. Hara (eds), *Flow-Induced Vibration and Wear*, Vol. 206, ASME, pp. 129–133.
- Coutanceau, M. and Bouard, R. (1977). Experimental determination of the main features of the viscous flow in the wake of a circular cylinder in uniform translation: steady flow, *J. Fluid Mech.* **79**.
- Dennis, S. C. R. and Chang, G.-Z. (1970). Numerical solutions for steady flow past a circular cylinder at Reynolds numbers up to 100, *J. Fluid Mech.* **42**.
- Dütsch, H., Durst, F., Becker, S. and Lienhart, H. (1998). Low-Reynolds-number flow around an oscillating cylinder at low Keulegan–Carpenter numbers, *J. Fluid Mech.* **360**: 249–271.
- Elston, J. (1997). Wake formation of a vibrating and rotating cylinder, *Final year project report*, Department of Mechanical Engineering, Monash University, Australia.
- Gerrard, J. H. (1978). The wakes of cylindrical bluff bodies at low reynolds number, *Philos. Trans. R. Soc. London Ser.A* **288**: 351.
- Griffin, O. M. and Ramberg, S. E. (1976). Vortex shedding from a cylinder vibrating inline with an incident uniform flow, *J. Fluid Mech.* **75**: 257–271.
- Hall, P. (1984). On the stability of the unsteady boundary layer on a cylinder oscillating transversely in a viscous fluid, *J. Fluid Mech.* **146**: 347–367.
- Hammache, M. and Gharib, M. (1991). An experimental study of the parallel and oblique vortex shedding from circular cylinders, *J. Fluid Mech.* **232**: 567–590.
- Henderson, R. D. (1995). Details of the drag curve near the onset of vortex shedding, *Phys. Fluids* **7**(9): 1–4.
- Henderson, R. D. (1997). Nonlinear dynamics and pattern formation in turbulent wake transition, *J. Fluid Mech.* **352**: 65–112.
- Henderson, R. D. and Barkley, D. (1996). Secondary instability in the wake of a circular cylinder, *Phys. Fluids* **8**: 1683–1685.
- Henderson, R. D. and Karniadakis, G. E. (1995). Unstructured spectral element methods for simulation of turbulent flows, *J. Comput. Phys.* **122**: 191–217.
- Honji, H. (1981). Streaked flow around an oscillating cylinder, *J. Fluid Mech.* **107**: 509–520.

- Hughes, T. J. R. (1987). *The finite element method: linear static and dynamic finite element analysis*, Prentice-Hall.
- Iliadis, G. and Anagnostopoulos, P. (1998). Viscous oscillatory flow around a circular cylinder at low Keulegan-Carpenter numbers and frequency parameters, *Intnl J. Num. Meth. Fluids* **26**: 403–442.
- Iooss, G. and Joseph, D. D. (1990). *Elementary Stability and Bifurcation Theory*, 2nd edn, Springer.
- Jackson, C. P. (1987). A finite-element study of the onset of vortex shedding in flow past variously shaped bodies, *J. Fluid Mech.* **182**: 23–45.
- Jauvtis, N. and Williamson, C. H. K. (2003). A high-amplitude 2T mode of vortex formation, and the effects of non-harmonic forcing in vortex-induced vibration., *Eur. J. Mech. B/Fluids* **23**.
- Jauvtis, N. and Williamson, C. H. K. (2004). the effects of two degrees of freedom on vortex-induced vibration, *JFM* **509**: 23–62.
- Justesen, P. (1991). A numerical study of oscillating flow around a circular cylinder, *J. Fluid Mech.* **222**: 157–196.
- Karniadakis, G. E. (1990). Spectral element-Fourier methods for incompressible turbulent flows, *Comp. Meth. Appl. Mech. & Engng* **80**: 367–380.
- Karniadakis, G. E., Israeli, M. and Orszag, S. A. (1991). High-order splitting methods for the incompressible Navier-Stokes equations, *J. Comput. Phys.* **97**(2): 414–443.
- Karniadakis, G. E. and Sherwin, S. J. (1999). *Spectral/hp Element Methods for CFD*, Oxford University Press.
- Keulegan, G. H. and Carpenter, L. H. (1958). Forces on cylinders and plates in an oscillating fluid, *J. Res. Nat. Bur. Stand.* **60**.
- Koopmann, G. H. (1967). The vortex wakes of vibrating cylinders at low Reynolds numbers, *J. Fluid Mech.* **28**: 501–512.
- Kuznetsov, Y. A. (1995). *Elements of Applied Bifurcation Theory*, 1st edn, Springer-Verlag.
- Leweke, T. and Provansal, M. (1995). The flow behind rings – bluff-body wakes without end-effects, *J. Fluid Mech.* **288**: 265–310.
- Lighthill, J. (1986). *An Informal Introduction to Theoretical Fluid Mechanics*, Oxford university press.
- Mansy, H., Yang, P.-M. and Williams, D. R. (1994). Quantitative measurements of three-dimensional structures in the wake of a circular cylinder, *J. Fluid Mech.* **270**: 277–296.
- Morton, B. R. (1984). The generation and decay of vorticity, *Geophys. Astrophys. Fluid Dyn.* **28**: 277–308.

- Nehari, D., Armenio, V. and Ballio, F. (2004). Three-dimensional analysis of the unidirectional oscillatory flow around a circular cylinder at low Keulegan–Carpenter and β numbers, *J. Fluid Mech.* **520**: 157–186.
- Ongoren, A. and Rockwell, D. (1988a). Flow structure from an oscillating cylinder. part 1. mechanisms of phase shift and recovery in the near wake, *J. Fluid Mech.* **191**: 197–223.
- Ongoren, A. and Rockwell, D. (1988b). Flow structure from an oscillating cylinder. part 2. mode competition in the near wake, *J. Fluid Mech.* **191**: 225–245.
- Orszag, S. A. (1971). Accurate solution of the Orr-Sommerfeld stability equation, *J. Fluid Mech.* **50**(689).
- Provansal, M., Mathis, C. and Boyer, L. (1987). Bénard–von Kármán instability: transient and forced regimes, *J. Fluid Mech.* **182**: 1–22.
- Saad, Y. (1992). *Numerical Methods for Large Eigenvalue Problems*, Algorithms and architectures for advanced scientific computing, Manchester University Press.
- Sarpkaya, T. (1986). Force on a circular cylinder in viscous oscillatory flow at low Keulegan–Carpenter numbers, *J. Fluid Mech.* **165**: 61–71.
- Sarpkaya, T. (2002). Experiments on the stability of sinusoidal flow over a circular cylinder, *J. Fluid Mech.* **457**: 157–180.
- Sarpkaya, T. (2004). A critcial review of the intrinsic nature of vortex-induced vibrations, *J. Fluids & Struct.* **19**: 389–447.
- Sarpkaya, T. and Isaacson, M. (1981). *Mechanics of Wave Forces on Offshore Structures*, Van Nostrand Reinhold Company.
- Schlichting, H. (1932). Berechnung ebner periodisher grerenzschichtstromungen, *Phys. Z.* **33**(327).
- Strouhal, V. (1878). Über eine besondere art der toneregung, *Ann. Physik Chemie* **5**: 216–251.
- Taneda, S. (1956). Experimental investigation of the wakes behind cylinders and plates at low Reynolds numbers, *J. Phys. Soc. Jpn* **11**: 302.
- Taneda, S. (1978). Visual observations of the flow past a circular cylinder performing a rotary oscillation, *Journal of the Physical Society of Japan* **45**(3): 1038–1043.
- Tatsuno, M. and Bearman, P. W. (1988). Visual study of the flow induced by a cylinder performing sinusoidal oscillations, *Bulletin 66*, Research Institute for Applied Mechanics, Kyushu University.
- Tatsuno, M. and Bearman, P. W. (1990). A visual study of the flow around an oscillating circular cylinder at low Keulegan–Carpenter numbers and low Stokes numbers, *J. Fluid Mech.* **211**: 157–182.
- Thompson, M. C., Hourigan, K. and Sheridan, J. (1995). Three-dimensional mode development in low reynolds number flow over a cylinder, *12th Australasian Fluid Mechanics Conference*, Sydney.

- Thompson, M., Hourigan, K. and Sheridan, J. (1996). Three-dimensional instabilities in the wake of a circular cylinder, *Experimental Thermal and Fluid Science* **12**: 190–196.
- Tokumaru, P. T. and Dimotakis, P. E. (1991). Rotary oscillation control of a cylinder wake, *J. Fluid Mech.* **224**: 77–90.
- Triantafyllou, M. S., Triantafyllou, G. S. and Yue, D. K. P. (2000). Hydrodynamics of fishlike swimming, *Ann. Rev. Fluid Mech.* **32**: 33–53.
- Tuckerman, L. S. and Barkley, D. (2000). Bifurcation analysis for timesteppers, in E. Doedel and L. S. Tuckerman (eds), *Numerical Methods for Bifurcation Problems and Large-Scale Dynamical Systems*, Springer, pp. 453–566.
- Van Dyke, M. (ed.) (1982). *An Album of Fluid Motion*, The Parabolic Press.
- Wilhelm, D. and Kleiser, L. (2001). Stability analysis for different formulations of the nonlinear term in $p_n - p_{N-2}$ spectral element discretizations of the Navier–Stokes equations, *J. Comput. Phys.* **174**: 306–326.
- Williamson, C. H. K. (1985). Sinusoidal flow relative to circular cylinders, *J. Fluid Mech.* **155**: 141–174.
- Williamson, C. H. K. (1987). Three-dimensional transition in the near wake of a cylinder, *Bull. Am. Phys. Soc.* .
- Williamson, C. H. K. (1988). The existence of two stages in the transition to three-dimensionality of a cylinder wake, *Phys. Fluids* **31**: 3165–3168.
- Williamson, C. H. K. (1989). Oblique and parallel modes of vortex shedding in the wake of a circular cylinder at low Reynolds numbers, *J. Fluid Mech.* **206**: 579–627.
- Williamson, C. H. K. (1996a). Three-dimensional wake transition, *JFM* **328**: 345–407.
- Williamson, C. H. K. (1996b). Vortex dynamics in the cylinder wake, *Annual Review of Fluid Mechanics* **28**: 477–539.
- Williamson, C. H. K. and Govardhan, R. (2004). Vortex-induced vibrations, *Ann. Rev. Fluid Mech.* **36**: 413–455.
- Williamson, C. H. K. and Roshko, A. (1988). Vortex formation in the wake of an oscillating cylinder, *J. Fluids & Struct.* **2**: 355–381.
- Williamson, C. H. K. and Roshko, A. (1990). Measurements of base pressure in the wake of a cylinder at low Reynolds numbers, *Z. Flugwiss. Weltraumforsch.* **14**: 38–46.
- Wu, J., Sheridan, J., Soria, J. and Welsh, M. C. (1994). An experimental investigation of streamwise vortices in the wake of a bluff body, *J. Fluids & Struct.* **8**: 621–625.
- Yang, Y. and Rockwell, D. (2002). Wave interaction with a vertical cylinder: Spanwise flow patterns and loading, *J. Fluid Mech.* **460**: 93–129.
- Zhang, J. and Dalton, C. (1999). The onset of three-dimensionality in an oscillating flow past a fixed circular cylinder, *Intnl J. Num. Meth. Fluids* **30**: 19–42.